



**HAL**  
open science

# The Matryoshka paradigm: Application to a priori stochastic homogenization of bone elasticity

Daide Gagliardi

► **To cite this version:**

Daide Gagliardi. The Matryoshka paradigm: Application to a priori stochastic homogenization of bone elasticity. Structural Biology [q-bio.BM]. Université Paris-Est, 2016. English. NNT: 2016PESC1115 . tel-01563185

**HAL Id: tel-01563185**

**<https://theses.hal.science/tel-01563185>**

Submitted on 17 Jul 2017

**HAL** is a multi-disciplinary open access archive for the deposit and dissemination of scientific research documents, whether they are published or not. The documents may come from teaching and research institutions in France or abroad, or from public or private research centers.

L'archive ouverte pluridisciplinaire **HAL**, est destinée au dépôt et à la diffusion de documents scientifiques de niveau recherche, publiés ou non, émanant des établissements d'enseignement et de recherche français ou étrangers, des laboratoires publics ou privés.

THÈSE DE DOCTORAT de l'*Université Paris-Est*  
*École Doctorale SIE - Sciences, Ingénierie et Environnement*

Spécialité : MÉCANIQUE

présentée par  
DAVIDE GAGLIARDI

LE PARADIGME DE LA MATRYOSHKA.  
APPLICATION À L'HOMOGENÉISATION STOCHASTIQUE  
DES PROPRIÉTÉS MATÉRIELLES DU TISSU OSSEUX

réalisée au  
LABORATOIRE MODÉLISATION ET SIMULATION MULTI ECHELLE  
(MSME UMR 8208 CNRS)

soutenue le 15 décembre 2016 devant le jury composé de :

---

M. Jean-Marie CROLET,	<i>Professeur</i> <i>Université de Franche-Comté</i>	Examineur (Président)
M. Ridha HAMBLI,	<i>Professeur</i> <i>Université d'Orléans</i>	Rapporteur
M. Marc MIGNOLET,	<i>Professeur</i> <i>Arizona State University</i>	Rapporteur
M. Salah NAILI,	<i>Professeur</i> <i>Université Paris-Est Créteil</i>	Directeur de thèse
M. Vittorio SANSALONE,	<i>Maître de Conférences (HDR)</i> <i>Université Paris-Est Créteil</i>	Co-Directeur de thèse
M. Christian SOIZE,	<i>Professeur</i> <i>Université Paris-Est Marne-la-Vallée</i>	Examineur

---



THE MATRYOSHKA PARADIGM.  
APPLICATION TO A PRIORI STOCHASTIC HOMOGENIZATION  
OF BONE ELASTICITY

by  
DAVIDE GAGLIARDI

THESIS submitted for the degree of  
DOCTOR OF PHILOSOPHY in MECHANICS  
at the *Université Paris-Est*

*École Doctorale SIE - Sciences, Engineering and Environment*

realized in the  
LABORATORY OF MULTI-SCALE MODELING AND SIMULATION  
(MSME UMR 8208 CNRS)

defended on December the 15th 2016 in front of the following examination board:

---

M. Jean-Marie CROLET,	<i>Professor</i> <i>Université de Franche-Comté</i>	Examiner (Chairman)
M. Ridha HAMBALI,	<i>Professor</i> <i>Université d'Orléans</i>	Advisor
M. Marc MIGNOLET,	<i>Professor</i> <i>Arizona State University</i>	Advisor
M. Salah NAILLI,	<i>Professor</i> <i>Université Paris-Est Créteil</i>	PhD Supervisor
M. Vittorio SANSALONE,	<i>Associate Professor</i> <i>Université Paris-Est Créteil</i>	PhD Co-Supervisor
M. Christian SOIZE,	<i>Professor</i> <i>Université Paris-Est Marne-la-Vallée</i>	Examiner

---



*Two roads diverged in a yellow wood,*

...

*Two roads diverged in a wood, and I—*

*I took the one less traveled by,*

*And that has made all the difference.*

---

R.Frost,  
*The Road Not Taken*  
(Mountain Interval).



## Acknowledgements

There are many people to whom I owe much.

Firstly I would like to express my sincere gratitude to my supervisors. Prof. Salah Naili, who accepted me to develop this multidisciplinary research and constantly suggested me the main directions to follow and tools to be adopted. I will never appreciate enough your patience in making me focus on the main goals of this thesis and in attenuating my exuberance in generalizing solutions. I want to thank Dr. Vittorio Sansalone, who offered invaluable assistance and support, inspiring me to constantly search ways to to simplify difficult concepts, and making me pay attention to the audience to whom the message was to be delivered (the title of this work, *matrjoshka paradigm* is a clear example of this). I would like to thank each member of my dissertation committee: Prof.s Marc Mignolet, Ridha Hambli, Jean-Marie Crolet and Christian Soize for doing me the honor to evaluate this thesis.

Next, I would like to acknowledge the Université Paris-Est for the financial support to this research technical instrumentations, as well as the Italian Università di Roma Tor Vergata for transmitting me the necessary transversal competences to achieve this result.

I wish to tribute to all the academics that made me to grow and who spurred me to give my best. My grateful thoughts go to Prof.s: Roberta Dal Passo, Alessandra Cutrí, Paolo Podio-Guidugli, Giovanni Bellettini, Benedetto Scoppola, Sergio Galeani, Giuseppe Balestrino, Andrey Varlamov, Vieri Mastropietro last but not least Giuseppe Tomassetti, who introduced me into the world of academic research. A special thought goes out to Prof. Luigi del Re of the JKU of Linz, with whom I first approached academic research working two months before starting this new adventure. I would like to address the earnest thanks to Paolo Podio-Guidugli, for the words of encouragement he had for me at the late stage of this work.

Then, there are a few people I wish to credit for their presence by my side and who were important during these three years. I would like to start expressing my gratefulness to all the MSME team. I would like to thank my earliest travel companions: Antoissee and Son, with whom I started the same path from the beginning, for their friendship and empathic support. My colleagues and officemates, Romain, Erica, Adrian and Sarah for their sympathy, and for sharing with me joys and pains of this journey. Giuseppe, for supporting me throughout this period, also by sharing the story of his previous Franco-Italian Ph.D. experience during an evening in Lion and, for the constant supply of coffee capsules. A special thank goes to also to Ilaria and Antoine that never failed to encourage me and helped me in preparing the post-defence-reception. I thank also my former colleagues Thibault, Hieu, Mathieu, Alexandre, Gilles for their friendship and advice, whose works and interests I would have liked to know better. Hung-Son and Clara that gave me access to the laboratory and research facilities. Without their technical support it would not have been possible to perform this research. Also I want to acknowledge all my friends, those of the residence AEPP in Paris: Raphael, Anie, Mikael, Marie and Danil that patiently soothed my difficult moments and all those on the other side of the Alps Alessio, Antonio, Patrik that I never forgot.

Finally I want to mention my family. Antonio, Giovanna, Bianca, you never lacked me to provide the support and told me the best words when I needed. Last but not least I want to thank you Maria Cristina, the very goad during these days, who taught me the true meaning of sacrifice.



# Contents

1	Contexte et motivation . . . . .	12
2	Organisation du manuscrit . . . . .	14
2.1	Résumé des chapitres . . . . .	15
2.2	Chapitre 1 . . . . .	15
2.3	Chapitre 2 . . . . .	16
2.4	Chapitre 3 . . . . .	17
2.5	Chapitre 4 . . . . .	18
<b>1</b>	<b>Stochastic multiscale modelling of cortical bone elasticity based on high-resolution imaging</b>	<b>22</b>
1.1	Introduction . . . . .	24
1.2	Materials and methods . . . . .	26
1.2.1	Experimental data . . . . .	26
1.2.2	Model . . . . .	28
1.3	Results . . . . .	36
1.3.1	Volume fractions . . . . .	36
1.3.2	Elastic moduli . . . . .	38
1.4	Discussion . . . . .	43
1.4.1	The multiscale model: a compromise between accuracy and simplicity . .	44
1.4.2	The stochastic multiscale model: a comprehensive description of bone . .	46
1.4.3	The nominal model: a simple and accurate estimate of expected elastic moduli . . . . .	46
1.4.4	Whole bone: heterogeneity <i>vs.</i> homogeneity . . . . .	47
1.4.5	Limitations and future research directions . . . . .	48
1.5	Conclusion . . . . .	50
<b>2</b>	<b>Tissue mineral density measured at the sub-millimeter scale provides reliable statistical estimates of elastic properties of bone matrix</b>	<b>59</b>
2.1	Introduction . . . . .	61
2.2	Materials and Methods . . . . .	63
2.2.1	Imaging . . . . .	63
2.2.2	Representative volume elements . . . . .	63
2.2.3	Experimental compositional data: HP and TMD . . . . .	64
2.2.4	Hierarchical description of bone and volume fractions . . . . .	66

2.2.5	Stochastic modeling of uncertain composition of bone US . . . . .	67
2.2.6	Continuum micromechanical models of bone ultrastructure . . . . .	71
2.3	Results & Discussion . . . . .	75
2.3.1	Statistical results . . . . .	75
2.3.2	Parameters of the stochastic and nominal models . . . . .	76
2.3.3	TMD/Vox and VF/Vox concepts . . . . .	76
2.3.4	TMD/RVE and VF/RVE concepts . . . . .	82
2.3.5	Voxel-scale <i>vs.</i> RVE-scale concepts . . . . .	86
2.4	Conclusion . . . . .	88
2.4.1	TMD-based <i>vs.</i> RVE-based concepts . . . . .	90
2.4.2	Voxel-scale <i>vs.</i> RVE-scale concepts . . . . .	91
2.4.3	Limitations and perspectives . . . . .	92
2.5	Appendix . . . . .	94
A	Numerical solution of the stochastic model . . . . .	94
B	Closure of the symmetry group under average operator . . . . .	95
C	Dispersion parameter of rules of mixtures . . . . .	96
D	Other results on TMD and VF/Vox concept . . . . .	97
<b>3</b>	<b>Estimation of bone-elasticity. <i>A priori</i> influence of the couple TMD-HP by a model based on <math>\mu</math>CT Imaging. A multi-techniques validation.</b>	<b>102</b>
3.1	Introduction . . . . .	104
3.2	Material and Methods . . . . .	106
3.2.1	Hierarchical description of cortical bone . . . . .	106
3.2.2	What information on cortical bone from $\mu$ CT? . . . . .	107
3.2.3	Experimental data from SR – $\mu$ CT imaging . . . . .	108
3.2.4	Statistical information on HP and $\overline{\text{TMD}}$ from SR – $\mu$ CT images . . . . .	110
3.2.5	Volume fractions of essential constituents . . . . .	110
3.2.6	Overview on the homogenization . . . . .	111
3.2.7	Elastic properties of essential constituents . . . . .	117
3.2.8	Stochastic micromechanical ( $S\mu$ M) model of cortical bone . . . . .	117
3.2.9	Nominal micromechanical ( $N\mu$ M) model of cortical bone . . . . .	121
3.2.10	Micro-finite element ( $\mu$ FE) model of cortical bone . . . . .	122
3.2.11	Micro-Fast Fourier Transform ( $\mu$ FFT) model of cortical bone . . . . .	122
3.3	Results and discussion . . . . .	123
3.3.1	Numerical set up of the stochastic models of $\overline{\text{TMD}}$ and HP. . . . .	123
3.3.2	Stochastic and nominal micromechanical models of cortical bone elasticity	125
3.3.3	Results of the $\mu$ FE and $\mu$ FFT models . . . . .	127
3.3.4	Validation of the $S\mu$ M of cortical bone: by comparison with the $\mu$ FE and $\mu$ FFT estimates . . . . .	129
3.3.5	Accuracy of the stochastic model . . . . .	130
3.4	Conclusion and perspective . . . . .	132
3.5	Appendix . . . . .	134
A	<b>Kelvin’ representation of a 4th-order tensor</b> . . . . .	<b>134</b>

<b>B</b>	<b>Representation of classes of material symmetry</b>	135
<b>C</b>	<b>Jensen' inequality</b>	136
<b>D</b>	<b>Tables of the FFT and FEM results</b>	137
<b>E</b>	<b>Supplementary figures</b>	137
<b>F</b>	<b>Effects of the threshold <math>q</math> on HP, <math>\overline{\text{TMD}}</math> and nominal elastic <i>moduli</i></b>	137

#### 4 The Matr-yoshka paradigm.

##### Stochastic model for random matrices and fields with symmetry properties.

##### Application to bone tissue. 146

4.1	Introduction	148
4.2	The general problem	149
4.2.1	Motivation and minimal available information	149
4.2.2	Anisotropic problem from a minimal available information	150
4.3	Constraint on the subspace of a material symmetry class	153
4.3.1	Constraint on the subspace of a material symmetry class for the normalized random matrix	154
4.3.2	Generation of the random vector $\mathbf{G}$	156
4.3.3	Estimation of mathematical expectation	159
4.4	From random matrix to random fields	161
4.4.1	Small or moderate number of points	161
4.4.2	Large number of points	162
4.5	Applications to random matrices	165
4.5.1	Isotropic class	165
4.5.2	Transversely isotropic class	168
4.5.3	Orthotropic class	171
4.6	Numerical results	174
4.6.1	Examples of random matrices for the isotropic material class	174
4.6.2	Example of the random field for isotropic material class	176
4.7	Conclusion and perspective	178
4.8	Appendix	179
<b>A</b>	<b>Kelvin' representation of a 4th-order tensor</b>	179
<b>B</b>	<b>Representation of classes of material symmetry</b>	180

#### A Scientific Production 185

# List of Figures

1	Structure hiérarchisée de l'os, de l'échelle de l'organe à celle du nanomètre. . . . .	12
2	Exemples de modèles du tissu osseux basés sur l'imagerie : micro-mécanique, méthode aux éléments finis, transformée rapide de Fourier . . . . .	13
3	Images prises par tomodensitométrie (CT-scan) de la partie proximale du fémur humain <i>in vivo</i> (à gauche) et <i>in vitro</i> (à droite). . . . .	13
4	Image d'une Matryoshka, plus communément appelée poupée russe. . . . .	15
5	Modèle simplifié de l'os cortical utilisé dans la thèse. . . . .	16
1.1	Reconstructed 3-D model of the bone sample and Cartesian frame. . . . .	27
1.2	From left to right: Three cross-sections of the bone sample at $z = 150, 350, 550 \mu m$ , respectively. RVEs are marked by green squares (colors in online version). . . . .	28
1.3	Sketch of the multiscale model. . . . .	29
1.4	Algorithm used for solving the stochastic multiscale model. . . . .	35
1.5	PDFs of the random volume fractions estimated on the basis of $N = 10^6$ statistically independent realisations. Red, green and blue solid lines represent the distributions of the statistically independent realisations of $F_{\text{pore}}^{\text{cort}}$ , $F_{\text{col}}^{\text{ultra}}$ , and $F_{\text{HA}}^{\text{foam}}$ , respectively. Red, green and blue knots and dotted vertical lines depict the corresponding mean values. (Colors in online version.) . . . . .	38
1.6	<i>Statistics</i> of the random volume fractions and their <i>statistical estimators</i> as a function of the number of realisations. Red, green and blue lines, bars and symbols refer to $F_{\text{pore}}^{\text{cort}}$ , $F_{\text{col}}^{\text{ultra}}$ , and $F_{\text{HA}}^{\text{foam}}$ , respectively. Diamonds, triangles and circles refer to $F_{\text{pore}}^{\text{cort}}$ , $F_{\text{col}}^{\text{ultra}}$ , and $F_{\text{HA}}^{\text{foam}}$ , respectively. On the top: Mean values and dispersions (straight dashed lines) and their statistical estimators (solid lines). On the bottom: Magnitude of the relative errors of the statistical estimators of the mean values and dispersions. Dark coloured lines are exponential trend lines. (Colors in online version.) . . . . .	39
1.7	Axial (left) and shear (right) elastic moduli along the axis and in the cross section of the femoral neck, that is $Y_3$ and $G_{12}$ , respectively. Red crosses refer to the realisations of the random elastic moduli. Brown straight lines refer to the <i>statistics</i> of the random elastic moduli. Solid, thick-dashed and thin-dashed straight brown lines refer to the mean values, 50% and 95% confidence intervals of the random moduli, respectively. Solid black straight lines refer to the nominal elastic moduli. (Colors in online version.) . . . . .	41

1.8	Axial (left) and shear (right) moduli along the axis and in the cross section of the femoral neck, that is $Y_3$ and $G_{12}$ , respectively. Solid, thick-dashed and thin-dashed brown lines refer to the <i>statistical estimators</i> of the mean values, 50% and 95% confidence intervals of the random elastic moduli, respectively. Solid black straight lines refer to the nominal elastic moduli. (Colors in online version.) . . .	41
1.9	Approximations of PDFs of the random elastic moduli. Vertical brown straight lines refer to the <i>statistics</i> of the random elastic moduli. Solid, thick-dashed and thin-dashed brown lines refer to the mean values, 50% and 95% confidence intervals of these random moduli, respectively. Solid black straight lines refer to the nominal elastic moduli. (Colors in online version.) . . . . .	42
1.10	Comparison between the elastic moduli of the actual RVEs and the <i>statistics</i> of the random elastic moduli. Blue circles refer to the 12 RVEs in Tab. 1.1. Solid, thick-dashed and thin-dashed brown lines refer to the mean values, 50% and 95% confidence intervals of the random moduli, respectively. Solid black straight lines refer to the nominal elastic moduli. (Colors in online version.) . . . . .	44
2.1	On the left: Segmented bone sample; blue lines denote a cylindrical surface at approximately 1.5 mm from the periosteum. On the right: Location of the RVEs (unit of length: $\mu m$ ); the centers of RVEs lie on the cylindrical surface sketched on the left. . . . .	64
2.2	Representation of the RVEs. Colors refer to the GLs of the original images. Asterisks indicate the RVEs used for calibration purposes. . . . .	65
2.3	Sketch of the procedure for evaluating the TMD and VFs within each RVE. . .	66
2.4	Sketch of the multiscale model. Cortical tissue (on the left) and ultra-structure (US, in the middle) are represented in the cross section plane of the bone sample, orthogonal to the axis of the Haversian canals. Haversian canals and collagen fibers are modeled as cylindrical inclusions in the cortical tissue and US, respectively. Mineral foam (MF, on the right) is modeled as a disordered mixture of mineral and water spherical particles (orientation is not meaningful). . . . .	71
2.5	<b>TMD/Vox and VF/Vox concepts.</b> Convergence of the statistical estimators of the random TMD in the TMD/Vox concept (green lines) and of the random VFs in the VF/Vox concept (red lines). On the left: relative error on the mean values; On the right: absolute error on the dispersions. . . . .	77
2.6	<b>TMD/Vox and VF/Vox concepts.</b> Convergence of the statistical estimators of some random elastic moduli of the MF. On the left: Young modulus; On the right: Poisson coefficient. Green and red lines refer to the TMD/Vox and VF/Vox concepts, respectively. Solid and dashed lines refer to mean values and 50% confidence intervals, respectively. Black lines refer to the nominal model. . .	78

2.7	<b>TMD/Vox and VF/Vox concepts.</b> Convergence of the statistical estimators of some random elastic moduli of the US. On the left: axial modulus $Y_3$ ; On the right: lateral contraction coefficient $\nu_{31}$ (subscripts refer to the frame in Fig. 2.1). Green and red lines refer to the TMD/Vox and VF/Vox concepts, respectively. Solid and dashed lines refer to mean values and 50% confidence intervals, respectively. Black lines refer to the nominal model. . . . .	78
2.8	<b>TMD/Vox and VF/Vox concepts.</b> Scattered values and PDFs of the random TMD and VFs based on experimental data at the voxel scale. (a) Scatter plot of the realizations of the random VFs in concepts TMD/Vox (green dots) and VF/Vox (red dots) and analytical relationship between the two VFs encoded in Eqs. (2.7) (blue line). (b)-(d) PDFs of the TMD and of the random VFs in concepts TMD/Vox (green lines) and VF/Vox (red lines) and experimental PDF (blue lines). . . . .	80
2.9	<b>TMD/Vox and VF/Vox concepts.</b> Relative error on the mean values (on the left) and absolute error on the dispersions (on the right) of the random TMD and VFs after $10^6$ realizations, see Eq. (2.14). Green and red bars refer to TMD/Vox and VF/Vox concepts, respectively. Symbols * denote the derived random variables ( <i>i.e.</i> , VFs in the TMD/Vox concept and TMD in the VF/Vox concept). . . . .	81
2.10	<b>TMD/Vox and VF/Vox concepts.</b> Random elastic moduli of the isotropic mineral foam predicted by the TMD/Vox (green data) and VF/Vox (red data) concepts. PDFs (first row, subplots (a)-(b)) and scattered values (second row, subplots (c)-(d)) of the Young modulus (left column) and Poisson coefficient (right column). Blue lines in subplots (a)-(b) refer to the PDFs obtained by homogenization of the actual voxel-scale data. Blue lines in subplots (c)-(d) depict the relationship between the TMD and the elastic moduli when using Eq. (2.5)(c); moreover, black crosses depict the results of the nominal model. . . . .	84
2.11	<b>TMD/Vox and VF/Vox concepts.</b> Random elastic moduli of the transversely isotropic ultrastructure predicted by the TMD/Vox (green data) and VF/Vox (red data) concepts. PDFs (first row, subplots (a)-(b)) and scattered values (second row, subplots (c)-(d)) of elastic moduli $Y_3$ (left column) and $\nu_{31}$ (right column); Subscripts refer to the frame in Fig. 2.1. Blue lines in subplots (a)-(b) refer to the PDFs obtained by homogenization of the actual voxel-scale data. Blue lines in subplots (c)-(d) depict the relationship between the TMD and the elastic moduli when using Eq. (2.5)(c); moreover, black crosses depict the results of the nominal model. . . . .	85
2.12	<b>TMD/RVE and VF/RVE concepts.</b> Convergence of the statistical estimators of the mean value (solid lines) and 50 % confidence interval (dashed lines) of some random elastic moduli of the ultrastructure. On the left: axial modulus $Y_3$ ; On the right: lateral contraction coefficient $\nu_{31}$ of the bone US (subscripts refer to the frame in Fig. 2.1). Green and red lines refer to the TMD/RVE and VF/RVE concepts, respectively. Black lines refer to the nominal model. . . . .	86

2.13	<b>TMD/RVE and VF/RVE concepts.</b> Scattered values and PDFs of the random TMD and VFs based on experimental data at the RVE scale. (a) Scatter plot of the realizations of the random VFs in concepts TMD/RVE (green dots) and VF/RVE (red dots) and analytical relationship between the two VFs encoded in Eq. (2.7) (blue line). (b)-(d) PDFs of the random TMD and VFs corresponding to concepts TMD/RVE (green lines) and VF/RVE (red lines); . . . . .	87
2.14	<b>TMD/RVE and VF/RVE concepts.</b> Random elastic moduli of the MF predicted by the TMD/RVE (green data) and VF/RVE (red data) concepts. PDFs (first row, subplots (a)-(b)) and scattered values (second row, subplots (c)-(d)) of the Young modulus (left column) and Poisson coefficient (right column). Blue lines in subplots (c)-(d) depict the relationship between the TMD and the elastic moduli when making use of Eqs. (2.7); moreover, black crosses depict the results of the nominal model. . . . .	90
2.15	<b>TMD/RVE and TMD/RVE concepts.</b> Random elastic moduli of the transversely isotropic ultrastructure predicted by the TMD/RVE (green data) and VF/RVE (red data) concepts. PDFs (first row, subplots (a)-(b)) and scattered values (second row, subplots (c)-(d)) of elastic moduli $Y_3$ (left column) and $\nu_{31}$ (right column); Subscripts refer to the frame in Fig. 2.1. Blue lines in subplots (c)-(d) depict the relationship between the TMD and the elastic moduli when making use of Eqs. (2.7); moreover, black crosses depict the results of the nominal model. . . . .	91
2.16	Elastic moduli of the ultrastructure. Comparison between the elastic moduli of actual RVEs (blue and light blue circles, see Fig. 2.1) and the corresponding statistics predicted by the TMD/RVE concept (green lines; solid, thick-dashed and thin-dashed lines refer to mean values, 50% and 90% confidence intervals, respectively). Black lines depict the nominal values. . . . .	92
2.17	Elastic moduli of the resulting isotropic model mineral foam and of transverse isotropic model of ultra-structure. . . . .	101
3.1	Multi-scale description of cortical bone. . . . .	107
3.2	Experimental information obtained from SR- $\mu$ CT images. (a) Typical graylevel cross section; Haversian porosity (HP) and ultrastructure (US) correspond to black and gray regions, respectively. (b) Typical RVE, <i>i.e.</i> cubic region with edge length of 50 voxels $\sim 0.5$ mm; GLs are represented using the “jet” color-map of Matlab. (c) GL distribution in the RVE and threshold $q$ between HP and US. (d) TMD distribution in the US and average value $\overline{\text{TMD}}$ . . . . .	108
3.3	Global and local reference frames on the bone sample and on a typical RVE, respectively, and localization of the RVEs (red and light red cubes refer to <i>Calib</i> and <i>Ctrl</i> datasets, respectively). See text for more details. . . . .	109
3.4	Sketch of the procedure for evaluating the HP, $\overline{\text{TMD}}$ , and VFs in a RVE. . . . .	111
3.5	Scatter plot of the pairs of measures $(\overline{\text{TMD}}, \text{HP})$ for each of RVE $_i$ related to the <i>Calib</i> (solid circles) and <i>Ctrl</i> (empty circles) datasets. . . . .	118

3.6	Convergence plots of the stochastic models of $\overline{\text{TMD}}$ (green lines with ‘x’ markers) and HP (dark red lines with ‘o’ markers): Relative error of the mean values (on the left) and absolute error of the dispersions (on the right) as a function of the number of realizations. . . . .	124
3.7	Convergence plots of the random elastic <i>moduli</i> of CB (green lines): Mean values and confidence intervals of the axial modulus $Y_3$ (on the left) and of the lateral contraction ratio $\nu_{31}$ (on the right) as a function of the number of realizations. Black lines depict the nominal values. Subscripts refer to the frames depicted in Fig. 3.3. . . . .	125
3.8	Reconstruction of the most anisotropic RVEs. . . . .	127
3.9	Distance of the anisotropic elastic tensors of the RVEs obtained by means of the $\mu\text{FFT}$ and $\mu\text{FE}$ models from transverse isotropy (on the left) and orthotropic (on the right) symmetry classes. . . . .	128
3.10	Elastic <i>moduli</i> of cortical bone. Differences between $\mu\text{FE}$ and $\mu\text{FFT}$ estimations on individual RVEs (crosses) and average differences (solid lines). . . . .	129
3.11	Relative differences of the FEM and FFT estimate from the $S\mu\text{M}$ model. Axial <i>modulus</i> in the direction of bone axis ( $Y_3$ ) and lateral contraction ratio ( $\nu_{31}$ ). . .	131
3.12	Comparison of the estimation of the elastic <i>moduli</i> as function of TMD and HP measure : (1) parametric study (gray surface); (2) region of the surface corresponding to the 50%, 95% and 99% confidence intervals of the stochastic model (green area with multiple transparencies); (3) estimations of the 12 RVEs by $\mu\text{FE}$ (blue dots); (4) FFT (red triangles); (5) Nominal model (+). . . . .	132
3.13	Axial <i>modulus</i> in the direction of bone axis $Y_3$ and lateral contraction ratio $\nu_{31}$ .	133
3.14	Comparison of the estimation of the elastic moduli as function of TMD and HP measure: (1) - parametric study (gray surface); (2) - region of the surface corresponding to the 50%; 95%; 99% confidence intervals of the of stochastic model ( green area with multiple transparencies); (3) - estimations of the 12 RVEs by $\mu\text{FE}$ (blue dots); (4) - FFT (red triangles); (5) - Nominal model (+). .	143
3.15	Comparison of the estimation of the elastic moduli as function of TMD and HP measure : (1) - parametric study (gray surface); (2) - region of the surface corresponding to the 50%; 95%; 99% confidence intervals of the of stochastic model ( green area with multiple transparencies); (3) - estimations of the 12 RVEs by $\mu\text{FE}$ (blue dots); (4) - FFT (red triangles); (5) - Nominal model (+). .	144
3.16	Comparison of estimation of elastic moduli as function of TMD and HP measure : 1 - Nominal model (black line) 2 - Average value of random realization of the Stoc. TMD-HP model, 3 - 50% and 95% Confidence interval of the Stoc. TMD-HP model 4 - $\mu\text{FE}$ model realization . . . . .	145
4.1	Scheme for the construction of the matrix representation of a random elastic tensor fluctuating inside a prescribed material symmetry class. . . . .	153
4.2	Drawing of some example of realization of random field with spatial correlation. Three iso-surfaces of these fields are plotted. . . . .	164
4.3	Evolution of the map $k \mapsto \text{convMes}(k)$ defined by (4.3.31) for $k = 1, \dots, 10^7$ . . .	175

4.4	PDF of the couple $[G_1, G_2]$ corresponding to the initial Lagrange's multiplier(left) on the interval $k \in [M_0, M]$ . Evolution of the couple $[\mathbf{U}_1^k, \mathbf{V}^k]$ for the first instants after $k = M_0$ (right). . . . .	176
4.5	Random fields with spatial correlation. Regular discretization of the set $\Omega = [0, 4]^3$ in $n_p = 4913$ points. On the top the components of the auxiliary Gaussian random fields $\widehat{\Xi}^1(x)$ and $\widehat{\Xi}^2(x)$ simulated with the same autocorrelation length $L_1 = L_2 = L_3 = 1$ and parameter $\nu = 30$ . On the bottom the realizations of the bulk <i>modulus</i> random field $K(x)$ and the shear <i>modulus</i> random field $\mu(x)$ corresponding to the auxiliary random fields. The isosurfaces corresponding to the estimated quantiles $q = 5\%, 25\%, 50\%, 75\%$ and $95\%$ are added. . . . .	178

# List of Tables

1.1	Spatial averages and dispersions of experimental values of HP, TMD, and volume fractions of bone constituents for individual RVEs, the whole ensemble, and the whole ensemble but RVEs #9 and #10. Location of RVEs refers to the $(z, \theta)$ coordinates described in Sec. 1.2.1. N/A: Not applicable. . . . .	37
1.2	Statistics of the random moduli, nominal elastic moduli, and their relative differences (Eq. (1.29)). Random moduli - $Y_1$ : axial modulus in the cross-section plane; $Y_3$ : axial modulus along the axis of the femoral neck; $G_{12}$ : shear modulus in the cross-section; $G_{13} = G_{23}$ : shear modulus in the sagittal plane; $V_{12} = V_{21}$ : lateral contraction modulus in the cross-section; $V_{13} = V_{23}$ : lateral contraction modulus in the sagittal plane ( <i>i.e.</i> , contraction in the cross-section plane due to a unit extension in the axial direction). Subscripts $\{1, 2, 3\}$ refer to the Cartesian frame in Fig. 1.1. Dispersion values are dimensionless. Nominal moduli and relative differences follow the same notation. . . . .	40
2.1	Stochastic and nominal modeling concepts. . . . .	72
2.2	Experimental statistics at the voxel scale (databases $\mathcal{DB}_{\text{TMD}}^{\text{exp}}$ , $\mathcal{DB}_{f_{\text{I}}}^{\text{exp}}$ , and $\mathcal{DB}_{f_{\text{II}}}^{\text{exp}}$ ). The last row of the table indicates the modeling concepts using these data. . . . .	76
2.3	Experimental statistics at the voxel scale for each RVE. . . . .	76
2.4	Experimental statistics at RVE scale (databases $\mathcal{DB}_{\text{TMD}}^{\text{exp}}$ , $\mathcal{DB}_{f_{\text{I}}}^{\text{exp}}$ , and $\mathcal{DB}_{f_{\text{II}}}^{\text{exp}}$ ). The last row of the table indicates the modeling concepts using these data. . . . .	77
2.5	Optimal Lagrange multipliers for the four modeling concepts. . . . .	77
2.6	<b>TMD/Vox and VF/Vox concepts.</b> Elastic properties of the MF: nominal model and statistics ( $N_{\text{s.i.r.}} = 10^5$ realizations) of the stochastic concepts TMD/Vox and VF/Vox. $Y$ : Young modulus; $G$ : shear modulus; $\nu$ : Poisson coefficient. . . . .	82
2.7	<b>TMD/Vox and VF/Vox concepts.</b> Elastic properties of the US: nominal model and statistics ( $N_{\text{s.i.r.}} = 10^5$ realizations) of the stochastic concepts TMD/Vox and VF/Vox. $Y_i$ : axial modulus in the direction $i$ ; $G_{ij}$ : shear modulus in the plane $ij$ ; $\nu_{ij}$ : lateral contraction coefficient in the plane $ij$ ; Subscripts refer to the frame in Fig. 2.1. . . . .	83
2.8	<b>TMD/Vox and VF/Vox concepts.</b> Scalar dispersions of the random elastic tensors of MF and US. . . . .	83

---

2.9	<b>TMD/RVE and VF/RVE concepts.</b> Elastic properties of the MF: nominal model and statistics (resulting from $N_{\text{s.i.r.}} = 10^5$ realizations) of the stochastic models of concepts TMD/RVE and VF/RVE. $Y$ : Young modulus; $G$ : shear modulus; $\nu$ : Poisson coefficient. . . . .	88
2.10	<b>TMD/RVE and VF/RVE concepts.</b> Elastic properties of the US: nominal model and statistics (resulting from $N_{\text{s.i.r.}} = 10^5$ realizations) of the stochastic models of concepts TMD/RVE and VF/RVE. $Y_i$ : axial modulus in the direction $\mathbf{e}_i$ ; $G_{ij}$ : shear modulus in the plane $(\mathbf{e}_i, \mathbf{e}_j)$ ; $\nu_{ij}$ : lateral contraction coefficient in the plane $(\mathbf{e}_i, \mathbf{e}_j)$ ; Subscripts refer to the frame in Fig. 2.1. . . . .	89
2.11	<b>TMD/RVE and VF/RVE concepts.</b> Scalar dispersions of the random elastic tensors of MF and US. . . . .	89
3.1	Elastic properties of essential constituents of bone. . . . .	117
3.2	Experimental statistics of the <i>Calib</i> dataset. . . . .	124
3.3	Elastic <i>moduli</i> of cortical bone: <i>nominal</i> values and statistics (resulting from $N = 10^5$ realizations) of the <i>stochastic</i> model. . . . .	125
3.4	Mean values of the base coefficients (see Appendix <b>B</b> ) of the random elastic tensors of MF, US and CB. . . . .	126
3.5	Scalar dispersions of the random elastic tensors of MF, US and CB. . . . .	126
3.6	Average differences between the $\mu$ FE and $\mu$ FFT estimations of the elastic <i>moduli</i> of cortical bone. . . . .	129
3.7	Stochastic model of <i>Cortical bone</i> approximation to $\mu$ FE and $\mu$ FFT estimations of elastic properties. Average value of the relative difference. . . . .	130
3.8	Estimation by FFT methods. Projection onto the transverse isotropic subspace $\text{TIE}_n$ . . . . .	137
3.9	Estimation by FEM methods. Projection onto the transverse isotropic subspace $\text{TIE}_n$ . . . . .	138
3.10	Effects of the variations of $q$ on the first and second order statistics of HP, $\overline{\text{TMD}}$ and <i>nominal</i> elastic <i>moduli</i> of cortical bone. . . . .	139
4.1	Average tensors of three homogenized materials: mineral foam (MF), ultra-structure (US) and cortical bone (CB). Coefficients of the representations on the respective basis. . . . .	174
4.2	Overall measure of variation of stochastic tensor of for mineral-foam (MF), ultra-structure (US) and cortical bone (CB), resulting from the stochastic model. . . . .	175
4.3	Results of the optimization of the index function through MATLAB Optimization toolbox. Evolution of the cost index defined by (4.5.21). . . . .	176

# Introduction générale

## 1 Contexte et motivation

Non seulement la structure hiérarchisée du tissu osseux mais aussi son hétérogénéité et son anisotropie, caractéristiques propres à la plupart des matériaux vivants, rendent en pratique impossible la définition d'un modèle déterministe fiable de ses propriétés matérielles.

Du fait de la complexité de cette structure hiérarchisée, montrée schématiquement sur la Fig. 1 (Rho et al., 1998), des approches multi-échelles sont nécessaires pour décrire les propriétés mécaniques du tissu osseux à l'échelle de l'organe en prenant en compte son organisation et sa composition aux échelles sous-jacentes.

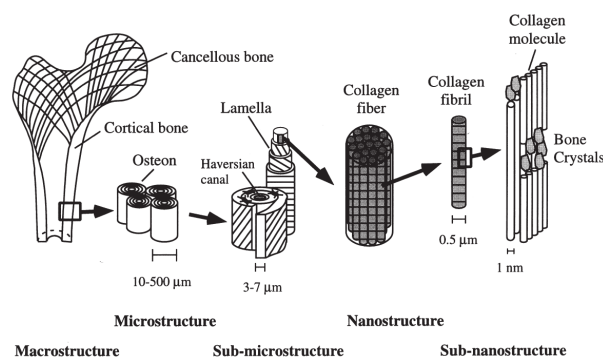


FIGURE 1 : Structure hiérarchisée de l'os, de l'échelle de l'organe à celle du nanomètre.

Dans cet esprit, de nombreuses méthodes, dites d'*homogénéisation*, ont été proposées permettant de déduire les propriétés effectives (ou encore efficaces) du tissu osseux en combinant opportunément les propriétés mécaniques de ses constituants essentiels. Ces méthodes peuvent être regroupées en deux classes principales : les méthodes analytiques (et semi-analytiques) et celles purement numériques. Parmi les premières, on trouve les méthodes d'homogénéisation en champs moyen (dites aussi micro-mécaniques) (Suquet, 1997; Hellmich et al., 2004) et asymptotique (Aoubiza et al., 1996; Predoi-Racila and Crolet, 2008; Parnell et al., 2012; Rohan et al., 2012) ainsi que d'autres techniques *ad hoc* (Yoon and Cowin, 2008). Dans la seconde classe, on peut inclure les approches cherchant à identifier les propriétés efficaces d'un milieu hétérogène par la solution de problèmes aux limites équivalents à travers des méthodes numériques telles que la méthode aux éléments finis (FEM) (Barkaoui and Hambli, 2011, 2014; Chen et al., 2017)

ou la méthode de la transformée de Fourier rapide (FFT) (Moulinec and Suquet, 1998; Brisard and Dormieux, 2010; Monchiet and Bonnet, 2012).

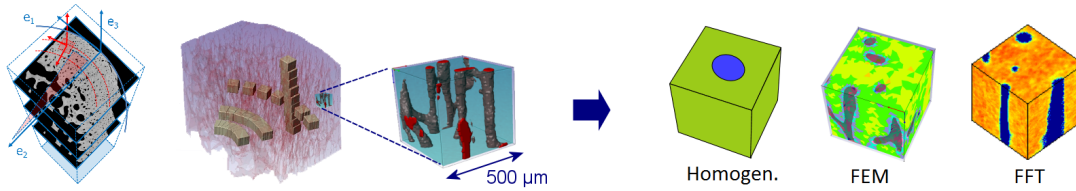


FIGURE 2 : Exemples de modèles du tissu osseux basés sur l'imagerie : micro-mécanique, méthode aux éléments finis, transformée rapide de Fourier

Les informations sur la microstructure osseuse demandées par ces méthodes peuvent être obtenues par des techniques expérimentales diverses parmi lesquelles les techniques d'imagerie occupent une place de choix (voir Fig. 2). Celles-ci sont basées essentiellement sur l'analyse de la propagation d'ondes acoustiques (Naili et al., 2010; Haiat et al., 2011) ou électro-magnétiques (Nuzzo et al., 2002) dans le tissu osseux. En particulier, les différents types de tomographie aux rayons X permettent de caractériser la morphologie et la constitution du tissu osseux *in vitro* à des échelles spatiales allant du millimètre au nanomètre. Cependant, comme le montre la Fig. 3 (Liebl et al., 2015), cette caractérisation présente d'évidentes limites *in vivo* du fait des doses maximales de rayonnement admissibles en clinique.

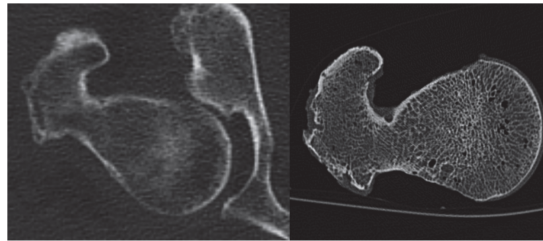


FIGURE 3 : Images prises par tomodensitométrie (CT-scan) de la partie proximale du fémur humain *in vivo* (à gauche) et *in vitro* (à droite).

La résolution spatiale des scanners cliniques actuellement disponibles est limitée à la centaine de micromètres (Burghardt et al., 2011). Bien que cette résolution soit vraisemblablement amenée à s'améliorer dans les années à venir suivant les avancées technologiques des dispositifs d'imagerie, elle ne permet pas aujourd'hui d'obtenir des informations précises aux échelles sub-millimétriques, comme cela est souvent demandé par les modèles multi-échelles. Il s'ensuit que, lorsque des images *in vivo* sont utilisées pour extraire des informations sur la microstructure osseuse, les incertitudes affectant celles-ci posent des questions sur la fiabilité des résultats produits par les modèles qui les utilisent comme données d'entrée.

Dans une démarche d'aide au diagnostic clinique, l'objectif de cette thèse est de développer une modélisation robuste pour obtenir les propriétés élastiques du tissu osseux à l'échelle de l'organe en intégrant l'incertitude des mesures expérimentales issues de l'imagerie.

---

La théorie des probabilités offre le cadre et les outils nécessaires pour traiter toute sorte d'incertitude dans la modélisation des données expérimentales et des modèles mécaniques. Ces outils fondamentaux, perfectionnés au cours des dernières cinquante années, ont permis d'approcher plusieurs problèmes scientifiques comme la modélisation des processus stochastiques et des champs aléatoires (Doob, 1953; Gikhman and Skorokhod, 1979; Krée and Soize, 1986; Kapur and Kesavan, 1992), des processus de diffusion et des équations différentielles stochastiques (Itô and McKean, 1965; Arnold, 1973; Gikhman and Skorokhod, 1979; Khasminskii, 2011; Rozanov, 2013; Krée and Soize, 1986), ainsi que le traitement de signaux aléatoires (Soi, 1993).

Contrairement à d'autres domaines de la mécanique et du génie civil, l'application des approches stochastiques aux sciences du vivant est très récente et n'a pas, jusqu'à présent, exprimé tout son potentiel. C'est précisément dans ce cadre que se situe ce travail de thèse.

Le point de départ de notre travail a été un modèle multi-échelle du tissu osseux basé sur l'imagerie qui a été développé récemment dans notre laboratoire (Sansalone et al., 2010). Ce modèle utilise des images obtenues par rayonnement synchrotron pour décrire la composition du tissu osseux au travers des échelles, puis la théorie de la *micro-mécanique des milieux continus* pour déduire les variations de ses propriétés élastiques à l'échelle de l'organe. Les images obtenues au synchrotron permettant une description précise du tissu osseux à l'échelle de la dizaine de micromètres, ce modèle est foncièrement de nature déterministe. Le cœur de notre travail de recherche a porté sur la prise en compte des incertitudes expérimentales au sein de ce modèle et dans la quantification de leurs effets au travers des échelles. Pour cela, les paramètres incertains du modèle ont été traités comme des variables, voire des champs, aléatoires dont on a cherché à donner une représentation stochastique aussi objective que possible. Pour construire les lois de probabilité desdites variables aléatoires, notre choix s'est orienté sur le *principe du maximum d'entropie* (MaxEnt). La modélisation stochastique du tissu osseux a ainsi été abordée en s'appuyant d'une part sur la *micro-mécanique des milieux continus* et d'autre part sur le *principe du maximum d'entropie*. C'est cette association qui a donné naissance au *paradigme Matryoshka*.

Par *paradigme Matryoshka* (introduit dans le titre de la thèse) nous entendons :  
*Toute procédure complexe, constituée par plusieurs étapes non banales, ayant pour objectif de reproduire un comportement physique spécifique incertain.*

Cette définition inclut en même temps la modélisation stochastique des matériels à travers :

1. l'application de diverses méthodes d'homogénéisation (micro-mécanique, FEM, FFT) à des données expérimentales incertaines ;
2. la modélisation directe des propriétés mécaniques aléatoires (matrices et champs de matrices d'élasticité aléatoires).

## 2 Organisation du manuscrit

Le corps de ce document est composé de quatre chapitres, chacun desquels développe de façon autonome le sujet de la modélisation stochastique du tissu osseux par rapport à des questions spécifiques et représente un article publié (chapitre 1), soumis (chapitre 2) ou en cours de soumission (chapitres 3 et 4). *Les chapitres 1 à 3* abordent le sujet de la modélisation des incertitudes

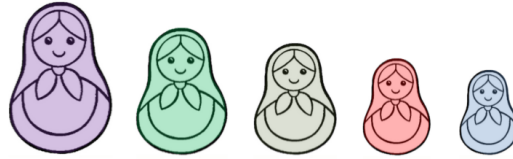


FIGURE 4 : Image d'une Matryoshka, plus communément appelée poupée russe.

sur des données expérimentales obtenues par micro-tomographie et leurs effets sur les résultats des modèles d'homogénéisation. Cela constitue une première déclinaison du paradigme Matryoshka où l'incertitude présente au niveau expérimental est propagée d'une échelle à l'autre des modèles multi-échelles. Le résultat (tenseur élastique aléatoire) à chaque échelle peut être vu comme une couche de la Matryoshka. *Le chapitre 4* aborde le sujet de la construction des propriétés mécaniques de l'os de façon indépendante à travers la construction directe des matrices ou des champs aléatoires. La procédure proposée permet de construire des champs aléatoires de tenseurs élastiques ayant des propriétés matérielles données (classe de symétrie, corrélation spatiale) comme résultat d'une opportune séquence d'opérations. Celle-ci, à nouveau, peut être vue comme une déclinaison différente du paradigme de Matryoshka.

## 2.1 Résumé des chapitres

### 2.2 Chapitre 1

Le premier chapitre décrit en détail le cadre méthodologique général associant micro-mécanique des milieux continus et modélisation stochastique par le principe MaxEnt. Une première version du modèle micro-mécanique stochastique est également proposée. En partant du modèle micro-mécanique déterministe du tissu osseux cortical dont la description multi-échelles est montrée sur la Fig. 5, les fractions volumiques décrivant la composition du tissu osseux aux différentes échelles ont été considérées comme des paramètres incertains connus uniquement en termes statistiques (valeur moyenne et dispersion, estimées à partir d'images obtenues par rayonnement synchrotron). Ces paramètres incertains ont donc été modélisés comme des variables aléatoires dont les lois de probabilité ont été obtenues par application du principe MaxEnt.

Ce modèle micro-mécanique stochastique a permis de caractériser les propriétés élastiques hétérogènes et anisotropes du tissu osseux à l'échelle de l'organe en termes statistiques (valeur moyenne, dispersion, intervalles de confiances ...). Cette démarche a été validée en la comparant avec la méthode d'homogénéisation numérique par éléments finis, plus raffinée mais énormément plus lourde en termes de calcul. Le modèle stochastique s'est avéré très précis pour ce qui concerne des valeurs moyennes des coefficients élastiques. Cependant, des erreurs par excès ont été observées sur les intervalles de confiance, traduisant le fait que les effets des incertitudes expérimentales ont été surestimés sur les coefficients élastiques du tissu osseux.

Ces erreurs observées sur les intervalles de confiance ont motivé les études conduites dans les chapitres 2 et 3. Afin de mieux comprendre les mécanismes de propagation des incertitudes, notre étude a été réalisée en deux étapes : nous nous sommes d'abord concentrés sur la matrice

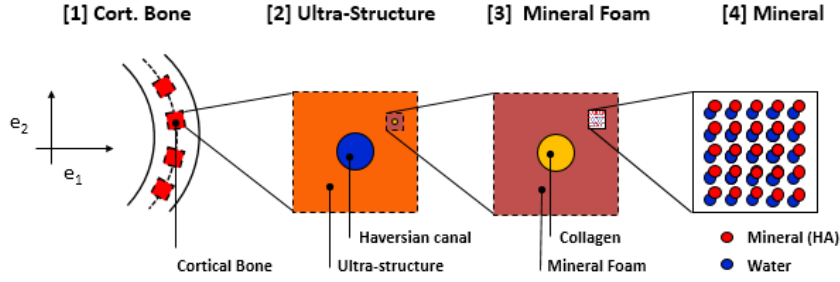


FIGURE 5 : Modèle simplifié de l'os cortical utilisé dans la thèse.

osseuse (ou ultrastructure) (voir chapitre 2) pour élargir ensuite notre analyse jusqu'au tissu cortical en prenant en compte la porosité Haversienne (voir chapitre 3).

## 2.3 Chapitre 2

Dans ce chapitre, nous nous sommes focalisés sur la matrice solide du tissu osseux (l'ultrastructure montrée sur la Fig. 5) pour explorer les différents choix de modélisations envisageables et les mécanismes de propagation des incertitudes correspondants. Le concept proposé dans le chapitre 1 modélise les fractions volumiques comme des variables aléatoires statistiquement indépendantes, la valeur moyenne et la dispersion de chaque fraction volumique étant fixées sur la base de statistiques expérimentales calculées à l'échelle de la dizaine de micromètres. Dans ce chapitre, nous avons questionné ces deux choix. Tout d'abord, quelle est la meilleure façon pour décrire l'incertitude dans la composition de la matrice osseuse ? Et ensuite, à quelle échelle devrait-on effectuer les mesures expérimentales pour alimenter le modèle stochastique ?

Concernant la première question, nous avons étudié deux cas de figures en considérant comme paramètres incertains les fractions volumiques (du collagène dans l'ultrastructure et du minéral dans la mousse minérale) ou bien la densité minérale du tissu (TMD). Celle-ci est liée directement aux niveaux de gris des images et permet, moyennant une relation empirique, de calculer les deux fractions volumiques. De fait, la TMD représente une variable observable contrairement aux fractions volumiques qui sont déduites à partir de celle-ci. Si introduire l'incertitude directement sur les fractions volumiques amène à des fluctuations statistiquement indépendantes des teneurs en collagène et minéral, introduire l'incertitude sur la TMD amène à une corrélation entre ces fluctuations. Cette étude démontre que la propagation de l'incertitude sur les coefficients élastiques de l'ultrastructure est essentiellement la même dans les deux cas.

La deuxième question a trait à la résolution spatiale des dispositifs d'imagerie qu'on devrait utiliser pour obtenir les données d'entrée du modèle. Dans le chapitre 1, les statistiques expérimentales sur la composition de la matrice osseuse ont été obtenues à l'échelle de la dizaine de micromètres, soit la taille du voxel des images. Nous avons considéré ici un cas de figure plus proche de la réalité clinique, à savoir des statistiques expérimentales relatives à l'échelle de plusieurs centaines de micromètres. On remarquera que cela correspond à la taille du volume élémentaire représentatif (RVE) du tissu cortical. Les modèles stochastiques correspondant à ces deux choix de calibration produisent des résultats semblables en termes de valeurs moyennes mais

fort différents en termes de dispersions des coefficients élastiques. En particulier, le deuxième s'avère bien plus précis et capable de prédire correctement les intervalles de confiance. Cette étude démontre que la résolution spatiale des scanners cliniques est suffisante pour obtenir des informations statistiques fiables sur les propriétés élastiques de l'ultrastructure.

Ce résultat prometteur de ce chapitre a été utilisé comme base de départ pour l'étude menée dans le chapitre 3 où cette analyse a été étendue jusqu'à l'échelle du tissu osseux en prenant en compte l'incertitude expérimentale sur la porosité haversienne (HP).

## 2.4 Chapitre 3

Dans le chapitre 3, les propriétés efficaces de l'os cortical ont été estimées à partir de la modélisation stochastique de deux seules variables aléatoires : la densité minérale du tissu (TMD) et la porosité haversienne (HP). Les résultats du modèle micromécanique stochastique issu du couple (TMD, HP) ont été comparés : (i) avec un modèle micromécanique nominal obtenu en alimentant le modèle micromécanique avec les valeurs moyennes du couple (TMD, HP) et (ii) avec deux modèles plus raffinés basés sur la FEM et la méthode FFT. Plusieurs études comparatives ont été menées dans ce chapitre. D'abord ont été comparés entre eux (i) les deux modèles micromécaniques (stochastique et nominale), puis (ii) les deux modèles détaillés (FEM et FFT) et enfin (iii) le modèle stochastique et les modèles FEM et FFT.

Le tenseur d'élasticité du modèle nominal s'est avéré très proche de la valeur moyenne des réalisations du modèle stochastique avec des différences inférieures à 0.1%. Ceci permet d'affirmer que le modèle nominal, même si équipé de la seule information moyenne sur les variables du modèle, donne une très bonne approximation du comportement élastique moyen de l'os corticale. Nous avons également étudié la relation entre le couple (TMD, HP) et les coefficients élastiques efficaces. Grâce à l'*inégalité de Jensen*, nous avons pu caractériser *a priori* les erreurs par excès ou par défaut entre les valeurs moyennes du modèle stochastique et les résultats du modèle nominal.

Parmi les méthodes numériques, la FEM demeure l'approche standard pour l'homogénéisation. Appliquée à des RVE de tissu cortical, elle peut en décrire de façon plus ou moins précise, en fonction du maillage obtenu, la morphologie et la distribution de la TMD. Moins connue que la FEM, l'approche par la FFT offre une alternative très intéressante car elle peut être directement appliquée aux images brutes en utilisant les voxels des images comme éléments du maillage, et cela avec des temps de calcul réduits par rapport à la FEM. Appliquées à quelques dizaines de RVE de tissu cortical, les deux méthodes ont montré en général des résultats similaires (notamment pour le module d'Young axial dans la direction de l'axe anatomique de l'os) bien que des différences importantes ont pu être observées sur des RVE spécifiques.

Il est à noter que les tenseurs élastiques du tissu cortical obtenus par les modèles micromécaniques sont isotropes transverses alors que ceux obtenus par FEM et FFT sont anisotropes. Nous avons quantifié l'écart entre ces deux classes de symétrie sur chaque RVE en projetant les tenseurs anisotropes obtenus par FEM et FFT sur les sous-classes d'orthotropie, puis d'isotropie transverse. Les différences entre les normes de Frobenius des tenseurs de départ et des tenseurs projetés étant de l'ordre de quelques pourcents, ceci justifie de façon indirecte les hypothèses faites par les modèles micromécaniques. En outre, pour chaque RVE, les résultats des modèles FEM et FFT ont été comparés avec ceux d'un modèle micromécanique équivalent

---

(c'est-à-dire, alimenté avec les valeurs de HP et TMD moyenne du RVE). Les différences observées étant de l'ordre de quelques pourcents pour la plupart des modules élastiques, ceci justifie le bien-fondé des hypothèses simplificatrices de l'approche micromécanique. Enfin, les valeurs moyennes et les intervalles de confiances du modèle micromécanique stochastique ont été comparés avec les résultats obtenus par FEM et FFT. Un excellent accord a été trouvé pour l'ensemble des coefficients élastiques du tissu osseux. Ces observations montrent que le modèle stochastique présenté dans ce chapitre est capable de donner une représentation fiable et précise des propriétés élastiques du tissu cortical et il a le potentiel pour devenir un outil numérique d'aide au diagnostic clinique.

## 2.5 Chapitre 4

Dans le chapitre 3, une première tentative de classification (donc d'identification) de la classe de symétrie matérielle de l'os cortical a été esquissée. Le modèle multi-échelle défini a permis d'approcher presque complètement la classe de symétrie matérielle obtenue par un calcul relativement précis. Le résultat à chaque échelle produit un tenseur élastique appartenant à une classe de symétrie bien définie laquelle est *isotrope* pour la mousse minérale, *isotrope transverse* pour l'ultra-structure et le tissu cortical.

Toutefois, le problème de la construction d'un tenseur élastique aléatoire fluctuant à l'intérieur d'une classe de symétrie matérielle donnée est un problème indépendant des méthodes d'homogénéisation. Ainsi, la solution de ce problème pourraient, en particulier, être utile dans le cadre général des méthodes d'homogénéisation. En effet, les réalisations aléatoires obtenues par la procédure issue de la solution de ce problème pourraient être utilisées comme données d'entrée dans tout autres chaînes d'homogénéisations.

La solution de ce problème général a été décrite par Soize et ses co-auteurs dans une série de travaux parus récemment (Soize, 2006; Guillemainot and Soize, 2013) pour ne citer que les travaux fondateurs. Certains compléments sur les classes de symétrie isotrope transverse et orthotrope sont proposés dans le chapitre 4 ainsi que l'application de la méthode au cas de l'homogénéisation des matériaux vivants.

La solution de ce problème réside dans l'application du principe du maximum d'entropie au cas des matrices aléatoires qui exhibent une symétrie donnée. La solution proposée permet aussi, avec une seule étape supplémentaire, de construire des champs de matrices aléatoires avec une symétrie donnée et une longueur de corrélation spatiale donnée. La méthode de construction de la matrice aléatoire est composée d'une suite d'opérations, en générale non linéaires, opportunément choisies pour relaxer les contraintes que la solution doit satisfaire dans l'utilisation du principe du maximum d'entropie. Pour cette raison, la méthode proposée est à l'image de la de-construction d'une poupe russe (Matryoshka) laquelle, même dans son appellation, fait écho à la construction mathématique utilisée (Matrice-Matryoshka).

La procédure a été appliquée pour construire les propriétés mécaniques de la mousse minérale *isotrope* obtenue par la méthode d'homogénéisation dans le chapitre 3. L'information disponible est le tenseur élastique moyen et sa dispersion. Un exemple de champ aléatoire de cette mousse minérale avec une longueur de corrélation donnée est aussi présenté. Enfin, les relations nécessaires pour appliquer la procédure à d'autres classes de symétries matérielles, isotrope transverse et orthotrope, utiles pour l'os cortical sont décrites.

## Bibliography

- Mathematical Methods in Signal Analysis (in French)*. Masson, Paris, 1993.
- B. Aoubiza, J.M. Crolet, and A. Meunier. On the mechanical characterization of compact bone structure using the homogenization theory. *Journal of Biomechanics*, 29(12):1539–1547, 1996.
- L. Arnold. *Stochastic Differential Equations : Theory and Applications*. John Wiley and Sons, New York, 1973.
- A. Barkaoui and R. Hambli. Finite element 3d modeling of mechanical behavior of mineralized collagen microfibrils. *J Appl Biomater Biomech*, 9(3):199–205, 2011.
- A. Barkaoui and R. Hambli. Nanomechanical properties of mineralised collagen microfibrils based on finite elements method: biomechanical role of cross-links. *Computer Methods in Biomechanics and Biomedical Engineering*, 17(4):1590–1601, 2014.
- B. Brisard and L. Dormieux. FFT-based methods for the mechanics of composites: A general variational framework. *Computational Materials Science*, 49(3):663–771, 2010.
- A.J. Burghardt, T.M. Link, and S. Majumdar. High-resolution computed tomography for clinical imaging of bone microarchitecture. *Clinical Orthopaedics and Related Research*, 469(8):2179–2193, 2011.
- Y. Chen, E. Dall’Arab, E. Sales, K. Manda, R. Wallace, P. Pankaj, and M. Viceconti. Micro-ct based finite element models of cancellous bone predict accurately displacement once the boundary condition is well replicated: A validation study. *Journal of the Mechanical Behavior of Biomedical Materials*, 65:644–651, 2017.
- J.L. Doob. Stochastic processes. 1953. *New York*, 1953.
- L. Gikhman and A.V. Skorokhod, editors. *The Theory of Stochastic Processes*. Springer-Verlag, Berlin, 1979.
- J. Guillemainot and C. Soize. Stochastic model and generator for random fields with symmetry properties: application to the mesoscopic modeling of elastic random media. *Multiscale Modeling and Simulation (A SIAM Interdisciplinary Journal)*, 11(3):840–870, 2013.
- G. Haiat, S. Naili, M.-B. Vu, C. Desceliers, and C. Soize. Equivalent contributing depth investigated by a lateral wave with axial transmission in heterogeneous viscoelastic cortical bone. *J. Acoust. Soc. Am.*, 129(4):EL114–EL120, 2011.
- C. Hellmich, F.-J. Ulm, and L. Dormieux. Can the diverse elastic properties of trabecular and cortical bone be attributed to only a few tissue-independent phase properties and their interactions? *Biomechanics and Modeling in Mechanobiology*, 2:219–238, 2004.
- K. Itô and H.P. McKean, editors. *Diffusion Processes and Their Sample Paths*. Springer-Verlag, Berlin, 1965.

- J.N. Kapur and H.K. Kesavan. *Entropy Optimization Principles with Applications*. Academic Press, San Diego, 1992.
- R. Khasminskii. *Stochastic stability of differential equations*, volume 66. Springer Science & Business Media, 2011.
- P. Krée and C. Soize. *Mathematics of Random Phenomena*. Reidel, Dordrecht, 1986.
- H. Liebl, E. Grande Garcia, F. Holzner, P.B. Noel, R. Burgkart, E.J. Rummeny, T. Baum, and J.S. Bauer. *In-Vivo* assessment of femoral bone strength using finite element analysis (FEA) based on routine MDCT imaging: A preliminary study on patients with vertebral fractures. *PLoS One*, 10(2):1–15, 2015.
- V. Monchiet and G. Bonnet. A polarization-based FFT iterative scheme for computing the effective properties of elastic composites with arbitrary contrast. *International Journal for Numerical Methods in Engineering*, 89(11):1419–1436, 2012.
- H. Moulinec and P. Suquet. A numerical method for computing the overall response of nonlinear composites with complex microstructure. *Computer Methods in Applied Mechanics and Engineering*, 157:69 – 94, 1998.
- S. Naili, M.B. Vu, Q. Grimal, M. Talmant, C. Desceliers, C. Soize, and G. Haiat. Influence of viscoelastic and viscous absorption on ultrasonic wave propagation in cortical bone: Application to axial transmission. *J. Acoust. Soc. Am.*, 127(4):2622–2634, 2010.
- S. Nuzzo, F. Peyrin, P. Cloetens, J. Baruchel, and G. Boivin. Quantification of the degree of mineralization of bone in three dimensions using synchrotron radiation microtomography. *Med. Phys.*, 29(11):2672–2681, 2002.
- W.J. Parnell, M.B. Vu, Q. Grimal, and S. Naili. Analytical methods to determine the effective mesoscopic and macroscopic elastic properties of cortical bone. *Biomech. Model. Mechanobiol.*, 11(6):883–901, 2012.
- M. Predoi-Racila and J. M. Crolet. Human cortical bone: the sinupros model. *Comput. Methods Biomech. Biomed. Engin.*, 11(2):169–187, 2008.
- J.-Y. Rho, L. Kuhn-Spearing, and P. Zioupos. Mechanical properties and the hierarchical structure of bone. *Medical Engineering & Physics*, 20:92–102, 1998.
- E. Rohan, S. Naili, R. Cimirman, and T. Lemaire. Multiscale modeling of a fluid saturated medium with double porosity: Relevance to the compact bone. *Journal of the Mechanics and Physics of Solids*, 60(5):857–881, 2012.
- Y. Rozanov. *Random fields and stochastic partial differential equations*, volume 438. Springer Science & Business Media, 2013.
- V. Sansalone, S. Naili, V. Bousson, C. Bergot, F. Peyrin, J.D. Laredo, and G. Haiat. Determination of the heterogeneous anisotropic elastic properties of human femoral bone: from nanoscopic to organ scale. *J. Biomech.*, 43(10):1857–1863, 2010.

- C. Soize. Non-gaussian positive-definite matrix-valued random fields for elliptic stochastic partial differential operators. *Computer Methods in Applied Mechanics and Engineering*, 195(1-3): 26–64, 2006.
- P. Suquet, editor. *Continuum micromechanics*. Number 377 in CISM Lecture Notes. Springer-Verlag, Wien, 1997.
- Y.J. Yoon and S.C. Cowin. An estimate of anisotropic poroelastic constants of an osteon. *Biomechanics and Modeling in Mechanobiology*, 7(1):13–26, 2008.

## Chapter 1

# Stochastic multiscale modelling of cortical bone elasticity based on high-resolution imaging

---

V. Sansalone, D. Gagliardi, C. Desceliers, V. Bousson, J.D. Laredo, F. Peyrin, G. Haïat, and S. Naili. Stochastic multiscale modelling of cortical bone elasticity based on high-resolution imaging. *Biomech. Model. Mechanobiol.*, 15(1):111-131, 2016.

---

## Abstract

Accurate and reliable assessment of bone quality requires predictive methods which could probe bone microstructure and provide information on bone mechanical properties. Multiscale modelling and simulation represent a fast and powerful way to predict bone mechanical properties based on experimental information on bone microstructure as obtained through X-ray based methods. However, technical limitations of experimental devices used to inspect bone microstructure may produce blurry data, especially in *in vivo* conditions. Uncertainties affecting the experimental data (input) may question the reliability of the results predicted by the model (output). Since input data are uncertain, deterministic approaches are limited and new modelling paradigms are required. In this chapter, a novel stochastic multiscale model is developed to estimate the elastic properties of bone while taking into account uncertainties on bone composition. Effective elastic properties of cortical bone tissue were computed using a multiscale model based on continuum micromechanics. Volume fractions of bone components (collagen, mineral, and water) were considered as random variables whose probabilistic description was built using the Maximum Entropy principle. The relevance of this approach was proved by analysing a human bone sample taken from the inferior femoral neck. The sample was imaged using synchrotron radiation micro-computed tomography. 3-D distributions of Haversian porosity and tissue mineral density extracted from these images supplied the experimental information needed to build the stochastic models of the volume fractions. Thus, the stochastic multiscale model provided reliable statistical information (such as mean values and confidence intervals) on bone elastic properties at the tissue scale. Moreover, the existence of a simpler “nominal model”, accounting for the main features of the stochastic model, was investigated. It was shown that such a model does exist and its relevance was discussed.

## 1.1 Introduction

At the organ scale, bone is organised in two compartments: the cortical and trabecular compartments, both contributing to bone strength (Manske et al., 2009). Bone strength depends on both bone quantity and bone quality (Donnelly, 2011). Bone quantity refers to the amount of bone mass. Bone quality is a more subtle and hazy feature (Bouxsein, 2003) encompassing multiple parameters, but, in general, it refers to the volumetric composition and microarchitecture of bone. Indeed, bone is a complex material showing a hierarchical structure spanning several length scales, from the molecular scale to the organ one (Rho et al., 1998; Hulmes, 2002; Fratzl et al., 2004). Loss of bone mass or abnormal microarchitecture—often associated to bone diseases such as osteoporosis—may lead to reduced bone strength and increased risk of fracture.

In clinical practice, the bone mineral density (BMD) at the hip—as measured with Dual X-ray absorptiometry (DXA) techniques—is still considered as the gold standard for assessing the risk of fracture. However, BMD only measures bone mass (*i.e.* bone quantity) but is unable to assess microstructural features such as volumetric bone composition and microarchitecture (*i.e.* bone quality). Several studies have shown Haversian Porosity (HP) and Tissue Mineral Density (TMD) to be among the most relevant determinants of bone strength and associated fracture risk (Burr, 2004; Currey, 1988; Bell et al., 1999; Vajda and Bloebaum, 1999; Bousson et al., 2001; Crabtree et al., 2001; Sasso et al., 2008; Zebaze et al., 2010). HP and TMD describe different features of bone microstructure. HP refers to the volume fraction of Haversian and Volkmann’s canals (typical diameter of several tens to a few hundreds micrometres) in bone tissue. TMD represents the degree of mineralisation of the solid bone matrix (Boivin and Meunier, 2002; Bouxsein et al., 2010).

In the femoral neck, a critical anatomical site for osteoporotic fractures, osteoporotic bone structure is characterised by progressive thinning of the cortical shell and loss of trabecular mass (Mayhew et al., 2005). Spatial variations of HP and TMD in the femoral hip region induce heterogeneity of cortical bone at the organ scale (Bensamoun et al., 2004b,a; Yamato et al., 2006; Sasso et al., 2007, 2008; Mathieu et al., 2013). This heterogeneity strongly affects the mechanical response of bone as it was widely documented by studies on ultrasonic wave propagation (Haiat et al., 2009; Naili et al., 2010; Haiat et al., 2011; Grimal et al., 2014) and nanoindentation (Yao et al., 2011; Vayron et al., 2012, 2014).

Establishing reliable mathematical relationships between available experimental data (BMD, HP, TMD ...) and mechanical properties (stiffness, strength ...) is important to predict the fracture risk. In this respect, multiscale modelling and simulation approaches can be useful to account for the specific volumetric composition and organisation of bone components at each scale. Several multiscale approaches have been proposed to model the mechanical properties of bone tissue, including continuum micromechanics (Hellmich et al., 2004b; Fritsch and Hellmich, 2007; Grimal et al., 2011b; Parnell et al., 2012), asymptotic homogenisation (Aoubiza et al., 1996; Parnell et al., 2012; Predoi-Racila and Crolet, 2008), and other techniques (Yoon and Cowin, 2008a,b; Ghanbaria and Naghdabadi, 2009).

Recently, a multiscale model based on continuum micromechanics was proposed by our group to estimate the elastic properties of bone tissue (Sansalone et al., 2010, 2012a,b). The experimental information was obtained using synchrotron radiation micro-computed tomography

(SR- $\mu$ CT) which provided a 3-D mapping of the HP and TMD with a spatial resolution of about 10  $\mu$ m. The SR- $\mu$ CT images were used to determine the heterogeneous composition of bone and, in turn, to compute the heterogeneous elastic properties of one (Sansalone et al., 2010, 2012b) or several (Sansalone et al., 2012a) bone samples obtained from the inferior femoral neck of elderly patients.

Experimental information which can be obtained *in vivo* through standard medical devices such as DXA devices or quantitative CT (QCT) is much less accurate. Lack of accuracy is related to a low spatial resolution and polyenergetic X-ray beam. In any case, the lower the accuracy of the experimental data, the higher the uncertainty affecting the values of the derived modelling parameters. Uncertainty on the modelling parameters increases with zooming down into the nanostructure of bone. Current *in vivo* experimental techniques cannot easily provide accurate information about the morphology, volumetric content, spatial arrangement and mechanical behavior of bone components. For instance, orientation of the collagen as well as size, shape and organization of the hydroxyapatite mineral in the bone lamellae remain largely uncovered. (Collagen and mineral are the two major components of bone solid matrix.) Only recent breakthroughs in synchrotron tomographic imaging have given access to direct 3-D information on the bone structure at the nanoscale level (Langer et al., 2012; Varga et al., 2013).

Dealing with uncertain data requires new modelling paradigms. There exist several approaches to take into account such uncertainties among which the theory of probability (Arnold, 1973; Feller, 1971; Halmos, 1976; Krée and Soize, 1986) has proved, during last decades, its efficiency and robustness. In particular, the Maximum Entropy (MaxEnt) principle (Jumarie, 2000; Kapur and Kesavan, 1992) was successfully applied to several problems of elasticity to build robust probability distributions of random variables and random fields ensuring both the mathematical and the physical consistency of the probabilistic descriptions (Soize, 2006, 2008, 2001; Guilleminot et al., 2011; Guilleminot and Soize, 2012, 2013a,b).

Uncertainties of model parameters is an important problem in biomechanics at all scales. Modelling uncertainties and computing stochastic responses may be useful to assess robustness of subject-specific predictive models in musculoskeletal biomechanics (Valente et al., 2014). Aiming at characterising the mechanical properties of bone *in vivo*, both hierarchical structure of bone *and* the uncertainties existing on experimental data should account for. So far, there are only a few research works having addressed these two issues at once. A stochastic multiscale method based on asymptotic homogenisation theory was recently proposed to take into account the uncertainties caused by image-based modelling and trabecular stiffness orientation in predicting the elastic moduli of trabecular bone (Basaruddin et al., 2015). Another contribution was recently proposed by our group by introducing a stochastic treatment of the elastic properties of bone components in a multiscale model of bone solid matrix based on continuum micromechanics theory (Sansalone et al., 2014). Therein, in the framework of a parametric probabilistic approach, elastic coefficients of bone components were considered as random variables and their probability density functions (PDFs) obtained using the MaxEnt principle.

In this chapter, we address the complementary issue of uncertainty on volumetric bone composition. Aiming at moving toward *in vivo* applications, uncertainty on subject-specific bone microstructure have to be taken into account to estimate the mechanical properties of bone. In this respect, two main goals will be pursued in this work.

The *first goal* of this chapter is to describe a new modelling approach suitable to estimate bone elastic properties while taking into account uncertainties on the composition of bone microstructure. Following the ideas set forth in the scope of uncertain elastic properties of bone components (Sansalone et al., 2014), we will develop a stochastic multiscale model of cortical bone by introducing a stochastic treatment of the volume fractions of bone components in the multiscale model of bone developed by our group (Sansalone et al., 2010). PDFs of the volume fractions will be constructed using the MaxEnt principle and available experimental data. Our experimental data are represented by statistical information on the 3-D distributions of HP and TMD obtained by analysis of high resolution SR- $\mu$ CT images of one bone sample of the inferior femoral neck of an elderly patient. It will be shown that this approach can effectively describe the elastic properties of cortical bone at the organ scale. The final outcome of the model is given in terms of expected values, confidence intervals and other statistics of these properties.

Granted the suitability of the stochastic model, the *second goal* is to understand whether a simpler description is possible. To this aim, we will assess to which extent the stochastic model could be described by a simpler, deterministic model. Indeed, the computational cost of the stochastic model is quite high and there is an interest for computationally spare alternatives. We will focus on two questions: Does a simpler model exist, providing “good” estimates of expected elastic properties of bone? If so, how accurate and reliable are these estimates? We will show that such a model exists and discuss its relevance.

The chapter is organized as follows. The stochastic multiscale model of bone is presented in Sec. 1.2. This section is introduced by a brief presentation of the experimental data used to develop the model. Then, the theoretical development and the solution algorithm of the stochastic multiscale model are presented in detail. A simpler nominal model and a Finite Element model are also presented. Numerical results are thoroughly presented in Sec. 1.3 bringing up the relevance of the different modelling approaches proposed. In Sec. 1.4 the findings of this study are discussed focusing on the two goals set forth. Limitations and further developments are also addressed. Eventually, in Sec. 3.4 the conclusions of this work are drawn, focusing on the two goals set forth, and its limitations and further developments are discussed.

## 1.2 Materials and methods

### 1.2.1 Experimental data

#### Preparation and imaging of the bone sample

The experimental procedure for preparing and imaging the bone sample was thoroughly presented elsewhere (Sansalone et al., 2010). We recall here below the key points for sake of completeness and refer to that paper for more details.

A bone sample was extracted from the inferior femoral neck of a 79 year old patient during standard hemiarthroplasty. The bone sample was imaged using synchrotron radiation micro-computed tomography (SR- $\mu$ CT) at the European Synchrotron Radiation Facility (ESRF, Grenoble, France). The sample was imaged at the ID19 beamline using a monochromatic X-ray beam tuned at 25 KeV. The 3-D image was reconstructed using a customized Filtered Back Projection algorithm developed at ESRF. The outcome was a 3-D grayscale (range: [0, 255])

mapping of the linear attenuation  $\mu$  of the monochromatic X-ray beam at 25 *KeV*. The reconstruction was performed in a volume of interest of  $660 \times 660 \times 523$  isotropic voxels (size 10.13  $\mu\text{m}$ ). The 3-D volume reconstructed is shown in Fig. 1.1. A Cartesian frame is also shown. The unit vector  $\mathbf{e}_3$  is aligned with the axis of the femoral neck and the unit vectors  $\mathbf{e}_1$  and  $\mathbf{e}_2$  lie in the plane of the cross section of the sample.

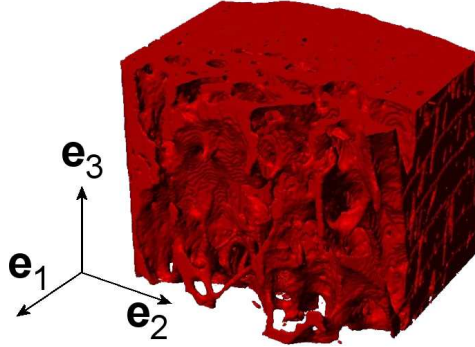


Figure 1.1: Reconstructed 3-D model of the bone sample and Cartesian frame.

The grayscale 3-D mapping was analysed in order to separate two regions: the voids (Haversian Porosity (HP) and space surrounding the sample) and the solid matrix of bone. Voxels having a grayscale level higher than a fixed threshold were assigned to the bone matrix region, whereas the others were assigned to the void region. In this study, the threshold was fixed to 130. (The value of the threshold was found not to significantly affect the elastic coefficients of bone tissue as predicted by the model described below in Sec. 1.2.2.) Grayscale levels in the bone matrix region were converted in a 3-D voxel-wise mapping of Tissue Mineral Density (TMD) thanks to the linear relationship existing between the X-ray beam attenuation  $\mu$  and the TMD, reading  $\mu = 3.32 \times \text{TMD} + 0.51$ , where  $\mu$  is expressed in  $\text{cm}^{-1}$  and the TMD is expressed in  $\text{g}/\text{cm}^3$ . This expression was calibrated using the theoretical values for hydroxyapatite and water at 25 *KeV* of the DABAX database. A detailed description of the segmentation process can be found in the appendix of Sansalone et al. (2010).

### Data analysis: HP and TMD

In previous work (Sansalone et al., 2010, 2012b), HP and TMD were analysed in radial Regions of Interest (RoIs) and axial slices (radial and axial directions refer to the anatomical axis of the sample). The thickness of RoIs and slices was 50 voxels (*i.e.* about half a millimetre). In this work, a finer analysis is performed. HP and TMD have been analysed in several cubic Representative Volume Elements (RVEs) with edges of about half a millimetre (equal to the thickness of the RoIs and slices of our previous studies).

SimpleWare 5.0 ScanIP+™ software was used to extract and analyse  $N_{\text{RVE}} = 12$  cubic RVEs from the 3-D model of the bone sample. Positions of the RVEs were chosen in order to span the whole cortical region of the sample, see Fig. 1.2. RVEs were extracted at about 1.5 *mm* from the periosteum (distance measured with respect to the centre of the RVEs) and at different hoop and axial positions with respect to a cylindrical frame centred at the anatomical

axis of the bone sample. Let  $\theta$  be the angular coordinate in the cross section plane ( $\mathbf{e}_1, \mathbf{e}_2$ ) and  $z$  be an abscissa along the femoral neck axis  $\mathbf{e}_3$ . Coordinates of the centre of the RVEs were set at  $\theta \in \{-40, -20, 0, 20\}^\circ$  (with  $0^\circ$  being the inferior axis of the femoral neck) and  $z \in \{1.5, 3.5, 5.5\} \text{ mm}$  (distance from the distal part of the sample). RVEs were oriented following a circular arc corresponding to the anatomical hoop direction of the sample.

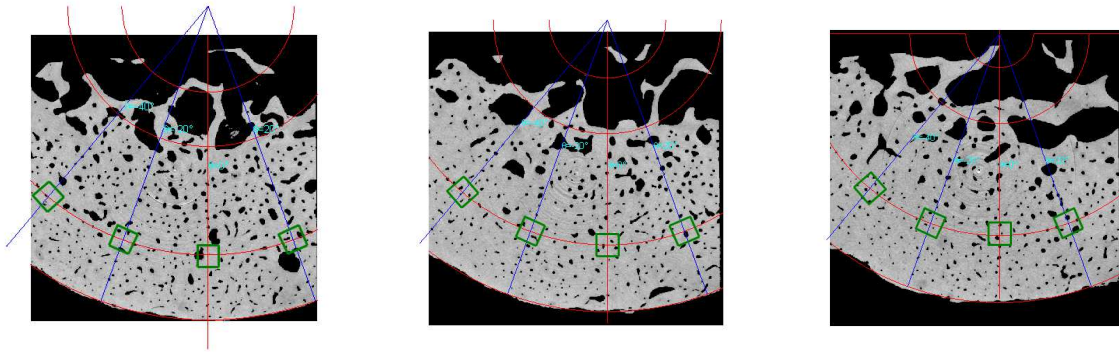


Figure 1.2: From left to right: Three cross-sections of the bone sample at  $z = 150, 350, 550 \mu\text{m}$ , respectively. RVEs are marked by green squares (colors in online version).

Each RVE was analyzed to compute its HP and TMD. The HP is meaningful at the scale of the tissue whereas the TMD is defined at the voxel scale (within the solid bone matrix) and is heterogeneous within each RVE. Therefore, one scalar value of HP and a 3-D voxel-wise distribution of TMD were obtained for each RVE. All the RVEs were also analysed collectively to obtain experimental information representative of the whole cortical region. Recalling that one RVE represents one material point at the organ scale, hereinafter terms *local* and *global* will refer to one RVE and all the RVEs, respectively.

Then, several experimental databases were constituted: (i) One global database collecting the  $N_{\text{RVE}}$  values of HP; (ii) One local database for each RVE collecting the voxel-wise values of TMD within the solid matrix; let  $N_{\text{vox}}^i$  be the number of TMD values for the  $i$ -th RVE; (iii) One global database of TMD gathering the TMD databases of all the RVEs, for a total of  $N_{\text{vox}} = \sum_{i=1}^{N_{\text{RVE}}} N_{\text{vox}}^i$  voxel-wise values of TMD. Note that the  $N_{\text{RVE}}$  databases (ii) refer to one RVE whereas the two databases (i) and (iii) refer to the whole cortical region.

These experimental databases were further used to compute the volume fractions of bone components as explained in Sec. 1.2.2. Moreover, statistics on the experimental databases of HP and TMD were computed. In particular, the mean values and dispersions of experimental data will be referred to as  $\mu_{\text{exp}}(\bullet)$  and  $\delta_{\text{exp}}(\bullet)$ , respectively, where  $\bullet$  is either HP or TMD.

## 1.2.2 Model

A stochastic multiscale model of cortical bone was developed by introducing a stochastic treatment of some modelling parameters (volume fractions of bone components) in the deterministic multiscale model proposed in previous work by our group (Sansalone et al., 2010, 2012a,b).

### Deterministic multiscale model of cortical bone

A multiscale model was recently proposed by our group to study bone elasticity at the organ scale (Sansalone et al., 2010). Extending the ideas set forth by Hellmich and coworkers (Hellmich et al., 2004a), the model uses a continuum micromechanics approach (Suquet, 1997; Nemat-Nasser and Hori, 1999) to estimate elastic properties of cortical bone at the tissue scale. In the framework of continuum micromechanics, the homogenised elastic tensor  $\mathbb{c}_{\text{hom}}$  of a multiphase medium can be computed by solving the equation (Sansalone et al., 2014):

$$g(\mathbb{c}_{\text{hom}}; \{f_r\}, \{\mathbb{c}_r\}) = 0, \quad r = 1, \dots, N_{\text{ph}} \quad (1.1)$$

where  $\{f_r\}$  and  $\{\mathbb{c}_r\}$  are the volume fractions and elastic tensors of the  $N_{\text{ph}}$  constituent phases, respectively.

The multiscale model considers three scales below the organ scale: the cortical tissue (characteristic length of several hundred micrometres), made of cylindrical pores embedded in the bone ultrastructure—the solid bone matrix; the ultrastructure (several micrometres), made of cylindrical collagen molecules embedded in a mineral foam; and the mineral foam (few hundred nanometres), made of hydroxyapatite (HA) crystals interpenetrated by water-filled spaces. All the components were considered as elastically isotropic and their properties were taken from Kotha and Guzelsu (2000). The multiscale model is depicted in Fig. 1.3 where the four scales and the three homogenisation steps (see below) are sketched.

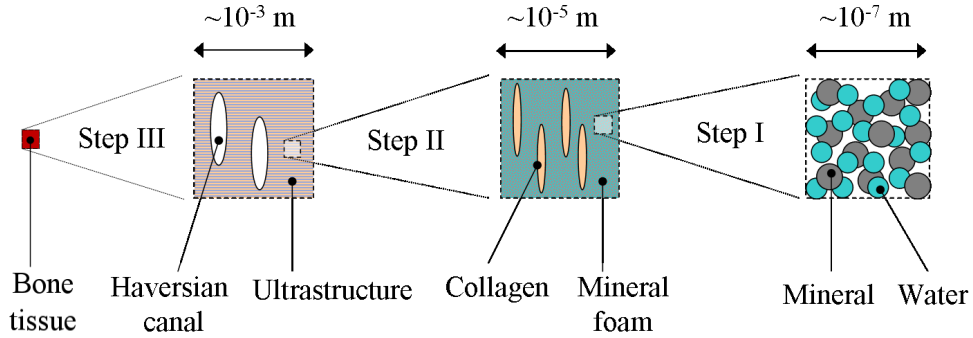


Figure 1.3: Sketch of the multiscale model.

The following cascade of formal problems—corresponding to three homogenisation steps—has to be solved in order to compute the elastic tensor of cortical tissue  $\mathbb{c}_{\text{cort}}$ :

$$g_{\text{I}}^{\text{SC}}(\mathbb{c}_{\text{foam}}; \{f_{\text{HA}}^{\text{foam}}, f_{\text{w}}^{\text{foam}}\}, \{\mathbb{c}_{\text{HA}}, \mathbb{c}_{\text{w}}\}) = 0 \quad \rightarrow \quad \mathbb{c}_{\text{foam}}, \quad (1.2)$$

$$g_{\text{II}}^{\text{MT}}(\mathbb{c}_{\text{ultra}}; \{f_{\text{col}}^{\text{ultra}}, f_{\text{foam}}^{\text{ultra}}\}, \{\mathbb{c}_{\text{col}}, \mathbb{c}_{\text{foam}}\}) = 0 \quad \rightarrow \quad \mathbb{c}_{\text{ultra}}, \quad (1.3)$$

$$g_{\text{III}}^{\text{MT}}(\mathbb{c}_{\text{cort}}; \{f_{\text{pore}}^{\text{cort}}, f_{\text{ultra}}^{\text{cort}}\}, \{\mathbb{c}_{\text{pore}}, \mathbb{c}_{\text{ultra}}\}) = 0 \quad \rightarrow \quad \mathbb{c}_{\text{cort}}. \quad (1.4)$$

Superscripts SC and MT refer to the Self-Consistent and Mori-Tanaka schemes, respectively, which are used at the different scales to compute the homogenised elastic tensors. The Self-Consistent scheme is implicit. Therefore, Eq. (1.2) has to be solved iteratively for  $\mathbb{c}_{\text{foam}}$ . The

Mori-Tanaka scheme is explicit. Therefore, Eq. (1.3) and Eq. (1.4) can be explicitly solved for  $\mathbb{c}_{\text{ultra}}$  and  $\mathbb{c}_{\text{cort}}$ , respectively.

In Eq. (1.2),  $f_{\text{HA}}^{\text{foam}}$  and  $f_{\text{w}}^{\text{foam}} = 1 - f_{\text{HA}}^{\text{foam}}$  are the volume fractions of HA mineral and water in the mineral foam, respectively. In Eq. (1.3),  $f_{\text{col}}^{\text{ultra}}$  and  $f_{\text{foam}}^{\text{ultra}} = 1 - f_{\text{col}}^{\text{ultra}}$  are the volume fractions of collagen and mineral foam in the ultrastructure, respectively. In Eq. (1.4),  $f_{\text{pore}}^{\text{cort}}$  and  $f_{\text{ultra}}^{\text{cort}} = 1 - f_{\text{pore}}^{\text{cort}}$  are the volume fractions of the Haversian pores and ultrastructure in the cortical tissue, respectively. A similar notation is used for the elastic tensors. Thus  $\mathbb{c}_{\text{HA}}$ ,  $\mathbb{c}_{\text{w}}$ ,  $\mathbb{c}_{\text{col}}$ , and  $\mathbb{c}_{\text{pore}}$  are the elastic tensors of the HA mineral, water, collagen, and Haversian pores, respectively. Moreover  $\mathbb{c}_{\text{foam}}$ ,  $\mathbb{c}_{\text{ultra}}$ , and  $\mathbb{c}_{\text{cort}}$  are the homogenised elastic tensors of the mineral foam, ultrastructure, and cortical tissue, respectively.

### Probabilistic model of the uncertain volume fractions

Using deterministic models assumes that the modelling parameters are well identified. However, most of the time, only partial information is available on these parameters and their actual values, obtained through experimental measurements, are uncertain. Among others approaches, probability theory provides an effective and robust framework to take into account such uncertainties (Feller, 1971; Arnold, 1973; Halmos, 1976; Krée and Soize, 1986).

In the framework of a parametric probabilistic approach, uncertainties on a modelling parameter  $x$  are taken into account by replacing  $x$  by a real-valued random variable  $X$ . (Hereafter, capital letters will refer to random variables.) It is assumed that the probability law of  $X$  is defined by a Probability Density Function (PDF)  $x \mapsto p_X(x)$  on  $\mathbb{R}$  (the set of the real numbers). The construction of the probability law of the random variables must be carefully carried out in order to embed the available statistical information on  $x$  and to respect well-posedness of the elasticity problem. In this work, the construction of the probabilistic model is carried out by using the MaxEnt principle (Jaynes, 1957a,b; Jumarie, 2000; Kapur and Kesavan, 1992; Soize, 2001). In the context of the information theory, entropy has been introduced as a measure of the uncertainty for probability distributions (Shannon, 1948) and the MaxEnt principle consists in maximizing this entropy subjected to constraints defined by the available information. The entropy associated to the PDF  $p_X$  is defined as:

$$S(p_X) = - \int_{\mathbb{R}} p_X(x) \log(p_X(x)) dx \quad (1.5)$$

The MaxEnt principle was used to model uncertainties on the elastic moduli of bone components in previous work (Sansalone et al., 2014). Hereinafter, the same strategy is used to account for uncertainties on the volume fractions only. Let  $x$  be either of the volume fractions  $f_{\text{HA}}^{\text{foam}}$ ,  $f_{\text{col}}^{\text{ultra}}$ , and  $f_{\text{pore}}^{\text{cort}}$ . Thus, the uncertain variable  $x$  is modelled by a random variable  $X$  with PDF  $p_X$ . The available information on  $X$  is assumed to be: (i) The support of  $X$  is  $\mathcal{S}_X = [0, 1]$ ; (ii) The mean value of  $X$  is  $\mu_X$ ; (iii) The dispersion of  $X$  is  $\delta_X = \sigma_X/\mu_X$ , where  $\sigma_X$  is the

standard deviation of  $X$ . The normalisation condition of the PDF and above constraints read:

$$\int_{[0,1]} p_X(x) dx = 1, \quad (1.6)$$

$$\int_{[0,1]} x p_X(x) dx = \mu_X, \quad (1.7)$$

$$\int_{[0,1]} x^2 p_X(x) dx = (1 + \delta_X^2) \cdot \mu_X^2. \quad (1.8)$$

In our case, the MaxEnt principle consists in maximising the entropy in Eq. (1.5) subject to constraints in Eqs. (1.6)-(1.8). The ensuing form of the PDF turns out to be:

$$p_X^{\lambda^*}(x) = \mathbb{1}_{[0,1]}(x) e^{-\lambda_0^* - \lambda_1^* x - \lambda_2^* x^2}, \quad (1.9)$$

where the vector  $\lambda^* = \{\lambda_0^*, \lambda_1^*, \lambda_2^*\}$  collects the Lagrange multipliers associated to the constraints in Eqs. (1.6)-(1.8), respectively. It can be shown that  $\lambda^*$  can be obtained by minimising the Hamiltonian function defined by:

$$\mathcal{H}(\lambda) := \lambda_0 + \lambda_1 \mu_X + \lambda_2 (1 + \delta_X^2) \mu_X^2 + \int_{[0,1]} e^{-\lambda_0 - \lambda_1 x - \lambda_2 x^2} dx. \quad (1.10)$$

Therefore, the solution vector  $\lambda^*$  reads:

$$\lambda^* = \arg \min_{\lambda \in \mathbb{R}^3} \mathcal{H}(\lambda), \quad (1.11)$$

where the operator  $\arg \min$  stands for the argument of the minimum.

### Stochastic multiscale model of cortical bone

The stochastic multiscale model of cortical bone is constructed by substituting the volume fractions  $f_{\text{HA}}^{\text{foam}}$ ,  $f_{\text{col}}^{\text{ultra}}$ , and  $f_{\text{pore}}^{\text{cort}}$  by the random variables  $F_{\text{HA}}^{\text{foam}}$ ,  $F_{\text{col}}^{\text{ultra}}$ , and  $F_{\text{pore}}^{\text{cort}}$  in Eq. (1.2) (homogenisation step I), Eq. (1.3) (homogenisation step II), and Eq. (1.4) (homogenisation step III), respectively. Thus, the stochastic versions of these equations read:

$$g_{\text{I}}(\mathbb{C}_{\text{foam}}; F_{\text{HA}}^{\text{foam}}, \{\mathbb{C}_{\text{HA}}, \mathbb{C}_{\text{w}}\}) = 0 \quad \rightarrow \quad \mathbb{C}_{\text{foam}}, \quad (1.12)$$

$$g_{\text{II}}(\mathbb{C}_{\text{ultra}}; F_{\text{col}}^{\text{ultra}}, \{\mathbb{C}_{\text{col}}, \mathbb{C}_{\text{foam}}\}) = 0 \quad \rightarrow \quad \mathbb{C}_{\text{ultra}}, \quad (1.13)$$

$$g_{\text{III}}(\mathbb{C}_{\text{cort}}; F_{\text{pore}}^{\text{cort}}, \{\mathbb{C}_{\text{pore}}, \mathbb{C}_{\text{ultra}}\}) = 0 \quad \rightarrow \quad \mathbb{C}_{\text{cort}}. \quad (1.14)$$

For sake of simplicity, only the independent random volume fractions were introduced in the above equations. Since the volume fractions are random variables, the homogenised elastic tensors of the mineral foam ( $\mathbb{C}_{\text{foam}}$ ), ultrastructure ( $\mathbb{C}_{\text{ultra}}$ ) and cortical tissue ( $\mathbb{C}_{\text{cort}}$ ) turn out to be random tensors.

## Nominal multiscale model of cortical bone

The stochastic multiscale model can be compared with a *nominal model* obtained using *nominal* values of the volume fractions. The nominal model would refer to the whole cortical region. Therefore, nominal values of the volume fractions were set to their global experimental mean values. Using these input data in the deterministic model of Eqs. (1.2)-(1.4), the *nominal elastic tensors* are obtained:

$$g_I(\mathbb{C}_{\text{foam}}^\mu; \mu_{\text{exp}}(f_{\text{HA}}^{\text{foam}}), \{\mathbb{C}_{\text{HA}}, \mathbb{C}_{\text{w}}\}) = 0 \quad \rightarrow \quad \mathbb{C}_{\text{foam}}^\mu, \quad (1.15)$$

$$g_{II}(\mathbb{C}_{\text{ultra}}^\mu; \mu_{\text{exp}}(f_{\text{col}}^{\text{ultra}}), \{\mathbb{C}_{\text{col}}, \mathbb{C}_{\text{foam}}^\mu\}) = 0 \quad \rightarrow \quad \mathbb{C}_{\text{ultra}}^\mu, \quad (1.16)$$

$$g_{III}(\mathbb{C}_{\text{cort}}^\mu; \mu_{\text{exp}}(f_{\text{pore}}^{\text{cort}}), \{\mathbb{C}_{\text{pore}}, \mathbb{C}_{\text{ultra}}^\mu\}) = 0 \quad \rightarrow \quad \mathbb{C}_{\text{cort}}^\mu, \quad (1.17)$$

where  $\mathbb{C}_{\text{foam}}^\mu$ ,  $\mathbb{C}_{\text{ultra}}^\mu$ , and  $\mathbb{C}_{\text{cort}}^\mu$  are the nominal elastic tensors of the mineral foam, ultrastructure, and cortical tissue, respectively.

## Model parameters

The multiscale model previously described allows estimating the effective elastic tensor of an RVE of cortical bone (tissue scale) based on the local values of some modelling parameters describing the local bone microstructure. In this work cubic RVEs are considered, see Sec. 1.2.1. Modelling parameters are the elastic tensors and volume fractions of bone elementary components. Additional assumptions are made on the geometric arrangement of bone components at the different scales (Sansalone et al., 2010), leading to different expressions of the Eshelby tensors (Eshelby, 1957; Suvorov and Dvorak, 2002) underlying functions  $g_I$ ,  $g_{II}$ , and  $g_{III}$ .

For sake of simplicity, all the bone components were considered as linearly elastic, isotropic materials. Elastic tensors of HA mineral ( $\mathbb{C}_{\text{HA}}$ ), water ( $\mathbb{C}_{\text{w}}$ ), and collagen ( $\mathbb{C}_{\text{col}}$ ) were constructed using data taken from Kotha and Guzelsu (2000). Moreover, Haversian pores were considered as saturated by water, thus  $\mathbb{C}_{\text{pore}} = \mathbb{C}_{\text{w}}$ .

Volume fractions  $f_{\text{HA}}^{\text{foam}}$ ,  $f_{\text{col}}^{\text{ultra}}$ , and  $f_{\text{pore}}^{\text{cort}}$  were computed based on experimental measures of HP and TMD (Sansalone et al., 2010). Values of HP and TMD were analysed: (i) in each RVE—in order to obtain *local* statistical information representative of one RVE; (ii) gathering the data of all the RVEs—in order to obtain *global* statistical information representative of the whole cortical region.

Individual RVEs were analysed first. Within each RVE, the volume fraction of Haversian pores,  $f_{\text{pore}}^{\text{cort}}$ , is equal to the HP. Thus one value of  $f_{\text{pore}}^{\text{cort}}$  is obtained for each RVE. Moreover,  $f_{\text{col}}^{\text{ultra}}$  and  $f_{\text{HA}}^{\text{foam}}$  were computed from the voxel-wise 3-D distribution of TMD, leading to a voxel-wise 3-D distribution of these volume fractions in the bone solid matrix. First, volume fractions of collagen, HA and water were computed at the scale of the ultrastructure:

$$\begin{cases} f_{\text{HA}}^{\text{ultra}} = \text{TMD}/\rho_{\text{HA}}, \\ f_{\text{col}}^{\text{ultra}} + f_{\text{HA}}^{\text{ultra}} + f_{\text{w}}^{\text{ultra}} = 1, \\ \frac{f_{\text{col}}^{\text{ultra}}}{f_{\text{w}}^{\text{ultra}}} = 0.36 + 0.084 e^{6.7 f_{\text{HA}}^{\text{ultra}}}, \end{cases} \quad (1.18)$$

where  $\rho_{\text{HA}}$  is the mass density of the HA and the third equation is an empirical relation obtained through measurements of volume fractions in demineralised bone (Broz et al., 1995). Then,

volume fractions of HA and water were computed at the scale of the mineral foam as:

$$\begin{cases} f_{\text{HA}}^{\text{foam}} = \frac{f_{\text{HA}}^{\text{ultra}}}{f_{\text{HA}}^{\text{ultra}} + f_{\text{w}}^{\text{ultra}}}, \\ f_{\text{w}}^{\text{foam}} = \frac{f_{\text{w}}^{\text{ultra}}}{f_{\text{HA}}^{\text{ultra}} + f_{\text{w}}^{\text{ultra}}}. \end{cases} \quad (1.19)$$

For the  $i$ -th RVE, the outcome is one value of  $f_{\text{pore}}^{\text{cort}}$  and two databases collecting the  $N_{\text{vox}}^i$  values of  $f_{\text{col}}^{\text{ultra}}$  and  $f_{\text{HA}}^{\text{foam}}$  at each voxel of the solid matrix. Statistics on these databases were computed, namely the mean values  $\mu_{\text{exp}}(\bullet)$  and dispersions  $\delta_{\text{exp}}(\bullet)$ , with  $\bullet \in \{f_{\text{col}}^{\text{ultra}}, f_{\text{HA}}^{\text{foam}}\}$ .

The data of all the RVEs were further gathered to obtain three global databases of the volume fractions. The global database of  $f_{\text{pore}}^{\text{cort}}$  was made of the  $N_{\text{RVE}}$  items, whereas the global databases of  $f_{\text{col}}^{\text{ultra}}$  and  $f_{\text{HA}}^{\text{foam}}$  were made of  $N_{\text{vox}}$  items. Statistics on these databases were computed, namely the mean values  $\mu_{\text{exp}}(\bullet)$  and dispersions  $\delta_{\text{exp}}(\bullet)$ , with  $\bullet \in \{f_{\text{pore}}^{\text{cort}}, f_{\text{col}}^{\text{ultra}}, f_{\text{HA}}^{\text{foam}}\}$ . These global experimental statistics were used as *available information* to build the stochastic model of the random volume fractions described in Sec. 1.2.2, see Step I of the solution algorithm described in Sec. 1.2.2.

It should be noted that the multiscale model described above requires individual phases to be homogeneous within the RVE at each scale. This implies that only one value of  $f_{\text{HA}}^{\text{foam}}$ ,  $f_{\text{col}}^{\text{ultra}}$  and  $f_{\text{pore}}^{\text{cort}}$  can be considered for the whole solid matrix of the RVE. Since  $f_{\text{HA}}^{\text{foam}}$  and  $f_{\text{col}}^{\text{ultra}}$  are heterogeneous within the RVE, an effective value has to be selected to make computations. In the deterministic case, it is customary to take the local mean values as representative of the underlying heterogeneous distributions. This was the choice made in our nominal model of Sec. 1.2.2.

## Numerical solution of the stochastic multiscale model

The system of stochastic equations Eqs. (1.12)-(1.14) was solved in three steps.

**Step 1 / PDFs of the random volume fractions.** First, the PDFs of the random volume fractions  $F_{\text{pore}}^{\text{cort}}$ ,  $F_{\text{col}}^{\text{ultra}}$ , and  $F_{\text{HA}}^{\text{foam}}$  were determined. This requires computing the parameters  $\lambda_0^*$ ,  $\lambda_1^*$  and  $\lambda_2^*$  appearing in Eq. (1.9). This step was performed using the built-in optimisation functions of Matlab (version R2007b) software to solve the constrained optimisation problem in Eq. (1.11) and obtain the solution vector  $\boldsymbol{\lambda}^* = \{\lambda_0^*, \lambda_1^*, \lambda_2^*\}$ . Constraints associated with Eqs. (1.7)-(1.8) require the mean values and dispersions of the random volume fractions. The mean value and dispersion of the random volume fraction  $X$  (any of  $F_{\text{pore}}^{\text{cort}}$ ,  $F_{\text{col}}^{\text{ultra}}$ , and  $F_{\text{HA}}^{\text{foam}}$ ) were estimated by the *global* statistics of the experimental values of  $x$  (any of  $f_{\text{pore}}^{\text{cort}}$ ,  $f_{\text{col}}^{\text{ultra}}$ , and  $f_{\text{HA}}^{\text{foam}}$ ), that is we set:

$$\mu_X := \mu_{\text{exp}}(x), \quad \delta_X := \delta_{\text{exp}}(x). \quad (1.20)$$

**Step 2 / Statistically independent realisations of the random volume fractions.** Second, a large number  $N$  of statistically independent realisations of the random volume fractions were computed using the Monte Carlo method (Knuth, 1981; Rubinstein, 1981). In particular, the pseudo-inverse method (Devroye, 1986) was used to sample the support of the random volume fractions (the unit interval) according to the PDF given in Eq. (1.9) and with the

values of  $\lambda$  computed in the previous step. In brief, statistically independent realisations  $X(a_i)$  ( $i = 1, \dots, N$ ) of random variable  $X$  are obtained as:

$$X(a_i) = \left(F_X^\lambda\right)^{-1} (U(a_i)), \quad (1.21)$$

where  $F_X^\lambda(x) = \int_0^x p_X^\lambda(\xi) d\xi$  is the cumulative density function of  $X$  and  $U(a_i)$  is a realisation of a uniform random variable  $U$  with values in  $[0, 1]$ . The outcome was three databases of  $N$  statistically independent realisations of the random volume fractions, that is:  $\{F_{\text{HA}}^{\text{foam}}(a_i)\}$ ,  $\{F_{\text{col}}^{\text{ultra}}(a_i)\}$ , and  $\{F_{\text{pore}}^{\text{cort}}(a_i)\}$ .

Statistical estimators of the statistics of the random volume fractions  $F_{\text{HA}}^{\text{foam}}$ ,  $F_{\text{col}}^{\text{ultra}}$ , and  $F_{\text{pore}}^{\text{cort}}$  were computed using these databases. In particular, the statistical estimators of the mean value, standard deviation, and dispersion of the random volume fraction  $X$  are defined as:

$$\mu_N(X) = \frac{1}{N} \sum_{i=1}^N X(a_i), \quad (1.22)$$

$$\sigma_N(X) = \left\{ \frac{1}{N-1} \sum_{i=1}^N (X(a_i) - \mu_N(X))^2 \right\}^{\frac{1}{2}}, \quad (1.23)$$

$$\delta_N(X) = \frac{\sigma_N(X)}{\mu_N(X)}. \quad (1.24)$$

Convergence of the statistical estimators of the mean values and dispersions ( $\mu_N(X)$  and  $\delta_N(X)$ ) toward the mean values and dispersions ( $\mu_X$  and  $\delta_X$ ) of the random volume fractions was assessed. This allowed estimating the number  $N'$  of realisations needed for achieving convergence of the statistical estimators in terms of volume fractions.

**Step 3 / Homogenisation: stochastic model.** Third,  $N'$  statistically independent realisations of the random elastic tensors were computed. For each statistically independent realisation  $a_i$  ( $i = 1, \dots, N'$ ) of the random volume fractions, statistically independent realisations of the homogenised elastic tensors of the mineral foam, ultrastructure, and cortical tissue were obtained by solving the following formal equations successively:

$$g_{\text{I}}(\mathbb{C}_{\text{foam}}(a_i); F_{\text{HA}}^{\text{foam}}(a_i), \{\mathbb{C}_{\text{HA}}, \mathbb{C}_{\text{w}}\}) = 0 \quad \rightarrow \quad \mathbb{C}_{\text{foam}}(a_i), \quad (1.25)$$

$$g_{\text{II}}(\mathbb{C}_{\text{ultra}}(a_i); F_{\text{col}}^{\text{ultra}}(a_i), \{\mathbb{C}_{\text{col}}, \mathbb{C}_{\text{foam}}(a_i)\}) = 0 \quad \rightarrow \quad \mathbb{C}_{\text{ultra}}(a_i), \quad (1.26)$$

$$g_{\text{III}}(\mathbb{C}_{\text{cort}}(a_i); F_{\text{pore}}^{\text{cort}}(a_i), \{\mathbb{C}_{\text{pore}}, \mathbb{C}_{\text{ultra}}(a_i)\}) = 0 \quad \rightarrow \quad \mathbb{C}_{\text{cort}}(a_i). \quad (1.27)$$

The outcome was three databases of  $N'$  statistically independent realisations of the homogenised elastic tensors, that is  $\{\mathbb{C}_{\text{foam}}(a_i)\}$ ,  $\{\mathbb{C}_{\text{ultra}}(a_i)\}$ , and  $\{\mathbb{C}_{\text{cort}}(a_i)\}$ .

Statistical estimators of the statistics (mean values, dispersions, confidence intervals ...) of the random elastic tensors  $\mathbb{C}_{\text{foam}}$ ,  $\mathbb{C}_{\text{ultra}}$ , and  $\mathbb{C}_{\text{cort}}$  were computed using these databases as in Eqs. (1.22)-(1.24). It is worth noting that the mean value and dispersion of the random elastic tensors are not known. However, as long as convergence is reached in terms of volume fractions after  $N'$  independent realisations, it was assumed that the same would hold for the

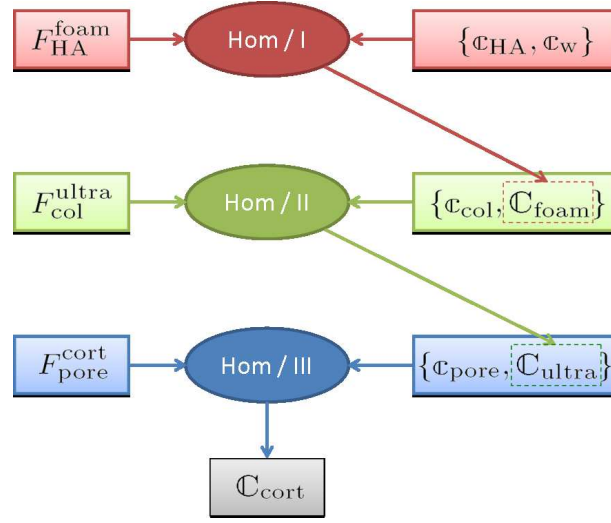


Figure 1.4: Algorithm used for solving the stochastic multiscale model.

elastic tensors. Thus, statistics of the random elastic tensors were set to the statistical estimators computed after  $N'$  independent realisations, namely:

$$\mu_Y := \mu_{N'}(Y), \quad \delta_Y := \delta_{N'}(Y), \quad (1.28)$$

with  $Y \in \{\mathbb{C}_{\text{foam}}, \mathbb{C}_{\text{ultra}}, \mathbb{C}_{\text{cort}}\}$ .

The algorithm for computing  $\mathbb{C}_{\text{cort}}(a_i)$  is schematically depicted in Fig. 1.4 and was implemented in a Matlab (Matlab) code. It is worth noting that each elastic tensor  $\mathbb{C}_{\text{cort}}(a_i)$  is the effective elastic tensor of a *fictitious* RVE characterised by homogeneous volume fractions  $F_{\text{HA}}^{\text{foam}}(a_i)$ ,  $F_{\text{col}}^{\text{ultra}}(a_i)$ , and  $F_{\text{pore}}^{\text{cort}}(a_i)$ .

#### Step 4 / Homogenisation: nominal model.

Eventually, the nominal model of Eqs. (1.15)-(1.17) was used to compute the homogenised *nominal* elastic tensors of the mineral foam, ultrastructure and cortical tissue, that is  $\mathbb{c}_{\text{foam}}^\mu$ ,  $\mathbb{c}_{\text{ultra}}^\mu$ , and  $\mathbb{c}_{\text{cort}}^\mu$ , respectively. Nominal elastic tensors were compared with the *mean values* of the *random* elastic tensors, that is  $\mu_{\mathbb{C}_{\text{foam}}}$ ,  $\mu_{\mathbb{C}_{\text{ultra}}}$ , and  $\mu_{\mathbb{C}_{\text{cort}}}$ , respectively.

Comparison was made with respect to individual elastic moduli. Let  $y^\mu$  be a nominal elastic modulus of  $\mathbb{c}_{\text{cort}}^\mu$ ,  $Y$  the corresponding random elastic modulus of  $\mathbb{C}_{\text{cort}}$ , and  $\mu_Y$  the mean value of  $Y$ . Elastic moduli  $y^\mu$  and  $\mu_Y$  were compared by computing their relative difference:

$$\text{err}(y^\mu) = \left| \frac{y^\mu - \mu_Y}{\mu_Y} \right|. \quad (1.29)$$

### Finite element model

Each RVE was modelled using the Finite Element (FE) Method. A tetrahedral mesh of the 3-D geometric model was generated using SimpleWare 5.0 FE+™ software. The meshing process adapted the mesh size to the geometry of the Haversian pore and solid matrix (ultrastructure)

regions and accounted for the heterogeneous distribution of TMD in the solid matrix. The mesh was then exported to a text file adapted for COMSOL Multiphysics<sup>®</sup> (version 4.2a) software. A COMSOL Multiphysics<sup>®</sup> script was developed to compute the effective elastic tensor of the RVE. To this aim, six boundary problems of linear elasticity were solved corresponding to homogeneous axial and shear strains on the boundary of the RVE. The FE model was made of about  $3 \times 10^5$  Lagrangian FEs with quadratic interpolation. For each RVE, the script performed the following steps:

1. Reading the mesh file exported by SimpleWare FE+<sup>™</sup>.
2. Converting the grayscale level of each mesh element into volume fractions of collagen, HA mineral and water at the ultrastructural level, see Eq. (1.18).
3. Computing the elastic tensor of each mesh element of the solid matrix ( $\mathbb{c}_{\text{ultra}}$ ) based on the volume fractions computed above and by performing the first two homogenisation steps described in Sec. 1.2.2, see Eqs. (1.2)-(1.3).
4. Setting the elastic tensor of the mesh elements belonging to the Haversian pore region to  $\mathbb{c}_w$ .
5. Applying six Dirichlet boundary conditions (BCs) on the whole boundary of the RVE corresponding to homogeneous boundary strains, namely three 1-D axial and three simple shear strains, and solving the corresponding linear elasticity problem using a stationary solver.
6. Postprocessing the results of the FE computations to compute the effective elastic tensor of the RVE,  $\mathbb{c}_{\text{cort}}^{\text{FEM}}$ .
7. Exporting the results of the FE computations (in particular, the tensor  $\mathbb{c}_{\text{cort}}^{\text{FEM}}$ ) to an Excel spreadsheet.
8. Extracting the relevant elastic moduli from the tensor  $\mathbb{c}_{\text{cort}}^{\text{FEM}}$ .

## 1.3 Results

### 1.3.1 Volume fractions

In Tab. 1.1 we show the experimental mean values ( $\mu_{\text{exp}}$ ) and dispersions ( $\delta_{\text{exp}}$ ) of HP, TMD, and volume fractions of bone components for individual RVEs (local statistics) and for all the RVEs together (global statistics, last but one row).

The HP of all the RVEs but two is comprised between 4% and 9%, what is quite usual for cortical bone. In two cases (RVEs #9 and #10), the HP is unusually high (about 20% and 15%, respectively). The TMD of each RVEs and the global mean value of TMD are all about  $1 \text{ g/cm}^3$ . The TMD distributions of RVEs #9 and #10 do not significantly differ from those of the other RVEs. As reported in Sansalone et al. (2012b), the local TMD slightly decreases in the axial direction when moving from the distal to the proximal part of the sample (that is, for increasing values of  $z$  at fixed values of  $\theta$ ).

RVE	$(z, \theta)$ [mm, °]	HP		TMD		$f_{\text{pore}}^{\text{cort}}$		$f_{\text{col}}^{\text{ultra}}$		$f_{\text{HA}}^{\text{foam}}$	
		$\mu_{\text{exp}}$ [%]	$\delta_{\text{exp}}$ [-]	$\mu_{\text{exp}}$ [g/cm <sup>3</sup> ]	$\delta_{\text{exp}}$ [-]	$\mu_{\text{exp}}$ [-]	$\delta_{\text{exp}}$ [-]	$\mu_{\text{exp}}$ [-]	$\delta_{\text{exp}}$ [-]	$\mu_{\text{exp}}$ [-]	$\delta_{\text{exp}}$ [-]
1	(5.5, -40)	6.47	N/A	0.98	0.0627	0.0647	N/A	0.354	0.0135	0.504	0.0696
2	(3.5, -40)	6.49	N/A	1.02	0.0622	0.0649	N/A	0.357	0.0135	0.528	0.0689
3	(1.5, -40)	4.15	N/A	1.05	0.0543	0.0415	N/A	0.359	0.0117	0.544	0.0601
4	(5.5, -20)	5.26	N/A	0.96	0.0703	0.0526	N/A	0.352	0.0151	0.492	0.0781
5	(3.5, -20)	6.21	N/A	0.98	0.0677	0.0621	N/A	0.354	0.0146	0.508	0.0752
6	(1.5, -20)	8.46	N/A	1.02	0.0649	0.0846	N/A	0.357	0.0139	0.530	0.0719
7	(5.5, 0)	8.80	N/A	0.96	0.0795	0.0880	N/A	0.352	0.0170	0.493	0.0882
8	(3.5, 0)	5.91	N/A	1.00	0.0685	0.0591	N/A	0.355	0.0147	0.516	0.0760
9 *	(1.5, 0)	20.7	N/A	1.02	0.0800	0.207	N/A	0.357	0.0138	0.530	0.0708
10 *	(5.5, 20)	15.5	N/A	0.98	0.0707	0.155	N/A	0.354	0.0152	0.505	0.0785
11	(3.5, 20)	5.89	N/A	1.03	0.0579	0.0589	N/A	0.358	0.0125	0.534	0.0641
12	(1.5, 20)	7.39	N/A	1.02	0.0649	0.0739	N/A	0.357	0.0138	0.530	0.0719
All		8.44	0.571	1.00	0.0715	0.0844	0.571	0.356	0.0154	0.518	0.0794
All but *		6.50	0.216	1.00	0.0717	0.0650	0.216	0.356	0.0155	0.518	0.0796

Table 1.1: Spatial averages and dispersions of experimental values of HP, TMD, and volume fractions of bone constituents for individual RVEs, the whole ensemble, and the whole ensemble but RVEs #9 and #10. Location of RVEs refers to the  $(z, \theta)$  coordinates described in Sec. 1.2.1. N/A: Not applicable.

The same remarks as for the HP and TMD apply to the volume fraction of the Haversian pores in the tissue ( $f_{\text{pore}}^{\text{cort}}$ ) on the one side and to the volume fractions of the collagen in the ultrastructure ( $f_{\text{col}}^{\text{ultra}}$ ) and of the mineral in the mineral foam ( $f_{\text{HA}}^{\text{foam}}$ ) on the other side. Based on the data reported in Tab. 1.1, the standard deviations of the volume fractions (computed with respect to all the 12 RVEs) are:  $\sigma_{\text{exp}}(f_{\text{pore}}^{\text{cort}}) = 0.0482$ ,  $\sigma_{\text{exp}}(f_{\text{col}}^{\text{ultra}}) = 0.0055$ , and  $\sigma_{\text{exp}}(f_{\text{HA}}^{\text{foam}}) = 0.0411$ . It can be noticed that the standard deviations of  $f_{\text{pore}}^{\text{cort}}$  and  $f_{\text{HA}}^{\text{foam}}$  are quite similar although their dispersions are not.

Experimental mean values and dispersions of the volume fractions  $f_{\text{pore}}^{\text{cort}}$ ,  $f_{\text{col}}^{\text{ultra}}$ , and  $f_{\text{HA}}^{\text{foam}}$  in the last but one row of Tab. 1.1 (row “All”) were used as input data for the probabilistic models of the random volume fractions  $F_{\text{pore}}^{\text{cort}}$ ,  $F_{\text{col}}^{\text{ultra}}$ , and  $F_{\text{HA}}^{\text{foam}}$ . A total of  $N = 10^6$  statistically independent realisations of each volume fraction were computed.

Approximations of the PDFs of the random volume fractions are shown in Fig. 1.5. Red, green and blue lines represent the distributions of the statistically independent realisations of  $F_{\text{pore}}^{\text{cort}}$ ,  $F_{\text{col}}^{\text{ultra}}$ , and  $F_{\text{HA}}^{\text{foam}}$ , respectively. Red, green and blue knots and dotted vertical lines depict the corresponding mean values. The realisations  $F_{\text{col}}^{\text{ultra}}(a_i)$  stay very close to the mean value of  $F_{\text{col}}^{\text{ultra}}$ , while the realisations  $F_{\text{pore}}^{\text{cort}}(a_i)$  and  $F_{\text{HA}}^{\text{foam}}(a_i)$  spread out, according to the larger values of the standard deviations of  $F_{\text{pore}}^{\text{cort}}$  and  $F_{\text{HA}}^{\text{foam}}$ . Note that the dispersion—the ratio between the standard deviation and the mean value—is a *relative* marker of spreading of data and smaller values of dispersion do not necessarily lead to tighter distributions.

Convergence of the statistical estimators of the mean values ( $\mu_N$ ) and dispersions ( $\delta_N$ ) of the random volume fractions toward the mean values ( $\mu$ ) and dispersions ( $\delta$ ) was assessed. It is worth recalling that statistics of the random volume fractions were set to the experimental statistics in the last but one row of Tab. 1.1, that is  $\mu = \mu_{\text{exp}}$  and  $\delta = \delta_{\text{exp}}$ . The magnitudes of

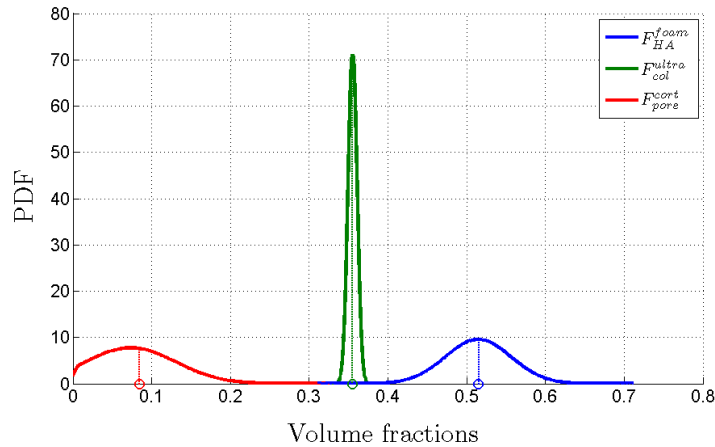


Figure 1.5: PDFs of the random volume fractions estimated on the basis of  $N = 10^6$  statistically independent realisations. Red, green and blue solid lines represent the distributions of the statistically independent realisations of  $F_{\text{pore}}^{\text{cort}}$ ,  $F_{\text{col}}^{\text{ultra}}$ , and  $F_{\text{HA}}^{\text{foam}}$ , respectively. Red, green and blue knots and dotted vertical lines depict the corresponding mean values. (Colors in online version.)

the relative errors between experimental statistics (taken as references) and statistical estimators after  $N = 10^6$  statistically independent realisations were smaller than 0.1%. This validated the random generator in Eq. (1.21) used for constructing the statistically independent realisations of the random volume fractions. The statistical estimators of the mean values and dispersions of the random volume fractions are shown in Fig. 1.6 as a function of the number  $n$  of realisations. Red, green and blue lines and bars refer to  $F_{\text{pore}}^{\text{cort}}$ ,  $F_{\text{col}}^{\text{ultra}}$ , and  $F_{\text{HA}}^{\text{foam}}$ , respectively. Plots in the left and right columns refer to the mean values and dispersions, respectively. On the top, the statistical estimators of the mean values ( $\mu_n$ ) and dispersions ( $\delta_n$ ) of the random volume fractions are depicted by solid lines in semi-logarithmic scale. Moreover, the mean values ( $\mu$ ) and dispersions ( $\delta$ ) of the random volume fractions are depicted by dashed lines. As the number of realisations  $n$  increases, the statistical estimators ( $\mu_n$  and  $\delta_n$ ) are computed on larger and larger databases  $\{F_{\text{pore}}^{\text{cort}}(a_i)\}_n$ ,  $\{F_{\text{col}}^{\text{ultra}}(a_i)\}_n$ , and  $\{F_{\text{HA}}^{\text{foam}}(a_i)\}_n$  and converge to the statistics ( $\mu$  and  $\delta$ ) of the random volume fractions as  $n \rightarrow N$ . On the bottom, the magnitudes of the relative errors of the statistical estimators of the mean values and dispersions,  $\text{err}(\mu_n) = |(\mu_n - \mu)/\mu|$  and  $\text{err}(\delta_n) = |(\delta_n - \delta)/\delta|$ , respectively, are shown in logarithmic scale. Exponential trend lines (dark coloured lines) are also shown. It can be noticed that the relative errors on the mean values and dispersions become smaller than 1% and 0.1% after  $10^4$  and  $10^5$  statistically independent realisations, respectively.

### 1.3.2 Elastic moduli

A total of  $N' = 10^5$  runs of the multiscale model were performed using the database of volume fractions previously built. The outcome was a database of  $N'$  statistically independent real-

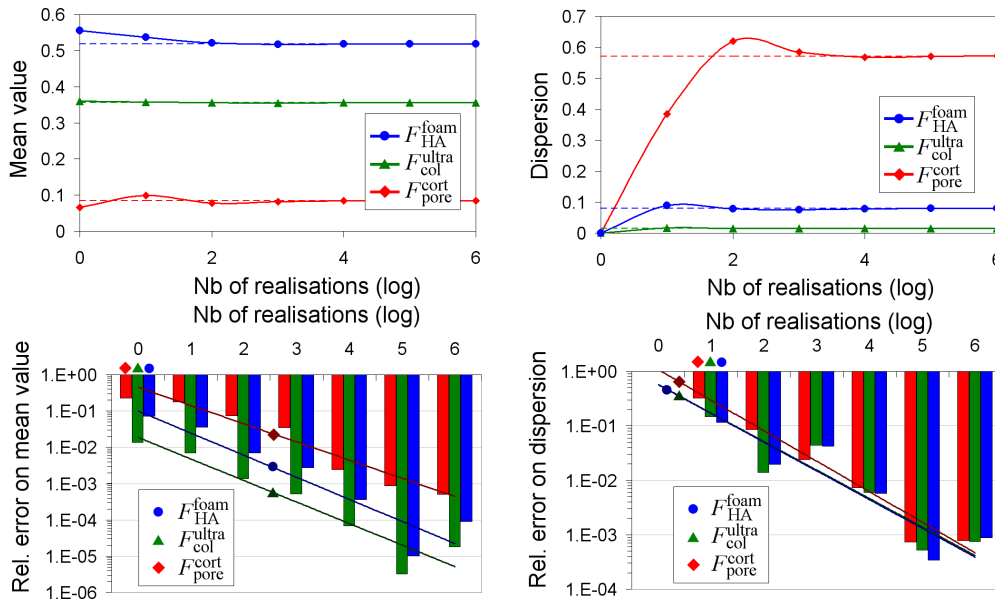


Figure 1.6: *Statistics* of the random volume fractions and their *statistical estimators* as a function of the number of realisations. Red, green and blue lines, bars and symbols refer to  $F_{\text{pore}}^{\text{cort}}$ ,  $F_{\text{col}}^{\text{ultra}}$ , and  $F_{\text{HA}}^{\text{foam}}$ , respectively. Diamonds, triangles and circles refer to  $F_{\text{pore}}^{\text{cort}}$ ,  $F_{\text{col}}^{\text{ultra}}$ , and  $F_{\text{HA}}^{\text{foam}}$ , respectively. On the top: Mean values and dispersions (straight dashed lines) and their statistical estimators (solid lines). On the bottom: Magnitude of the relative errors of the statistical estimators of the mean values and dispersions. Dark coloured lines are exponential trend lines. (Colors in online version.)

isations of random elastic tensors of the cortical tissue,  $\{\mathbb{C}_{\text{cort}}(a_i)\}$ , with  $i = 1, \dots, N'$ . The nominal elastic tensor of the cortical tissue,  $\mathbb{c}_{\text{cort}}^\mu$ , was also computed. In view of the assumptions made in Sec. 1.2.2, tensors  $\mathbb{c}_{\text{cort}}^\mu$  and  $\{\mathbb{C}_{\text{cort}}(a_i)\}$  turn out to be transversely isotropic, the isotropy plane being the cross-section of the femoral neck.

Statistics of the random elastic moduli were computed. The nominal elastic moduli were compared with the mean values of the random moduli to assess the relevance of the nominal model.

In view of the transverse isotropy of  $\mathbb{C}_{\text{cort}}$ , we focused on the axial moduli in the cross-section ( $Y_1$ ) and along the axis ( $Y_3$ ) of the femoral neck, the shear moduli in the cross-section ( $G_{12}$ ) and in the sagittal plane ( $G_{13} = G_{23}$ ), and the lateral contraction moduli in the cross-section ( $V_{12} = V_{21}$ ) and in the sagittal plane ( $V_{13} = V_{23}$ ), that is the contraction in the cross-section plane due to a unit extension in the axial direction. Subscripts  $\{1, 2, 3\}$  refer to the Cartesian frame in Fig. 1.1. Note that axial and lateral contraction moduli correspond to the Young's modulus and Poisson ratio, respectively, for an isotropic material.

Statistics of the random elastic moduli, nominal elastic moduli and relative differences as in Eq. (1.29) are reported in Tab. 1.2. The differences between the mean values of the random elastic moduli and the nominal elastic moduli are always smaller than 10%. Therefore, the

Stochastic model	$Y_1$ [GPa]	$Y_3$ [GPa]	$G_{12}$ [GPa]	$G_{13}$ [GPa]	$V_{12}$ [-]	$V_{13}$ [-]
Mean value	5.6416	7.5952	2.0485	2.3228	0.3917	0.2629
Std. deviation	2.3751	3.8096	0.8983	1.1055	0.0505	0.0542
Dispersion [-]	0.4210	0.5016	0.4385	0.4759	0.1288	0.2062
2.5% quantile	1.7007	1.8900	0.5767	0.5968	0.3341	0.1826
25% quantile	3.9172	4.6905	1.3949	1.5023	0.3643	0.2216
75% quantile	7.1296	9.9348	2.6044	3.0019	0.4091	0.3000
97.5% quantile	10.8355	16.2558	4.0361	4.8067	0.4777	0.3742
Nominal model	$y_1^\mu$ [GPa]	$y_3^\mu$ [GPa]	$g_{12}^\mu$ [GPa]	$g_{13}^\mu$ [GPa]	$v_{12}^\mu$ [-]	$v_{13}^\mu$ [-]
	5.4358	7.0657	1.9619	2.1861	0.3854	0.2546
Relative difference Eq. (1.29)	$\text{err}(y_1^\mu)$ [%]	$\text{err}(y_3^\mu)$ [%]	$\text{err}(g_{12}^\mu)$ [%]	$\text{err}(g_{13}^\mu)$ [%]	$\text{err}(v_{12}^\mu)$ [%]	$\text{err}(v_{13}^\mu)$ [%]
	3.6478	6.9717	4.2281	5.8888	1.6178	3.1668

Table 1.2: Statistics of the random moduli, nominal elastic moduli, and their relative differences (Eq. (1.29)). Random moduli -  $Y_1$ : axial modulus in the cross-section plane;  $Y_3$ : axial modulus along the axis of the femoral neck;  $G_{12}$ : shear modulus in the cross-section;  $G_{13} = G_{23}$ : shear modulus in the sagittal plane;  $V_{12} = V_{21}$ : lateral contraction modulus in the cross-section;  $V_{13} = V_{23}$ : lateral contraction modulus in the sagittal plane (*i.e.*, contraction in the cross-section plane due to a unit extension in the axial direction). Subscripts  $\{1, 2, 3\}$  refer to the Cartesian frame in Fig. 1.1. Dispersion values are dimensionless. Nominal moduli and relative differences follow the same notation.

deterministic elastic tensor computed through the nominal model provides a quite reasonable approximation of the random elastic tensor computed through the stochastic model. Moreover, leaving aside parallel programming, the computational time required to compute the (deterministic) nominal elastic tensor is  $N'$  orders of magnitude smaller than that required to estimate the random elastic tensor of the stochastic model. (The stochastic model requires additional computational time to store the large amount of data of the  $N'$  realisations and compute statistics.)

The axial modulus along the axis ( $Y_3$ , on the top) and the shear modulus in the cross-section plane ( $G_{12}$ , on the bottom) of the femoral neck, are shown in Fig. 1.7. Red crosses refer to the realisations of the random elastic moduli. Straight lines refer to the *statistics* of the random moduli (which do not depend on the realisations) and to the nominal model. Solid, thick-dashed and thin-dashed brown lines refers to the mean values, 50% and 95% confidence intervals of the random moduli, respectively. Confidence intervals are plotted based on the quantiles given in Tab. 1.2. Solid black lines refer to the nominal elastic moduli.

The statistical estimators of the mean values and confidence intervals of the random elastic moduli  $Y_3$  and  $G_{12}$  are presented in Fig. 1.8 as a function of the number of realisations  $n$ . Statistical estimators of the mean values and dispersions of the random elastic moduli converge towards the mean values and dispersions of the random elastic moduli as the number of independent realisations increases ( $n \rightarrow N'$ ). (Recall that statistics of the random elastic moduli are set to the statistical estimators computed on  $N' = 10^5$  statistically independent realisations.) As for the volume fractions, convergence is almost achieved after  $n = 10^4$  statistically independent

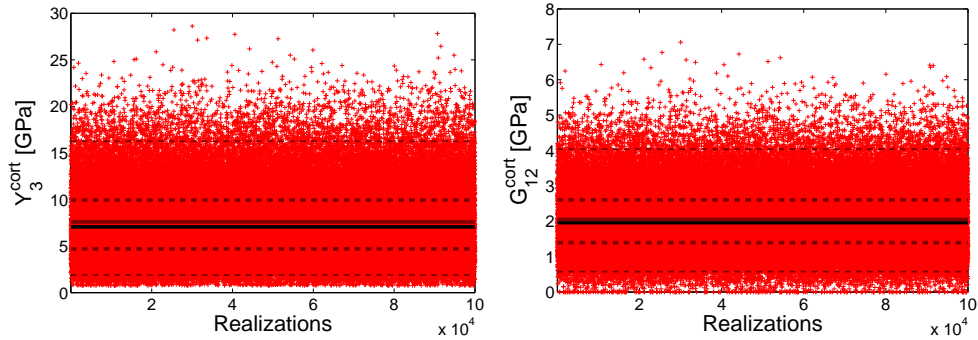


Figure 1.7: Axial (left) and shear (right) elastic moduli along the axis and in the cross section of the femoral neck, that is  $Y_3$  and  $G_{12}$ , respectively. Red crosses refer to the realisations of the random elastic moduli. Brown straight lines refer to the *statistics* of the random elastic moduli. Solid, thick-dashed and thin-dashed straight brown lines refer to the mean values, 50% and 95% confidence intervals of the random moduli, respectively. Solid black straight lines refer to the nominal elastic moduli. (Colors in online version.)

realisations, the relative errors of the statistical estimators being smaller than a few percent.

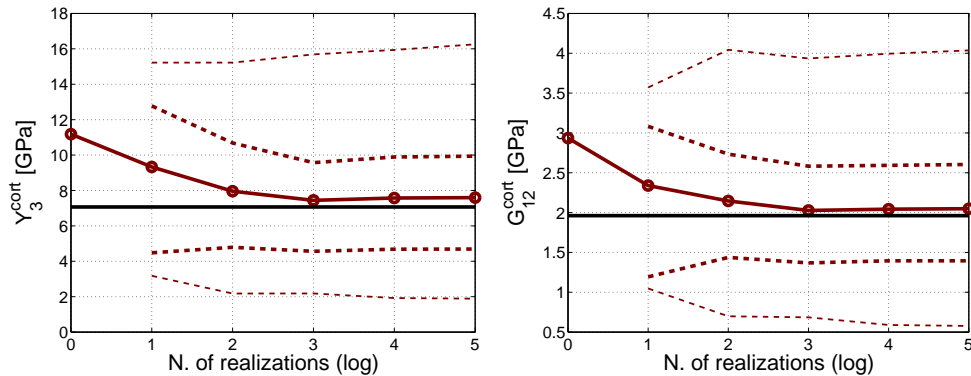


Figure 1.8: Axial (left) and shear (right) moduli along the axis and in the cross section of the femoral neck, that is  $Y_3$  and  $G_{12}$ , respectively. Solid, thick-dashed and thin-dashed brown lines refer to the *statistical estimators* of the mean values, 50% and 95% confidence intervals of the random elastic moduli, respectively. Solid black straight lines refer to the nominal elastic moduli. (Colors in online version.)

In Fig. 1.9 the estimated PDFs of the realised elastic moduli are presented. Solid, thick dashed and thin dashed brown lines refer to the averages, 50% and 95% confidence intervals of these random moduli, respectively. Solid black lines refer to the nominal elastic moduli. The PDFs of the random elastic moduli are quite asymmetric and do not show a Gauss-like shape.

Results of the multiscale models were compared with a reference FE model. FE estimates of the elastic tensors,  $\mathbb{C}_{\text{cort}}^{\text{FEM}}(j)$  with  $j = 1, \dots, 12$ , were computed for the 12 RVEs identified in Sec. 1.2.1. Unlike elastic tensors  $\mathbb{C}_{\text{cort}}(a_i)$ —which represent fictitious RVEs with idealised

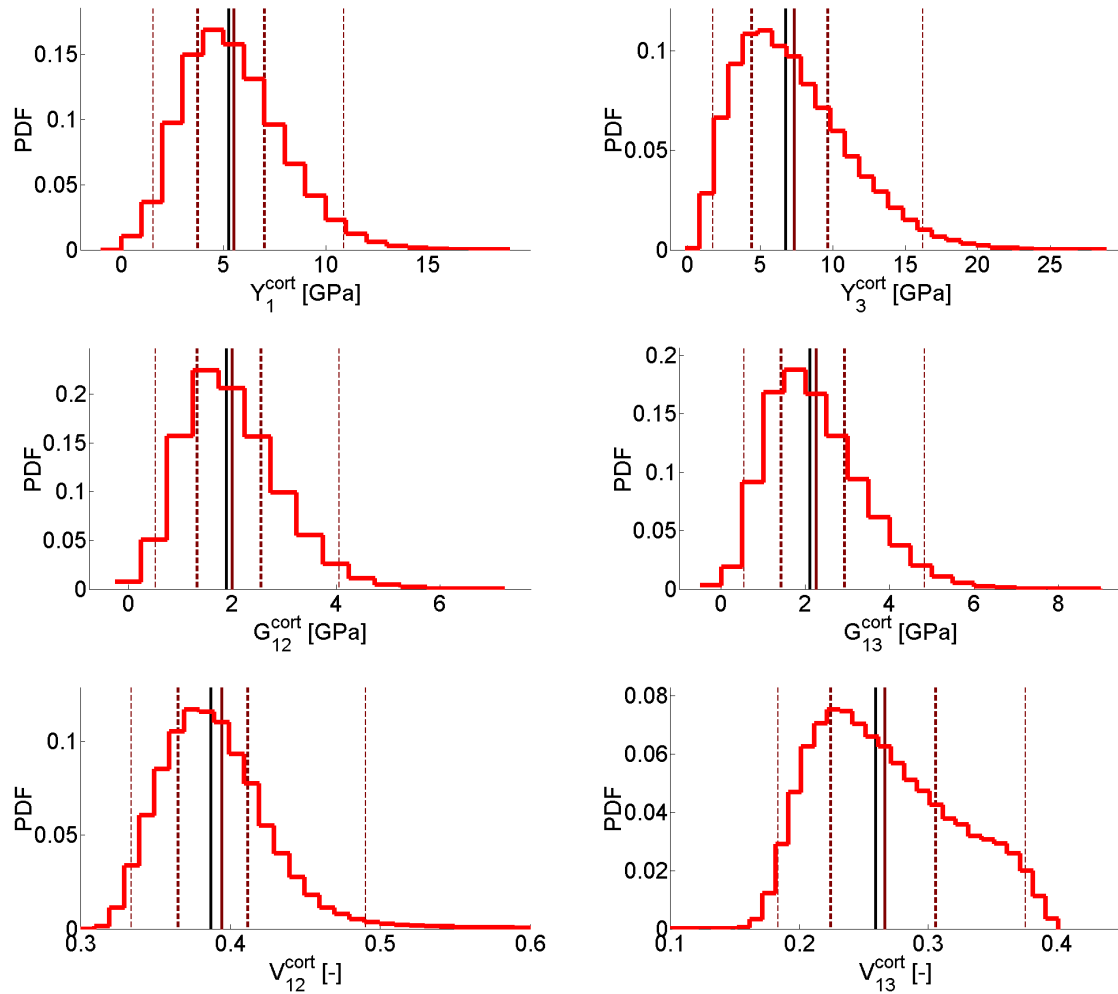


Figure 1.9: Approximations of PDFs of the random elastic moduli. Vertical brown straight lines refer to the *statistics* of the random elastic moduli. Solid, thick-dashed and thin-dashed brown lines refer to the mean values, 50% and 95% confidence intervals of these random moduli, respectively. Solid black straight lines refer to the nominal elastic moduli. (Colors in online version.)

pore geometry and homogeneous ultrastructure, each FE tensor  $\mathbb{c}_{\text{cort}}^{\text{FEM}}(j)$  accounts for the specific Haversian pore geometry and heterogeneous ultrastructure of one actual RVE. Therefore, tensors  $\mathbb{c}_{\text{cort}}^{\text{FEM}}(j)$  should be regarded as references for the multiscale model to be compared with. First of all, the accuracy of the multiscale model was assessed for the 12 RVEs. The homogenised elastic tensor of each RVE was computed using the deterministic, homogenised model presented in Sec. 1.2.2 and taking the HP and mean value of TMD of the RVE (see Tab. 1.1) as input data. The deterministic, homogenised model provided results very similar to those of the FEM model. The relative differences of the Frobenius norms of the homogenised and FE elastic tensors were

smaller than a few percent for all the 12 RVEs (data not shown).

Comparison between the stochastic model, the nominal model and the FE model is shown in Fig. 1.10. Results of the FE model are represented by blue circles in Fig. 1.10. Solid, dashed and dotted brown lines refers to the averages, 95% and 50% confidence intervals of the random moduli, respectively. Solid black lines refer to the nominal elastic moduli. The elastic moduli of all the 12 RVEs were found to fall within the 95% confidence interval of the stochastic model. Moreover, most of these elastic moduli were found to fall within the 50% confidence interval of the stochastic model. Three RVEs show some elastic moduli falling out of the 50% confidence interval, namely RVEs #3, #9, and #10. These RVEs are characterised by lowest (RVE #3) and highest (RVEs #9 and #10) values of HP, leading to highest and lowest elastic moduli, respectively.

## 1.4 Discussion

Multiscale modelling and simulation are powerful methods to predict bone mechanical properties as long as information on bone organisation and composition at different structural scales is available. Experimental information on microstructural features can be accounted for in multiscale models and FE simulations (Bourne and van der Meulen, 2004; Hellmich et al., 2008; Sansalone et al., 2010; Wagner et al., 2011; Sansalone et al., 2012b; Blanchard et al., 2013; Graeff et al., 2013; Sreenivasan et al., 2013). In particular, Haversian porosity (HP) and mineral content of bone matrix (TMD) are known to relate with the mechanical properties of bone (Burr, 2004). Information on HP and TMD can be provided by experimental measurements at the relevant scales, *i.e.* a few hundreds micrometres and several micrometres for the HP and TMD, respectively. X-Ray based devices are commonly used in scientific research and clinical practice to probe bone microstructure. Advanced imaging techniques as SR- $\mu$ CT can provide quite accurate information on bone microstructure at the micrometric scale or even below (Nuzzo et al., 2002; Bousson et al., 2004) but are limited to *in vitro* studies on small human bone samples. Medical devices currently used in clinical practice, such as DXA devices or QCT scans, have much coarser spatial resolution (typically one *mm* to several hundreds  $\mu$ m) and cannot provide as much accurate information. More recently, improved 3-D imaging techniques have been introduced such as  $\mu$ -CT, high-resolution peripheral quantitative  $\mu$ -CT (HR-pQCT), and multidetector CT (MDCT) (Burghardt et al., 2011). These techniques allow imaging bone *in vivo* with spatial resolution ranging from a few to several hundreds micrometres. Last generation  $\mu$ CTs allow *ex vivo* examinations of human specimens as big as entire vertebrae, with spatial resolutions in the 10  $\mu$ m range, which opens a new way for looking at entire bones in 3-D (Perilli et al., 2012). However, technical limitations related to image quality, radiation dose considerations, and subject motion make it hard to obtain accurate information on HP and TMD through these techniques in *in vivo* conditions. Technology is rapidly evolving in the field of medical imaging and improvements can be expected in next years or decades. However, at the present, *in vivo* medical images turn out to be too much blurred for extracting accurate information on bone microstructure. Uncertainties affecting available *in vivo* information on bone microstructure may question the reliability of results obtained by multiscale models using these data as entry (Valente et al., 2014). As long as input data are uncertain, deterministic approaches may become unreliable and new modelling paradigms are required.

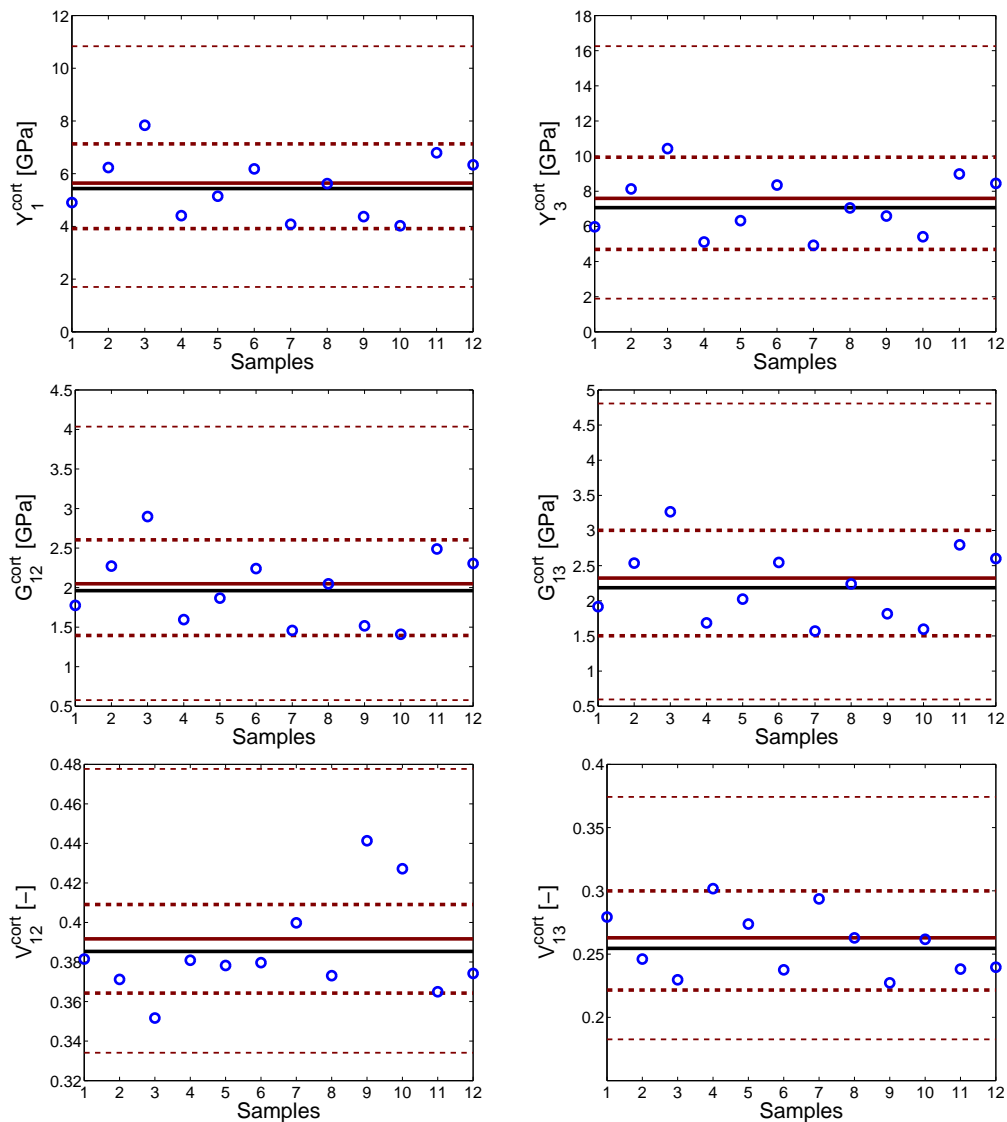


Figure 1.10: Comparison between the elastic moduli of the actual RVEs and the *statistics* of the random elastic moduli. Blue circles refer to the 12 RVEs in Tab. 1.1. Solid, thick-dashed and thin-dashed brown lines refer to the mean values, 50% and 95% confidence intervals of the random moduli, respectively. Solid black straight lines refer to the nominal elastic moduli. (Colors in online version.)

#### 1.4.1 The multiscale model: a compromise between accuracy and simplicity

The multiscale description of bone used in this study was developed in order to achieve a good compromise between accuracy (in the predicted elastic coefficients) and simplicity (required by the limited available experimental information). Both nominal and stochastic multiscale

models use continuum micromechanics theory and rely on the same assumptions in terms of microstructural organisation of bone at the different scales (mineral foam, ultrastructure, cortical tissue). Limitations related to these assumptions as well as experimental validation have been discussed in previous studies (Sansalone et al., 2010, 2012b). Some of this hypothesis have been investigated by other authors by comparing model predictions with experimental values.

Direct comparison with experimental data is not possible. On the one side, we were not able to perform mechanical testing. On the other side, comparison with data available in literature is tricky since elastic moduli strongly depend on microstructural features (namely the TMD) which we could not find in literature.

**RVE size.** A cornerstone of any homogenisation model is the concept of RVE. The size of our RVE was chosen looking at the dependency of the elastic coefficients of the cortical tissue—as predicted by the nominal model—on the RVE size (data not shown). It was found that the minimum RVE size should be about half a millimetre. This value is coherent with the findings of other authors (Grimal et al., 2011a) who have addressed this issue using different approaches. Moreover, within the RVE, our model assumes homogeneous material properties around the pores at the tissue scale. This assumption is supported by acoustic measures which revealed a small variation of elastic properties of bone matrix at the millimetre scale (Granke et al., 2011).

**Microarchitecture.** Both Haversian pores (at the tissue scale) and collagen (at the ultrastructural scale) were assumed to be of cylindrical shape and aligned with the femoral neck axis. However, Haversian pores have a more complex geometry (see Fig. 1.2) and collagen orientation changes from one lamella to another (Reisinger et al., 2011; Spiesz et al., 2011; Granke et al., 2013). Moreover, mineral particles (at the mineral foam scale) were assumed to be spherical whereas they are actually platelets with thickness of a few nanometres and length and width of a few to several tens of nanometres (Rho et al., 1998; Deuerling et al., 2009). While on the one hand our hypothesis of cylindrical pores at the tissue scale seems reasonable (Granke et al., 2015), our assumptions at the lower scales (aligned collagen fibers and spherical mineral particles) may lead to inaccurate predictions (Deuerling et al., 2009). Other micro- and nano-scale features such as the morphology of the lacuno-canalicular network and the mineralisation at the nanoscale can affect bone elasticity, strength and failure (Tai et al., 2008; Langer et al., 2012; Schrof et al., 2014). All these microarchitectural features should be investigated and their effects on the tissue level properties assessed.

**How many scales?** The usefulness of a detailed description of bone micro- and nanostructure below the tissue scale is a matter of debate. Our model considers three microstructural levels below the organ and lies in between two families of approaches. On the one side, some authors used very detailed descriptions of bone hierarchical structure (Yoon and Cowin, 2008a,b; Fritsch and Hellmich, 2007) which fit quite well with experimental measures at different microstructural scales. However, these approaches need experimental input data which are hardly available in a subject-specific study. Other authors suggested that simpler models, basically based on the porosity at the tissue level (Dong and Guo, 2006; Granke et al., 2011, 2015), could be enough to catch the main elastic properties of bone. In this case, some discrepancies between experimental measures and model predictions were observed which could be attributed to variations in the elastic properties of microstructural features of bone (Dong and Guo, 2006; Granke et al., 2015). This interpretation is coherent with our findings (*e.g.* RVEs n. 1 and 2 which have quite similar

HP and different TMD, see Tab. 1.1).

### 1.4.2 The stochastic multiscale model: a comprehensive description of bone

The *first goal* of this work was to develop a modelling strategy taking into account the uncertain composition of bone. To this aim, a stochastic multiscale model of cortical bone was developed. To the best of our knowledge, this is the first attempt to compute the elastic properties of cortical bone taking into account simultaneously its multiscale structure *and* the experimental uncertainty on the amount of its elementary components. The deterministic multiscale model of Sansalone et al. (2010, 2012b) was extended in a stochastic framework by treating the volume fractions of bone components as random variables. The non-Gaussian probabilistic models of the volume fractions were obtained using the MaxEnt principle. The experimental information needed to construct the PDFs of the volume fractions was obtained through high-resolution SR- $\mu$ CT images of the inferior part of a human femoral neck sample. Image analysis of several RVEs in the cortical part of the sample allowed computing the mean value and dispersion of each volume fraction. The stochastic multiscale model was used to quantify the uncertainties relative to the random elastic tensor of cortical tissue and its mean value. Statistics of random elastic moduli (mean value, standard deviation, confidence interval ...) were compared with the nominal elastic moduli on the one side and with detailed FE models of the RVEs on the other side.

The stochastic model turns out to provide a reliable representation of the elastic properties of cortical tissue. All the FE results fall within the 90% confidence interval of the stochastic model. Moreover, all the FE results fall within the 50% confidence interval of the stochastic model but a few exceptions (3 RVEs out of 12, characterised by an unusually high or low HP), see Fig. 1.10. It should be noted that the outcome of the stochastic model has to be regarded in statistical terms. As long as bone composition at a given anatomical location is known in statistical terms (*e.g.* average and dispersion), it provides reliable information about the expected value of the local elastic properties and the confidence interval of that estimate. One might expect the elastic moduli of roughly half of the actual RVEs to fall within the 50% confidence interval of the stochastic model. However, this latter seems to provide a much safer envelop. Fig. 1.10 shows that between 75% and 100% of the actual RVEs fall within the 50% confidence interval. This might be due to the information introduced in the MaxEnt principle. This information would lead to PDFs of the *random* volume fractions which are more spread out than those of the *actual* volume fractions. On the one side, some information might be missing: For instance, the bounds 0 and 1 could be considered as repulsive values. On the other side, estimates of mean value and dispersion of random volume fractions could be improved: For instance, instead of considering them as experimentally known values, they could be computed by solving an optimisation problem based on the *maximum likelihood principle*.

### 1.4.3 The nominal model: a simple and accurate estimate of expected elastic moduli

The *second goal* of this chapter was to identify whether a simpler model exists providing results comparable to those of the stochastic multiscale model. Indeed, while providing a comprehen-

sive representation of bone elasticity, the stochastic model presents some drawbacks which may prevent its direct application for end-user clinical purposes. First of all, the stochastic model requires a high computational time. In this study, the computational time on a standard desktop computer was about half an hour to generate the database of  $N = 10^6$  volume fractions and half a day to perform  $N' = 10^5$  runs of the three-step homogenisation procedure. Despite this time is quite reasonable for research purposes, it might be not for end-user clinical purposes. Parallelising the computer code would reduce the computational cost. (Roughly speaking, computational time would be divided by the number of parallel processors.) However, this is not worth considering in clinical practice. Moreover, the stochastic model requires *both* the mean values *and* the dispersions of the volume fractions to be estimated, which might not be straightforward. Therefore, the interest for a faster and simpler model is apparent. A candidate meeting these requirements is the *nominal model* introduced in Sec. 1.2.2. The nominal model only needs the mean values of the volume fractions as input data and provides run-time results. Nominal elastic moduli stay quite close to the mean values of the random elastic moduli, with differences of a few percent, see Tab. 1.2. As long as errors smaller than 10% are acceptable, the nominal model provides a “good” estimate of expected bone elastic moduli. However, it should be reminded that the nominal model is intrinsically unable to provide information about the reliability of these estimates—a shortcoming of any deterministic approach.

#### 1.4.4 Whole bone: heterogeneity *vs.* homogeneity

Another shortcoming of the nominal model lies in the fact that it cannot account for the heterogeneity of bone at the organ scale. Our experimental data cover the whole cortical region. Then, one should be allowed to use these data to analyse the whole cortical region. The stochastic model would use these data (namely, the mean values and dispersions of the bone volume fractions) to generate a random distribution of elastic tensors at each point of the bone cortex. This result should be regarded in a statistical sense: the spatial distribution of elastic tensors generated by the stochastic model will be statistically equivalent to the spatial distribution of actual elastic tensors.

Both HP and TMD—and therefore elastic properties—of bone tissue are heterogeneously distributed at the organ scale. The stochastic model could be used to generate a heterogeneous distribution of elastic properties statistically equivalent to the actual one and therefore to set up a FE analysis at the organ scale. The elastic properties of each FE meshing the bone could be randomly generated by the stochastic model. In general, the randomly generated elastic properties of each FE will be different from the actual ones (which are related to the local values of HP and TMD). However, the spatial distributions of randomly generated and actual elastic tensors will be statistically equivalent. In other words, one would obtain the same macroscopic results (such as maximum displacement or limit load) from FE meshes with either heterogeneous randomly-generated elastic properties or heterogeneous actual elastic properties.

By contrast, the nominal model would predict the same elastic response at each point of the bone. Using the nominal model to set up a FE analysis of the whole bone would lead to homogeneous material properties everywhere in the mesh. Is this simplification acceptable? Fig. 1.10 shows that the values of the elastic moduli of individual RVEs obtained through the FE model can be quite different from the elastic moduli predicted by the nominal model (as well as

the mean values of the stochastic model), the relative errors approaching 50% in some cases. The average errors on the axial and shear moduli are about 20% and those on the lateral contraction moduli are slightly smaller than 10%. Indeed, bone turns out to be highly heterogeneous at the organ scale and the elastic properties can vary considerably within a distance of a few millimetres (as in the bone sample considered in this study), see *e.g.* the axial modulus along the femoral neck axis of RVEs #10 ( $z = 5.5 \text{ mm}$ ,  $\theta = 20^\circ$ ,  $y_3^{\text{FEM}} \simeq 5 \text{ GPa}$ ) and #11 ( $z = 3.5 \text{ mm}$ ,  $\theta = 20^\circ$ ,  $y_3^{\text{FEM}} \simeq 9 \text{ GPa}$ ). Therefore, attention should be paid in considering bone as homogeneous at the organ scale.

#### 1.4.5 Limitations and future research directions

To conclude, a few remarks on the scope and limitations of the proposed modelling strategy are in order. Some limitations of our study are related to the multiscale description of bone and the associated modelling choices. Some of these issues were addressed in Sec. 1.4.1 and thoroughly discussed in previous work (Sansalone et al., 2010, 2012b). Other limitations are more closely related to the stochastic treatment of modelling variables and will be discussed here below.

**Statistical population.** First of all, only 12 RVEs were considered in this study. This makes largely unreliable the values of the experimental (global) statistics of  $f_{\text{pore}}^{\text{cort}}$ . A larger number of RVEs should be used to improve accuracy and reliability of the experimental statistics of  $f_{\text{pore}}^{\text{cort}}$ . For instance, the global mean value of HP is higher than 8% and its global dispersion is higher than 0.5—a quite high value corresponding to a standard deviation of almost 5%. Such high values of the global mean value and dispersion are mainly due to the contribution of RVEs #9 and #10. Excluding these RVEs from the statistical analysis (last row), the global mean value of HP drops to 6.5% and its global dispersion to 0.2 (corresponding to a standard deviation of 1.4%). By contrast, experimental statistics on  $f_{\text{col}}^{\text{ultra}}$  and  $f_{\text{HA}}^{\text{foam}}$  are computed on large numbers of voxel-wise values ( $N_{\text{vox}}^i \sim 10^5$  and  $N_{\text{vox}} > 10^6$  for local and global statistics, respectively). Therefore, no significant errors are expected on those statistics. It should also be noted that this study considered just one bone sample from one anatomical site of one donor. Different results may be obtained for different anatomical sites or donors of different ages or pathological conditions. A longitudinal and cross-sectional study is needed in order to assess the suitability of this approach and the conclusions of this study on different statistical populations.

**Statistical independence.** Experimental volume fractions  $f_{\text{HA}}^{\text{foam}}$ ,  $f_{\text{col}}^{\text{ultra}}$ , and  $f_{\text{pore}}^{\text{cort}}$  are computed based on two pieces of experimental information (HP and TMD), see Sec. 1.2.2. Experimental statistics of  $f_{\text{HA}}^{\text{foam}}$ ,  $f_{\text{col}}^{\text{ultra}}$ , and  $f_{\text{pore}}^{\text{cort}}$  fed the stochastic models of the random volume fractions  $F_{\text{HA}}^{\text{foam}}$ ,  $F_{\text{col}}^{\text{ultra}}$ , and  $F_{\text{pore}}^{\text{cort}}$ , respectively, which were considered as statistically independent. Nevertheless, statistical dependence may exist between these random variables. In order to take statistical dependence into account in the MaxEnt principle, objective information is needed. This information could be provided by analysing the dependence (*e.g.* correlation) possibly existing between the experimental variables. This issue was not investigated yet. Therefore, statistical independence remains a safe hypothesis in the framework of the MaxEnt principle.

**Random variables vs. random fields.** Volume fractions are modelled as random variables without spatial correlation. Should this model be used to generate a FE mesh at the organ scale, no relationship would exist between the elastic properties of adjacent points. This

is largely unrealistic. As previous studies have shown, elastic moduli in the femoral neck are not only heterogeneous—as already underlined—but also show a global tendency to decrease radially from the periosteum inwards (Sansalone et al., 2010, 2012a) and axially from the distal to the proximal part of the femoral neck (Sansalone et al., 2012b). These variations have been shown to be related to the anatomical variations of HP—increasing from the periosteum inward—and TMD—decreasing from the distal to the proximal part. Moreover, at each point of the femoral neck, the values of HP and TMD may correlate, which would induce dependency between the volume fractions. All these features should be taken into account in the stochastic model of volume fractions and are addressed in a forthcoming work.

**Random elastic properties and microarchitecture.** Moreover, only the volume fractions were considered as random parameters. Both elastic properties and geometric organisation of bone components were fixed to some reference values. However, aiming at patient-specific modelling, modelling of both these features needs to be improved and included in a comprehensive model where all the parameters are described according to the available information. On the one side, elastic coefficients of bone components were already modelled as random variables in previous work (Sansalone et al., 2014). Randomness in the values of the elastic coefficients accounts for the imperfect knowledge of the effective elastic behavior of bone components at the nanoscale. In that work, all the bone components were considered as elastically isotropic. For sake of coherency, we made the same assumption in this work. However, at the least collagen should be considered transversely isotropic (Hellmich et al., 2004a)—as already done in previous work of our group (Sansalone et al., 2010). On the other side, the idealised microarchitecture assumed in this study should be revisited to comply with a more realistic description. Again, a stochastic treatment might be useful to account for the limited data available on bone microarchitecture.

**Validation.** Furthermore, the stochastic model needs to be validated at the organ scale. At the present, only a numerical validation was performed for each RVE (data not shown). The stochastic model is expected to produce an accurate description of the overall elastic response at the organ scale. Experimental or detailed numerical results at the organ scale are required to prove the reliability of model predictions.

***In vivo* experimental data.** Eventually, this study was based on high resolution SR- $\mu$ CT images which allowed obtaining a detailed description of bone microstructure and accurate statistical information on HP and TMD in a small bone sample. Aiming at translating this approach to *in vivo* conditions, some critical issues arise concerning the experimental data. On the one side, the physics of imaging (for instance, dose in X-ray CT) limits the spatial resolution of clinical CT scanners. Peripheral CT scans can achieve a spatial resolution of about  $80 \mu\text{m}$ . However, the spatial resolution of clinical scanners for imaging spine and hip is of several hundreds of micrometres, which is inadequate for highly accurate cortical measurements (Genant and Jiang, 2006). On the other side, clinical applications cannot be restricted to small anatomical sites as in this study. Imaging whole organs (or large parts of them) with a resolution of several micrometres requires managing very big data. Nowadays, the need for accurate measurements at the microstructural scale on whole bones constitutes a critical bottleneck for the approach proposed in this work to be transferred to clinical practice. In order to overcome this difficulty, a robust protocol is necessary to retrieve statistical information at the finer scales—required

by the model—from measurements at the coarser scales—typical of medical devices. The improvement of imaging resolution would become non-essential if useful information from bone microarchitecture, such as heterogeneity of spatial mineral distribution, can be extracted from the low-resolution images. Several multi-modal studies exist which compare and correlate experimental data coming from different imaging techniques (Grampp et al., 1997; Heilmann et al., 1998; Rossini et al., 1998; Genant et al., 2000; Apostol et al., 2006; Bagi et al., 2006; Chappard et al., 2006; Engelke et al., 2009; Guglielmi et al., 2011; Itô, 2000; Nishiyama and Boyd, 2011; Link, 2012; Baum et al., 2013; Lewiecki, 2013). These studies point out the difficulty to retrieve accurate microstructural information from 2-D or 3-D medical devices. Recently, a stochastic approach was proposed to examine 2-D DXA images and quantitatively assess the heterogeneity of spatial mineral distribution (Dong and Wang, 2013) opening the way to further studies in this direction.

## 1.5 Conclusion

Lack of patient-specific data and uncertainties affecting available information on bone microstructure, especially *in vivo* and at the small scales of its hierarchical structure, may question the reliability of results provided by models based on these experimental input data. In order to overcome these difficulties, we proposed in this chapter a novel modelling approach taking into account *both* the hierarchical structure of bone *and* the uncertainty existing on the experimental data. The hierarchical structure of bone is accounted for using a continuum micromechanics approach. Uncertain experimental data are treated as random variables and their probability distributions are built using the MaxEnt principle. The outcome is a stochastic multiscale model which uses statistics (mean and dispersion) on experimental measures of bone composition to provide statistics (mean, dispersion, confidence intervals, ...) on the elastic properties of the cortical tissue. The stochastic multiscale model was validated against detailed FE calculations and proved to describe correctly the heterogeneous elastic properties of cortical tissue at the organ scale. A simpler nominal multiscale model was also proposed which may be useful when heterogeneity can be neglected. Experimental input data of this study were provided by SR- $\mu$ CT images of a femoral neck sample. These images provided detailed statistics on bone composition which were used for both the stochastic multiscale model and the FE analysis. This work is a first step in patient-specific modelling and several limitations exist which will be addressed in future work. Some limitations are related to the modelling (spatial correlation of experimental data and uncertainty on the microarchitecture are not accounted for) and others to the technology of the clinical devices which, at present, cannot provide the experimental data required by the model.

## Bibliography

- B. Aoubiza, J.M. Crolet, and A. Meunier. On the mechanical characterization of compact bone structure using the homogenization theory. *Journal of Biomechanics*, 29(12):1539–1547, 1996.
- L. Apostol, V. Boudousq, O. Basset, C. Odet, S. Yot, J. Tabary, J.M. Dinten, E. Boiler, P.O. Kotzki, and F. Peyrin. Relevance of 2d radiographic texture analysis for the assessment of 3d bone micro-architecture. *Med Phys*, 33(9):3546–3556, 2006.
- L. Arnold. *Stochastic Differential Equations : Theory and Applications*. John Wiley and Sons, New York, 1973.
- C.M. Bagi, N. Hanson, C. Andresen, R. Pero, R. Lariviere, C.H. Turner, and A. Laib. The use of micro-ct to evaluate cortical bone geometry and strength in nude rats: correlation with mechanical testing, pqct and dxa. *Bone*, 38(1):136–144, 2006.
- K.S. Basaruddin, N. Takano, and T. Nakano. Stochastic multi-scale prediction on the apparent elastic moduli of trabecular bone considering uncertainties of biological apatite (bap) crystal-lite orientation and image-based modelling. *Comput Methods Biomech Biomed Engin*, 18(2): 162–174, 2015.
- T. Baum, D.C. Karampinos, H. Liebl, E.J. Rummeny, S. Waldt, and J.S. Bauer. High-resolution bone imaging for osteoporosis diagnostics and therapy monitoring using clinical mdct and mri. *Curr Med Chem*, 20(38):4844–4852, 2013.
- K.L. Bell, N. Loveridge, J. Power, N. Garrahan, B.F. Meggitt, and J. Reeve. Regional differences in cortical porosity in the fractured femoral neck. *Bone*, 24(1):57–64, 1999.
- S. Bensamoun, J.-M. Gherbezza, J.-F. de Belleval, and M.-C. Ho Ba Tho. Transmission scanning acoustic imaging of human cortical bone and relation with the microstructure. *Clinical Biomechanics*, 19:639–647, 2004a.
- S. Bensamoun, M.-C. Ho Ba Tho, S. Luu, J.-M. Gherbezza, and J.-F. de Belleval. Spatial distribution of acoustic and elastic properties of human femoral cortical bone. *J. Biomech.*, 37:503–510, 2004b.
- R. Blanchard, A. Dejaco, E. Bongaers, and C. Hellmich. Intravoxel bone micromechanics for microct-based finite element simulations. *J. Biomech.*, 46(15):2710–2721, 2013.
- G. Boivin and P.J. Meunier. The degree of mineralization of bone tissue measured by computerized quantitative contact microradiography. *Calcif. Tissue Int.*, 70(6):503–511, 2002.
- B.C. Bourne and M.C. van der Meulen. Finite element models predict cancellous apparent modulus when tissue modulus is scaled from specimen ct-attenuation. *J Biomech*, 37(5): 613–621, 2004.
- V. Bousson, A. Meunier, C. Bergot, E. Vicaut, M.A. Rocha, M.H. Morais, A.M. Laval-Jeantet, and J.D. Laredo. Distribution of intracortical porosity in human midfemoral cortex by age and gender. *J. Bone Miner. Res.*, 16(7):1308–1317, 2001.

- V. Bousson, F. Peyrin, C. Bergot, M. Hausard, A. Sautet, and J.D. Laredo. Cortical bone in the human femoral neck: three-dimensional appearance and porosity using synchrotron radiation. *J. Bone Miner. Res.*, 19(5):794–801, 2004.
- M.L. Bouxsein. Bone quality: where do we go from here? *Osteoporos. Int.*, 14(S5):S118–S127, 2003.
- M.L. Bouxsein, S.K. Boyd, B.A. Christiansen, R.E. Guldborg, K.J. Jepsen, and R. Müller. Guidelines for assessment of bone microstructure in rodents using micro-computed tomography. *J. Bone Miner. Res.*, 25(7):1468–1486, 2010.
- J.J. Broz, S.J. Simske, and A.R. Greenberg. Material and compositional properties of selectively demineralised cortical bone. *J. Biomech.*, 28(11):1357–1368, 1995.
- A.J. Burghardt, T.M. Link, and S. Majumdar. High-resolution computed tomography for clinical imaging of bone microarchitecture. *Clinical Orthopaedics and Related Research*, 469(8):2179–2193, 2011.
- D.B. Burr. Bone quality: understanding what matters. *J. Musculoskelet. Neuronal Interact.*, 4(2):184–186, 2004.
- C. Chappard, A. Basillais, L. Benhamou, A. Bonassie, B. Brunet-Imbault, N. Bonnet, and F. Peyrin. Comparison of synchrotron radiation and conventional x-ray microcomputed tomography for assessing trabecular bone microarchitecture of human femoral heads. *Med Phys*, 33(9):3568–3577, 2006.
- N. Crabtree, N. Loveridge, M. Parker, N. Rushton, J. Power, K.L. Bell, T.J. Beck, and J. Reeve. Intracapsular hip fracture and the region-specific loss of cortical bone: analysis by peripheral quantitative computed tomography. *J. Bone Miner. Res.*, 16(7):1318–1328, 2001.
- J.D. Currey. The effect of porosity and mineral content on the young’s modulus of elasticity of compact bone. *Journal of Biomechanics*, 21(2):131–139, 1988.
- J.M. Deurling, W. Yue, A.A. Espinoza Orías, and R.K. Roeder. Specimen-specific multi-scale model for the anisotropic elastic constants of human cortical bone. *J Biomech*, 42(13):2061–2067, 2009.
- L. Devroye. *Non Uniform Random Variate Generation*. Springer Verlag, New York, 1986.
- X. Dong and X.E. Guo. Prediction of cortical bone elastic constants by a two-level micromechanical model using a generalized self-consistent method. *J Biomech Eng*, 128(3):309–316, 2006.
- X. Dong and X. Wang. Assessment of bone fragility with clinical imaging modalities. *Hard Tissue*, 2(1):7, 2013.
- E. Donnelly. Methods for assessing bone quality: a review. *Clin Orthop Relat Res*, 469(8):2128–2138, 2011.

- 
- K. Engelke, C. Libanati, Y. Liu, H. Wang, M. Austin, T. Fuerst, B. Stampa, W. Timm, and H.K. Genant. Quantitative computed tomography (qct) of the forearm using general purpose spiral whole-body ct scanners: accuracy, precision and comparison with dual-energy x-ray absorptiometry (dxa). *Bone*, 45(1):110–118, 2009.
- J. Eshelby. The determination of the elastic field of an ellipsoidal inclusion, and related problems. *Proc. R. Soc. London, Ser. A*, 241:376–396, 1957.
- W. Feller. *An Introduction to Probability Theory and its Applications*. John Wiley and Sons, New York, 1971.
- P. Fratzl, H.S. Gupta, E.P. Paschalis, and P. Roschger. Structure and mechanical quality of the collagen-mineral nano-composite in bone. *Journal of Materials Chemistry*, 14:2115–2123, 2004.
- A. Fritsch and C. Hellmich. ‘Universal’ microstructural patterns in cortical and trabecular, extracellular and extravascular bone materials: Micromechanics-based prediction of anisotropic elasticity. *Journal of Theoretical Biology*, 244(4):597–620, 2007.
- H.K. Genant and Y. Jiang. Advanced imaging assessment of bone quality. *Annals of the New York Academy of Sciences*, 1068:410–428, 2006.
- H.K. Genant, C. Gordon, Y. Jiang, T.M. Link, D. Hans, S. Majumdar, and T.F. Lang. Advanced imaging of the macrostructure and microstructure of bone. *Hormone Research in Paediatrics*, 54(S1):24–30, 2000.
- J. Ghanbaria and R. Naghdabadi. Nonlinear hierarchical multiscale modeling of cortical bone considering its nanoscale microstructure. *Journal of Biomechanics*, 42(10):1560–1565, 2009.
- C. Graeff, F. Marin, H. Petto, O. Kayser, A. Reisinger, J. Peña, P. Zysset, and C.C. Glüer. High resolution quantitative computed tomography-based assessment of trabecular microstructure and strength estimates by finite-element analysis of the spine, but not dxa, reflects vertebral fracture status in men with glucocorticoid-induced osteoporosis. *Bone*, 52(2):568–577, 2013.
- S. Grampp, H.K. Genant, A. Mathur, P. Lang, M. Jergas, M. Takada, C.C. Glüer, Y. Lu, and M. Chavez. Comparisons of noninvasive bone mineral measurements in assessing age-related loss, fracture discrimination, and diagnostic classification. *J Bone Miner Res*, 12(5):697–711, 1997.
- M. Granke, Q. Grimal, A. Saïed, P. Nauleau, F. Peyrin, and P. Laugier. Change in porosity is the major determinant of the variation of cortical bone elasticity at the millimeter scale in aged women. *Bone*, 49(5):1020–1026, 2011.
- M. Granke, A. Gourrier, F. Rupin, K. Raum, F. Peyrin, M. Burghammer, A. Saïed, and P. Laugier. Microfibril orientation dominates the microelastic properties of human bone tissue at the lamellar length scale. *PLoS One*, 8(3):e58043, 2013.

- M. Granke, Q. Grimal, W.J. Parnell, K. Raum, A. Gerisch, F. Peyrin, A. Saïed, and P. Laugier. To what extent can cortical bone millimeter-scale elasticity be predicted by a two-phase composite model with variable porosity? *Acta Biomater*, 12:207–215, 2015.
- Q. Grimal, K. Raum, A. Gerisch, and P. Laugier. A determination of the minimum sizes of representative volume elements for the prediction of cortical bone elastic properties. *Biomech Model Mechanobiol*, 10:925–937, 2011a.
- Q. Grimal, G. Rus, W.J. Parnell, and P. Laugier. A two-parameter model of the effective elastic tensor for cortical bone. *J. Biomech.*, 44(8):1621–1625, 2011b.
- Q. Grimal, D. Rohrbach, J. Grondin, R. Barkmann, C.C. Glüer, K. Raum, and P. Laugier. Modeling of femoral neck cortical bone for the numerical simulation of ultrasound propagation. *Ultrasound in Medicine & Biology*, 40(5):1015–1026, 2014.
- G. Guglielmi, S. Muscarella, and A. Bazzocchi. Integrated imaging approach to osteoporosis: state-of-the-art review and update. *Radiographics*, 31(5):1343–1364, 2011.
- J. Guillemot and C. Soize. Probabilistic modeling of apparent tensors in elastostatics: A maximum approach under material symmetry and stochastic boundedness constraints. *Probabilistic Engineering Mechanics*, 28(SI):118–124, 2012.
- J. Guillemot and C. Soize. On the statistical dependence for the components of random elasticity tensors exhibiting material symmetry properties. *Journal of Elasticity*, 111(2):109–130, 2013a.
- J. Guillemot and C. Soize. Stochastic model and generator for random fields with symmetry properties: application to the mesoscopic modeling of elastic random media. *Multiscale Modeling and Simulation (A SIAM Interdisciplinary Journal)*, 11(3):840–870, 2013b.
- J. Guillemot, A. Noshadravan, C. Soize, and R.G. Ghanem. A probabilistic model for bounded elasticity tensor random fields with application to polycrystalline microstructures. *Comput. Methods Appl. Mech. Engrg.*, 200(17–20):1637–1648, 2011.
- G. Haiat, S. Naili, Q. Grimal, M. Talmant, C. Desceliers, and C. Soize. Influence of a gradient of material properties on ultrasonic wave propagation in cortical bone: Application to axial transmission. *J. Acoust. Soc. Am.*, 125(6):4043–4052, 2009.
- G. Haiat, S. Naili, M.-B. Vu, C. Desceliers, and C. Soize. Equivalent contributing depth investigated by a lateral wave with axial transmission in heterogeneous viscoelastic cortical bone. *J. Acoust. Soc. Am.*, 129(4):EL114–EL120, 2011.
- P. Halmos. *Measure Theory*, volume 1 : Basics. Springer-Verlag, Berlin, 2nd edition, 1976.
- P. Heilmann, C. Wüster, C. Prolingheuer, M. Götz, and R. Ziegler. Measurement of forearm bone mineral density: comparison of precision of five different instruments. *Calcif Tissue Int*, 62(2):383–387, 1998.

- 
- C. Hellmich, J. Barthelemy, and L. Dormieux. Mineral-collagen interactions in elasticity of bone ultrastructure - a continuum micromechanics approach. *European Journal of Mechanics - A/Solids*, 23:783–810, 2004a.
- C. Hellmich, F.-J. Ulm, and L. Dormieux. Can the diverse elastic properties of trabecular and cortical bone be attributed to only a few tissue-independent phase properties and their interactions? *Biomechanics and Modeling in Mechanobiology*, 2:219–238, 2004b.
- C. Hellmich, C. Kober, and B. Erdmann. Micromechanics-based conversion of ct data into anisotropic elasticity tensors, applied to fe simulations of a mandible. *Ann Biomed Eng*, 23: 783–810, 2008.
- D.J. Hulmes. Building collagen molecules, fibrils, and suprafibrillar structures. *Journal of Structural Biology*, 137:2–10, 2002.
- M. Itô. Recent progress in bone imaging for osteoporosis research. *Journal of Bone and Mineral Metabolism*, 29(2):131–140, 2000.
- E.T. Jaynes. Information theory and statistical mechanics. *Physical Review*, 106(4):620–630, 1957a.
- E.T. Jaynes. Information theory and statistical mechanics. *Physical Review*, 108(2):171–190, 1957b.
- G. Jumarie. *Maximum Entropy, Information Without Probability and Complex Fractals*. Kluwer Academic Publishers, Dordrecht/Boston/London, 2000.
- J.N. Kapur and H.K. Kesavan. *Entropy Optimization Principles with Applications*. Academic Press, San Diego, 1992.
- D.E. Knuth. *The Art of Computer programming, Vol. 2, Seminumerical Algorithms*. Addison-Wesley, 1981.
- S.P. Kotha and N. Guzelsu. The effects of interphase and bonding on the elastic modulus of bone: changes with age-related osteoporosis. *Medical Engineering and Physics*, 22(8):575–585, 2000.
- P. Krée and C. Soize. *Mathematics of Random Phenomena*. Reidel, Dordrecht, 1986.
- M. Langer, A. Pacureanu, H. Suhonen, Q. Grimal, P. Cloetens, and F. Peyrin. X-ray phase nanotomography resolves the 3d human bone ultrastructure. *PLoS One*, 7(8):e35691, 2012.
- E.M. Lewiecki. Imaging technologies for assessment of skeletal health in men. *Curr Osteoporos Rep*, 11(1):1–10, 2013.
- T.M. Link. Osteoporosis imaging: state of the art and advanced imaging. *Radiology*, 263(1): 3–17, 2012.

- S.L. Manske, T. Liu-Ambrose, D.M.L. Cooper, S. Kontulainen, P. Guy, B.B. Forster, and H.A. McKay. Cortical and trabecular bone in the femoral neck both contribute to proximal femur failure load prediction. *Osteop. Int.*, 20(3):445–453, 2009.
- V. Mathieu, C. Chappard, R. Vayron, A. Michel, and G. Haiat. Radial anatomic variation of ultrasonic velocity in human cortical bone. *Ultrasound Med Biol*, 39(11):2185–2193, 2013.
- Matlab. *Matlab R2007b Documentation*.
- P.M. Mayhew, C.D. Thomas, J.G. Clement, N. Loveridge, T.J. Beck, W. Bonfield, C.J. Burgoyne, and J. Reeve. Relation between age, femoral neck cortical stability, and hip fracture risk. *Lancet*, 366:129–135, 2005.
- S. Naili, M.B. Vu, Q. Grimal, M. Talmant, C. Desceliers, C. Soize, and G. Haiat. Influence of viscoelastic and viscous absorption on ultrasonic wave propagation in cortical bone: Application to axial transmission. *J. Acoust. Soc. Am.*, 127(4):2622–2634, 2010.
- S. Nemat-Nasser and M. Hori. *Micromechanics: overall properties of heterogeneous materials*. Applied Mathematics and Mechanics. North-Holland, 2nd edition, 1999.
- K.K. Nishiyama and S.K. Boyd. In vivo assessment of trabecular and cortical bone microstructure. *Clin Calcium*, 21(7):1011–1019, 2011.
- S. Nuzzo, F. Peyrin, P. Cloetens, J. Baruchel, and G. Boivin. Quantification of the degree of mineralization of bone in three dimensions using synchrotron radiation microtomography. *Med. Phys.*, 29(11):2672–2681, 2002.
- W.J. Parnell, M.B. Vu, Q. Grimal, and S. Naili. Analytical methods to determine the effective mesoscopic and macroscopic elastic properties of cortical bone. *Biomech. Model. Mechanobiol.*, 11(6):883–901, 2012.
- E. Perilli, I.H. Parkinson, and K.J. Reynolds. Micro-CT examination of human bone: from biopsies towards the entire organ. *Ann. Ist. Super. Sanita*, 48(1):75–82, 2012.
- M. Predoi-Racila and J. M. Crolet. Human cortical bone: the sinupros model. *Comput. Methods Biomech. Biomed. Engin.*, 11(2):169–187, 2008.
- A.G. Reisinger, D.H. Pahr, and P.K. Zysset. Elastic anisotropy of bone lamellae as a function of fibril orientation pattern. *Biomechanics and Modeling in Mechanobiology*, 10(1):67–77, 2011.
- J.-Y. Rho, L. Kuhn-Spearing, and P. Zioupos. Mechanical properties and the hierarchical structure of bone. *Medical Engineering & Physics*, 20:92–102, 1998.
- M. Rossini, O. Viapiana, and S. Adami. Instrumental diagnosis of osteoporosis. *Aging*, 10(3):240–248, 1998.
- R.Y. Rubinstein. *Simulation and the Monte Carlo Method*. John Wiley and Sons, 1981.

- 
- V. Sansalone, S. Naili, V. Bousson, C. Bergot, F. Peyrin, J.D. Laredo, and G. Haiat. Determination of the heterogeneous anisotropic elastic properties of human femoral bone: from nanoscopic to organ scale. *J. Biomech.*, 43(10):1857–1863, 2010.
- V. Sansalone, V. Bousson, S. Naili, C. Bergot, F. Peyrin, J.D. Laredo, and G. Haiat. Anatomical distribution of the degree of mineralization of bone tissue in human femoral neck: Impact on biomechanical properties. *Bone*, 50(4):876–884, 2012a.
- V. Sansalone, V. Bousson, S. Naili, C. Bergot, F. Peyrin, J.D. Laredo, and G. Haiat. Effects of the axial variations of porosity and mineralization on the elastic properties of the human femoral neck. *Computer Modeling in Engineering & Sciences*, 87(5):387–409, 2012b.
- V. Sansalone, S. Naili, and C. Desceliers. A stochastic homogenization approach to estimate bone elastic properties. *Comptes Rendus Mecanique*, 342(5):326–333, 2014.
- M. Sasso, G. Haiat, Y. Yamato, S. Naili, and M. Matsukawa. Frequency dependence of ultrasonic attenuation in bovine cortical bone: an in vitro study. *Ultrasound Med. Biol.*, 33(12):1933–1942, 2007.
- M. Sasso, G. Haiat, Y. Yamato, S. Naili, and M. Matsukawa. Dependence of ultrasonic attenuation on bone mass and microstructure in bovine cortical bone. *J. Biomech.*, 41(2):347–355, 2008.
- S. Schrof, P. Varga, L. Galvis, K. Raum, and A. Masic. 3d raman mapping of the collagen fibril orientation in human osteonal lamellae. *J Struct Biol*, 187(3):266–275, 2014.
- C. Shannon. A mathematical theory of communication. *Tech. J.* 27, Bell Syst., 1948.
- C. Soize. Maximum entropy approach for modeling random uncertainties in transient elastodynamics. *Journal of the Acoustical Society of America*, 109(5):1979–1996, 2001.
- C. Soize. Non-gaussian positive-definite matrix-valued random fields for elliptic stochastic partial differential operators. *Computer Methods in Applied Mechanics and Engineering*, 195(1-3):26–64, 2006.
- C. Soize. Tensor-valued random fields for meso-scale stochastic model of anisotropic elastic microstructure and probabilistic analysis of representative volume element size. *Probabilistic Engineering Mechanics*, 23(2-3):307–323, 2008.
- E.M. Spiesz, W. Kaminsky, and P.K. Zysset. A quantitative collagen fibers orientation assessment using birefringence measurements: Calibration and application to human osteons. *J Struct Biol*, 176(3):302–306, 2011.
- D. Sreenivasan, M. Watson, K. Callon, M. Dray, R. Das, A. Grey, J. Cornish, and J. Fernandez. Integrating micro CT indices, CT imaging and computational modelling to assess the mechanical performance of fluoride treated bone. *Medical Engineering and Physics*, 35(12):1793–1800, 2013.

- P. Suquet, editor. *Continuum micromechanics*. Number 377 in CISM Lecture Notes. Springer-Verlag, Wien, 1997.
- A.P. Suvorov and G.J. Dvorak. Rate form of the Eshelby and Hill tensors. *International Journal of Solids and Structures*, 39(21):5659–5678, 2002.
- K. Tai, G. Pelled, D. Sheyn, A. Bershteyn, L. Han, I. Kallai, Y. Zilberman, C. Ortiz, and D. Gazit. Nanobiomechanics of repair bone regenerated by genetically modified mesenchymal stem cells. *Tissue Eng Part A*, 14(10):1709–1720, 2008.
- E.G. Vajda and R.D. Bloebaum. Age-related hypermineralization in the female proximal human femur. *Anat. Rec.*, 255(2):202–211, 1999.
- G. Valente, L. Pitto, D. Testi, A. Seth, S.L. Delp, R. Stagni, M. Viceconti, and F. Taddei. Are subject-specific musculoskeletal models robust to the uncertainties in parameter identification? *PLoS One*, 9(11):e112625, 2014.
- P. Varga, A. Pacureanu, M. Langer, H. Suhonen, B. Hesse, Q. Grimal, P. Cloetens, K. Raum, and F. Peyrin. Investigation of the three-dimensional orientation of mineralized collagen fibrils in human lamellar bone using synchrotron x-ray phase nano-tomography. *Acta Biomaterialia*, 9(9):8118–8127, 2013.
- R. Vayron, E. Barthel, V. Mathieu, E. Soffer, F. Anagnostou, and G. Haiat. Nanoindentation measurements of biomechanical properties in mature and newly formed bone tissue surrounding an implant. *J Biomech Eng*, 134(2):021007, 2012.
- R. Vayron, M. Matsukawa, R. Tsubota, V. Mathieu, E. Barthel, and G. Haiat. Evolution of bone biomechanical properties at the micrometer scale around titanium implant as a function of healing time. *Phys Med Biol*, 59(6):1389–1406, 2014.
- D.W. Wagner, D.P. Lindsey, and G.S. Beaupre. Deriving tissue density and elastic modulus from microct bone scans. *Bone*, 49(5):931–938, 2011.
- Y. Yamato, M. Matsukawa, T. Otani, K. Yamazaki, and A. Nagano. Distribution of longitudinal wave properties in bovine cortical bone in vitro. *Ultrasonics*, 44(Suppl 1):e233–e237, 2006.
- H. Yao, M. Dao, D. Carnelli, K. Tai, and C. Ortiz. Size-dependent heterogeneity benefits the mechanical performance of bone. *J. Mech. Phys. Solids*, 59:64–74, 2011.
- Y. J. Yoon and S. C. Cowin. The estimated elastic constants for a single bone osteonal lamella. *Biomechanics and Modeling in Mechanobiology*, 7(1):1–11, 2008a.
- Y. J. Yoon and S. C. Cowin. An estimate of anisotropic poroelastic constants of an osteon. *Biomechanics and Modeling in Mechanobiology*, 7(1):13–26, 2008b.
- R.M. Zebaze, A. Ghasem-Zadeh, A. Bohte, S. Iuliano-Burns, M. Mirams, R.I. Price, E.J. Mackie, and E. Seeman. Intracortical remodelling and porosity in the distal radius and post-mortem femurs of women: a cross-sectional study. *Lancet*, 375(9727):1729–1736, 2010.

## Chapter 2

# Tissue mineral density measured at the sub-millimeter scale provides reliable statistical estimates of elastic properties of bone matrix

---

D. Gagliardi, V. Sansalone, C. Desceliers, and S. Naili. Tissue mineral density measured at the sub-millimeter scale can provide reliable statistics of elastic properties of bone matrix. *Biomechanics and modeling in mechanobiology*, (submitted) Nov. 2016.

## Abstract

Reliability of multiscale models of bone is related to the accuracy of the experimental information available on bone microstructure. X-ray based imaging techniques allow to inspect bone structure and mineralization *in vitro* at the micrometer scale. However, spatial resolution achievable *in vivo* is much coarser and can produce blurry, uncertain information on bone microstructure. Working with uncertain data calls for new modeling paradigms able to propagate uncertainty through the scales. In this chapter we investigate the effects of uncertain bone mineralization on the elastic coefficients of the bone matrix. To this aim, some stochastic concepts were developed and compared with one another in order to identify the best way to account for uncertain input data. These concepts step from a deterministic micromechanical model of bone matrix which was extended in order to account for uncertain bone composition. Uncertainty was introduced by assuming to know only mean value and dispersion of the parameters describing bone composition. Thus, these parameters were modeled as random variables and their distribution functions were obtained using the Maximum entropy (MaxEnt) principle. Either the tissue mineral density (TMD) or the ensuing volume fractions of collagen and mineral were used to describe uncertain bone composition. Moreover, mean value and dispersion were estimated at the scales of either ten or a few hundreds micrometers, representative of standard *in vitro* and *in vivo* spatial resolutions, respectively. Analysis of these modeling concepts suggests that TMD measured at the sub-millimeter scale can be used to obtain reliable statistical information about the elastic coefficients of bone matrix.

## 2.1 Introduction

Characterizing bone mechanical properties has been—and still is—a major issue due to the complexity of bone hierarchical structure (Rho et al., 1998) and the difficulty to inspect it, especially *in vivo*. Clinical measures such as bone mineral density (BMD) are unable to fully explain bone quality and strength (Dall’Ara et al., 2013). Since the pioneering work of Currey in the eighties (Currey, 1988), the relevance of Haversian porosity (HP) and tissue mineral density (TMD, *i.e.* the degree of mineralization of the bone matrix) has been acknowledged and increasingly investigated (Bousson et al., 2004). On the one side, the progress made in recent decades has been made possible by the development of new imaging and mechanical techniques with increased power and resolution (Currey, 2009). On the other side, theoretical and computational modeling has offered unique opportunities to interpret and understand experimental measures.

Nowadays, finite element (FE) simulations represent a standard approach to investigate stress/strain distribution as well as to estimate effective elastic properties of bone at several scales (Blanchard et al., 2013; Granke et al., 2015; Zadpoor and Weinans, 2015; van Rietbergen and Ito, 2015; Pottecher et al., 2016). Additional insights can be provided by multiscale techniques accounting for bone heterogeneity and anisotropy. Among others, homogenization theory (Predoi-Racila and Crolet, 2008; Parnell et al., 2011) and continuum micromechanics (Hellmich et al., 2004) were successfully used to compute bone elastic properties using constitutive and morphological information on the elementary constituents of bone (basically collagen, mineral, and water). More recently, modeling approaches were coupled with high-resolution micro-computed tomography ( $\mu$ CT) imaging to derive 3D maps of elastic properties of bone samples *ex vivo* (Hellmich et al., 2008; Sansalone et al., 2010). A major difficulty in transposing these approaches to the clinical practice is related to obtaining reliable input data using standard clinical devices. Indeed, clinical CT scans may provide blurry data which these approaches, being deterministic in nature, cannot properly deal with. In particular, they are intrinsically unable to quantify the effects of the uncertainty affecting the input data onto the model predictions.

Uncertainty quantification in multi-scale modeling of composites has been recently faced by means of stochastic approaches aiming at mimicking the key features of typical experimental data, with a given degree of accuracy. Among others, we recall the Maximum Likelihood principle, the Maximum Entropy (MaxEnt) principle (Soize, 2001), and the polynomial chaos decomposition (Soize and Ghanem, 2004)). In particular, the MaxEnt principle has been recently used by our group to model uncertain input data in a continuum micromechanical model of bone elasticity. In our previous work, the focus was set on either the elastic properties (Sansalone et al., 2014) or the volume fractions (VFs) (Sansalone et al., 2016) of bone constituents. In this latter work, uncertainty on VFs was estimated from the 3D spatial distribution of HP and TMD in a bone sample harvested from the inferior femoral neck of an elderly patient. The sample was imaged using synchrotron radiation  $\mu$ CT (SR- $\mu$ CT) with a spatial resolution of about 10  $\mu$ m. Despite this resolution is quite standard in *ex vivo* imaging, it is hardly achieved by clinical scans *in vivo* which have typical spatial resolution of about 100  $\mu$ m or less (Burghardt et al., 2011). SR- $\mu$ CT images were then analyzed to obtain statistical information (mean value and dispersion) about the distribution of HP and TMD in the cortical tissue. HP was measured with a spatial resolution of about 500  $\mu$ m micrometers—*i.e.* the typical size of a representative

volume element (RVE) of cortical tissue (Grimal et al., 2011). TMD was measured with a spatial resolution of about  $10\ \mu\text{m}$ —*i.e.* the voxel size. Feeding the stochastic model with this statistical information allowed simulating an uncertainty scenario where HP and TMD were assumed to be known just in statistical terms. The model allowed propagating the uncertainty on input data up to the tissue scale and estimating mean value and confidence intervals of the elastic coefficients of the cortical tissue. These latter were compared with detailed micro-finite element analysis ( $\mu\text{FEA}$ ) of several RVEs of the sample—to be considered as reference values. The stochastic model succeeded in predicting the mean value of the elastic coefficients but not the confidence intervals which turned out to be larger than expected (almost all the  $\mu\text{FEA}$  results fell within the 50% confidence predicted by the stochastic model). Therefore, the effects of the uncertainty affecting HP and TMD (input) were somehow overestimated in the computed elastic coefficients (output).

The main goal of this chapter is to improve the results of Sansalone et al. (2016) and provide more reliable estimates of bone elastic coefficients—in particular, more realistic confidence intervals—based on uncertain compositional data. Implications on the related experimental issues will be also discussed. The focus will be set on the solid matrix of bone—also referred to as ultrastructure (US)—and two main questions will be investigated.

The first question concerns the choice of the variables describing the composition of the US. In quantitative  $\mu\text{CT}$  images, information on US composition is carried by the gray level (GL) of the voxels. GL is linearly related to the mineral content of the voxels, that is the TMD. This latter, in turn, allows computing the VFs of collagen, mineral and water in the US (Broz et al., 1995). In a deterministic framework, TMD and VFs are related by a one-to-one relation and US composition is equivalently described in terms of either choice. As soon as US composition is uncertain, both TMD and VFs can be described as random variables with statistics (such as mean value and dispersion) defined by the available experimental data. In a stochastic framework, choosing either TMD or VFs as primary modeling variables may not be equivalent. In this chapter we will compare these choices in order to identify the more suitable approach.

The second question concerns the scale at which experimental measures should be made in order to obtain reliable values of the US elastic moduli. This question is related to an hypothesis underlying the continuum micromechanical model used in (Sansalone et al., 2010) to compute the elastic coefficients of bone, namely the assumption of homogeneous US within each RVE—*i.e.* at the tissue scale. In order to comply with this hypothesis, the actual, heterogeneous US of each RVE was replaced with an effective, homogeneous US obtained by spatial average of the actual US voxels (*i.e.*, the voxels belonging to the US). This approach was then extended by (Sansalone et al., 2016) to build a stochastic model of the US. In short, a database of  $N_{\text{vox}} > 10^6$  voxels was generated by collecting *all* the US voxels of a dozen of RVEs of cortical tissue; then, statistics of this experimental database were used to build a stochastic model of the US. Each realization of this model is meant to represent the homogeneous US of a virtual RVE. Thus, this model uses input data at the voxel scale to produce output results at the RVE scale. In this chapter we will investigate this point in detail by comparing the results of stochastic models of US based on voxel-scale and tissue-scale experimental data.

The work is organized as follows. In Sec. 2.2 we will first present our experimental data.

Then, we will present the theoretical development and numerical implementation of four stochastic concepts, focusing on a new, TMD-based stochastic model of bone US. We will thoroughly present and discuss our numerical results in Sec. 2.3 underlining the differences between the different modeling approaches with respect to the two main questions raised before (TMD-based *vs.* VF-based modeling; voxel-scale *vs.* RVE-scale statistics). Finally, in Sec. 2.4 we will draw the conclusions of this work and set forth future research directions.

## 2.2 Materials and Methods

### 2.2.1 Imaging

For sake of clarity, we resume here the main steps of the imaging protocol and refer to Sansalone et al. (2016) for more details. A bone sample, extracted from the inferior femoral neck of a 79-year-old patient undergoing standard hemiarthroplasty, has been imaged using synchrotron radiation micro-computed tomography (SR- $\mu$ CT) at the European Synchrotron Radiation Facility (ESRF, Grenoble, France). Image reconstruction was performed in a volume of interest (VoI) of  $660 \times 660 \times 523$  isotropic voxels (voxel size  $10.13 \mu\text{m}$ ). The outcome was a 3-D gray-level (GL) map (GL range:  $[0, 255]$ ) of the linear attenuation coefficient of the monochromatic X-ray beam. Regions corresponding to Haversian pores (HP) and ultrastructure (US) were identified by fixing a GL threshold  $q = 130$ , so as GL ranges associated to HP and US were set to  $\mathcal{GL}_{\text{HP}} := [0, q]$  and  $\mathcal{GL}_{\text{US}} := [q + 1, 255]$ , respectively.

Since SR- $\mu$ CT images are quantitative, GL of US voxels can be related to the mineral content, *i.e.* the tissue mineral density (TMD) (Nuzzo et al., 2002) through an affine relation:

$$\text{TMD} = c_0 + c_1 \times \text{GL}. \quad (2.1)$$

Coefficients  $c_0$  and  $c_1$  in Eq. (2.1) depend on the specific imaging device and have to be calibrated with respect to phantoms of known composition. In this study:

$$c_0 = -\frac{0.5082}{3.319} \quad \text{and} \quad c_1 = \frac{5.5}{255 \times 3.319}. \quad (2.2)$$

### 2.2.2 Representative volume elements

Several representative volume elements (RVEs) were selected in the cortical part of the VoI. Following Sansalone et al. (2016), RVEs were taken as cubic regions with edge length of 50 voxels, *i.e.* about  $0.5 \text{ mm}$ . 3-D geometric models of the RVEs were obtained using SimpleWare 5.0 ScanIP software (Simpleware 5.0 ScanIP+, 2012) at about  $1.5 \text{ mm}$  from the periosteum (distance measured with respect to the center of the RVEs) and at different hoop and axial positions with respect to a cylindrical frame centered at the anatomical axis of the bone sample. The bone sample and the location of the RVEs are presented in Fig. 2.1, where the unit vector  $\mathbf{e}_3$  is aligned with the axis of the femoral neck and the unit vectors  $\mathbf{e}_1$  and  $\mathbf{e}_2$  lie in the plane of the cross section of the sample. Blue RVEs in Fig. 2.1 ( $N_{\text{RVE}} = 12$ ) were used to calibrate the model, whereas light blue RVEs were used for validation purposes.

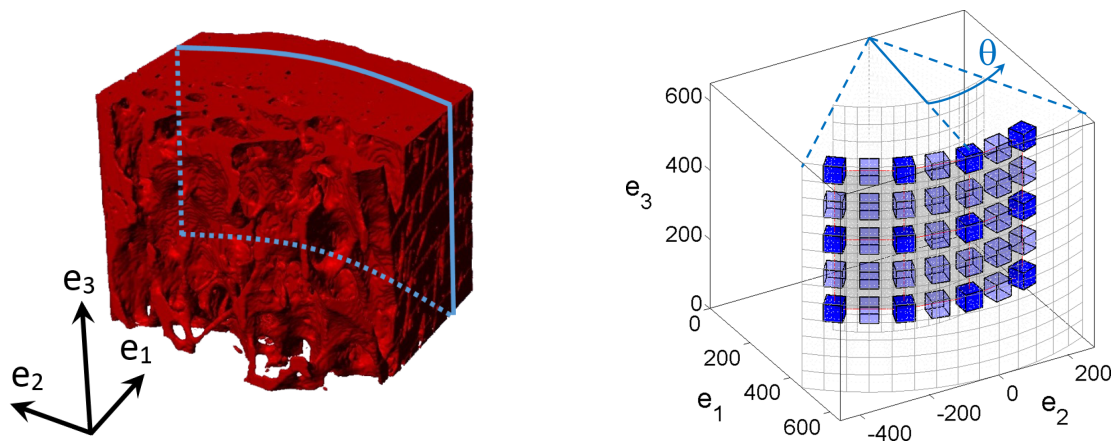


Figure 2.1: On the left: Segmented bone sample; blue lines denote a cylindrical surface at approximately 1.5 mm from the periosteum. On the right: Location of the RVEs (unit of length:  $\mu\text{m}$ ); the centers of RVEs lie on the cylindrical surface sketched on the left.

RVEs are represented in detail in Fig. 2.2. Colors refer to the GLs of the voxels, with HP voxels in blue and US voxels in yellow to red. Symbols  $z$  and  $\theta$  refer to the axial and hoop coordinates of the centers of the RVEs, respectively. The axial coordinate  $z$  is the distance of the center of the RVE from the distal part of the sample ( $z = 0$ ). The hoop coordinate  $\theta$  is the angle measured counterclockwise with respect to the inferior axis of the sample ( $\theta = 0$ ).

### 2.2.3 Experimental compositional data: HP and TMD

Information on the composition of the cortical tissue was obtained by analyzing the RVEs selected for calibration purposes (blue RVEs in Fig. 2.1). This dataset constitutes a systematic sampling of the overall population of cortical RVEs and was used to infer statistics (namely, mean value and dispersion) of HP and TMD in the cortical tissue.

HP was measured at the *RVE scale* (500  $\mu\text{m}$ , also referred to as *tissue scale*), leading to one value of HP per RVE, by dividing the number of voxels with GL in  $\mathcal{GL}_{\text{HP}}$  by the total number of voxels of the RVE. TMD was measured at the voxel scale (10  $\mu\text{m}$ , also referred to as *US scale*), leading to a 3-D heterogeneous distribution of TMD in each RVE, by means of Eq. (2.1). Moreover, *effective* values of TMD at the RVE scale, named  $\overline{\text{TMD}}$ , were computed by averaging the voxel-wise distribution of TMD within the US of each RVE, leading to one value of  $\overline{\text{TMD}}$  per RVE. These latter were assumed to represent RVE-scale measures. Databases were then constituted collecting all this experimental compositional information, namely: a database  $\mathcal{DB}_{\text{HP}}^{\text{exp}}$  collecting the  $N_{\text{RVE}}$  values of HP at the RVE scale; a database  $\mathcal{DB}_{\overline{\text{TMD}}}^{\text{exp}}$  collecting the  $N_{\text{RVE}}$  values of  $\overline{\text{TMD}}$  at the RVE scale; and a database  $\mathcal{DB}_{\text{TMD}}^{\text{exp}}$  collecting the  $N_{\text{vox}} > 10^6$  values of TMD at the voxel scale (*all* the US voxels of *all* the RVEs).

Statistical information on the composition of the whole cortical tissue was inferred by the descriptive statistics of these databases. Let  $X$  be either of HP, TMD, or  $\overline{\text{TMD}}$ , whose experimental measures  $x_i$  ( $i = 1, \dots, N$ ) are collected in the database  $\mathcal{DB}_X^{\text{exp}}$ . ( $N = N_{\text{RVE}}$  for

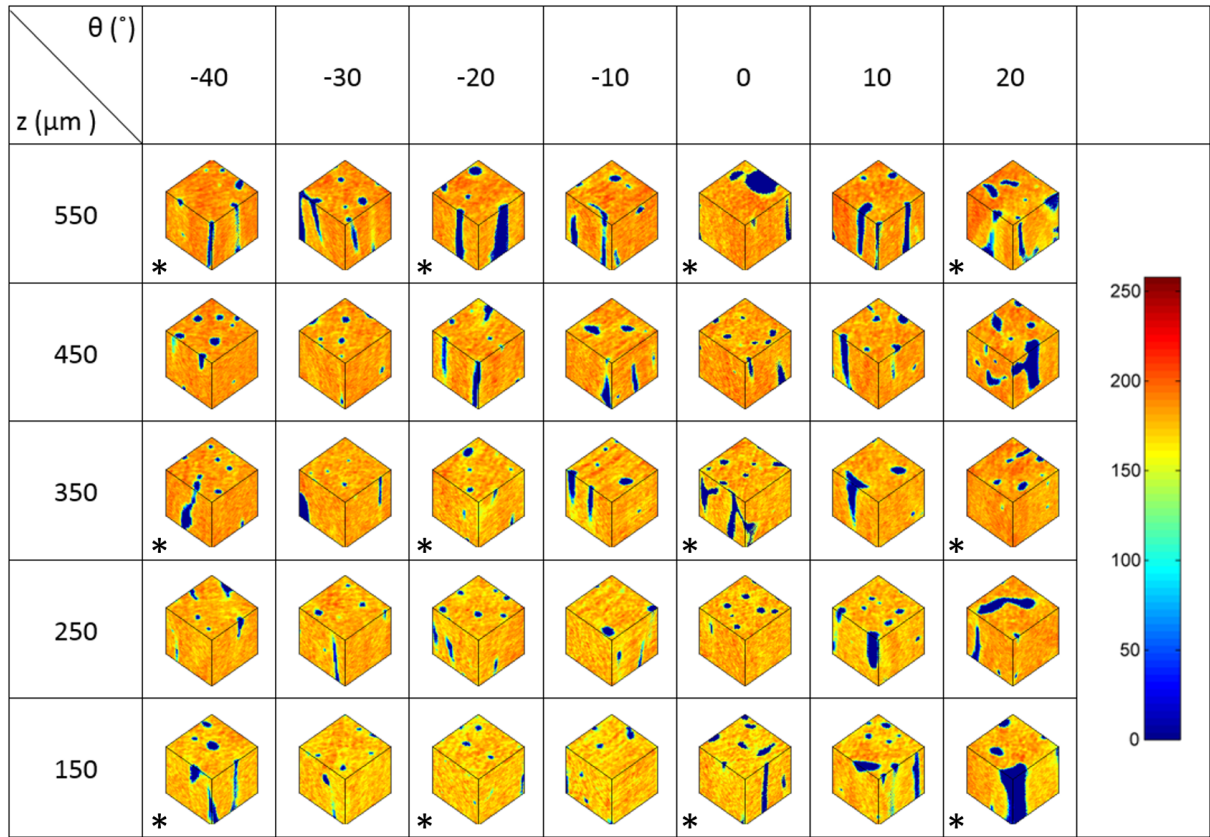


Figure 2.2: Representation of the RVEs. Colors refer to the GLs of the original images. Asterisks indicate the RVEs used for calibration purposes.

HP and  $\overline{\text{TMD}}$  and  $N = N_{\text{vox}}$  for TMD.) Mean value, standard deviation, and dispersion of  $X$ , named  $\mu_X^{\text{exp}}$ ,  $\sigma_X^{\text{exp}}$ , and  $\delta_X^{\text{exp}}$ , respectively, were estimated through the corresponding descriptive statistics:

$$\mu_X^{\text{exp}} := \mu_X^N, \quad \sigma_X^{\text{exp}} := \sigma_X^N, \quad \text{and} \quad \delta_X^{\text{exp}} := \delta_X^N, \quad (2.3)$$

where:

$$\begin{aligned} \mu_X^N &= \frac{1}{N} \sum_{i=1}^N x_i, \\ \sigma_X^N &= \left( \frac{1}{N-1} \sum_{i=1}^N (x_i - \mu_X^N)^2 \right)^{1/2}, \\ \delta_X^N &= \frac{\sigma_X^N}{\mu_X^N}. \end{aligned} \quad (2.4)$$

## 2.2.4 Hierarchical description of bone and volume fractions

Following Sansalone et al. (2010), a multiscale description of cortical bone was adopted. At the scale of several hundreds micrometers (*tissue scale*), cortical tissue was considered as made up of Haversian pores, HP, embedded in a solid matrix called ultrastructure, US. At the scale of a few tens micrometers (*US scale*), US was considered as made up of collagen fibers embedded in a mineral foam (MF). Eventually, at the scale of several tens nanometers (referred to as *MF scale*), MF was considered as a mixture of mineral and water.

Experimental data obtained in Sec. 2.2.3 were used to compute bone composition at each scale in terms of volume fractions (VFs). The procedure is sketched in Fig. 2.3 and resumed here below.

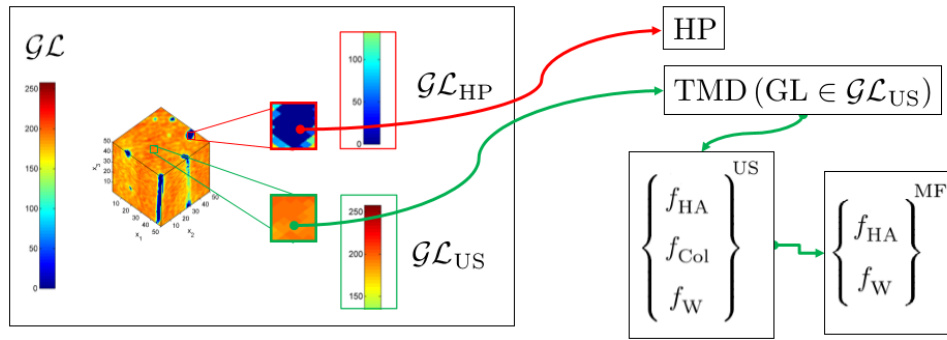


Figure 2.3: Sketch of the procedure for evaluating the TMD and VFs within each RVE.

**Tissue scale.** Within each RVE, the HP directly provides the VFs of pores ( $f_{\text{HP}}^{\text{Cort}} = \text{HP}$ ) and solid matrix ( $f_{\text{US}}^{\text{Cort}} = 1 - \text{HP}$ ) in the cortical tissue.

**US scale.** For each US voxel, the VF of the mineral can be directly computed from the local value of TMD. In order to obtain the VFs of collagen and water, an empirical relation was added (Broz et al., 1995), leading to the system of nonlinear equations:

$$\begin{cases} f_{\text{HA}}^{\text{US}} = \frac{\text{TMD}}{\rho_{\text{HA}}}, \\ f_{\text{Col}}^{\text{US}} + f_{\text{HA}}^{\text{US}} + f_{\text{W}}^{\text{US}} = 1, \\ \frac{f_{\text{Col}}^{\text{US}}}{f_{\text{W}}^{\text{US}}} = 0.36 + 0.084 \times \exp(6.7 \times f_{\text{HA}}^{\text{US}}), \end{cases} \quad (2.5)$$

where  $f_{\text{HA}}^{\text{US}}$ ,  $f_{\text{Col}}^{\text{US}}$ , and  $f_{\text{W}}^{\text{US}}$  are the VFs of the hydroxyapatite (HA) mineral, collagen, and water in the US, respectively, and  $\rho_{\text{HA}} = 3 \text{ g/cm}^3$  is the mass density of the mineral. For each RVE, the *effective* VFs of mineral, collagen, and water in the US (named  $\bar{f}_{\text{HA}}^{\text{US}}$ ,  $\bar{f}_{\text{Col}}^{\text{US}}$ , and  $\bar{f}_{\text{W}}^{\text{US}}$ , respectively) were also computed from  $\overline{\text{TMD}}$  following the same procedure.

**MF scale.** For each US voxel, the VFs of mineral and water in the MF (named  $f_{\text{HA}}^{\text{MF}}$  and  $f_{\text{W}}^{\text{MF}}$ , respectively) were computed as:

$$\begin{cases} f_{\text{HA}}^{\text{MF}} = \frac{f_{\text{HA}}^{\text{US}}}{(f_{\text{HA}}^{\text{US}} + f_{\text{W}}^{\text{US}})}, \\ f_{\text{W}}^{\text{MF}} = \frac{f_{\text{W}}^{\text{US}}}{(f_{\text{HA}}^{\text{US}} + f_{\text{W}}^{\text{US}})}. \end{cases} \quad (2.6)$$

For each RVE, the same relations were used to compute the effective VFs of mineral and water in the MF (named  $\bar{f}_{\text{HA}}^{\text{MF}}$  and  $\bar{f}_{\text{W}}^{\text{MF}}$ , respectively).

Focusing on the two questions set in the introduction, hereinafter we will be concerned with the US and MF. Bone composition at the US scale was characterized by  $f_{\text{Col}}^{\text{US}}$ , with its complement  $f_{\text{MF}}^{\text{US}} = f_{\text{HA}}^{\text{US}} + f_{\text{W}}^{\text{US}} = 1 - f_{\text{Col}}^{\text{US}}$  being the VF of the MF in the US. In turn, composition of the MF was characterized by  $f_{\text{HA}}^{\text{MF}}$ , with  $f_{\text{W}}^{\text{MF}} = 1 - f_{\text{HA}}^{\text{MF}}$ . For the sake of brevity, Eqs. (2.5)-(2.6) can be reduced to:

$$\begin{cases} f_{\text{Col}}^{\text{US}} \equiv f_{\text{II}} = \hat{f}_{\text{II}}(\text{TMD}), \\ f_{\text{HA}}^{\text{MF}} \equiv f_{\text{I}} = \hat{f}_{\text{I}}(\text{TMD}), \end{cases} \quad (2.7)$$

highlighting that both VFs are computed from the TMD. Similar relations apply when considering the effective mineralization of bone US, namely:

$$\begin{cases} \bar{f}_{\text{Col}}^{\text{US}} \equiv \bar{f}_{\text{II}} = \hat{f}_{\text{II}}(\overline{\text{TMD}}), \\ \bar{f}_{\text{HA}}^{\text{MF}} \equiv \bar{f}_{\text{I}} = \hat{f}_{\text{I}}(\overline{\text{TMD}}). \end{cases} \quad (2.8)$$

Databases of VFs were constituted by analyzing the RVEs selected for calibration purposes. This led, on the one side, to databases  $\mathcal{DB}_{f_{\text{II}}}^{\text{exp}}$  and  $\mathcal{DB}_{f_{\text{I}}}^{\text{exp}}$  containing the  $N_{\text{vox}}$  voxel-wise values of VFs of collagen in the US and of mineral in the MF, respectively; and on the other side, to databases  $\mathcal{DB}_{\bar{f}_{\text{II}}}^{\text{exp}}$  and  $\mathcal{DB}_{\bar{f}_{\text{I}}}^{\text{exp}}$  containing the  $N_{\text{RVE}}$  RVE-wise values of the corresponding effective VFs. Descriptive statistics of these databases were further computed using Eqs. (2.4) to infer statistical information on the VFs which were meant to be representative of the whole cortical tissue.

### 2.2.5 Stochastic modeling of uncertain composition of bone US

Image-based mechanical models of bone can be affected by the accuracy of input data obtained through image analysis. In this work, the focus is set on the uncertainty affecting the composition of bone US in the multiscale framework described in Sec. 2.2.4.

This section is devoted to modeling the uncertain composition of bone US. Following the approach of Sansalone et al. (2016), probability theory is used to account for this uncertainty and parameters describing US bone composition are modeled as random variables with prescribed statistics provided by experimental measures. Different modeling assumptions will be considered leading to four different stochastic descriptions of uncertain bone composition: (i) On the one side, bone composition will be described in terms of either TMD or VFs (Sec. 2.2.5); (ii) On

the other side, stochastic models will be built using either voxel-scale or RVE-scale statistical information (Sec. 2.2.5).

Information about bone composition will be further used in Sec. 2.2.6 to estimate the elastic coefficients of bone using a micromechanical model. Two features of this model have to be kept in mind in our stochastic modeling, namely: (*i'*) the micromechanical model uses as input data the VFs at each scale and (*ii'*) bone US is assumed to be homogeneous within each RVE. First, in view of (*i'*), both TMD-based and VF-based approaches will be concerned with the uncertainty on the VFs. In a VF-based approach, uncertainty directly affects the VFs. In a TMD-based approach, uncertainty affects the TMD and is then propagated to the VFs through Eqs. (2.7). Second, in view of (*ii'*), each realization of the stochastic models is meant to represent the composition of the homogenous matrix of one RVE, irrespective of the scale (either voxel or RVE) of the underlying experimental data.

TMD-based and VF-based approaches require building specific stochastic models for the random variable modeling the uncertain TMD (to be called random TMD for short and denoted  $TMD$ ) and for the two random variables modeling the uncertain VFs  $f_I$  and  $f_{II}$  (to be called random VFs for short and denoted  $F_I$  and  $F_{II}$ , respectively), respectively. In previous work (Sansalone et al., 2016), a VF-based approach was proposed and the stochastic models of the random VFs were obtained using the Maximum Entropy (MaxEnt) principle. Here below, the same strategy is used to obtain the stochastic model of the random TMD needed in a TMD-based approach.

### Stochastic model of TMD

In the RVE, the experimental TMD is heterogeneous in space at the RVE scale. Nevertheless, hereinafter, we are not interested in modeling the spatial variations of the TMD at the RVE scale. This would require modeling the TMD as a random field  $\{\tilde{\theta}(M)\}_{M \in RVE}$  and defining the whole system of its marginal laws. Rather, we introduce in this section a stochastic model of the random TMD which is homogenous in space within the RVE. Let us assume that the TMD is a stationary random field  $\{\tilde{\theta}(M)\}_{M \in RVE}$ . Consequently, the marginal law  $x \mapsto p_{\tilde{\theta}(M)}(M; x)$  of the random field  $\{\tilde{\theta}(M)\}_{M \in RVE}$  is actually independent of the spatial coordinate  $M$  and can be written as  $p_{\tilde{\theta}(M)}(x)$ . We then model the random TMD as a random variable  $TMD$  whose probability density function  $p_{TMD}$  is such that  $p_{TMD}(x) = p_{\tilde{\theta}(M)}(x)$ .

The MaxEnt principle (Jaynes, 1957a,b; Soize, 2001) allows building a probability density function (PDF)  $p_X(x)$  of a random variable  $X$  by maximizing the Shannon's entropy (Shannon, 1948) under a set of constraints. Shannon's entropy measures the uncertainty associated to a probability distribution. Therefore, it is minimal for Dirac-distributed random variables and maximal for uniformly distributed random variables. The general form of the Shannon's entropy is:

$$\mathcal{S}(p_X) = \int_{S_X} -\ln(p_X(x)) p_X(x) dx. \quad (2.9)$$

Constraints represent the available information on  $X$  and can be expressed in terms of its statistical moments. Specifically, available information on  $X$  was assumed to be given in terms of its support  $S_X$ , mean value  $\mu_X$  and standard deviation  $\sigma_X$ —or, equivalently, dispersion

$\delta_X = \sigma_X/\mu_X$ . Let  $\mathbb{E}(f(X))$  be the expected value of a function  $f$ :

$$\mathbb{E}(f(X)) = \int_{\mathfrak{R}} f(X) \times p_X(x) dx, \quad (2.10)$$

where  $\mathfrak{R}$  is the real axis. Then, the following constraints were imposed:

$$(\mathcal{C}_i) \quad \mathbb{E}(f_i(X)) = m_i, \quad i = 0, \dots, 2, \quad (2.11)$$

with

$$\begin{aligned} f_0(x) &= 1_{S_X}(x), & m_0 &= 1; \\ f_1(x) &= x, & m_1 &= \mu_X^{\text{exp}}; \\ f_2(x) &= x^2, & m_2 &= (\mu_X^{\text{exp}})^2 \times (1 + (\delta_X^{\text{exp}})^2). \end{aligned} \quad (2.12)$$

In the above equations,  $1_{S_X}$  is the support function of  $X$  and  $\mu_X^{\text{exp}}$  and  $\delta_X^{\text{exp}}$  are experimental statistics. Constraint  $(\mathcal{C}_0)$  is the normalization condition on the PDF of  $X$ . Constraints  $(\mathcal{C}_1)$  and  $(\mathcal{C}_2)$  set the values of the two first momenta of  $X$  through the available experimental information. This is equivalent to enforce the mean value and dispersion of  $X$  to be equal to their corresponding experimental values, *i.e.*  $\mu_X = \mu_X^{\text{exp}}$  and  $\delta_X = \delta_X^{\text{exp}}$ .

Let  $TMD$  be the random variable modeling the TMD. It turns out that  $S_{TMD}$  is the image of  $\mathcal{GL}_{US}$  (the range of GLs associated to the US) through Eq. (2.1), *i.e.*  $S_{TMD} \simeq [0.7, 1.5] \text{ g/cm}^3$ ; moreover, constraints  $(\mathcal{C}_1)$  and  $(\mathcal{C}_2)$  read  $\mu_{TMD} = \mu_{TMD}^{\text{exp}}$  and  $\delta_{TMD} = \delta_{TMD}^{\text{exp}}$ , respectively, where  $\mu_{TMD}^{\text{exp}}$  and  $\delta_{TMD}^{\text{exp}}$  are the experimental statistics computed in Sec. 2.2.3 on a voxel-wise basis. The solution of the above constrained maximization problem provides the PDF of  $TMD$ , whose expression reads (Soize, 2004):

$$p_{TMD}(x) := 1_{S_{TMD}}(x) e^{-(\lambda_0 + \lambda_1 x + \lambda_2 x^2)}, \quad (2.13)$$

where  $\lambda_0$ ,  $\lambda_1$ , and  $\lambda_2$  are Lagrange multipliers associated to the constraints in Eqs. (2.11). The procedure leading to this result is detailed in App. A. The PDF coming from this specific problem turns out to be the truncation of the PDF of a Gaussian random variable on the support  $S_{TMD}$ . Note that this expression is of the same exponential form as those of the random VFs obtained in Sansalone et al. (2016) using a VF-based approach.

### Numerical solution of the stochastic models

Let  $X$  be a *primary* random variable, *i.e.* the random TMD in a TMD-based approach or a random VF in a VF-based approach, and  $p_X$  its PDF. Numerical solution of the stochastic model is performed by means of a Monte-Carlo numerical solver which requires computing a large number of statistically independent (s.i.) realizations of  $X$  by sampling  $p_X$ . Sampling was performed using the *pseudo-inverse* method (Devroye, 1986). This procedure is detailed in App. A.

Mean value and dispersion of  $X$  were estimated by means of the statistical estimators in Eqs. (2.4), with  $x_i \equiv X(a_i)$ , *i.e.* the  $i$ -th s.i. realization of  $X$ . The number of realizations was fixed so as to achieve convergence of these statistical estimators to the corresponding experimental values. Let the absolute and relative errors be defined as:

$$\Delta^N(*_X) := *_X^N - *_X^{\text{exp}}, \quad \Delta_{\%}^N(*_X) := \frac{\Delta^N(*_X)}{*_X^{\text{exp}}}, \quad (2.14)$$

where  $*_X^N$  and  $*_X^{\text{exp}}$  are descriptive and experimental statistics (mean value  $\mu_X$ , dispersion  $\delta_X$ , ...) of  $X$  and  $N$  is the number of s.i. realizations of  $X$ . Convergence was assumed to be achieved as soon as the errors  $\Delta_{\%}^N(\mu_X)$  and  $\Delta^N(\delta_X)$  became smaller than a fixed threshold. Hereinafter,  $N_{\text{s.i.r.}}$  will denote the number of s.i. realizations needed to achieve convergence.

Realizations of  $X$  were collected for further analysis, leading to the constitution of database  $\mathcal{DB}_{TMD}$  in the TMD-based approach and of two databases  $\mathcal{DB}_{F_I}$  and  $\mathcal{DB}_{F_{II}}$  in the VF-based approach.

### TMD-based vs. VF-based approaches

Composition of bone US can be described in terms of either VFs ( $f_{\text{Col}}^{\text{US}}$  and  $f_{\text{HA}}^{\text{MF}}$ ) or TMD. The two approaches are largely equivalent in a deterministic framework since Eqs. (2.7) are one-to-one mappings between individual values of TMD and VFs for a large range of values of TMD (up to about  $\text{TMD} \approx 1.35$ , *i.e.*  $f_{\text{Col}}^{\text{US}} \approx 0.371$  and  $f_{\text{HA}}^{\text{MF}} \approx 0.715$ ). However, in a stochastic framework, the two approaches are based on different experimental data and therefore lead to different descriptions of the uncertain bone composition.

In the TMD-based approach, the primary random variable is  $TMD$ , whose stochastic model is based on experimental statistics of TMD at the voxel scale—namely mean value  $\mu_{TMD}^{\text{exp}}$  and dispersion  $\delta_{TMD}^{\text{exp}}$ . In order to describe bone composition at the MF and US scales, the random VFs associated to  $TMD$ , hereinafter named  $F_I^d$  and  $F_{II}^d$ , have to be computed. (Superscript  $d$  denotes that  $F_I^d$  and  $F_{II}^d$  are *derived* random variables.) Thus, for each s.i. realization  $TMD(a_i)$ , the corresponding values of the random VFs, named  $F_I^d(a_i)$  and  $F_{II}^d(a_i)$ , can be computed through Eqs. (2.7):

$$\begin{cases} F_{II}^d(a_i) = \hat{f}_{II}(TMD(a_i)) , \\ F_I^d(a_i) = \hat{f}_I(TMD(a_i)) . \end{cases} \quad (2.15)$$

Note that  $F_I^d$  and  $F_{II}^d$  are not s.i. from each other being both computed from  $TMD$ .

In the VF-based approach (Sansalone et al., 2016), the primary random variables are  $F_I$  and  $F_{II}$ , whose stochastic models are based on experimental statistics of VFs at the voxel scale—namely mean values  $\mu_{f_I}^{\text{exp}}$  and  $\mu_{f_{II}}^{\text{exp}}$  and dispersions  $\delta_{f_I}^{\text{exp}}$  and  $\delta_{f_{II}}^{\text{exp}}$ . Realizations of  $F_I$  and  $F_{II}$  describe bone composition at the MF and US scales, respectively. Moreover, they can be used to compute the corresponding values of the random TMD, hereinafter named  $TMD^d$ . More precisely, realizations  $F_I(a_i)$  and  $F_{II}(a_i)$  can be inserted in Eqs. (2.5)(a-b) and Eq. (2.6)(a) to compute the corresponding value  $TMD^d(a_i)$ . Note that the empirical relation in Eq. (2.5)(c) is not used to compute  $TMD^d(a_i)$  since  $F_I(a_i)$  and  $F_{II}(a_i)$  are realizations of s.i. random variables.

### Voxel-scale vs RVE-scale approaches

Stochastic models of  $TMD$ ,  $F_I$  and  $F_{II}$  were obtained using voxel-scale experimental measures. The same approach was used to obtain stochastic models of these random variables based on experimental data at the RVE scale. A superposed bar will denote these new random variables. Random variables modeling the uncertain, effective TMD and VFs at the RVE scale will be therefore denoted  $\overline{TMD}$ ,  $\overline{F}_I$ , and  $\overline{F}_{II}$ , respectively. In a TMD-based approach, the stochastic model of  $\overline{TMD}$  was obtained based on the mean value  $\mu_{\overline{TMD}}^{\text{exp}}$  and dispersion  $\delta_{\overline{TMD}}^{\text{exp}}$  of  $\overline{TMD}$ .

S.i. realizations of  $\overline{TMD}$  were collected in the database  $\mathcal{DB}_{\overline{TMD}}$ . In a VF-based approach, the stochastic models of  $\overline{F}_I$  and  $\overline{F}_{II}$  were obtained based on the statistics of  $\overline{f}_I$  ( $\mu_{\overline{f}_I}^{\text{exp}}$  and  $\delta_{\overline{f}_I}^{\text{exp}}$ ) and  $\overline{f}_{II}$  ( $\mu_{\overline{f}_{II}}^{\text{exp}}$  and  $\delta_{\overline{f}_{II}}^{\text{exp}}$ ), respectively. S.i. realizations of  $\overline{F}_I$  and  $\overline{F}_{II}$  were collected in databases  $\mathcal{DB}_{\overline{F}_I}$  and  $\mathcal{DB}_{\overline{F}_{II}}$ , respectively.

### 2.2.6 Continuum micromechanical models of bone ultrastructure

Elastic coefficients of bone US were computed using a continuum micromechanics approach based on the hierarchical description of bone presented in Sec. 2.2.4. The model is depicted in Fig. 2.4. Following the *concept I* proposed by Hellmich et al. (2004), bone US (solid matrix embedding the Haversian canals at the tissue scale) is modeled as cylindrical collagen inclusions embedded in a MF. In turn, this latter is modeled as a disordered mixture of mineral and water spherical particles.

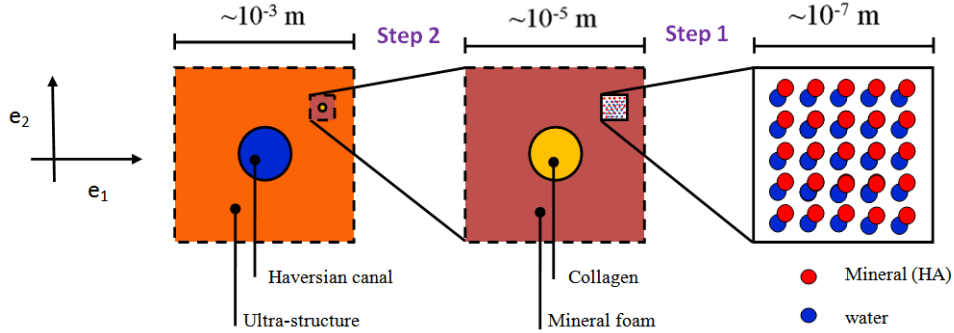


Figure 2.4: Sketch of the multiscale model. Cortical tissue (on the left) and ultra-structure (US, in the middle) are represented in the cross section plane of the bone sample, orthogonal to the axis of the Haversian canals. Haversian canals and collagen fibers are modeled as cylindrical inclusions in the cortical tissue and US, respectively. Mineral foam (MF, on the right) is modeled as a disordered mixture of mineral and water spherical particles (orientation is not meaningful).

Continuum micromechanics allows computing the effective (or homogenized) elastic properties of a material of matrix/inclusion type based on the VFs, elastic properties and geometrical arrangement of the constituent phases (Suvorov and Dvorak, 2002). In compact form, the homogenization procedure reads:

$$g_{\bullet}(\mathbb{c}_{hom}; \{f_r\}, \{\mathbb{c}_r\}) = 0, \quad r = 1, \dots, N_r, \quad (2.16)$$

where  $f_r$  and  $\mathbb{c}_r$  are the VF and the 4-th order elastic tensor of phase  $r$ ,  $N_r$  is the number of phases, and  $\mathbb{c}_{hom}$  is the homogenized 4-th order elastic tensor. Information on the shape and spatial arrangement of the phases is encoded in the function  $g$ . When a matrix phase is clearly identified,  $g$  should encode the Mori-Tanaka (MT) approximation. When phases interpenetrate with one another,  $g$  should encode the self-consistent (SC) approximation.

Aiming at computing the effective elastic properties of bone US, two homogenization steps are concerned, namely: (I) computing the effective elastic tensor of the MF,  $\mathbb{c}_{MF}$ , based on the

VFs and elastic tensors of mineral and water; and (II) computing the effective elastic tensor of the US,  $\mathbb{C}_{\text{US}}$ , based on the VFs and elastic tensors of collagen and MF. Therefore, the whole homogenization procedure reads:

$$\begin{aligned} g_{\text{I}}(\mathbb{C}_{\text{MF}}; f_{\text{I}}, \{\mathbb{C}_{\text{HA}}, \mathbb{C}_{\text{W}}\}) = 0 &\rightarrow \mathbb{C}_{\text{MF}}, \\ g_{\text{II}}(\mathbb{C}_{\text{US}}; f_{\text{II}}, \{\mathbb{C}_{\text{Col}}, \mathbb{C}_{\text{MF}}\}) = 0 &\rightarrow \mathbb{C}_{\text{US}}, \end{aligned} \quad (2.17)$$

where the mappings  $g_{\text{I}}$  and  $g_{\text{II}}$  encode the SC and MT approximations suitable for the MF and US, respectively;  $\mathbb{C}_{\bullet}$  is the elastic tensor of the material  $\bullet$  (subscripts are self-explaining); and  $f_{\text{I}}$  and  $f_{\text{II}}$  are the VFs of the mineral in the MF and of the collagen in the US, respectively (see Sec. 2.2.4). For sake of simplicity, we assumed both water, mineral, and collagen to be isotropic materials using the data of Kotha and Guzelsu (2000). Thus, MF and US turn out to be isotropic and transversely isotropic materials, respectively. We refer to Sansalone et al. (2010, 2016) for more details on the homogenization procedure.

The above general framework was used to develop four stochastic and two deterministic micromechanical modeling concepts which are resumed in Tab. 2.1 and described in the next sections.

Concept	Exp. data	Scale of exp. meas.	Primary rnd. var.	Ref.
VF/Vox	$\{\mu_{f_{\text{I}}}^{\text{exp}}, \delta_{f_{\text{I}}}^{\text{exp}}\}$ and $\{\mu_{f_{\text{II}}}^{\text{exp}}, \delta_{f_{\text{II}}}^{\text{exp}}\}$	10 $\mu\text{m}$	$F_{\text{I}}$ and $F_{\text{II}}$	Sansalone et al. (2016)
TMD/Vox	$\{\mu_{\text{TMD}}^{\text{exp}}, \delta_{\text{TMD}}^{\text{exp}}\}$	10 $\mu\text{m}$	$TMD$	New
VF/RVE	$\{\mu_{\bar{f}_{\text{I}}}^{\text{exp}}, \delta_{\bar{f}_{\text{I}}}^{\text{exp}}\}$ and $\{\mu_{\bar{f}_{\text{II}}}^{\text{exp}}, \delta_{\bar{f}_{\text{II}}}^{\text{exp}}\}$	500 $\mu\text{m}$	$\bar{F}_{\text{I}}$ and $\bar{F}_{\text{II}}$	New
TMD/RVE	$\{\mu_{\text{TMD}}^{\text{exp}}, \delta_{\text{TMD}}^{\text{exp}}\}$	500 $\mu\text{m}$	$\bar{TMD}$	New
Nominal/Vox	$\mu_{f_{\text{I}}}^{\text{exp}}$ and $\mu_{f_{\text{II}}}^{\text{exp}}$	10 $\mu\text{m}$	Deterministic	Sansalone et al. (2016)
Nominal/RVE	$\mu_{\bar{f}_{\text{I}}}^{\text{exp}}$ and $\mu_{\bar{f}_{\text{II}}}^{\text{exp}}$	500 $\mu\text{m}$	Deterministic	New

Table 2.1: Stochastic and nominal modeling concepts.

### Stochastic micromechanical models of bone ultrastructure

The micromechanical model presented above was used to quantify the effects of uncertain bone composition on the elastic coefficients of bone US. To this aim, parameters describing bone

composition in the model, *i.e.* the VFs of the mineral in the MF and of the collagen in the US were modeled as random variables while keeping fixed the elastic tensors ( $\mathbb{c}_{\text{Col}}$ ,  $\mathbb{c}_{\text{HA}}$ , and  $\mathbb{c}_{\text{W}}$ ), shape and spatial arrangement (mappings  $g_{\text{I}}$  and  $g_{\text{II}}$ ) of constituent phases. Since VFs are random variables, elastic tensors of MF and US turn out to be random tensors too.

Let  $X_{\text{I}}$  and  $X_{\text{II}}$  be the random VFs of the mineral in the MF and of the collagen in the US, respectively, and let  $\mathbb{C}_{\text{MF}}$  and  $\mathbb{C}_{\text{US}}$  be the random elastic tensors of MF and US, respectively, resulting from the homogenization procedure. Realizations  $\mathbb{C}_{\text{MF}}(a_i)$  and  $\mathbb{C}_{\text{US}}(a_i)$  of the random elastic tensors were computed using realizations  $X_{\text{I}}(a_i)$  and  $X_{\text{II}}(a_i)$  of the random VFs as input data of the micromechanical model encoded in Eqs. (2.17):

$$\begin{aligned} g_{\text{I}}(\mathbb{C}_{\text{MF}}(a_i); X_{\text{I}}(a_i), \{\mathbb{c}_{\text{HA}}, \mathbb{c}_{\text{W}}\}) = 0 &\quad \rightarrow \mathbb{C}_{\text{MF}}(a_i), \\ g_{\text{II}}(\mathbb{C}_{\text{US}}(a_i); X_{\text{II}}(a_i), \{\mathbb{c}_{\text{Col}}, \mathbb{C}_{\text{MF}}(a_i)\}) = 0 &\quad \rightarrow \mathbb{C}_{\text{US}}(a_i). \end{aligned} \quad (2.18)$$

It can be noticed that  $\mathbb{C}_{\text{MF}}(a_i)$  and  $\mathbb{C}_{\text{US}}(a_i)$  belong to the same elastic symmetry groups than  $\mathbb{c}_{\text{MF}}$  and  $\mathbb{c}_{\text{US}}$ . Thus,  $\mathbb{C}_{\text{MF}}$  and  $\mathbb{C}_{\text{US}}$  are isotropic and transversely isotropic random tensors, respectively.

Realizations of the random VFs can be obtained using either a VF-based approach or a TMD-based approach. Moreover, experimental data underlying either approach can be obtained either at the voxel or at the RVE scale. Therefore, four stochastic concepts were drawn up which are described here below.

**VF/Vox concept.** Concept *VF/Vox* is a stochastic micromechanical model describing uncertain US composition in terms of  $F_{\text{I}}$  and  $F_{\text{II}}$ , whose stochastic models are based on experimental measures at the voxel scale. Random elastic tensors of the MF and US were computed by means of Eqs. (2.18) with  $X_{\text{I}}(a_i) \sim F_{\text{I}}(a_i)$  and  $X_{\text{II}}(a_i) \sim F_{\text{II}}(a_i)$ . This concept corresponds to the one proposed in previous work of our group (Sansalone et al., 2016).

**TMD/Vox concept.** Concept *TMD/Vox* is a stochastic micromechanical model describing uncertain US composition in terms of *TMD*, whose stochastic model is based on experimental measures at the voxel scale. Random elastic tensors of the MF and US were computed by means of Eqs. (2.18) with  $X_{\text{I}}(a_i) \sim F_{\text{I}}^d(a_i) = \hat{f}_{\text{I}}(\text{TMD}(a_i))$  and  $X_{\text{II}}(a_i) \sim F_{\text{II}}^d(a_i) = \hat{f}_{\text{II}}(\text{TMD}(a_i))$ .

**VF/RVE concept.** Concept *VF/RVE* is a stochastic micromechanical model describing uncertain US composition in terms of  $\bar{F}_{\text{I}}$  and  $\bar{F}_{\text{II}}$ , whose stochastic models are based on experimental measures at the RVE scale. Random elastic tensors of the MF and US were computed by means of Eqs. (2.18) with  $X_{\text{I}}(a_i) \sim \bar{F}_{\text{I}}(a_i)$  and  $X_{\text{II}}(a_i) \sim \bar{F}_{\text{II}}(a_i)$ .

**TMD/RVE concept.** Concept *TMD/RVE* is a stochastic micromechanical model describing uncertain US composition in terms of  $\overline{\text{TMD}}$ , whose stochastic model is based on experimental measures at the RVE scale. Random elastic tensors of the MF and US were computed by means of Eqs. (2.18) with  $X_{\text{I}}(a_i) \sim \bar{F}_{\text{I}}^d(a_i) = \hat{f}_{\text{I}}(\overline{\text{TMD}}(a_i))$  and  $X_{\text{II}}(a_i) \sim \bar{F}_{\text{II}}^d(a_i) = \hat{f}_{\text{II}}(\overline{\text{TMD}}(a_i))$ .

### Statistical analysis of random elastic coefficients

Realizations of the random elastic tensors  $\mathbb{C}_{\text{MF}}$  and  $\mathbb{C}_{\text{US}}$  were further analyzed to retrieve relevant statistical information.

First, individual random elastic moduli were investigated. Specifically, statistics of the relevant random elastic moduli were estimated through the descriptive statistics of their realizations, Eqs. (2.4), *i.e.*  $\mu_X \simeq \mu_X^{N_{\text{s.i.r.}}}$ ,  $\sigma_X \simeq \sigma_X^{N_{\text{s.i.r.}}}$ , and  $\delta_X \simeq \delta_X^{N_{\text{s.i.r.}}}$ , with  $X$  being a random elastic modulus. Convergence of the statistical estimators was assessed. In view of the symmetry properties of  $\mathbb{C}_{\text{MF}}$  (isotropic) and  $\mathbb{C}_{\text{US}}$  (transversely isotropic), relevant elastic coefficients are:

**MF:** Young modulus ( $Y$ ) and Poisson coefficient ( $\nu$ );

**US:** axial moduli in the longitudinal ( $Y_3$ ) and transverse ( $Y_1$ ) directions; shear moduli in the sagittal ( $G_{13}$ ) and cross section ( $G_{12}$ ) planes; and lateral contraction coefficients in the sagittal (either of  $\nu_{13}$  or  $\nu_{31}$ ) and cross section ( $\nu_{12}$ ) planes of the bone sample.

Then, global fluctuations of the random elastic tensors around their mean values were investigated introducing a scalar measure of dispersion. Each 4-th order elastic tensor  $\mathbb{C}$  was expressed in Kelvin's form as a  $6 \times 6$  positive definite square matrix  $[\mathbb{C}]$ . Thus, the scalar dispersion of a random matrix  $[\mathbb{C}]$  was defined as:

$$d_{[\mathbb{C}]} = \sqrt{\frac{\mathbb{E}(\|[\mathbb{C}] - \mu_{[\mathbb{C}]}\|_F^2)}{\|\mu_{[\mathbb{C}]}\|_F^2}}, \quad (2.19)$$

where  $\|*\|_F$  is the Frobenius' norm of  $*$ . The mean value  $\mu_{[\mathbb{C}]}$  and the scalar dispersion  $d_{[\mathbb{C}]}$  of  $[\mathbb{C}]$  were estimated using the statistical estimators:

$$\begin{aligned} \mu_{[\mathbb{C}]}^N &= \frac{1}{N} \sum_{k=1}^N [\mathbb{C}(a_k)], \\ d_{[\mathbb{C}]}^N &= \sqrt{\frac{\frac{1}{N} \sum_{k=1}^N \|[\mathbb{C}(a_k)] - \mu_{[\mathbb{C}]}^N\|_F^2}{\|\mu_{[\mathbb{C}]}^N\|_F^2}}. \end{aligned} \quad (2.20)$$

It can be noticed that, thanks to the closure property of the elastic symmetry groups, the mean value of the random tensor  $\mathbb{C}$  belongs to the same elastic symmetry group than the realizations of this latter. Thus,  $\mu_{\mathbb{C}_{\text{MF}}}$  and  $\mu_{\mathbb{C}_{\text{US}}}$  are isotropic and transversely isotropic tensors, respectively.

### Nominal micromechanical model of bone ultrastructure

Two deterministic, *nominal models* referring to the voxel and RVE scales, respectively, were developed for comparison purposes. The two nominal models were obtained by using the mean values of the VFs measured at the voxel scale ( $\mu_{f_{\text{I}}}^{\text{exp}}$  and  $\mu_{f_{\text{II}}}^{\text{exp}}$ ) and at the RVE scale ( $\mu_{f_{\text{I}}}^{\text{exp}}$  and  $\mu_{f_{\text{II}}}^{\text{exp}}$ ), respectively, as input data of the homogenization procedure in Eqs. (2.17). Hereinafter, the nominal elastic tensors of MF and US will be named  $\mathbb{c}_{\text{MF}}$  and  $\mathbb{c}_{\text{US}}$ , respectively.

Nominal elastic tensors were compared with the mean values of the random elastic tensors, that is  $\mu_{\mathbb{C}_{\text{MF}}}$  and  $\mu_{\mathbb{C}_{\text{US}}}$ . Let  $y$  be a nominal elastic modulus and  $\mu_Y$  the mean value of the

corresponding random modulus. Elastic moduli  $y$  and  $\mu_Y$  were compared by computing their relative difference:

$$\Delta(y, \mu_Y) := \left| \frac{y - \mu_Y}{\mu_Y} \right|. \quad (2.21)$$

## 2.3 Results & Discussion

### 2.3.1 Statistical results

Statistics of experimental databases are resumed in Tabs. 2.2-2.4. Tab. 2.2 contains the voxel-scale statistics of TMD,  $f_I$ , and  $f_{II}$  (databases  $\mathcal{DB}_{\text{TMD}}^{\text{exp}}$ ,  $\mathcal{DB}_{f_I}^{\text{exp}}$ , and  $\mathcal{DB}_{f_{II}}^{\text{exp}}$ ). These data refer to all the solid voxels of all the RVEs. RVE-wise voxel-scale statistics are also shown in Tab. 2.3. RVE-wise mean values of TMD,  $f_I$ , and  $f_{II}$  reported in this table correspond to the RVE-scale values of  $\overline{\text{TMD}}$ ,  $\overline{f_I}$ , and  $\overline{f_{II}}$ , respectively. Eventually, Tab. 2.4 contains the RVE-scale statistics of HP,  $\overline{\text{TMD}}$ ,  $\overline{f_I}$ , and  $\overline{f_{II}}$  (databases  $\mathcal{DB}_{\text{HP}}^{\text{exp}}$ ,  $\mathcal{DB}_{\overline{\text{TMD}}}^{\text{exp}}$ ,  $\mathcal{DB}_{\overline{f_I}}^{\text{exp}}$ , and  $\mathcal{DB}_{\overline{f_{II}}}^{\text{exp}}$ ).

Mean values of  $\overline{\text{TMD}}$  reported in Tab. 2.3 are comprised in the range  $[0.957, 1.046] \text{ g/cm}^3$  that represents a tiny interval with respect to the whole range of values of the TMD corresponding to the solid voxels:  $[\text{TMD}(\text{GL} = 131), \text{TMD}(\text{GL} = 255)] = [0.618, 1.504] \text{ g/cm}^3$ . The dispersion of the TMD within each RVEs ( $\delta_{\text{TMD}}^{\text{exp}}$ , Tab. 2.3) vary between 0.054 and 0.080, proving an uneven scattering of the TMD at the voxel scale from one RVE to another. The mean values of the mineralization at the voxel scale ( $\mu_{\text{TMD}}^{\text{exp}}$ , Tab. 2.2) and at the RVE scale ( $\mu_{\overline{\text{TMD}}}^{\text{exp}}$ , Tab. 2.4) are quite similar (differences appear at the fourth significant digit). This is related to the fact that most of the RVEs have similar numbers of solid voxels. Conversely, the dispersion of the TMD at the voxel scale ( $\delta_{\text{TMD}}^{\text{exp}}$ , Tab. 2.2) is about 2.6 times higher than at RVE scale ( $\delta_{\overline{\text{TMD}}}^{\text{exp}}$ , Tab. 2.4) showing that voxel-scale TMD values are much more scattered than RVE-scale  $\overline{\text{TMD}}$  values. The same trend is observed with respect to the dispersion of TMD within each RVE ( $\delta_{\text{TMD}}^{\text{exp}}$ , Tab. 2.3) which turn out to be 2 – 3 times higher than the dispersion of  $\overline{\text{TMD}}$ . This is due to the fact that RVE-scale values of  $\overline{\text{TMD}}$  are already average values; therefore, statistics of  $\overline{\text{TMD}}$  get rid of most of voxel-scale fluctuations of TMD. It can be shown that, in an idealized case where each RVE would have the same HP (and thus,  $\overline{\text{TMD}}$  of each RVE would be computed by averaging always the same number of voxel-scale TMD values), the dispersion of  $\overline{\text{TMD}}$  at the RVE scale would be necessarily smaller than that of TMD at the voxel scale. The same trend is observed in the actual RVEs, although they have different values of HP.

The same considerations made for the mean value and dispersion of the TMD apply to the volume fractions. The mean values of the VFs of the mineral in the mineral foam and of the collagen in the ultrastructure are quite the same at both the voxel and RVE scales (Tab. 2.2 and Tab. 2.4, respectively), whereas dispersions at the voxel scale are 2 to 3 times higher than at the RVE scale. At both scales, the dispersion of the mineral VF is slightly higher to that of the TMD, whereas the dispersion of the collagen VF is 5 times smaller, proving that scattering of mineral content is much higher than that of collagen and that collagen content shows a weak dependency on the mineralization. This agrees with the idea that collagen content does not noticeably change in bone tissue after its initial formation, whereas mineral content increases with aging by progressive replacement of water (Fratzl et al., 1993).

Table 2.2: Experimental statistics at the voxel scale (databases  $\mathcal{DB}_{\text{TMD}}^{\text{exp}}$ ,  $\mathcal{DB}_{f_{\text{I}}}^{\text{exp}}$ , and  $\mathcal{DB}_{f_{\text{II}}}^{\text{exp}}$ ). The last row of the table indicates the modeling concepts using these data.

TMD [ $g/cm^3$ ]		$f_{\text{HA}}^{\text{MF}}$ [-]		$f_{\text{Col}}^{\text{US}}$ [-]	
$\mu^{\text{exp}}$	$\delta^{\text{exp}}$	$\mu^{\text{exp}}$	$\delta^{\text{exp}}$	$\mu^{\text{exp}}$	$\delta^{\text{exp}}$
0.999	0.073	0.517	0.080	0.355	0.016
TMD/Vox		VF/Vox			

Table 2.3: Experimental statistics at the voxel scale for each RVE.

RVE	$\theta$ [ $^\circ$ ]	$z$ [ $mm$ ]	HP [-]	TMD [ $g/cm^3$ ]		$f_{\text{HA}}^{\text{MF}}$ [-]		$f_{\text{Col}}^{\text{US}}$ [-]	
				$\mu^{\text{exp}}$	$\delta^{\text{exp}}$	$\mu^{\text{exp}}$	$\delta^{\text{exp}}$	$\mu^{\text{exp}}$	$\delta^{\text{exp}}$
1	-40	1.5	0.041	1.046	0.054	0.544	0.060	0.359	0.012
2	-40	3.5	0.065	1.018	0.062	0.528	0.069	0.357	0.014
3	-40	5.5	0.065	0.977	0.063	0.504	0.070	0.354	0.014
4	-20	1.5	0.085	1.021	0.065	0.530	0.072	0.357	0.014
5	-20	3.5	0.062	0.983	0.068	0.508	0.075	0.354	0.015
6	-20	5.5	0.053	0.955	0.070	0.492	0.078	0.352	0.015
7	0	1.5	0.207	1.009	0.080	0.522	0.089	0.356	0.017
8	0	3.5	0.059	0.997	0.068	0.516	0.076	0.355	0.015
9	0	5.5	0.088	0.957	0.079	0.493	0.088	0.352	0.017
10	20	1.5	0.074	1.022	0.064	0.530	0.071	0.357	0.014
11	20	3.5	0.059	1.029	0.058	0.534	0.064	0.358	0.012
12	20	5.5	0.155	0.978	0.071	0.505	0.079	0.354	0.015
				TMD		$\bar{f}_{\text{I}}$		$\bar{f}_{\text{II}}$	

### 2.3.2 Parameters of the stochastic and nominal models

Data in Tab. 2.2 and Tab. 2.4 have been used to build the four stochastic and two nominal modeling concepts listed in Tab. 2.1.

Each stochastic concept requires computing the PDFs of the relevant primary random variable(s). Eq. (2.13) provides the general form of these PDFs for both the TMD (see Sec. 2.2.5) and the VFs (Sansalone et al., 2016). Therefore, the solution of the stochastic model of any primary random variable requires computing the optimal values of the Lagrange multipliers  $\lambda_0$ ,  $\lambda_1$ , and  $\lambda_2$ . Computations were made using the procedure outlined in App. A and results are shown in Tab. 2.5.

Nominal models at the voxel and RVE scales have been developed by using the mean values of VFs reported in Tab. 2.2 and Tab. 2.4, respectively. Although they are conceptually different, these values are pretty the same and the two nominal models provide essentially the same results.

### 2.3.3 TMD/Vox and VF/Vox concepts

This section focuses on the results of concepts TMD/Vox and VF/Vox which are based on experimental statistics of TMD and VFs, respectively, measured at the voxel scale.

Table 2.4: Experimental statistics at RVE scale (databases  $\mathcal{DB}_{\text{TMD}}^{\text{exp}}$ ,  $\mathcal{DB}_{\bar{f}_I}^{\text{exp}}$ , and  $\mathcal{DB}_{\bar{f}_{II}}^{\text{exp}}$ ). The last row of the table indicates the modeling concepts using these data.

HP [-]		$\overline{\text{TMD}}$ [ $g/cm^3$ ]		$\bar{f}_{\text{HA}}^{\text{MF}}$ [-]		$\bar{f}_{\text{Col}}^{\text{US}}$ [-]	
$\mu^{\text{exp}}$	$\delta^{\text{exp}}$	$\mu^{\text{exp}}$	$\delta^{\text{exp}}$	$\mu^{\text{exp}}$	$\delta^{\text{exp}}$	$\mu^{\text{exp}}$	$\delta^{\text{exp}}$
0.084	0.547	0.999	0.028	0.517	0.031	0.355	0.006
TMD/RVE				VF/RVE			

Table 2.5: Optimal Lagrange multipliers for the four modeling concepts.

Concept	Primary rnd. var.	$\lambda_0$	$\lambda_1$	$\lambda_2$
VF/Vox	$F_{\text{HA}}^{\text{MF}}$	$7.4993 \times 10^1$	$-2.9877 \times 10^2$	$2.8887 \times 10^2$
	$F_{\text{Col}}^{\text{US}}$	$2.0448 \times 10^3$	$-1.1531 \times 10^4$	$1.6222 \times 10^4$
TMD/Vox	$\overline{\text{TMD}}$	$9.3360 \times 10^1$	$-1.9026 \times 10^2$	$9.5193 \times 10^1$
VF/RVE	$\bar{F}_{\text{HA}}^{\text{MF}}$	$4.6717 \times 10^2$	$-1.8193 \times 10^3$	$1.7592 \times 10^3$
	$\bar{F}_{\text{Col}}^{\text{US}}$	$1.2916 \times 10^4$	$-7.2712 \times 10^4$	$1.0230 \times 10^5$
TMD/RVE	$\overline{\text{TMD}}$	$5.8086 \times 10^2$	$-1.1679 \times 10^3$	$5.8442 \times 10^2$

### Convergence of the statistical estimators

Convergence plots of the statistical estimators of the mean values and dispersions of the primary random variables—*i.e.* the random TMD in the TMD/Vox concept (green lines) and the random VFs in the VF/Vox concept (red lines)—are shown in Fig. 2.5. Therein, the relative error on the mean values and the absolute errors on the dispersions (Eq. (2.14)) are plotted against the number of realizations of the random variables in log-log scale. The errors decrease following similar trends in all cases. Convergence was assumed to be achieved after  $10^5$  realizations, when the errors on both the mean values and dispersions became smaller than  $10^{-4}$ .

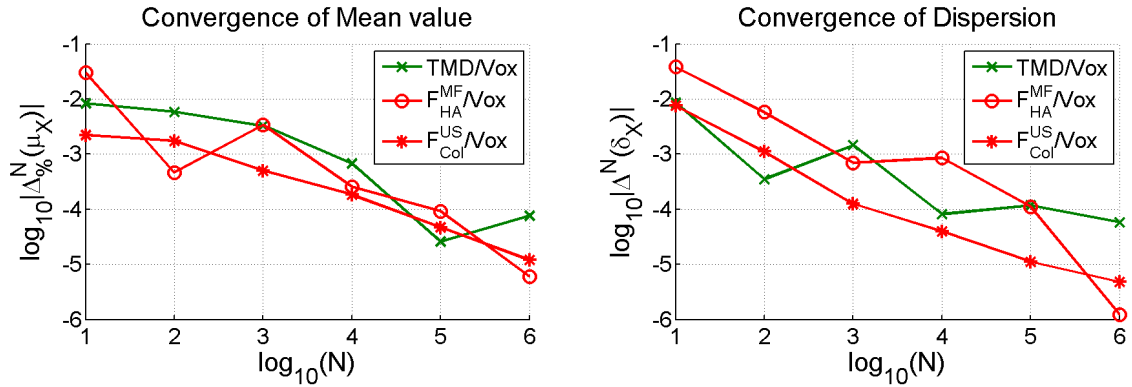


Figure 2.5: **TMD/Vox and VF/Vox concepts.** Convergence of the statistical estimators of the random TMD in the TMD/Vox concept (green lines) and of the random VFs in the VF/Vox concept (red lines). On the left: relative error on the mean values; On the right: absolute error on the dispersions.

Figs. 2.6-2.7 show that, after  $10^5$  realizations, convergence is also achieved for the statistical estimators of the random elastic moduli. Green and red lines refer to the TMD/Vox and VF/Vox concepts, respectively. Solid and dashed lines refer to the mean values and 50% confidence intervals, respectively. Moreover, black lines refer to the nominal model. Fig. 2.6 refers to the Young modulus and Poisson coefficient of the MF. Figs. 2.7 refers to the axial modulus  $Y_3$  and lateral contraction coefficient  $\nu_{31}$  of the US (subscripts refer to the frame in Fig. 2.1).

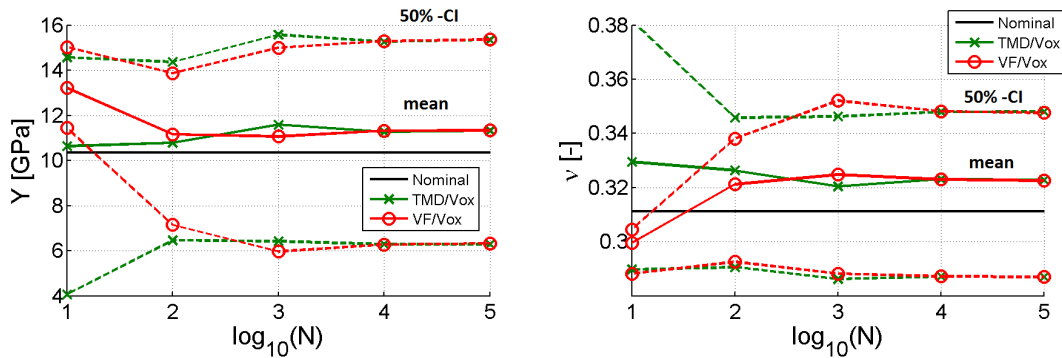


Figure 2.6: **TMD/Vox and VF/Vox concepts.** Convergence of the statistical estimators of some random elastic moduli of the MF. On the left: Young modulus; On the right: Poisson coefficient. Green and red lines refer to the TMD/Vox and VF/Vox concepts, respectively. Solid and dashed lines refer to mean values and 50% confidence intervals, respectively. Black lines refer to the nominal model.

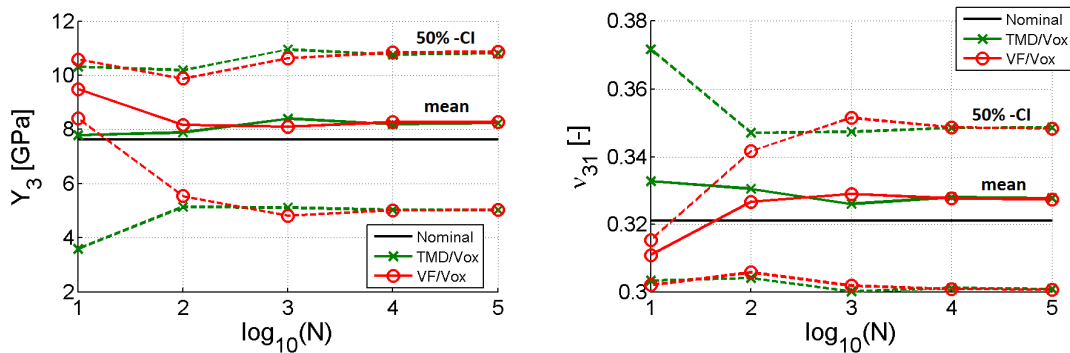


Figure 2.7: **TMD/Vox and VF/Vox concepts.** Convergence of the statistical estimators of some random elastic moduli of the US. On the left: axial modulus  $Y_3$ ; On the right: lateral contraction coefficient  $\nu_{31}$  (subscripts refer to the frame in Fig. 2.1). Green and red lines refer to the TMD/Vox and VF/Vox concepts, respectively. Solid and dashed lines refer to mean values and 50% confidence intervals, respectively. Black lines refer to the nominal model.

Therefore, unless otherwise specified, descriptive statistics computed on  $N_{s.i.r.} = 10^5$  realizations were used hereinafter to estimate the statistics of the random variables.

## TMD and VFs

Scattered values and PDFs of the random TMD and VFs related to concepts TMD/Vox (in green) and VF/Vox (in red) are shown in Fig. 2.8. Subplot (a) shows the realizations of the random VFs. Red dots represent the realizations of the pairs  $(F_{\text{I}}(a_i), F_{\text{II}}(a_i))$  generated by the VF/Vox concept and green dots represent the realizations of the pairs  $(F_{\text{I}}^d(a_i), F_{\text{II}}^d(a_i))$  generated by the TMD/Vox concept, with  $i = 1, \dots, N_{\text{s.i.r.}}$ . The blue line corresponds to the analytical relationship between the two VFs encoded in Eqs. (2.7) and used in the TMD/Vox concept to compute a pair of VFs from one realization of random TMD. Not surprisingly, all the pairs  $(F_{\text{I}}^d(a_i), F_{\text{II}}^d(a_i))$  generated by the TMD/Vox concept lie on this blue line since they are both computed from  $TMD(a_i)$  by means of Eqs. (2.7). By contrast, the pairs  $(F_{\text{I}}(a_i), F_{\text{II}}(a_i))$  generated by the VF/Vox concept spread around this line. This is coherent with the hypothesis made in the VF/Vox concept, where the VFs were modeled as s.i. random variables. From this hypothesis follows that the *joint distribution* (or joint PDF) of the pair of random VFs  $(F_{\text{I}}, F_{\text{II}})$  is the product of their marginal ones. Since the marginal distributions of the random VFs are truncated Gaussian distributions (see Sec. 2.2.5), the joint distribution is a truncated bell-shaped surface leading to the quasi-elliptical scattering of  $(F_{\text{I}}(a_i), F_{\text{II}}(a_i))$  observed in Fig. 2.8/(a). Subplots (b)-(d) show the PDFs of the random TMD and VFs obtained through the TMD/Vox (green lines) and VF/Vox (red lines) concepts as well as the experimental PDFs (blue lines). The PDFs of the random VFs provided by the two concepts are very similar to each other (subplots (c)-(d)) although some differences exist with respect to the experimental PDF. By contrast, looking at the random TMD (subplot (b)), the PDF of  $TMD$  computed in the TMD/Vox concept appears to approximate the experimental PDF better than that of  $TMD^d$  computed in the VF/Vox concept. This latter appears more spread out and has larger tails. This may be related to the different correlation between pairs of VFs in the two concepts. In the TMD/Vox concept, the two random VFs are nonlinearly correlated since both of them depend on the random TMD. Therefore, in a given event  $a_i$ , small/high values of  $F_{\text{I}}^d(a_i)$  are always associated to small/high values of  $F_{\text{II}}^d(a_i)$ —both of them resulting from small/high values of  $TMD(a_i)$ . By contrast, in the VF/Vox concept, the two random VFs are completely uncorrelated being s.i. random variables. Therefore, in a given event  $a_i$ , small/high values of  $F_{\text{I}}(a_i)$  can be associated to any value of  $F_{\text{II}}(a_i)$ .

The above conclusions are supported by analyzing the differences between the statistics of the stochastic concepts and of the experimental data after reaching convergence of the statistical estimators (in the sense of Sec. 2.3.3). Fig. 2.9 represents the relative errors of the mean values and dispersions of the random TMD and VFs related to concepts TMD/Vox (green bars) and VF/Vox (red bars), respectively, estimated through Eq. (2.14) on the basis of  $10^6$  realizations. As expected, statistics of the primary random variables (*i.e.*, TMD in the TMD/Vox concept and VFs in the VF/Vox concept) approximate very well the corresponding experimental statistics. Conversely, statistics of the derived random variables (*i.e.*, VFs in the TMD/Vox concept and TMD in the VF/Vox concept, denoted by a star in Fig. 2.9) are affected by higher errors. It is worth noting that, although the TMD/Vox and VF/Vox concepts show some differences in terms of statistics of TMD, they provide quite the same statistics with respect to the VFs.

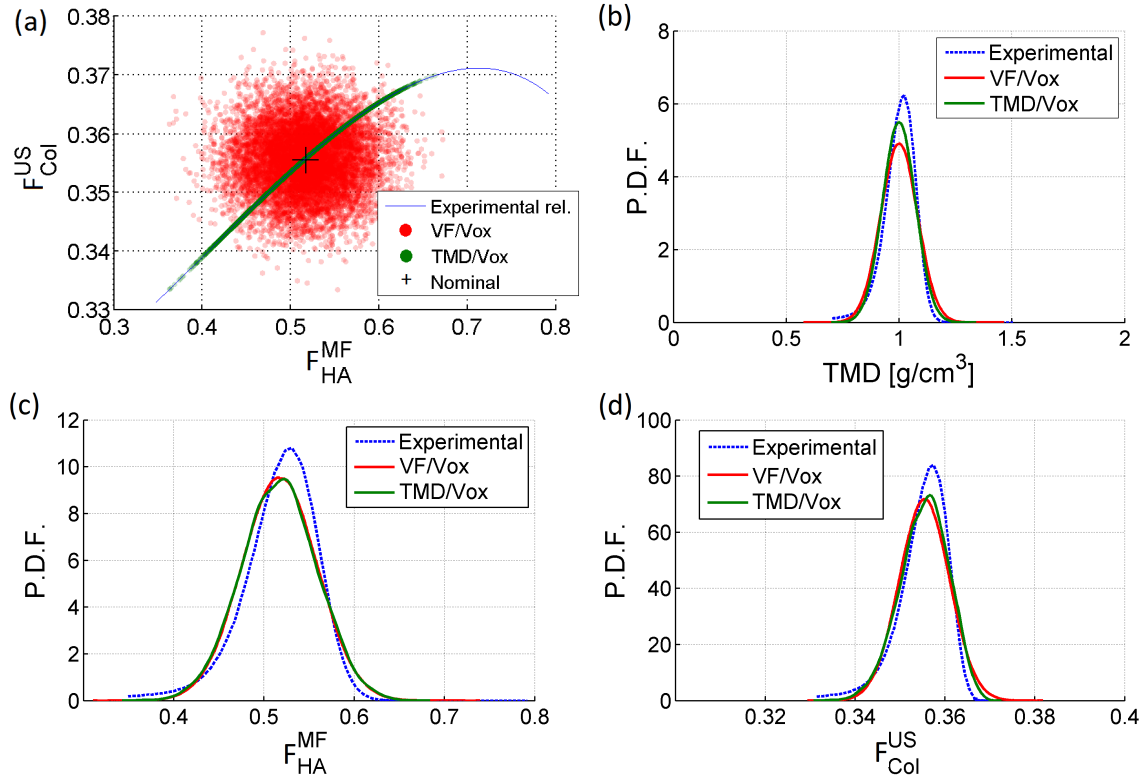


Figure 2.8: **TMD/Vox and VF/Vox concepts.** Scattered values and PDFs of the random TMD and VFs based on experimental data at the voxel scale. (a) Scatter plot of the realizations of the random VFs in concepts TMD/Vox (green dots) and VF/Vox (red dots) and analytical relationship between the two VFs encoded in Eqs. (2.7) (blue line). (b)-(d) PDFs of the TMD and of the random VFs in concepts TMD/Vox (green lines) and VF/Vox (red lines) and experimental PDF (blue lines).

### Elastic coefficients

Statistics of the random elastic moduli of MF and US predicted by concepts TMD/Vox and VF/Vox are shown in Tab. 2.6 and Tab. 2.7, respectively. Deterministic values predicted by the nominal model are shown as well. The two concepts provide very similar statistics for all the elastic coefficients. This can be explained noting that the statistics of the VFs (the only random parameters entering the computation of the elastic moduli, see Eqs. (2.18)) in the two concepts are very similar, see Fig. 2.9 and the discussion at the end of the previous section. A difference of about 10% is observed between the mean values of the elastic moduli and their nominal values at both the MF and US scales. This difference is due to the nonlinear relationship existing between the VFs and the elastic coefficients introduced by the homogenization procedure. Therefore, homogenized elastic coefficients based on the mean values of the VFs (nominal model) are not equivalent to the mean values of the homogenized elastic coefficients based on the realizations of the VFs (stochastic models). The dispersions of the elastic moduli turn out to be much higher

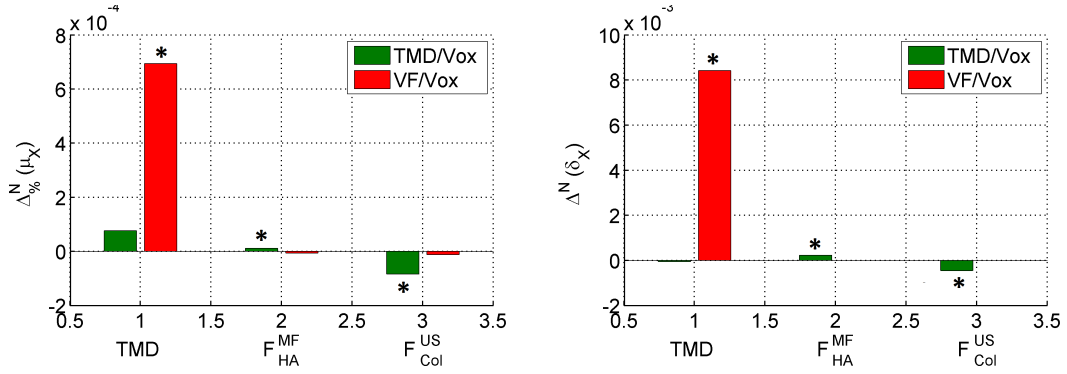


Figure 2.9: **TMD/Vox and VF/Vox concepts.** Relative error on the mean values (on the left) and absolute error on the dispersions (on the right) of the random TMD and VFs after  $10^6$  realizations, see Eq. (2.14). Green and red bars refer to TMD/Vox and VF/Vox concepts, respectively. Symbols \* denote the derived random variables (*i.e.*, VFs in the TMD/Vox concept and TMD in the VF/Vox concept).

than those of the TMD and VFs (Tab. 2.2). Since  $f_{HA}^{MF}$  is the main determinant of the elastic moduli, small variations of  $f_{HA}^{MF}$  induce large variations of the elastic moduli. Therefore, the realizations of the elastic moduli are more scattered than those of the TMD and VFs.

In order to get an overall picture of the fluctuations of the random elastic tensors around their mean values, the scalar dispersions of the corresponding random matrices were estimated through Eqs. (3.2.46) with  $N = N_{s.i.r.}$ . Results are summarized in Tabs. 2.8. These statistics show that the TMD/Vox and VF/Vox concepts predict very close values for the scalar dispersions of the random elastic tensors of both the MF and US. Moreover, it can be noticed that these scalar dispersions decrease along the sequence of the homogenization steps (Fig. 2.4; Step 1: MF, Step 2: US). This is basically due to the small dispersion of  $F_{Col}^{US}$ . This result can be proven explicitly if a simple rule-of-mixture is used for computing the homogenized elastic tensors—see App. C for more details.

Figs. 2.10-2.11 show the PDFs (subplots (a)-(b)) and scattered values (subplots (c)-(d)) of some random elastic moduli of the MF and US. PDFs predicted by TMD/Vox and VF/Vox concepts (subplots (a)-(b), green and red lines, respectively) are very similar to each other. However, both concepts do not provide accurate representations of the PDFs obtained by homogenizing all the actual voxel-scale data (blue lines). This confirms the observations made with respect to Tabs. 2.6-2.7. Subplots (c)-(d) show the scattering of the random elastic moduli. Blue lines depict the relationships between the TMD and the elastic moduli when making use of Eqs. (2.7). As expected, the realizations of the random elastic moduli of the TMD/Vox concept (green dots) lie on these lines. Conversely, the realizations of the VF/Vox concept (red dots) scatter around these lines. Therefore, although the PDFs of the two concepts are very similar to each other, scattering of the results is quite different.

Table 2.6: **TMD/Vox and VF/Vox concepts.** Elastic properties of the MF: nominal model and statistics ( $N_{\text{s.i.r.}} = 10^5$  realizations) of the stochastic concepts TMD/Vox and VF/Vox.  $Y$ : Young modulus;  $G$ : shear modulus;  $\nu$ : Poisson coefficient.

	$Y$ [GPa]	$G$ [GPa]	$\nu$ [-]
<b>Nominal model</b>	10.3525	3.9479	0.3111
<b>TMD/Vox concept</b>			
Mean value	11.3259	4.3622	0.3228
$err(y_*^\mu)$ , Eq. (2.21)	9.4024	10.4936	3.7476
Dispersion	0.5813	0.6041	0.1444
25% quantile	6.2835	2.3305	0.2870
75% quantile	15.3440	5.9611	0.3481
5% quantile	2.4940	0.8808	0.2681
95% quantile	23.6145	9.3108	0.4158
<b>VF/Vox concept</b>			
Mean value	11.3368	4.3664	0.3226
$err(y_*^\mu)$ , Eq. (2.21)	9.5071	10.6008	3.6846
Dispersion	0.5772	0.5998	0.1443
25% quantile	6.3228	2.3459	0.2870
75% quantile	15.3558	5.9659	0.3476
5% quantile	2.4826	0.8766	0.2682
95% quantile	23.5549	9.2867	0.4160

### 2.3.4 TMD/RVE and VF/RVE concepts

This section focuses on the results of concepts TMD/RVE and VF/RVE which are based on experimental statistics of TMD and VFs, respectively, measured at the RVE scale.

#### Convergence of the statistical estimators

Convergence of statistical estimators of the statistics of the random variables was first assessed. As in Sec. 2.3.3, it turned out that convergence was achieved after  $N_{\text{s.i.r.}} = 10^5$  realizations. Thus, descriptive statistics computed on  $N_{\text{s.i.r.}} = 10^5$  realizations were used hereinafter to estimate the statistics of the random variables.

As a matter of example, Figs. 2.12 show the convergence plots for the statistical estimators of the mean value and 50 % confidence interval of some random elastic moduli of the US, namely the axial modulus  $Y_3$  and the lateral contraction coefficient  $\nu_{31}$  (subscripts refer to the frame in Fig. 2.1). Green and red lines refer to the TMD/RVE and VF/RVE concepts, respectively. Moreover, black lines refer to the nominal model.

#### TMD and VFs

Scattered values and PDFs of the random effective TMD and VFs corresponding to concepts TMD/RVE (in green) and VF/RVE (in red) are shown in Fig. 2.13. Fig. 2.13(a) shows the realizations of the random effective VFs. Red dots represent the realizations of the pairs  $(\bar{F}_I(a_i), \bar{F}_{II}(a_i))$  generated by the VF/RVE concept and green dots represent the realizations of the pairs  $(\bar{F}_I^d(a_i), \bar{F}_{II}^d(a_i))$  generated by the TMD/RVE concept, with  $i = 1, \dots, N_{\text{s.i.r.}}$ . The

Table 2.7: **TMD/Vox and VF/Vox concepts.** Elastic properties of the US: nominal model and statistics ( $N_{\text{s.i.r.}} = 10^5$  realizations) of the stochastic concepts TMD/Vox and VF/Vox.  $Y_i$ : axial modulus in the direction  $i$ ;  $G_{ij}$ : shear modulus in the plane  $ij$ ;  $\nu_{ij}$ : lateral contraction coefficient in the plane  $ij$ ; Subscripts refer to the frame in Fig. 2.1.

	$Y_1$ [GPa]	$Y_3$ [GPa]	$G_{12}$ [GPa]	$G_{13}$ [GPa]	$\nu_{12}$ [-]	$\nu_{13}$ [-]
<b>Nominal model</b>	6.5274	7.6356	2.4368	2.5681	0.3393	0.2746
<b>TMD/Vox concept</b>						
Mean value	6.7602	8.2322	2.5288	2.7232	0.3489	0.2828
$err(y_*^\mu)$ , Eq. (2.21)	3.5666	7.8129	3.7744	6.0380	2.8259	3.0055
Dispersion	0.4219	0.5090	0.4336	0.4747	0.1392	0.2001
25% quantile	4.6671	5.0229	1.7241	1.7562	0.3295	0.2390
75% quantile	8.6012	10.8113	3.2348	3.5310	0.3535	0.3224
5% quantile	2.5709	2.5681	0.9201	0.9203	0.3197	0.2080
95% quantile	11.8295	16.0255	4.4818	5.0885	0.3971	0.3880
<b>VF/Vox concept</b>						
Mean value	6.8018	8.2730	2.5453	2.7401	0.3487	0.2825
$err(y_*^\mu)$ , Eq. (2.21)	4.2030	8.3477	4.4516	6.6952	2.7527	2.8908
Dispersion	0.4261	0.5106	0.4381	0.4783	0.1428	0.1996
25% quantile	4.6725	5.0345	1.7263	1.7589	0.3290	0.2391
75% quantile	8.6576	10.8681	3.2572	3.5535	0.3534	0.3216
5% quantile	2.5655	2.5627	0.9184	0.9186	0.3187	0.2088
95% quantile	11.9912	16.1657	4.5464	5.1537	0.3968	0.3876

Table 2.8: **TMD/Vox and VF/Vox concepts.** Scalar dispersions of the random elastic tensors of MF and US.

Concept	$d_{[\mathbb{C}_{\text{MF}}]}$	$d_{[\mathbb{C}_{\text{US}}]}$
<b>TMD/Vox</b>	0.4640	0.3412
<b>VF/Vox</b>	0.4606	0.3454

blue line corresponds to the analytical relationship between the two VFs encoded in Eq. (2.7) and used in the TMD/RVE concept to compute the pair  $(\bar{F}_{\text{I}}^d(a_i), \bar{F}_{\text{II}}^d(a_i))$  from one realization  $\overline{TMD}(a_i)$  by means of Eqs. (2.8). Similarly to Fig. 2.8(a), all the pairs  $(\bar{F}_{\text{I}}^d(a_i), \bar{F}_{\text{II}}^d(a_i))$  generated by the TMD/RVE concept lie on this line whereas the pairs  $(\bar{F}_{\text{I}}(a_i), \bar{F}_{\text{II}}(a_i))$  generated by the VF/Vox concept spread around it. Figs. 2.13(b)-(d) show the PDFs of the random effective TMD and VFs obtained using the TMD/RVE (green lines) and VF/RVE (red lines) concepts. The PDFs of the random effective VFs corresponding to the TMD/RVE and VF/RVE concepts (Figs. 2.13(c)-(d)) are very similar to each other. By contrast, some differences appear between the PDFs of  $\overline{TMD}$  (concept TMD/RVE) and  $\overline{TMD}^d$  (concept VF/RVE) depicted in Fig. 2.13(b). These results are qualitatively similar to those observed at the voxel-scale in Sec. 2.3.3, namely in Figs. 2.8(b-d).

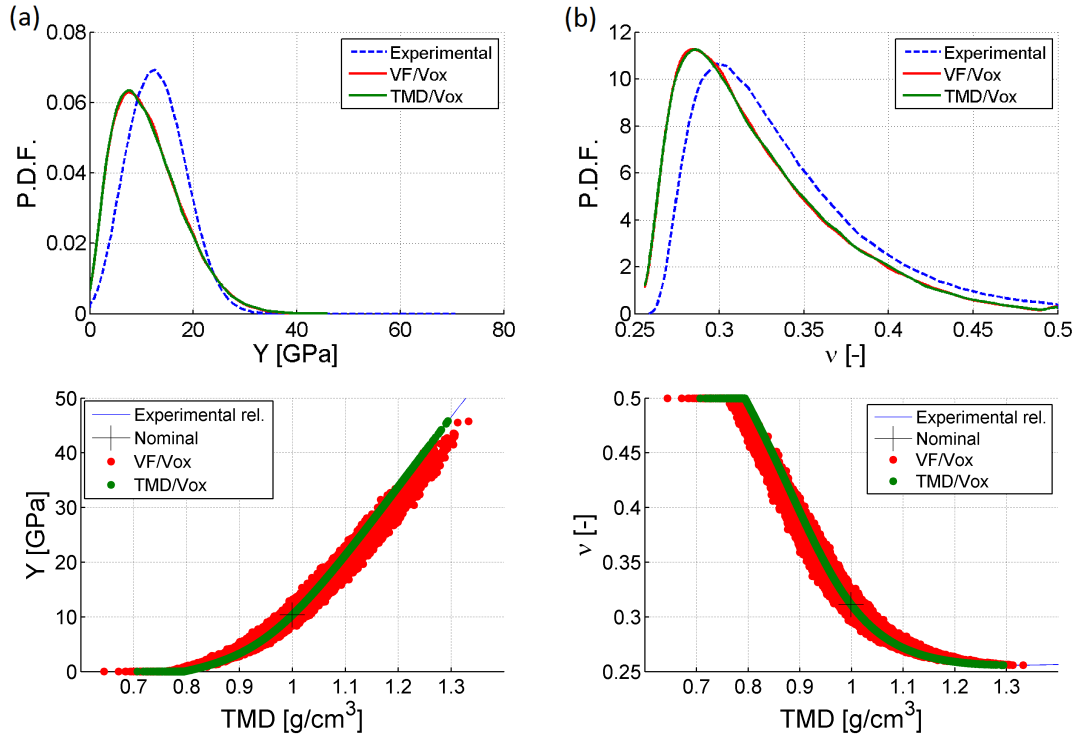


Figure 2.10: **TMD/Vox and VF/Vox concepts.** Random elastic moduli of the isotropic mineral foam predicted by the TMD/Vox (green data) and VF/Vox (red data) concepts. PDFs (first row, subplots (a)-(b)) and scattered values (second row, subplots (c)-(d)) of the Young modulus (left column) and Poisson coefficient (right column). Blue lines in subplots (a)-(b) refer to the PDFs obtained by homogenization of the actual voxel-scale data. Blue lines in subplots (c)-(d) depict the relationship between the TMD and the elastic moduli when using Eq. (2.5)(c); moreover, black crosses depict the results of the nominal model.

### Elastic coefficients

Statistics of the random elastic moduli of MF and US (concepts TMD/RVE and VF/RVE) are shown in Tab. 2.9 and Tab. 2.10, respectively. Deterministic values predicted by the nominal model are shown as well. Mean values and dispersions predicted by the two concepts are very similar to each at both the MF and US scales. Mean values of the elastic moduli predicted by the stochastic models stay quite close to the results of the nominal model, with differences smaller than 2%. The dispersion of all the axial and shear moduli is about 0.2, which is almost 7 times higher than that of  $\bar{f}_{HA}^{MF}$  (see Tab. 2.4), showing the same trend observed in Sec. 2.3.3 for concepts TMD/Vox and VF/Vox.

As for voxel-based concepts, the TMD/RVE and VF/RVE concepts predict very similar values for the scalar dispersion of the random elastic tensors of both the MF and US. Results are summarized in Tab. 2.11.

Figs. 2.14-2.15 show the PDFs (subplots (a)-(b)) and scattered values (subplots (c)-(d)) of

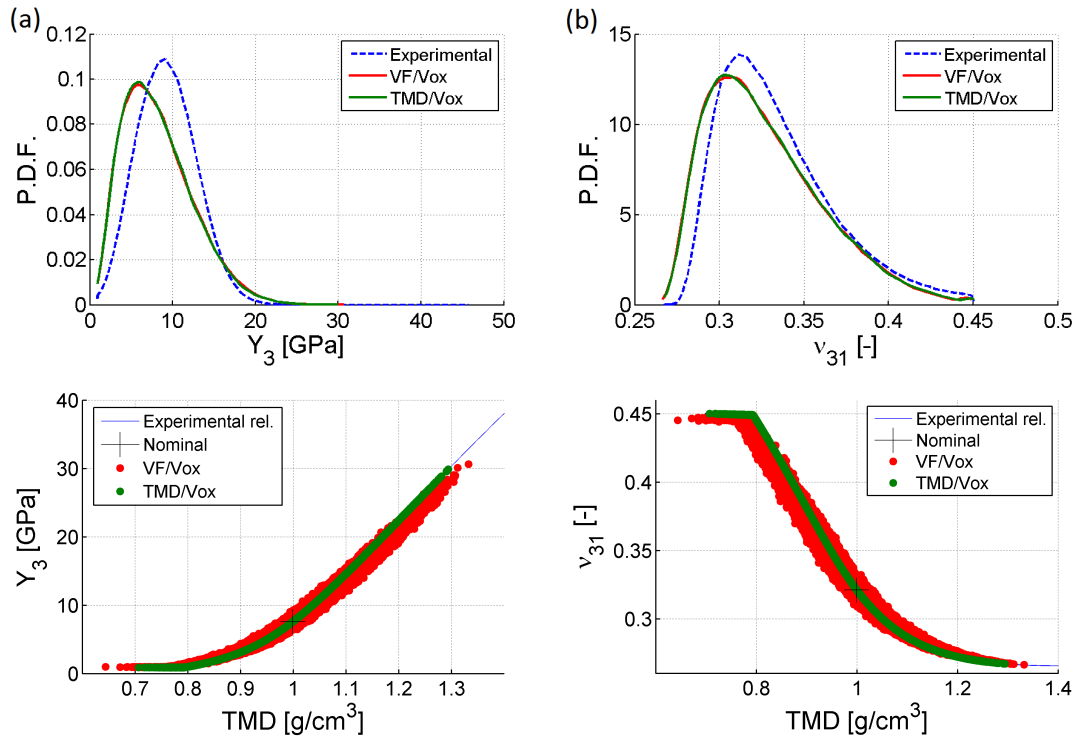


Figure 2.11: **TMD/Vox and VF/Vox concepts.** Random elastic moduli of the transversely isotropic ultrastructure predicted by the TMD/Vox (green data) and VF/Vox (red data) concepts. PDFs (first row, subplots (a)-(b)) and scattered values (second row, subplots (c)-(d)) of elastic moduli  $Y_3$  (left column) and  $\nu_{31}$  (right column); Subscripts refer to the frame in Fig. 2.1. Blue lines in subplots (a)-(b) refer to the PDFs obtained by homogenization of the actual voxel-scale data. Blue lines in subplots (c)-(d) depict the relationship between the TMD and the elastic moduli when using Eq. (2.5)(c); moreover, black crosses depict the results of the nominal model.

some random elastic moduli of the MF and US, respectively. PDFs predicted by TMD/RVE and VF/RVE concepts (subplots (a)-(b), green and red lines, respectively) are almost indistinguishable. Subplots (c)-(d) show the scattering of the random elastic moduli obtained through the TMD/RVE (green dots) and VF/RVE (red dots) concepts. Blue lines depict the relationships between the TMD and the elastic moduli when making use of Eqs. (2.7). Scattered elastic moduli of RVE-scale concepts follow the same trend observed in voxel-scale concepts: On the one side, results of the TMD/RVE concept lie on the blue lines; On the other side, results of the VF/RVE concept scatter around these lines. Once again, the PDFs of the elastic moduli of the TMD/RVE and VF/RVE concepts are very similar but the individual realizations are scattered differently.

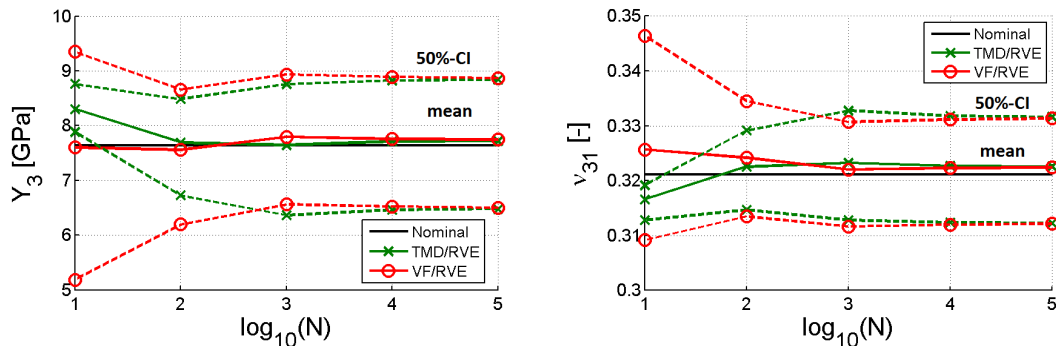


Figure 2.12: **TMD/RVE and VF/RVE concepts.** Convergence of the statistical estimators of the mean value (solid lines) and 50 % confidence interval (dashed lines) of some random elastic moduli of the ultrastructure. On the left: axial modulus  $Y_3$ ; On the right: lateral contraction coefficient  $\nu_{31}$  of the bone US (subscripts refer to the frame in Fig. 2.1). Green and red lines refer to the TMD/RVE and VF/RVE concepts, respectively. Black lines refer to the nominal model.

### 2.3.5 Voxel-scale vs. RVE-scale concepts

Results of voxel-based and RVE-based concepts are quite different. This is mostly related to the dispersion of the underlying experimental data. Voxel-scale TMD and VFs data are much more dispersed than RVE-scale data. Scattering of TMD and VFs data at the voxel and RVE scales reflects the variation of ultrastructure composition at the scale of several micrometers and of several hundreds micrometers, respectively. Since each value of TMD at the RVE scale is the spatial average of a large number (about  $10^5$ ) of voxel-scale data, RVE-scale data are necessarily less dispersed than voxel-scale data.

Statistics of elastic moduli predicted by voxel-scale and RVE-scale concepts are affected by the dispersion of the underlying input data. Actually, as the dispersion decreases, realizations of the random TMD and VFs tend to cluster around their experimental mean values and, therefore, realizations of the random elastic moduli tend to gather around the corresponding nominal value. This has two main consequences. On the one side, the mean values of the elastic moduli predicted by the RVE-scale concepts are closer to the nominal elastic moduli than those predicted by voxel-scale concepts. For instance, the differences between the nominal elastic modulus  $Y_3$  of the US and the corresponding mean values predicted by the TMD/RVE and TMD/Vox concepts are about 1.08% and 7.81%, respectively (see Tab. 2.10 and Tab. 2.7). On the other side, the dispersion and confidence intervals of the elastic moduli predicted by the RVE-scale concepts are significantly smaller than those of the voxel-scale concepts. For instance, the dispersions of the elastic tensors predicted by the RVE-based concepts are less than half of those predicted by the voxel-based concepts, see Tab. 2.8 and Tab. 2.11.

It is worth comparing the statistics of voxel-based and RVE-based stochastic concepts with the elastic moduli of individual RVEs predicted by the (deterministic) micromechanical model—hereinafter called RVE-wise elastic moduli for short. Following Sansalone et al. (2016), these

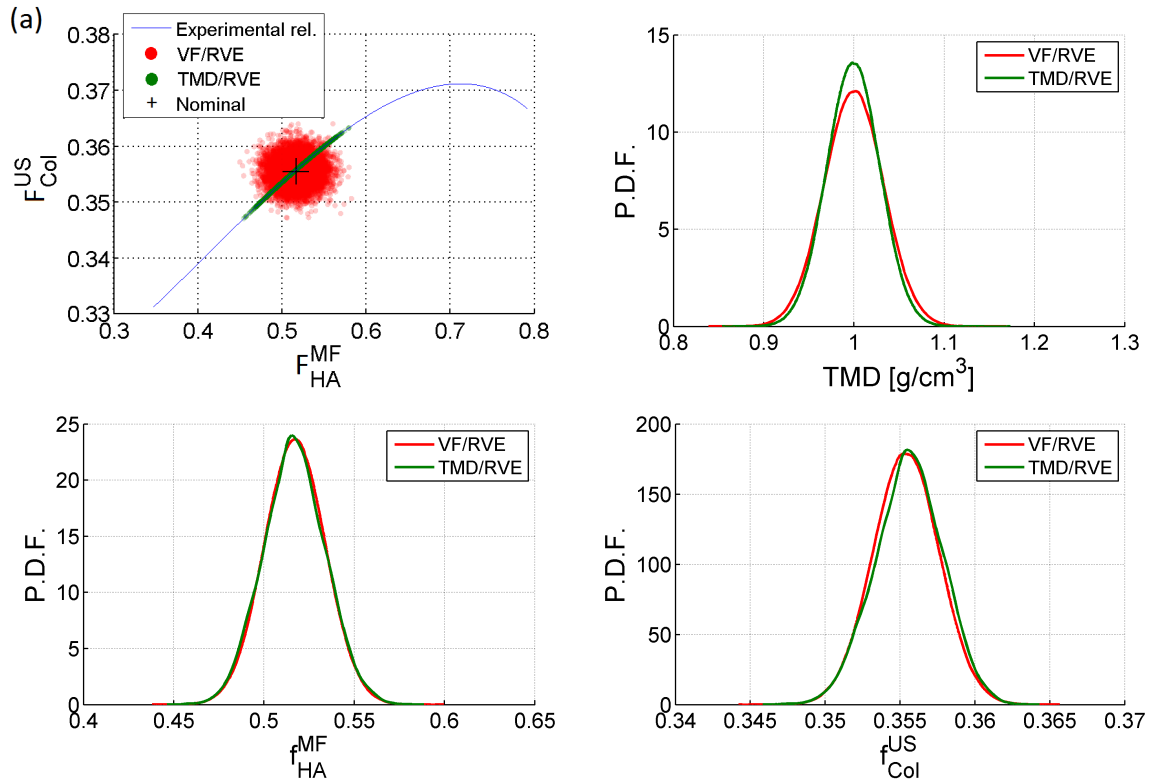


Figure 2.13: **TMD/RVE and VF/RVE concepts.** Scattered values and PDFs of the random TMD and VFs based on experimental data at the RVE scale. (a) Scatter plot of the realizations of the random VFs in concepts TMD/RVE (green dots) and VF/RVE (red dots) and analytical relationship between the two VFs encoded in Eq. (2.7) (blue line). (b)-(d) PDFs of the random TMD and VFs corresponding to concepts TMD/RVE (green lines) and VF/RVE (red lines);

latter were computed using the RVE-wise values of  $\overline{TMD}$  as input data for the homogenization model described in Sec. 2.2.6. Fig.2.16 compares the statistics of some elastic moduli predicted by the TMD/RVE concept with the corresponding RVE-wise elastic moduli. It can be noticed that these latter (blue and light blue circles, referring to the blue and light blue RVEs depicted in Fig. 2.1 and constituting the calibration and validation sets, respectively) are evenly scattered around the mean values predicted by the TMD/RVE concept (solid green lines). It can also be noticed that these mean values are well approximated by the nominal values (solid black lines). Moreover, 50% and 90% confidence intervals (thick and thin green dashed lines) contain almost half and almost all the RVE-wise values, respectively. Therefore, the 50% and 90% confidence intervals seem to be slightly smaller and larger, respectively, than one would expect. These errors may be due to the small number of individual RVE-wise values. In any case, predictions of the RVE-based concepts turn out to be much better than those of the voxel-based concepts which largely overestimate the confidence intervals (*e.g.*, see Fig. 10 in Sansalone et al. (2016) referring to the VF/Vox concept).

Table 2.9: **TMD/RVE and VF/RVE concepts.** Elastic properties of the MF: nominal model and statistics (resulting from  $N_{\text{s.i.r.}} = 10^5$  realizations) of the stochastic models of concepts TMD/RVE and VF/RVE.  $Y$ : Young modulus;  $G$ : shear modulus;  $\nu$ : Poisson coefficient.

	$Y$ [GPa]	$G$ [GPa]	$\nu$ [-]
<b>Nominal model</b>	10.3525	3.9479	0.3111
<b>TMD/RVE concept</b>			
Mean value	10.4914	4.0082	0.3136
$err(y_*^\mu)$ , Eq. (2.21)	1.3409	1.5271	0.7905
Dispersion	0.2591	0.2719	0.0590
25% quantile	8.5463	3.2256	0.3001
75% quantile	12.2465	4.7097	0.3247
5% quantile	6.3432	2.3540	0.2873
95% quantile	15.2562	5.9256	0.3474
<b>VF/RVE concept</b>			
Mean value	10.5186	4.0191	0.3134
$err(y_*^\mu)$ , Eq. (2.21)	1.6041	1.8024	0.7207
Dispersion	0.2574	0.2701	0.0586
25% quantile	8.5953	3.2452	0.3001
75% quantile	12.2599	4.7151	0.3243
5% quantile	6.3649	2.3625	0.2873
95% quantile	15.2536	5.9245	0.3471

## 2.4 Conclusion

In this chapter we investigated the effects of uncertain experimental data (input) on the elastic moduli of bone matrix (output). To this aim, we considered uncertain input data as random variables and used probability theory to build the related probability laws. These stochastic models were introduced in a micromechanical model of bone matrix to obtain a stochastic description of the elastic properties of this latter.

Several sources of uncertainty can arise in image-based multiscale modeling of bone: composition, geometry, microarchitecture, and so on and so forth. In this work we focused on the composition of bone matrix and applied our strategy to a cortical bone sample taken from the inferior femoral neck of an elderly patient. Basically, we started from images obtained with a spatial resolution of  $10 \mu\text{m}$  (referred to as *voxel scale*) to compute elastic properties of bone matrix at the scale of a few hundreds micrometers (referred to as *RVE scale*). Our work was developed in three main parts: first, the statistical analysis of experimental data; second, the stochastic modeling of bone compositional parameters; third, the micromechanical modeling in a stochastic framework.

**Statistical analysis.** Gray-levels of the images led to a voxel-scale, 3D distribution of *Tissue Mineral Density (TMD)* which, in turn, allowed computing the *volume fractions (VFs)* of elementary constituents of bone at each scale. The voxel-wise distribution of TMD was further averaged to obtain effective RVE-scale compositional information. Eventually, mean values and dispersions of TMD and VFs at both voxel- and RVE-scale were computed.

**Stochastic models.** We artificially introduced uncertainty in our data by assuming bone com-

Table 2.10: **TMD/RVE and VF/RVE concepts.** Elastic properties of the US: nominal model and statistics (resulting from  $N_{\text{s.i.r.}} = 10^5$  realizations) of the stochastic models of concepts TMD/RVE and VF/RVE.  $Y_i$ : axial modulus in the direction  $\mathbf{e}_i$ ;  $G_{ij}$ : shear modulus in the plane  $(\mathbf{e}_i, \mathbf{e}_j)$ ;  $\nu_{ij}$ : lateral contraction coefficient in the plane  $(\mathbf{e}_i, \mathbf{e}_j)$ ; Subscripts refer to the frame in Fig. 2.1.

	$Y_1$ [GPa]	$Y_3$ [GPa]	$G_{12}$ [GPa]	$G_{13}$ [GPa]	$\nu_{12}$ [-]	$\nu_{13}$ [-]
<b>Nominal model</b>	6.5274	7.6356	2.4368	2.5681	0.3393	0.2746
<b>TMD/RVE concept</b>						
Mean value	6.5530	7.7183	2.4472	2.5895	0.3402	0.2773
$err(y_*^\mu)$ , Eq. (2.21)	0.3915	1.0834	0.4262	0.8307	0.2534	1.0151
Dispersion	0.1796	0.2249	0.1847	0.2054	0.0216	0.0916
25% quantile	5.7276	6.4772	2.1300	2.2116	0.3350	0.2589
75% quantile	7.3308	8.8425	2.7456	2.9357	0.3445	0.2933
5% quantile	4.6963	5.0613	1.7352	1.7684	0.3296	0.2400
95% quantile	8.5658	10.7557	3.2212	3.5142	0.3532	0.3230
<b>VF/RVE concept</b>						
Mean value	6.5733	7.7434	2.4552	2.5982	0.3400	0.2771
$err(y_*^\mu)$ , Eq. (2.21)	0.7037	1.4118	0.7524	1.1699	0.2070	0.9177
Dispersion	0.1814	0.2258	0.1866	0.2070	0.0218	0.0907
25% quantile	5.7406	6.5005	2.1350	2.2179	0.3349	0.2589
75% quantile	7.3526	8.8663	2.7540	2.9447	0.3444	0.2926
5% quantile	4.6931	5.0630	1.7341	1.7678	0.3292	0.2402
95% quantile	8.6198	10.8062	3.2424	3.5357	0.3531	0.3226

Table 2.11: **TMD/RVE and VF/RVE concepts.** Scalar dispersions of the random elastic tensors of MF and US.

Concept	$d_{[\text{C}_{\text{MF}}]}$	$d_{[\text{C}_{\text{US}}]}$
<b>TMD/RVE</b>	0.2033	0.1462
<b>VF/RVE</b>	0.2022	0.1479

position to be known only in statistical terms. Thus, stochastic models of uncertain TMD and VFs were set up by means of the Maximum Entropy (MaxEnt) and using the experimental statistics of TMD and VFs, respectively, as input data.

**Micromechanical modeling.** We developed four stochastic micromechanical concepts by introducing the stochastic models developed above in the micromechanical model of bone matrix. The four concepts correspond to considering as primary random variables either the TMD or VFs, each of them based on either voxel-scale or RVE-scale statistical information.

Comparison of these four concepts allowed investigating the two main questions set in this chapter.

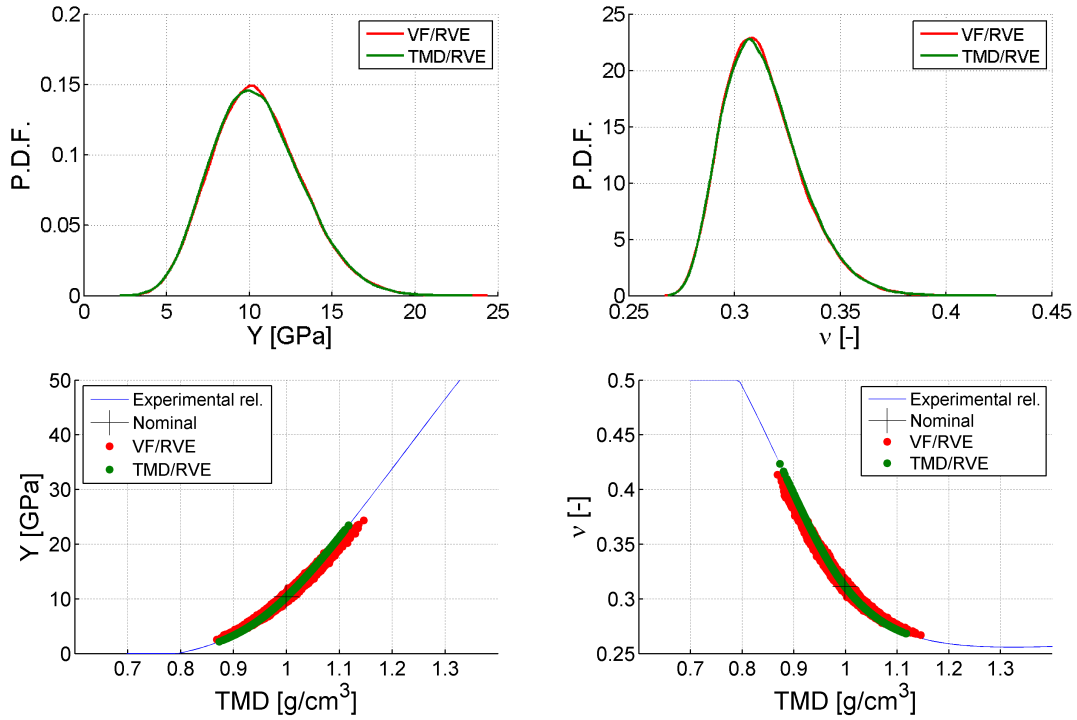


Figure 2.14: **TMD/RVE and VF/RVE concepts.** Random elastic moduli of the MF predicted by the TMD/RVE (green data) and VF/RVE (red data) concepts. PDFs (first row, subplots (a)-(b)) and scattered values (second row, subplots (c)-(d)) of the Young modulus (left column) and Poisson coefficient (right column). Blue lines in subplots (c)-(d) depict the relationship between the TMD and the elastic moduli when making use of Eqs. (2.7); moreover, black crosses depict the results of the nominal model.

### 2.4.1 TMD-based *vs.* RVE-based concepts

TMD-based and VF-based concepts provided very similar results in terms of statistics (mean value, dispersion, confidence intervals) of the elastic moduli. Some differences were observed with respect to the scattering of the elastic moduli. This is related to the way VFs are modeled in VF-based and TMD-based concepts. Random VFs describing uncertain bone composition are perfectly independent in VF-based concepts whereas they are perfectly dependent on each other in TMD-based concepts. Therefore, the two concepts describe two limit situations, the actual one being likely in between. In order to obtain a more realistic description of the random VFs, one could introduce some noise in the nonlinear relationship relating the VFs in the TMD-based concepts, *i.e.* Eq. (2.5)(c). By doing this, VFs will be described as weakly dependent random variables. Nevertheless, no noticeable effects are expected in terms of statistical description of the elastic moduli.

In the end, in authors' opinion, a TMD-based approach should be preferred since it introduces uncertainty on one observable variable (the TMD is linearly related to the gray level, that is to

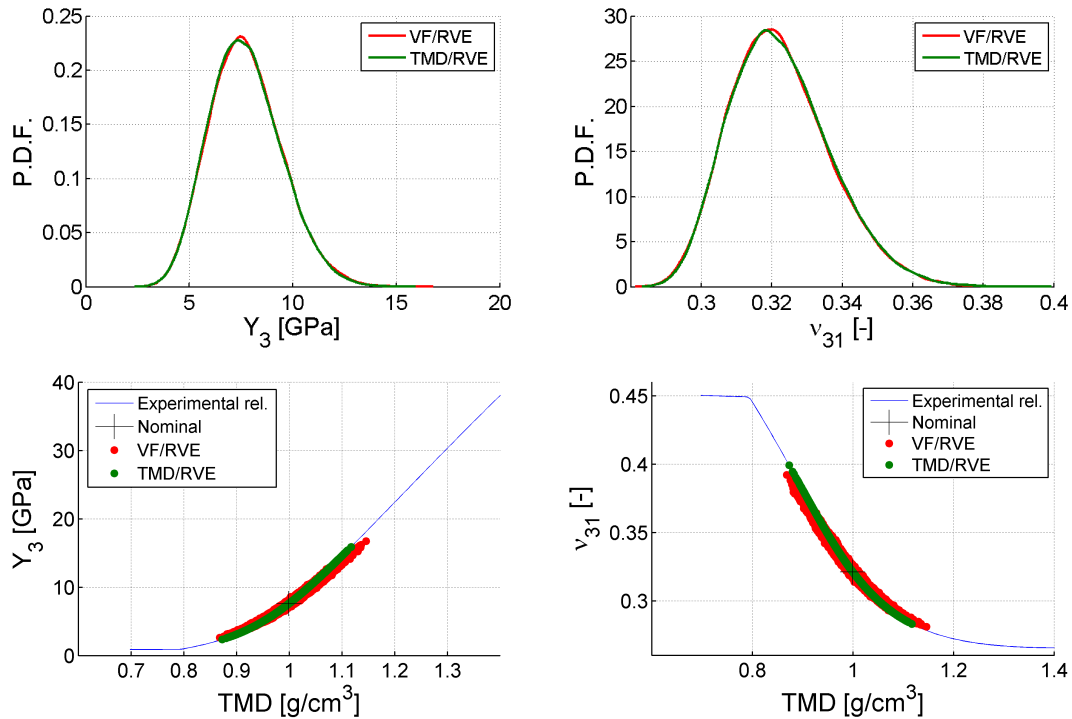


Figure 2.15: **TMD/RVE and VF/RVE concepts.** Random elastic moduli of the transversely isotropic ultrastructure predicted by the TMD/RVE (green data) and VF/RVE (red data) concepts. PDFs (first row, subplots (a)-(b)) and scattered values (second row, subplots (c)-(d)) of elastic moduli  $Y_3$  (left column) and  $\nu_{31}$  (right column); Subscripts refer to the frame in Fig. 2.1. Blue lines in subplots (c)-(d) depict the relationship between the TMD and the elastic moduli when making use of Eqs. (2.7); moreover, black crosses depict the results of the nominal model.

the X-ray absorption of the bone matrix) whereas a VF-based approach introduces uncertainty on two latent variables (the VFs of collagen and mineral) which are inferred from the TMD through a mathematical model.

#### 2.4.2 Voxel-scale *vs.* RVE-scale concepts

Concepts based on statistical information at the RVE scale proved to perform much better than concepts based on statistical information at the voxel scale. More precisely, RVE-scale concepts provided an accurate statistical description of the elastic moduli at the RVE scale, whereas voxel-scale concepts highly overestimated their scattering. This is mainly related to the fact that the dispersion of TMD at the voxel-scale is much higher than at the RVE scale. These results point out that, as long as elasticity of bone matrix is concerned, one should use experimental information at the scale of several hundreds micrometers—a spatial resolution achievable by clinical CT scanners—and get rid of finer-scale variability.

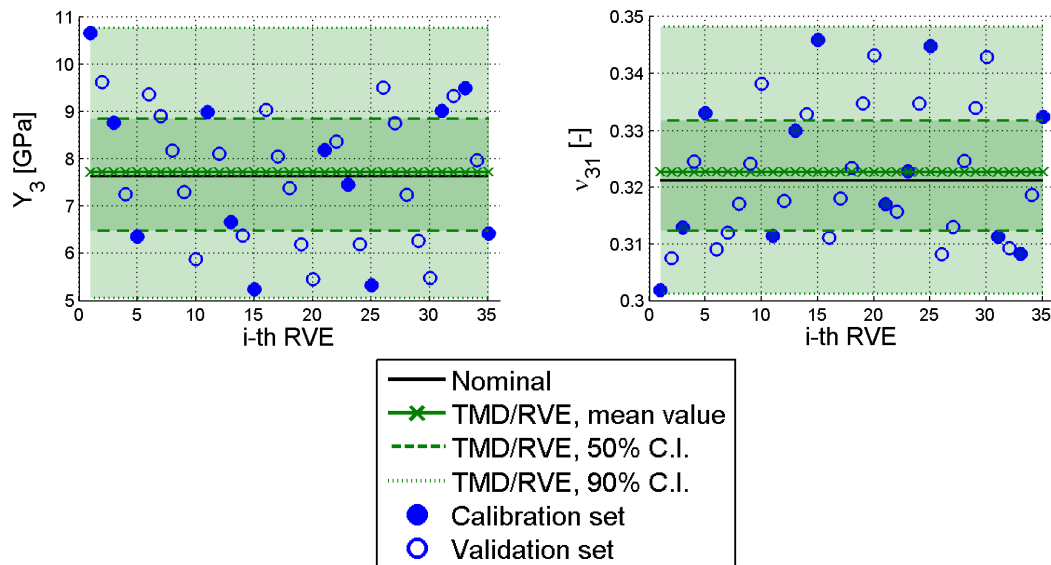


Figure 2.16: Elastic moduli of the ultrastructure. Comparison between the elastic moduli of actual RVEs (blue and light blue circles, see Fig. 2.1) and the corresponding statistics predicted by the TMD/RVE concept (green lines; solid, thick-dashed and thin-dashed lines refer to mean values, 50% and 90% confidence intervals, respectively). Black lines depict the nominal values.

Eventually, it is worth noting that these results can impact organ-scale models. In image-based Finite Element (FE) simulations of whole bone, material properties of bone are often considered heterogeneous at the organ scale but homogeneous within each FE (Hellmich et al., 2008; Zysset et al., 2013; Li et al., 2015; Zadpoor and Weinans, 2015; Pahr and Zysset, 2016). Since the typical size of the FEs is of the same order of magnitude than that of our RVE, our results support this assumption. It is worth noting that most of numerical methods devoted to simulate bone at the organ scale lean on similar assumptions.

### 2.4.3 Limitations and perspectives

Because of the nature of the two above questions, in this work we focused on the bone solid matrix of cortical bone. However, from a practical point of view, what matters are the elastic properties of the cortical tissue—*i.e.* bone matrix and Haversian pores. Therefore, the approach proposed in this work needs to be extended to the organ scale to obtain a stochastic description of the effective elastic properties of the cortical tissue. This work will be presented in the next chapter.

Because of the small size of the bone sample studied in this work, calibration and validation of RVE-scale concepts were limited. In future work, larger samples—perhaps whole organs—will be studied in order to check the reliability of our approach over large populations.

Furthermore, in this work TMD and VFs were considered as random variables. This approach neglects any spatial correlation at the organ-scale. As soon as spatial patterns exist, these

should be accounted for by modeling TMD and VFs as random-fields. Indeed, it was shown that patterns of Haversian porosity and TMD do exist in the femoral neck (Sansalone et al., 2010, 2012). Considering large bone samples will likely increase the need for moving towards this new modeling approach.

Eventually, results of this work, highlighting the relevance of images with spatial resolution compatible with clinical CT scanners, open the way to possible clinical applications. It should be noticed that the RVE-scale data used in this paper were obtained by averaging a wealth of voxel-scale data (about  $10^5$  measures per RVE). Averaging procedure reduces the noise possibly affecting the original measures, therefore leading to an increased signal-to-noise ratio (SNR) at the RVE scale. Therefore, the SNR of the *derived* RVE-scale data used in this paper is likely higher than that of *native* RVE-scale data, *i.e.* data directly measured at the RVE scale. Thus, images obtained with a spatial resolution as coarse as  $500\ \mu m$  (*i.e.*, the RVE size) will likely lead to blurrier data and increased dispersion of RVE-scale data. A good compromise might be obtained by using images with an intermediate spatial resolution. Images with spatial resolution of about  $100\ \mu m$  (which can be achieved by some clinical CT devices (Burghardt et al., 2011)) would provide more than 100 measures per RVE. Therefore, RVE-scale data obtained by averaging these measures are likely to have a sufficiently high SNR and therefore could be suitably used to compute the elastic properties of bone matrix at the tissue-scale. This is a key point which needs to be further investigated in order to move towards clinical applications of our work.

## 2.5 Appendix

### A Numerical solution of the stochastic model

#### Construction of the PDF by means of the MaxEnt principle

Let  $X$  be a random variable. The general expression of its PDF  $p_X$  maximizing the Shannon's entropy in Eq. (2.9) under the constraints in Eqs. (2.11) reads (Soize, 2004):

$$p_X(x) := I_{S_X}(x) e^{-(\lambda_0^* + \lambda_1^* x + \lambda_2^* x^2)}, \quad (2.22)$$

where  $\lambda_0^*$ ,  $\lambda_1^*$ , and  $\lambda_2^*$  are Lagrange multipliers associated to the constraints in Eqs. (2.11). Numerical values of these Lagrange multipliers can be conveniently obtained by reformulating the initial constrained maximization problem. Actually, since the Shannon's entropy has the role of a Lagrangian, the problem of maximizing the functional in Eq. (2.9) under the set of constraints in Eq. (2.12) is equivalent to finding the optimal vector of Lagrange multipliers  $\boldsymbol{\lambda}^* := [\lambda_0^*, \lambda_1^*, \lambda_2^*]$  that minimizes the corresponding Hamiltonian function  $\mathcal{H}$ , that is:

$$\boldsymbol{\lambda}^* := \arg \min_{\boldsymbol{\lambda}} \mathcal{H}(\boldsymbol{\lambda}), \quad (2.23)$$

with

$$\mathcal{H}(\boldsymbol{\lambda}) := \lambda_0 + \lambda_1 \times \mu_X + \lambda_2 \times (1 + \delta_X^2) \mu_X^2 + \int_{S_X} e^{-(\lambda_0 + \lambda_1 x + \lambda_2 x^2)} dx. \quad (2.24)$$

where  $\mu_X$  and  $\delta_X$  represent the available information (mean value and dispersion, respectively) on  $X$ .

The research of the optimal vector of Lagrange multipliers  $\boldsymbol{\lambda}^*$  has been accomplished using the built-in optimization functions of Matlab software (MATLAB, 2010). Convergence of the optimization problem depends on the initial guess of the control variable, *i.e.* the vector  $\boldsymbol{\lambda}^{(0)} = [\lambda_0^{(0)}, \lambda_1^{(0)}, \lambda_2^{(0)}]$ . A "good" initial guess can be set using a *heuristic*. For a PDF like that defined in Eq. (2.22), the proximity of the mode and the mean value of  $X$  and the integrability condition of the PDF lead to the following choice for the initial guess:

$$\begin{cases} \lambda_2^{(0)} > 0, \\ \lambda_1^{(0)} = -2 \mu_X^{\text{exp}} \lambda_2^{(0)}, \\ \lambda_0^{(0)} = \ln \left( \int_{S_X} e^{-(\lambda_1^{(0)} x + \lambda_2^{(0)} x^2)} dx \right). \end{cases} \quad (2.25)$$

Then, the problem of choosing an initial guess vector  $\boldsymbol{\lambda}^{(0)}$  reduces to choosing the initial guess of  $\lambda_2^{(0)}$  only. This choice can be guided by noticing that larger values of  $\lambda_2^{(0)}$  are associated with smaller values of the dispersion  $\delta_X$ . Therefore, a simple parametric study allows selecting a suitable value for  $\lambda_2^{(0)}$ .

## Generation of statistically independent realizations

In order to obtain a set of statistically independent realizations of the random variable  $X$ , the PDF  $p_X$  in Eq. (2.22) has been sampled using the *pseudo-inverse* method Devroye (1986). Let:

$$F_X(x) = \int_{\inf S_X}^x p_X(y) dy \quad (2.26)$$

be the *repartition function* (RF) of  $X$ . Firstly, the *pseudo-inverse*  $(F_X)^{-1}$  of the RF was numerically computed. Then,  $N$  realizations of a *uniform* random variable  $U$  with values in  $[0, 1]$  was computed, say  $U(a_i)$  with  $i = 1, \dots, N$ . Eventually,  $N$  realizations  $X(a_i)$  of  $X$  were computed as:

$$X(a_i) = (F_X)^{-1}(U(a_i)) . \quad (2.27)$$

## B Closure of the symmetry group under average operator

The concepts, we recall in the following, are borrowed from sect.14, 15, 16 of (Podio Guidugli, 2000). Classification of a linear elasticity tensor  $\mathfrak{c}$  consists in the research of the set of antisymmetric tensor  $\mathbf{Q}$  representing rotation ( $\mathbf{Q} \in Rot$ ) satisfying the relation :

$$\mathbf{Q}\mathfrak{c}\mathbf{E}\mathbf{Q}^T = \mathfrak{c}\mathbf{Q}\mathbf{E}\mathbf{Q}^T \quad \forall \mathbf{E} \in Sym \quad (2.28)$$

having  $\mathbf{E}$  the role of the symmetric part of the gradient of the deformation ( $\mathbf{E} \in Sym$ ).

For a given  $\mathfrak{c}$ , the collection  $\mathcal{G}_{\mathfrak{c}}$  of admissible  $\mathbf{Q} \in Rot$  satisfying the eq. 4.3.1 is called *symmetry group* of  $\mathfrak{c}$ . It should be proven that  $\mathcal{G}_{\mathfrak{c}}$  is a group ( we refer to sect.16 (Podio Guidugli, 2000) complete proof) but for the purposes of this article we will focus only on the closure properties of such set  $\mathcal{G}_{\mathfrak{c}}$  under the operation of sum. For this is sufficient to show that for any couple  $\mathfrak{c}, \mathfrak{d}$  of elastic tensor satisfying the 4.3.1 the sum tensor  $\mathfrak{f} := \mathfrak{c} + \mathfrak{d}$  verifies it too :

$$\begin{aligned} \mathbf{Q}(\mathfrak{c} + \mathfrak{d})\mathbf{E}\mathbf{Q}^T &= \mathbf{Q}\mathfrak{c}\mathbf{E}\mathbf{Q}^T + \mathbf{Q}\mathfrak{d}\mathbf{E}\mathbf{Q}^T = \\ &= \mathfrak{c}\mathbf{Q}\mathbf{E}\mathbf{Q}^T + \mathfrak{d}\mathbf{Q}\mathbf{E}\mathbf{Q}^T = \\ &= (\mathfrak{c} + \mathfrak{d})\mathbf{Q}\mathbf{E}\mathbf{Q}^T . \end{aligned} \quad (2.29)$$

This result allows to infer that: given the set of realizations  $\mathbb{C}(a_i)$ ,  $i = 1, \dots, N$  belonging to the same symmetry group  $\mathcal{G}_{\mathfrak{c}}$ , the stochastic estimator  $\hat{\mu}_{[\mathbb{C}]}^N$  of the mean value  $\mathbb{E}([\mathbb{C}])$ , resulting by the Kelvin's representation of  $\mathbb{C}(a_i)$ ,  $i = 1, \dots, N$  stays in the same symmetry group ( eq. ).

$$\begin{aligned} \mathbf{Q} \left( \hat{\mu}_{[\mathbb{C}]}^N \right) \mathbf{E}\mathbf{Q}^T &= \mathbf{Q} \left( \frac{1}{N} \sum_{k=1}^N \mathbb{C}(a_i) \right) \mathbf{E}\mathbf{Q}^T = \\ &= \left( \frac{1}{N} \sum_{k=1}^N \mathbb{C}(a_i) \right) \mathbf{Q}\mathbf{E}\mathbf{Q}^T \\ &= \hat{\mu}_{[\mathbb{C}]}^N \mathbf{Q}[\mathbf{E}]\mathbf{Q}^T \end{aligned} \quad (2.30)$$

In the specific context of the model presented in this work, the last result means that :

1. since the realizations  $\mathbb{C}_{MF}(a_i)$  of the *self-consistent* scheme belong to the group of symmetry of the *isotropic* class then the  $\hat{\mu}_{[\mathbb{C}_{MF}]}^N$  belongs to the *isotropic* class;

2. since the realizations  $\mathbb{C}_{UF}(a_i)$  of the *Mori-Tanaka* scheme belong to the group of symmetry of the *transverse isotropic* class ( with t.i. axe  $\mathbf{e}_3$  ) then the  $\hat{\mu}_{[\mathbb{C}_{US}]^N}$  belongs to the *transverse isotropic* class ( with t.i. axe  $\mathbf{e}_3$  ).

The preceding results justify the comparison between the characteristic elastic moduli of the same isotropic class of  $\hat{\mu}_{[\mathbb{C}_*]^N}$  of each step of the homogenization procedure presented in this work and the relative nominal model.

Finally we remark that, even than we have theoretically shown, the  $\hat{\mu}_{[\mathbb{C}_{US}]^N}$  should stay in the same isotropic class of the realizations used for calculating it, numerical approximations due to the application of homogenization schemes (SC and MT) and summation could affect the verification of the announced property. For this reason, the results shown in this work verify the condition of proximity given by the eq. (2.31) for  $\varepsilon < 10^{-13}$

$$\|\mathcal{P}\left(\hat{\mu}_{[\mathbb{C}_*]^N}\right) - \hat{\mu}_{[\mathbb{C}_*]^N}\|_F < \varepsilon \quad (2.31)$$

where  $\mathcal{P}(\mathbb{C})$  is the projection of  $\mathbb{C}$  on the vectorial space defined by the base of the isotropic group  $\mathcal{G}_c$  whom  $\mathbb{C}$  must belong to.

## C Dispersion parameter of rules of mixtures

### Derivation of the dispersion of Voigt approximation

Let  $\mathbb{c}_a^{Voigt}$  be the resulting elastic tensor of the Voigt approximation of a composite constituted by two phases having respectively elastic tensors  $\mathbb{c}_i$ ,  $i = 1, 2$  and volume fractions  $f_i$ ,  $i = 1, 2$ :

$$\mathbb{c}_a^{Voigt} = f_1 \times \mathbb{c}_1 + f_2 \times \mathbb{c}_2 \quad (2.32)$$

Let's suppose to evaluate the Voigt approximation for the random case where both volume fractions of the constituents are considered constants, but the elastic tensor of one of two phases (read  $i = 2$ ) is considered uncertain, i.e. :

$$\mathbb{C}_a^{Voigt} = f_1 \times \mathbb{c}_1 + f_2 \times \mathbb{C}_2. \quad (2.33)$$

Firstly we evaluate :

$$\begin{aligned} \mu_{[\mathbb{C}_a]} &= \mathbb{E}\{[\mathbb{C}_a]\} = f_2 \times \mu_{[\mathbb{C}_2]} + [\mathbf{d}_1] \\ \|\mu_{[\mathbb{C}_a]}\|_F^2 &= \|\mathbf{d}_1\|_F^2 + f_2^2 \times \|\mu_{[\mathbb{C}_2]}\|_F^2 + 2f_2 \times \text{tr}\{[\mathbf{d}_1] \mu_{[\mathbb{C}_2]}\} \end{aligned} \quad (2.34)$$

where we renamed  $[\mathbf{d}_1] = f_1 \times [\mathbb{c}_1]$ . Then :

$$\begin{aligned} \mathbb{E}\{\|[\mathbb{C}_a] - \mu_{[\mathbb{C}_a]}\|_F^2\} &= \mathbb{E}\left\{\text{tr}\left\{\left([\mathbb{C}_a] - \mu_{[\mathbb{C}_a]}\right)^2\right\}\right\} = \\ &= \mathbb{E}\left\{f_2^2 \times \text{tr}\left\{\left([\mathbb{C}_2] - \mu_{[\mathbb{C}_2]}\right)^2\right\}\right\} = \\ &= f_2^2 \times \mathbb{E}\left\{\text{tr}\left\{\left([\mathbb{C}_2] - \mu_{[\mathbb{C}_2]}\right)^2\right\}\right\} \end{aligned} \quad (2.35)$$

Finally :

$$\begin{aligned}
\delta_{[\mathbb{C}_a]}^2 \text{Voigt} &= \frac{\mathbb{E}\{\|[\mathbb{C}_a] - \mu_{[\mathbb{C}_a]}\|_F^2\}}{\|\mu_{[\mathbb{C}_a]}\|_F^2} = \\
&= \frac{f_2^2 \times \mathbb{E}\{\text{tr}\{([\mathbb{C}_2] - \mu_{[\mathbb{C}_2]})^2\}\}}{\|[\mathbb{d}_1]\|_F^2 + f_2^2 \|\mu_{[\mathbb{C}_2]}\|_F^2 + 2f_2 \times \text{tr}\{[\mathbb{d}_1]\mu_{[\mathbb{C}_2]}\}} = \\
&= \frac{f_2^2 \|\mu_{[\mathbb{C}_2]}\|_F^2 \times \delta_{[\mathbb{C}_2]}^2}{\|[\mathbb{d}_1]\|_F^2 + f_2^2 \|\mu_{[\mathbb{C}_2]}\|_F^2 + 2f_2 \times \text{tr}\{[\mathbb{d}_1]\mu_{[\mathbb{C}_2]}\}} = \\
&= \delta_{[\mathbb{C}_2]}^2 \times \frac{1}{1 + (\|[\mathbb{d}_1]\|_F^2 + 2f_2 \times \text{tr}\{[\mathbb{d}_1]\mu_{[\mathbb{C}_2]}\}) / f_2^2 \|\mu_{[\mathbb{C}_2]}\|_F^2} = \\
&< \delta_{[\mathbb{C}_2]}^2
\end{aligned} \tag{2.36}$$

where the fact  $\text{tr}\{[\mathbb{d}_1]\mu_{[\mathbb{C}_2]}\} > 0$  is due to the positive definiteness of the square symmetric matrices  $[\mathbb{d}_1]$  and  $\mu_{[\mathbb{C}_2]}$ . Indeed: named  $A$  and  $B$  respectively the positive square roots of  $[\mathbb{d}_1]$  and  $\mu_{[\mathbb{C}_2]}$

$$\text{tr}\{[\mathbb{d}_1]\mu_{[\mathbb{C}_2]}\} = \text{tr}\{AABB\} = \text{tr}\{(AB)^T AB\} = \sum_{ij} (AB)_{ij}^2 > 0. \tag{2.37}$$

## D Other results on TMD and VF/Vox concept

## Bibliography

- R. Blanchard, A. Dejaco, E. Bongaers, and C. Hellmich. Intravoxel bone micromechanics for microct-based finite element simulations. *J. Biomech.*, 46(15):2710–2721, 2013.
- V. Bousson, F. Peyrin, C. Bergot, M. Hausard, A. Sautet, and J.D. Laredo. Cortical bone in the human femoral neck: three-dimensional appearance and porosity using synchrotron radiation. *J. Bone Miner. Res.*, 19(5):794–801, 2004.
- J.J. Broz, S.J. Simske, and A.R. Greenberg. Material and compositional properties of selectively demineralised cortical bone. *Journal of Biomechanics*, 28(11):1357–1368, 1995.
- A.J. Burghardt, T.M. Link, and S. Majumdar. High-resolution computed tomography for clinical imaging of bone microarchitecture. *Clin. Orthop. Relat. Res.*, 469(8):2179–2193, 2011.
- J.D. Currey. The effect of porosity and mineral content on the young’s modulus of elasticity of compact bone. *Journal of Biomechanics*, 21(2):131–139, 1988.
- J.D. Currey. Measurement of the mechanical properties of bone. a recent history. *Clin. Orthop. Relat. Res.*, 467:1948–1954, 2009.
- E. Dall’Ara, B. Luisier, R. Schmidt, M. Pretterklieber, F. Kainberger, P. Zysset, and D. Pahr. Dxa predictions of human femoral mechanical properties depend on the load configuration. *Medical Engineering & Physics*, 35(11):1564–1572, 2013.
- L. Devroye. *Non Uniform Random Variate Generation*. Springer Verlag, New York, 1986.
- P. Fratzl, N. Fratzl-Zelman, and K. Klaushofer. Collagen packing and mineralization. an x-ray scattering investigation of turkey leg tendon. *Biophysical Journal*, 64(1):260–266, 1993.
- M. Granke, Q. Grimal, W.J. Parnell, K. Raum, A. Gerisch, F. Peyrin, A. Saïed, and P. Laugier. To what extent can cortical bone millimeter-scale elasticity be predicted by a two-phase composite model with variable porosity? *Acta Biomaterialia*, 12:207–215, 2015.
- Q. Grimal, K. Raum, A. Gerisch, and P. Laugier. A determination of the minimum sizes of representative volume elements for the prediction of cortical bone elastic properties. *Biomech. Model. Mechanobiol.*, 10(6):925–937, 2011.
- C. Hellmich, J. Barthelemy, and L. Dormieux. Mineral-collagen interactions in elasticity of bone ultrastructure - a continuum micromechanics approach. *European Journal of Mechanics - A/Solids*, 23:783–810, 2004.
- C. Hellmich, C. Kober, and B. Erdmann. Micromechanics-based conversion of ct data into anisotropic elasticity tensors, applied to fe simulations of a mandible. *Ann Biomed Eng*, 23: 783–810, 2008.
- E.T. Jaynes. Information theory and statistical mechanics. *Physical Review*, 106(4):620–630, 1957a.

- E.T. Jaynes. Information theory and statistical mechanics. *Physical Review*, 108(2):171–190, 1957b.
- S.P. Kotha and N. Guzelsu. The effects of interphase and bonding on the elastic modulus of bone: changes with age-related osteoporosis. *Medical Engineering & Physics*, 22(8):575–585, 2000.
- X. Li, M. Viceconti, M.C. Cohen, G.C. Reilly, M.J. Carré, and A.C. Offiah. Developing ct based computational models of pediatric femurs. *Journal of Biomechanics*, 48(10):2034–2040, 2015.
- MATLAB. *version 7.11 (R2010b)*. The MathWorks Inc., Natick, Massachusetts, 2010.
- S. Nuzzo, F. Peyrin, P. Cloetens, J. Baruchel, and G. Boivin. Quantification of the degree of mineralization of bone in three dimensions using synchrotron radiation microtomography. *Med. Phys.*, 29(11):2672–2681, 2002.
- D.H. Pahr and P.K. Zysset. Finite element-based mechanical assessment of bone quality on the basis of in vivo images. *Current Osteoporosis Reports*, (First Online):1–12, 2016. DOI: 10.1007/s11914-016-0335-y.
- W. J. Parnell, M. B. Vu, Q. Grimal, and S. Naili. Analytical methods to determine the effective mesoscopic and macroscopic elastic properties of cortical bone. *Biomech Model Mechanobiol*, 39(21):5659–5678, 2011.
- P. Podio Guidugli. *A Primer in Elasticity*. Springer Netherlands, 2000.
- P. Pottecher, K. Engelke, L. Duchemin, O. Museyko, T. Moser, D. Mitton, E. Vicaut, J. Adams, W. Skalli, J.D. Laredo, and V. Bousson. Prediction of hip failure load: In vitro study of 80 femurs using three imaging methods and finite element models-the european fracture study (effect). *Radiology*, 2016. Online, DOI: <http://dx.doi.org/10.1148/radiol.2016142796>.
- M. Predoi-Racila and J. M. Crolet. Human cortical bone: the sinupros model. *Comput. Methods Biomech. Biomed. Engin.*, 11(2):169–187, 2008.
- J.Y. Rho, L. Kuhn-Spearing, and P. Zioupos. Mechanical properties and the hierarchical structure of bone. *Medical Engineering & Physics*, 20(2):92–102, 1998.
- V. Sansalone, S. Naili, V. Bousson, C. Bergot, F. Peyrin, J. Zarka, J.-D. Laredo, and G. Haiat. Determination of the heterogeneous anisotropic elastic properties of human femoral bone: from nanoscopic to organ scale. *J. Biomech.*, 43(10):1857–1863, 2010.
- V. Sansalone, V. Bousson, S. Naili, C. Bergot, F. Peyrin, J.-D. Laredo, and G. Haiat. Anatomical distribution of the degree of mineralization of bone tissue in human femoral neck: impact on biomechanical properties. *Bone*, 50(4):876–884, 2012.
- V. Sansalone, S. Naili, and C. Desceliers. A stochastic homogenization approach to estimate bone elastic properties. *Comptes Rendus Mecanique*, 342(5):326–333, 2014.

- V. Sansalone, D. Gagliardi, C. Desceliers, V. Bousson, J.D. Laredo, F. Peyrin, G. Haïat, and S. Naili. Stochastic multiscale modelling of cortical bone elasticity based on high-resolution imaging. *Biomech. Model. Mechanobiol.*, 15(1):111–131, 2016.
- C. Shannon. A mathematical theory of communication. *Tech. J.* 27, Bell Syst., 1948.
- Simpleware 5.0 ScanIP+. *version 5.0*. Simpleware Ltd, Exeter, UK, 2012.
- C. Soize. Maximum entropy approach for modeling random uncertainties in transient elastodynamics. *Journal of the Acoustical Society of America*, 109(5):1979–1996, 2001.
- C. Soize. Probabilités et Modélisation des incertitudes. Eléments de base et concepts fondamentaux. Lecture notes, 2004.
- C. Soize and R. Ghanem. Physical systems with random uncertainties: chaos representations with arbitrary probability measure. *SIAM J. Sci. Comput.*, 26:395–410, 2004.
- A. Suvorov and G. Dvorak. Rate form of the eshelby and hill tensors. *International Journal of Solids and Structures*, 2002.
- B. van Rietbergen and K. Ito. A survey of micro-finite element analysis for clinical assessment of bone strength: The first decade. *J. Biomech.*, 48(5):823–841, 2015.
- A.A. Zadpoor and H. Weinans. Patient-specific bone modeling and analysis: The role of integration and automation in clinical adoption. *J. Biomech.*, 48(5):750–760, 2015.
- P.K. Zysset, E. Dall’Ara, P. Varga, and D.H. Pahr. Finite element analysis for prediction of bone strength. *BoneKEY Reports*, 2(386), 2013.

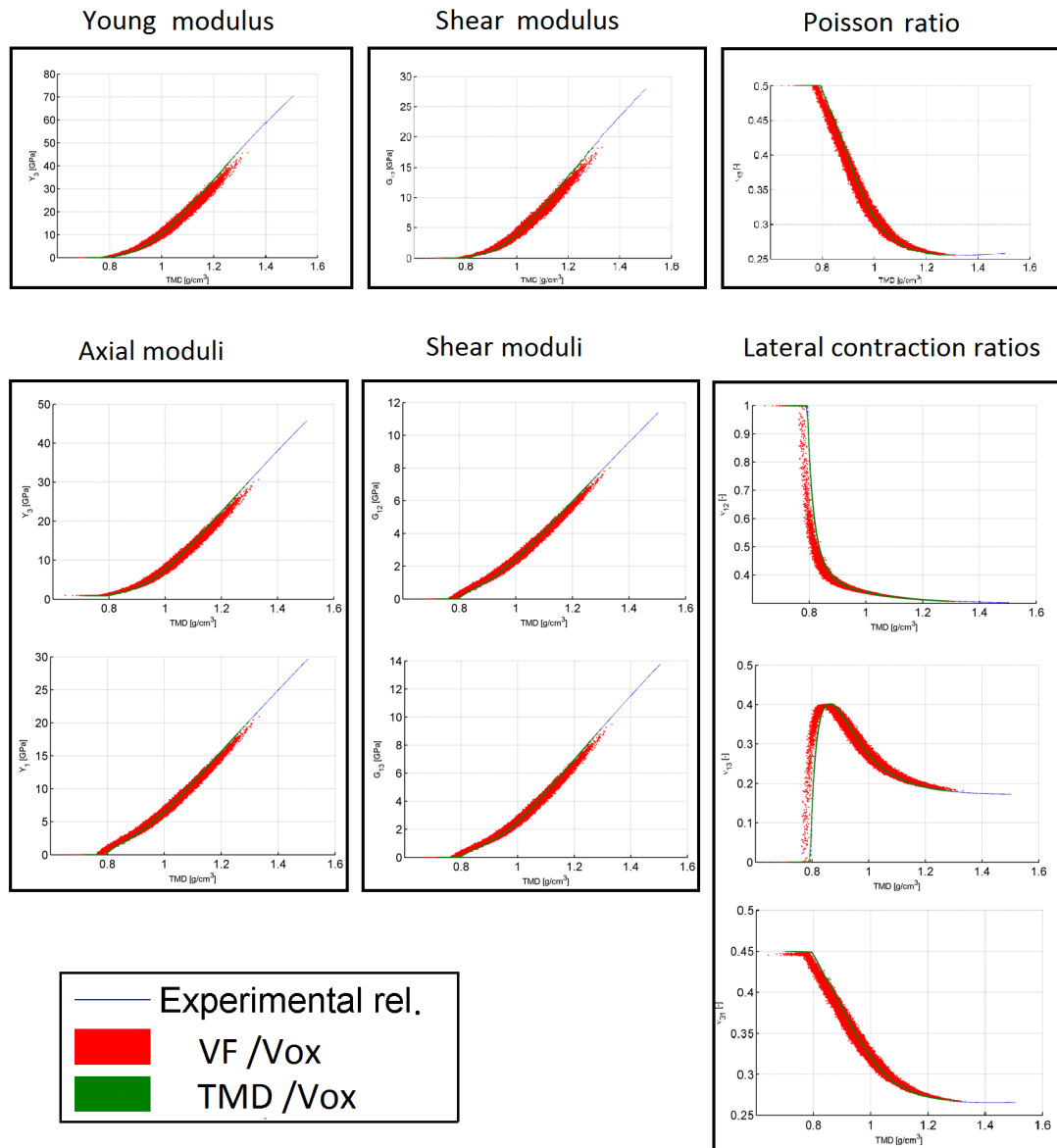


Figure 2.17: Elastic moduli of the resulting isotropic model mineral foam and of transverse isotropic model of ultra-structure.

## Chapter 3

# Estimation of bone-elasticity. *A priori* influence of the couple TMD-HP by a model based on $\mu$ CT Imaging. A multi-techniques validation.

---

D. Gagliardi, V. Sansalone, C. Desceliers and S. Naili. Estimation of bone-elasticity. *A priori* influence of the couple TMD-HP by a model based on  $\mu$ CT Imaging. A multi-techniques validation. *European Journal of Mechanics - A/Solids*, (submitted) Mar. 2017.

---

## Abstract

In previous chapter, we proposed a stochastic model to describe the elasticity of bone matrix (so-called ultrastructure, US) based on basic statistical information on the *tissue mineral density* (TMD). This information was obtained by analyzing high-resolution images of a human femoral neck realized by means of synchrotron radiation micro-computed tomography (SR –  $\mu$ CT). In this chapter, we extend this study by focusing at the upper scale where cortical bone is described as a two-phase mixture made up of water-filled Haversian pores (HP) embedded in the surrounding solid US. The goal of this work is to develop a stochastic model of cortical bone elasticity accounting for the effect of uncertainty affecting both phases, the US *via* the TMD and the HP.

Experimental information was assumed to be given in terms of mean values and dispersions of the average TMD (denoted  $\overline{\text{TMD}}$ ) and HP at the millimeter scale. To this aim, SR –  $\mu$ CT images were used to extract several representative volume elements (RVEs) spanning the whole cortical tissue which, in turn, were analyzed to obtain the required statistical information on  $\overline{\text{TMD}}$  and HP. This information has been used for constructing a stochastic multiscale model of cortical bone based on the Maximum Entropy (denoted MaxEnt) principle. This stochastic multiscale model is used in the estimation of the effective elastic properties of cortical bone (CB-S $\mu$ M) based on continuum micromechanics ( $\mu$ M). In parallel, a deterministic nominal multiscale model of cortical bone (CB-N $\mu$ M) was developed by using as input data the mean values of  $\overline{\text{TMD}}$  and HP. The elastic moduli estimated with CB-N $\mu$ M has been compared with the average value of the same counterpart obtained with the CB-S $\mu$ M model. The two estimates differ for less than 1%, proving the robustness of the CB-S $\mu$ M model. Moreover, the accuracy of the S $\mu$ M stochastic model has been tested. Estimations of the cortical bone elasticity of each RVE with the  $\mu$ M (cylindrical HP and homogeneous US), has been compared with other estimation obtained through others homogenization techniques: *finite elements* (FEM) and *fast Fourier transform* (FFT), both able to account for the real morphology of Havesian porosity and the heterogeneity of the ultrastructure. Results show that: 1- the transverse isotropic (TI) elastic  $\mu$ M model correctly approximates the FEM and FFT estimates ( $\sim 98\%$  TI); 2- the  $\mu$ M model accurately estimates the axial modulus ( $Y_3$ ) in longitudinal direction and the lateral contraction ratio  $\nu_{31}$ .

### 3.1 Introduction

Assessment of mechanical properties of bone *in vivo* represents a challenging and complex problem because of the hierarchical and heterogeneous structure of bone material as well as for its capability to adapt its material properties to the superimposed mechanical and biochemical *stimuli* (Cowin, 2001).

Zooming from the organ scale down, bone elementary components (basically collagen, mineral, and water) give rise to different structural patterns. Aiming at predicting the overall behavior of bone, several methods have been proposed to account for this hierarchical structure such as homogenization methods (Crolet et al., 1993; Racila and Crolet, 2007; Parnell et al., 2011; Rohan et al., 2012) mean-field approximations (Parnell et al., 2011; Hellmich et al., 2004), Finite Element (FE) numerical simulations (Barkaoui and Hambli, 2011, 2014) and many others.

All these methods require information about the constitutive behavior, relative amount and spatial arrangement of the structural units at each scale considered in the description of bone. Although this information can be obtained *in vitro* using different techniques (mechanical testing, chemical analysis, imaging) with a relatively high level of accuracy, it is still challenging to access detailed information about the microstructural organization of bone *in vivo*. Since reliability of model predictions rely on the accuracy of input data, the issue of dealing with uncertain data becomes of main importance in view of clinical applications. Moreover, in the framework of a computer-aided, patient-specific analysis, not only *accuracy* and *reliability* but also *simplicity* and *elaboration time* should be accounted for. In this context, it does make sense to develop a reliable, fast and easy-to-use model using minimal information about patient-specific bone microstructure.

Restricting our interest to modeling bone elasticity, analytical and semi-analytical methods often make use of a simplified description of bone in terms of morphology (structural units can be described by simple geometrical entities such as spheres, cylinders, ellipsoids, *etc.*) and elastic symmetry of its essential constituents (mineral is often modeled as an isotropic material, water as a compressible fluid, and collagen as either an isotropic or transversely isotropic material). Starting from these “universal” morphological and constitutive assumptions, the spatial heterogeneity of elastic properties of bone is described in terms of the relative amounts of its essential constituents. These approaches lead to relatively easy-to-use and time-efficient models which also proved to be accurate as long as input data (relative amount of bone constituents) are known. However, being inherently deterministic in nature, these models cannot provide any clue about the reliability of their predictions nor on the effects of uncertainty possibly affecting the input data or the model assumptions.

As far as we know, the effects of uncertain morphology of bone microstructure has not been investigated so far. Recently, Sansalone et al. (2014) discussed the issue of uncertain elastic properties of bone constituents at the nanoscale and propagated this uncertainty upwards to quantify its effects on the elastic properties of the bone solid matrix (so-called ultrastructure, US). Another pretty unexplored issue concerns the interfaces between different structural units, which are commonly assumed to be in perfect adhesion.

The issue of bone composition, related to the spatial heterogeneity and distribution of bone, seems to have received more attention in the biomechanical community. For instance, it has

been shown that bone mineralization density distribution (BMDD) is a reliable fingerprint of the health state of bone (Ruffoni et al., 2007). Assessing bone composition at microstructural scales requires experimental devices with suitable spatial resolution. In this context, X-ray based methods occupy a central place in clinics—where Dual-energy X-ray absorptiometry (DXA) is still the golden standard to diagnose and follow osteoporosis—as well as in research—where different types of micro-computed tomography ( $\mu$ CT) can be used to reveal tiny details of bone micro- and nano-structure. These methods can detect the attenuation of a radiative source due to the absorption of an interposed medium. In bone, attenuation is basically related to the mineral density. Synchrotron radiation  $\mu$ CT (SR- $\mu$ CT) is nowadays the more reliable technology to inspect bone morphology and composition at the micro- and nano-scale *in vitro* (Apostol et al., 2006; Langer et al., 2012). Last generation  $\mu$ CT devices also allow qualitative and quantitative assessment of bone at the micro-scale *in vitro* and, to a limited extent, *in vivo* (Burghardt et al., 2011). Due to X-ray dose limitations, *in vivo* human imaging has a spatial resolution limited to about one hundred micrometers and is restricted to analysis of structural parameters. These limitations make it impossible to obtain accurate information on bone composition at sub-millimeter scales *in vivo* and call for new modeling approaches capable to account for uncertain input data.

Our group has recently started investigating the propagation of uncertainty related to bone composition through the scales (Sansalone et al., 2016). Adopting the simplified representation of bone proposed in Sansalone et al. (2010), uncertain bone composition was assumed to be known in terms of statistics (mean value and dispersion) of volume fractions (VFs) computed from experimental data at the scale of about ten micrometers. Uncertain VFs were modeled as random variables and their stochastic models were obtained by means of the Maximum Entropy (MaxEnt) principle. Eventually, random VFs were introduced in a micromechanical model to compute statistics of bone elastic *moduli* of the cortical bone. These statistics turned out to overestimate the actual elastic *moduli*. In further work (Gagliardi et al., 2016 (submitted)), it was shown that the elastic coefficients of bone US are better represented by using the Tissue Mineral Density (TMD) to describe bone composition and using experimental data at the scale of several hundreds micrometers (that is, the size of the Representative Volume Element, RVE, of cortical bone). The average TMD at this scale was referred to as  $\overline{\text{TMD}}$ . In here, we aim at extending this analysis by investigating the propagation of uncertainty up to the tissue scale. Specifically, the stochastic model of US defined as *TMD/RVE concept* in (Gagliardi et al., 2016 (submitted)) is combined with a stochastic model of the Haversian porosity (HP) in order to obtain a stochastic micromechanical model of the cortical bone.

The purpose of this work is manifold:

- To analyze the combined effect of the variations of the pair (HP,  $\overline{\text{TMD}}$ ) on the elasticity of cortical bone;
- To validate the stochastic micromechanical model by comparison with more refined numerical models.

The first goal was achieved by using the pair (HP,  $\overline{\text{TMD}}$ ) to describe bone composition. Both

HP and  $\overline{\text{TMD}}$  were modeled as statistically independent random variables and their probability density functions (PDFs) were obtained by means of the MaxEnt principle fed with experimental statistical information (mean value and dispersion) at the tissue scale. This information has been estimated by analyzing a set of RVEs issued from SR –  $\mu$ CT images of the inferior femoral neck of an elderly patient. Eventually, the stochastic micromechanical model described in this work results from introducing this stochastic description of the pair (HP,  $\overline{\text{TMD}}$ ) in the micromechanical model proposed by Sansalone et al. (2010).

The second goal was achieved by comparing the statistics of the elastic *moduli* of cortical bone predicted by the stochastic micromechanical model with the elastic *moduli* of actual RVEs computed using detailed microstructural models based on the Finite Element Method ( $\mu$ FE) (Crolet et al., 1993; Granke et al., 2015) and on the Fast Fourier Transform ( $\mu$ FFT) (Moulinec and Suquet, 1998; Brisard and Dormieux, 2010; Monchiet and Bonnet, 2012; Monchiet, 2015). Both these models can account for the actual pore morphology and heterogeneity of bone RVEs, which have been set up accounting the morphology of the Haversian porosity and the variability of the solid matrix existent in the reference  $\mu$ CT dataset.

After this introduction on the rationale for studying the estimations of bone elasticity, the chapter is organized as follows. First, Sec. 3.2 describes the materials and methods employed in this study. The section starts with discussing our experimental data on bone composition and the related statistical information; then, an overview of some techniques providing the effective elastic properties of an heterogeneous material is presented, namely continuum micromechanics, FEM and FFT method. Eventually, several micromechanical and microstructural models of cortical bone elasticity are presented, including a new stochastic micromechanical model based on (HP,  $\overline{\text{TMD}}$ ) is detailed. Then, Sec. 3.3 is devoted to describing the results obtained through all these models. The results of the stochastic model are presented first. The effects of the gray-level threshold chosen to separate HP from US in the SR –  $\mu$ CT images are then investigated. Eventually, results of microstructural models based on the FEM and FFT method are presented and compared with those of the stochastic model. Finally, Sec. 3.4 draws the conclusions of this work and set the way ahead for future research.

## 3.2 Material and Methods

### 3.2.1 Hierarchical description of cortical bone

A four-scale description of cortical bone was proposed in (Sansalone et al., 2010). Below the organ scale, at the scale of several hundreds micrometers (tissue scale), cortical bone (CB) was considered as constituted of Haversian pores (HP) embedded in a solid matrix called ultrastructure (US). At the scale of a few tens micrometers (US scale), US was considered as made up of collagen (Col) fibers embedded in a mineral foam (MF). Eventually, at the scale of several tens nanometers (referred to as MF scale), MF was considered as a mixture of mineral (HA for Hydroxyapatite) and water (W). The model is depicted in Fig. 3.1.

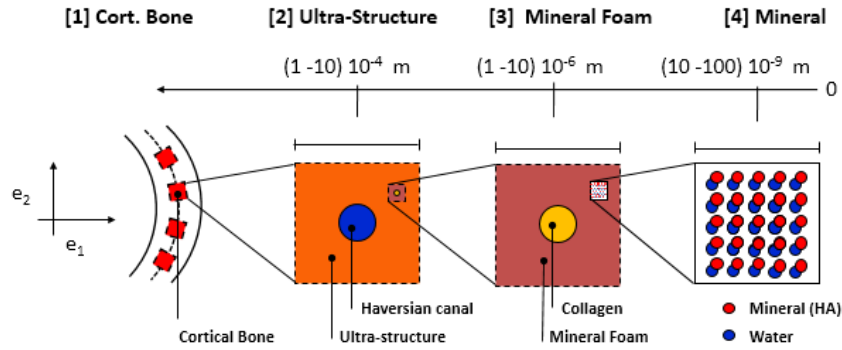


Figure 3.1: Multi-scale description of cortical bone.

### 3.2.2 What information on cortical bone from $\mu$ CT?

Gray levels (GL) in  $\mu$ CT images are related to the linear attenuation coefficient (LAC) of the X-ray beam passing through an interposed medium. The LAC is the fraction of attenuated incident photons per unit thickness of a material. In bone, attenuation is basically due to the mineral whereas the contribution of collagen and water is negligible. Therefore, the intensity of the LAC is related to the tissue mineral density (TMD) (see Fig. 3.2). An affine relationship exists between GL in SR- $\mu$ CT images and TMD of bone, reading:

$$\text{TMD} = \widehat{\text{TMD}}(\text{GL}) = c_0 + c_1 \times \text{GL}, \quad (3.2.1)$$

where TMD designates the value of the affine function  $\widehat{\text{TMD}}(\text{GL})$  for the value GL, coefficients  $c_0$  and  $c_1$  depend on the specific imaging device and have to be calibrated with respect to phantoms of known composition. In this study, coefficients  $c_0$  and  $c_1$  are given by Nuzzo et al. (2002):

$$c_0 = -\frac{0.5082}{3.319} \quad \text{and} \quad c_1 = \frac{5.5}{255 \times 3.319}. \quad (3.2.2)$$

By inspecting a typical SR- $\mu$ CT image, it is possible to distinguish regions corresponding to Haversian porosity (HP) and ultrastructure (US). By fixing a threshold  $q$  for the GLs of the HP, the whole range of GLs,  $\mathcal{GL} := [0, 255]$ , can be split into the ranges of GLs referring to HP and US voxels:  $\mathcal{GL}_{\text{HP}} := [0, q]$  and  $\mathcal{GL}_{\text{US}} := [q, 255]$ , respectively. Then, two pieces of information are embedded in quantitative  $\mu$ CT images, *i.e.* the mineralization of the ultrastructure obtained through Eq. (3.2.1) and the value of the HP (relative number of voxels having a GL given by  $gl_i$  in  $\mathcal{GL}_{\text{HP}}$ ):

$$\text{HP} = \frac{\sum_i \mathbb{1}_{\mathcal{GL}_{\text{HP}}}(gl_i)}{\sum_i \mathbb{1}_{\mathcal{GL}}(gl_i)}, \quad (3.2.3)$$

where  $\mathbb{1}_{\mathcal{I}}(x)$  represents the characteristic function of the set  $\mathcal{I}$ . Furthermore, tracing the probability density function (PDF) of the realizations of the grey levels GL, it is noticeable that the HP is approximated by the area under the PDF(GL) restricted to the domain  $\text{GL} \leq q$ , (*i.e.*  $\text{HP} \sim \mathbb{P}(\text{GL} \leq q)$ ).

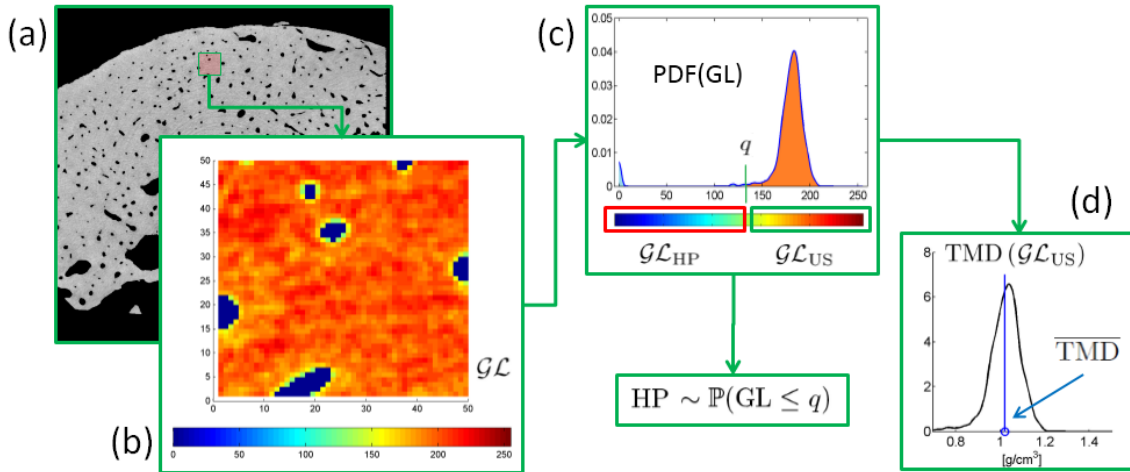


Figure 3.2: Experimental information obtained from SR- $\mu$ CT images. (a) Typical graylevel cross section; Haversian porosity (HP) and ultrastructure (US) correspond to black and gray regions, respectively. (b) Typical RVE, *i.e.* cubic region with edge length of 50 voxels  $\sim$  0.5 mm; GLs are represented using the “jet” color-map of Matlab. (c) GL distribution in the RVE and threshold  $q$  between HP and US. (d) TMD distribution in the US and average value  $\overline{TMD}$ .

It is worth noting that HP and TMD are defined at different scales. On the one side, HP is defined at the tissue scale and was measured on a RVE-wise basis (see inset (b) in Fig. 3.2 depicting a typical RVE is taken as a cubic region with edge length = 50 voxels  $\sim$  0.5 mm). On the other side, TMD is defined at the US scale and was measured on a voxel-wise basis (see inset (d) in Fig. 3.2, voxel size = 10.13  $\mu$ m). Moreover, starting from the TMD distributions of each RVE, tissue-scale average values of TMD, denoted  $\overline{TMD}$ , can be computed. Therefore, the pair (HP,  $\overline{TMD}$ ) collects experimental measures referring at the tissue scale.

### 3.2.3 Experimental data from SR – $\mu$ CT imaging

Experimental data are collected using the protocol described in our previous studies (Gagliardi et al., 2016 (submitted); Sansalone et al., 2016). For sake of completeness, the main steps are reported here below.

A bone sample, extracted from the inferior femoral neck of a 79-year-old patient undergoing standard hemiarthroplasty, has been imaged using synchrotron radiation micro-computed tomography (SR –  $\mu$ CT) at the European Synchrotron Radiation Facility (ESRF, Grenoble, France). Image reconstruction was performed in a *volume of interest* (VoI) of  $660 \times 660 \times 523$  isotropic voxels (size 10.13  $\mu$ m). The outcome was a 3-D GL mapping (GL range: [0, 255]) of the linear attenuation coefficient of the monochromatic X-ray beam. Regions corresponding to Haversian pores (HP) and ultrastructure (US) were identified by fixing a lower threshold  $q = 131$  for US voxels (see Sec. 3.2.2 for more details).

After segmentation of the bone sample with Simpleware ScanIP software (Simpleware 5.0 ScanIP+, 2012) 35 representative volume elements (RVEs) were selected in the cortical part of

the VoI spanning the sample in the axial and hoop direction. Following Sansalone et al. (2016), RVEs were taken as cubic regions with edge length of  $N_{\text{vox}} = 50$  voxels, *i.e.* about  $0.5 \text{ mm}$ . 3-D models of the RVEs were extracted from the bone sample at about  $1.5 \text{ mm}$  from the periosteum (distance measured with respect to the center of the RVEs) and at different hoop and axial positions with respect to a cylindrical frame centred at the anatomical axis of the bone sample, avoiding volume overlapping. The global reference frame on the bone sample, the local reference frame on a RVE and the location of the RVEs are presented in Fig. 3.3. For the global reference, the unit vector  $\mathbf{e}_3$  is aligned with the axis of the femoral neck and the unit vectors  $\mathbf{e}_1$  and  $\mathbf{e}_2$  lie in the plane of the cross section of the sample. For the local reference, the first axis  $\mathbf{e}_t$  is aligned to the tangential direction formed by the circumferential line (see Fig. 3.3), the second axis  $\mathbf{e}_r$  is oppositely aligned to the radial vector of the sample and the third axis  $\mathbf{e}_z$  is aligned to  $\mathbf{e}_3$  of the global reference. The origin of the local frame is placed at the center of the RVE. Coordinates  $x_3$  and  $\theta$  refer to the axial and hoop coordinates of the centers of the RVEs, respectively. The axial coordinate  $x_3$  is the distance of the center of the RVE from the distal part of the sample ( $x_3 = 0$ ). The hoop coordinate  $\theta$  is the angle measured counterclockwise with respect to the inferior axis of the sample ( $\theta = 0$ ). We refer to Gagliardi et al. (2016 (submitted)) for a more detailed picture of these RVEs. The complete dataset, statistically representing the whole VoI, has been divided in two parts. A calibration subset (*Calib* dataset, red RVEs in Fig. 3.3) consisting of 12 RVEs, has been used to obtain input data (statistics of HP and TMD) for the stochastic and nominal models (see Sec. 3.2.4). The remaining 23 RVEs have been used for validation purposes (*Ctrl* dataset, light red RVEs in Fig. 3.3). The complete dataset has been used to build microstructural  $\mu\text{FE}$  and  $\mu\text{FFT}$  models.

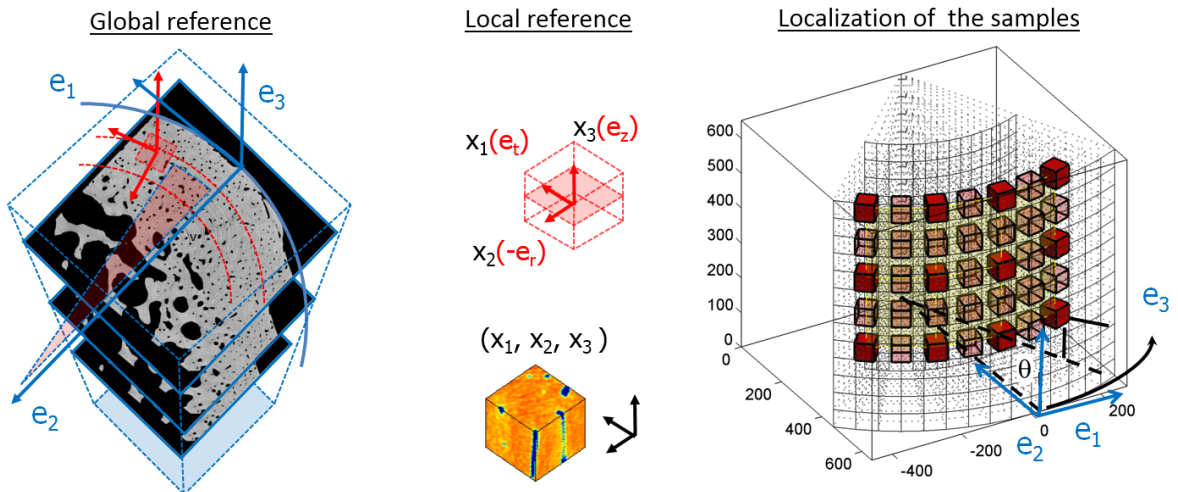


Figure 3.3: Global and local reference frames on the bone sample and on a typical RVE, respectively, and localization of the RVEs (red and light red cubes refer to *Calib* and *Ctrl* datasets, respectively). See text for more details.

### 3.2.4 Statistical information on HP and $\overline{\text{TMD}}$ from SR – $\mu$ CT images

Information on the composition of the cortical tissue was obtained by analyzing the *Calib* dataset of RVEs. This dataset constitutes a systematic sampling of the overall population of cortical RVEs and was used to estimate the statistics (namely, mean value and dispersion) of HP and  $\overline{\text{TMD}}$  in the cortical tissue. A database consisting of RVE-wise pairs (HP,  $\overline{\text{TMD}}$ ) was constituted. Within each RVE, the HP and the voxel-wise distribution of TMD were computed by means of Eqs. (3.2.1)-(3.2.3). Then, the voxel-wise distribution of TMD was averaged to compute  $\overline{\text{TMD}}$ .

Statistics (namely, mean value, standard deviation, and dispersion) of the database of (HP,  $\overline{\text{TMD}}$ ) RVE-wise values were computed and assumed to be representative of the tissue-scale composition of the whole cortical tissue. In the framework of a *parametric probabilistic* approach, the uncertainty on a measured variable real-valued random variable  $X$ . Hereafter, capital letters will refer to random variables. Let  $X$  be either of HP or  $\overline{\text{TMD}}$ , and let  $\mu_X^{\text{exp}}$ ,  $\sigma_X^{\text{exp}}$  and  $\delta_X^{\text{exp}}$  be the set of *known statistics* (the mean value, standard deviation, and dispersion of  $X$ , respectively). Their values were estimated through the respective stochastic estimators  $\hat{\mu}_X^N$ ,  $\hat{\sigma}_X^N$  and  $\hat{\delta}_X^N$ , reading:

$$\begin{aligned}\hat{\mu}_X^N &= \frac{1}{N} \sum_{k=1}^N x_k, \\ \hat{\sigma}_X^N &= \left[ \frac{1}{N-1} \sum_{k=1}^N (x_k - \hat{\mu}_X^N)^2 \right]^{\frac{1}{2}}, \\ \hat{\delta}_X^N &= \frac{\hat{\sigma}_X^N}{\hat{\mu}_X^N},\end{aligned}\tag{3.2.4}$$

where  $x_i$  is the  $i$ -th experimental measure of  $X$  and  $N$  is the number of measures. As long as measures  $x_i$  are statistically representative of the whole cortical tissue, descriptive statistics in Eq. (3.2.4) provide an accurate estimate of the overall experimental statistics:

$$\mu_X^{\text{exp}} \sim \hat{\mu}_X^N, \quad \sigma_X^{\text{exp}} \sim \hat{\sigma}_X^N, \quad \text{and} \quad \delta_X^{\text{exp}} \sim \hat{\delta}_X^N.\tag{3.2.5}$$

### 3.2.5 Volume fractions of essential constituents

The measures of HP and  $\overline{\text{TMD}}$  have been used to compute the (average) volume fractions (VFs) of each phase at each level of the hierarchical description of bone introduced in Sec. 3.2.1. The procedure was already described in Gagliardi et al. (2016 (submitted) and is summarized here below for sake of completeness.

**CB-scale.** Within each RVE of cortical bone (CB), the VF of HP (denoted by  $\phi_{\text{HP}}^{\text{CB}}$ ) was computed as the relative number of voxels with  $\text{GL} \in \mathcal{GL}_{\text{HP}}$  (see Eq. (3.2.3)). Then, the VF of the ultrastructure (US) turns out to be:  $\phi_{\text{US}}^{\text{CB}} = 1 - \phi_{\text{HP}}^{\text{CB}}$ .

**US-scale.** VFs of hydroxyapatite (HA), collagen (Col), and water (W) in the ultrastructure (US)  $\phi_{\text{HA}}^{\text{US}}$ ,  $\phi_{\text{Col}}^{\text{US}}$ , and  $\phi_{\text{W}}^{\text{US}}$ , respectively—were computed from  $\overline{\text{TMD}}$  by solving the nonlinear system (Broz et al., 1995):

$$\begin{cases} \phi_{\text{HA}}^{\text{US}} = \frac{\overline{\text{TMD}}}{\rho_{\text{HA}}}, \\ \phi_{\text{HA}}^{\text{US}} + \phi_{\text{Col}}^{\text{US}} + \phi_{\text{W}}^{\text{US}} = 1, \\ \frac{\phi_{\text{Col}}^{\text{US}}}{\phi_{\text{W}}^{\text{US}}} = \alpha + \beta \times \exp(\gamma \times \phi_{\text{HA}}^{\text{US}}), \end{cases}\tag{3.2.6}$$

where  $\alpha = 0.36$ ,  $\beta = 0.084$  and  $\gamma = 6.7$  (see Broz et al. (1995)). First,  $\phi_{\text{HA}}^{\text{US}}$  was directly computed by dividing  $\overline{\text{TMD}}$  by the mass density of the mineral ( $\rho_{\text{HA}} = 3 \text{ g/cm}^3$ ), *i.e.* (3.2.6)/1. Then,  $\phi_{\text{Col}}^{\text{US}}$  and  $\phi_{\text{W}}^{\text{US}}$  are computed by supplementing the volume balance equation (see Eq. (3.2.6)/2) with an empirical relation (see Eq. (3.2.6)/3) proposed by Broz et al. (1995).

**MF-scale.** VFs of mineral and water in the mineral foam (MF) have been evaluated from their counterparts at the US scale by simply preserving their relative amount after downscaling:

$$\begin{cases} \phi_{\text{HA}}^{\text{MF}} = \frac{\phi_{\text{HA}}^{\text{US}}}{(\phi_{\text{HA}}^{\text{US}} + \phi_{\text{W}}^{\text{US}})}, \\ \phi_{\text{W}}^{\text{MF}} = \frac{\phi_{\text{W}}^{\text{US}}}{(\phi_{\text{HA}}^{\text{US}} + \phi_{\text{W}}^{\text{US}})}. \end{cases} \quad (3.2.7)$$

Bone composition at the US and MF scales is fully described by  $\phi_{\text{Col}}^{\text{US}}$  and  $\phi_{\text{HA}}^{\text{MF}}$ , respectively. These VFs are both computed from  $\overline{\text{TMD}}$  by solving Eq. (3.2.6) and Eq. (3.2.7) which can be restated implicitly as:

$$\phi_{\text{Col}}^{\text{US}} = \hat{\phi}_{\text{Col}}^{\text{US}}(\overline{\text{TMD}}), \quad \phi_{\text{HA}}^{\text{MF}} = \hat{\phi}_{\text{HA}}^{\text{MF}}(\overline{\text{TMD}}). \quad (3.2.8)$$

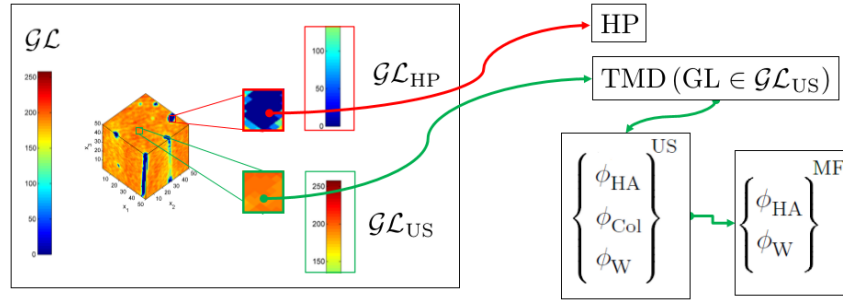


Figure 3.4: Sketch of the procedure for evaluating the HP,  $\overline{\text{TMD}}$ , and VFs in a RVE.

### 3.2.6 Overview on the homogenization

Homogenization is concerned with the problem of computing the effective mechanical properties of an heterogeneous medium. Restricting our attention to linearly elastic materials occupying a representative volume element (RVE), the problem can be stated as follows.

Let  $\Omega$  be the region of the three-dimensional space occupied by the RVE,  $\mathbb{c}(\mathbf{x})$  ( $\mathbf{x} \in \Omega$ ) the 4th-order elastic tensor field describing the point-wise elastic properties of the heterogeneous material. Thus, the point-wise constitutive relation reads:

$$\mathbf{S}(\mathbf{x}) := \mathbb{c}(\mathbf{x}) : \mathbf{E}(\mathbf{x}), \quad (3.2.9)$$

where the symbol “:” between two tensors denotes a double contraction of adjacent indexes of any couple of tensors,  $\mathbf{S}(\mathbf{x})$  is the 2nd-order *stress tensor* field and  $\mathbf{E}(\mathbf{x})$  is the 2nd-order

*infinitesimal strain tensor* field, that is the symmetric part of the gradient of the *displacement* field  $\mathbf{u}(\mathbf{x})$ :

$$\mathbf{E}(\mathbf{x}) := \text{Sym}(\nabla \mathbf{u}(\mathbf{x})) \equiv \frac{\nabla \mathbf{u}(\mathbf{x}) + (\nabla \mathbf{u}(\mathbf{x}))^T}{2}. \quad (3.2.10)$$

where  $\nabla$  is the gradient operator,  $(\star)^T$  is the transpose operator and  $\text{Sym}(\star)$  is the symmetry operator as defined by the relation (3.2.10).

Moreover, let  $\mathbf{S}^*$  and  $\mathbf{E}^*$  be the spatial averages of  $\mathbf{S}(\mathbf{x})$  and  $\mathbf{E}(\mathbf{x})$ , respectively, that is:

$$\mathbf{S}^* := \langle \mathbf{S}(\mathbf{x}) \rangle_{\Omega}, \quad \mathbf{E}^* := \langle \mathbf{E}(\mathbf{x}) \rangle_{\Omega}, \quad \langle \star \rangle_{\Omega} := \frac{1}{|\Omega|} \int_{\Omega} [\star](\mathbf{x}) \, d\mathbf{x}. \quad (3.2.11)$$

Then, the *homogenization problem* consists in looking for a 4th-order elastic tensor  $\mathfrak{c}^*$  such that:

$$\mathbf{S}^* = \mathfrak{c}^* : \mathbf{E}^*, \quad \text{for all admissible pair } (\mathbf{S}^*, \mathbf{E}^*) \quad (3.2.12)$$

In the above statement, admissibility of average stress and strain refers to the underlying stress and strain fields which are required to be the solution of the boundary value problem (BVP) at the RVE scale:

$$\begin{cases} \nabla \cdot \mathbf{S}(\mathbf{x}) = \mathbf{0}, & \forall \mathbf{x} \in \Omega, \\ f[\mathbf{u}(\mathbf{x}), \mathbf{t}(\mathbf{x})] = 0 & \forall \mathbf{x} \in \partial\Omega, \end{cases} \quad (3.2.13)$$

where  $\nabla \cdot$  is the divergence operator,  $\mathbf{t}$  is the boundary traction,  $\partial\Omega$  is the boundary of the domain  $\Omega$  and  $f$  is an operator which allows to specify the boundary conditions. The equation in the system (3.2.13) is known as the *equilibrium equation* of elasticity at which is associated with boundary conditions.

The expression of the boundary conditions in Eq. (3.2.13) is intentionally left implicit because it depends on the specific BVP (*e.g.* prescribed displacement, traction, periodicity ...) to be solved in order to compute  $\mathfrak{c}^*$ .

Hereinafter, Kelvin representation (denoted by brackets) will be widely used for representing stress, strain and elasticity tensors (see appendix **A**). Thus, 2nd-order stress and strain tensors will be represented as 6-dimensional vectors and elasticity tensors as  $6 \times 6$  symmetric matrices. For instance, the Kelvin form of the homogenized elastic law in Eq. (3.2.12) reads:

$$\begin{bmatrix} S_{11}^* \\ \vdots \\ \sqrt{2} S_{12}^* \end{bmatrix} = \begin{bmatrix} C_{1111}^* & \cdots & \sqrt{2} C_{1112}^* \\ \vdots & \ddots & \vdots \\ \sqrt{2} C_{1112}^* & \cdots & 2 C_{1212}^* \end{bmatrix} \cdot \begin{bmatrix} E_{11}^* \\ \vdots \\ \sqrt{2} E_{12}^* \end{bmatrix}. \quad (3.2.14)$$

It is worth noting that Eq. (3.2.14) shows clearly that  $\mathfrak{c}^*$  is fully determined from 6 linearly independent pairs ( $[\mathbf{S}^*], [\mathbf{E}^*]$ ).

### Continuum micromechanics

Continuum micromechanics provides estimates of the homogenized elasticity tensor  $\mathfrak{c}^*$  of heterogeneous materials with microstructure of matrix-inclusion type. We recall here the main ingredients of continuum micromechanics and refer to Suquet (1997); Nemat-Nasser and Hori

(1999); Zaoui (2002) for further details. Continuum micromechanics is based on the solution of the matrix-inclusion problem provided by Eshelby in the fifties (Eshelby, 1957). Eshelby's solution describes the elastic fields (strain, stress) generated by one ellipsoidal inclusion in an infinite isotropic elastic matrix under homogeneous strain/stress boundary conditions at infinity. Eshelby's solution was further extended to inclusions of different shapes, including cylinders and penny-shaped cracks (Laws, 1985), and to anisotropic matrices (Laws, 1977). General formulæ for dealing with ellipsoidal inclusions in an anisotropic solid can be found in Suvorov and Dvorak (2002).

*Micromechanical homogenization*—*i.e.* homogenization theory based on continuum micromechanics—can estimate the homogenized elastic tensor of a RVE made up of several phases with different distributions and shapes, whether or not organized in a matrix/inclusion-like microstructure. The homogenized elastic tensor turns out to be a weighted sum over the phases:

$$\mathbb{c}^* = \sum_r \phi_r \mathbb{c}_r : \mathbb{a}_r, \quad (3.2.15)$$

where  $\phi_r$  is the volume fraction of phase  $r$ ,  $\mathbb{c}_r$  and  $\mathbb{a}_r$  are the 4th-order *elasticity* and *localization* tensors of phase  $r$ , respectively. Note that the following condition is required  $\sum_{r=0, (N_p-1)} \phi_r = 1$  where  $(N_p - 1)$  is the total number of phases.

The *localization* tensor resumes the relation between the microscopic strain field  $\mathbf{E}(\mathbf{x})$  and the macroscopic strain  $\mathbf{E}^*$ , *i.e.*  $\mathbf{E}(\mathbf{x}) = \mathbb{a}_r(\mathbf{x}) : \mathbf{E}^*$ .

It can be shown that the expression of  $\mathbb{a}_r$  reads (Hellmich et al., 2004):

$$\mathbb{a}_r = (\mathbb{i} + \mathbb{p}_r^0 : (\mathbb{c}_r - \mathbb{c}_0))^{-1} : \left[ \sum_{s=0, N_p-1} \phi_s (\mathbb{i} + \mathbb{p}_s^0 : (\mathbb{c}_s - \mathbb{c}_0))^{-1} \right]^{-1}, \quad (3.2.16)$$

where  $\mathbb{c}_0$  represents the elasticity tensor of the matrix phase embedding all other phases;  $\mathbb{i}$  is the 4th order symmetric identity tensor (with  $\mathbb{i}_{ijkl} = 1/2 (\delta_{ij}\delta_{kl} + \delta_{ik}\delta_{jl})$ ,  $\delta_{ij}$  being the components of the Kronecker operator);  $\mathbb{p}_r^0$  is the so-called Hill tensor of the phase  $r$  embedded in the effective matrix. The expression of this latter depends on the shape of the phase  $r$  and on the elastic symmetry of the matrix. Explicit expressions of  $\mathbb{p}_r^0$  have been developed in some special cases (*e.g.* *cylindrical* or *spherical* inclusions in *transversely isotropic* matrix) but, in general, the Hill tensor has to be computed numerically (Suvorov and Dvorak, 2002).

The choice of the value of  $\mathbb{c}_0$  leads to different estimates of  $\mathbb{c}^*$ . Among others, two estimates are relevant to the context of this study. The Mori-Tanaka (MT) estimate (Nemat-Nasser and Hori, 1999) is well suited when the material microstructure is made up of uniformly dispersed inclusions in a homogeneous matrix. In this case, the effective matrix is an actual, well identified phase and therefore  $\mathbb{c}_0 = \mathbb{c}_{matrix}$ . Then, the MT estimate of  $\mathbb{c}^*$  can be readily computed from Eq. (3.2.15). The Self-Consistent (SC) estimate (Nemat-Nasser and Hori, 1999) is well suited when no actual matrix can be identified but the microstructure is rather made of interpenetrating (continuous or discontinuous) phases. In this case, the effective matrix is assumed to be the homogenized material itself and therefore  $\mathbb{c}_0 = \mathbb{c}^*$ . It follows that the SC estimate of  $\mathbb{c}^*$  shall be computed iteratively since  $\mathbb{c}^*$  appears on both sides of Eq. (3.2.15).

Looking at the structure of bone at each scale considered in this study, the SC scheme can be used to estimate the effective elastic tensor of the MF, then the MT scheme to estimate those of the US and of the CB. The expression of the SC estimate of  $\mathfrak{c}^*$  for a two-phase material such as the MF reads:

$$\mathfrak{c}^* = \left[ \phi_0 \mathfrak{c}_0 : (\mathfrak{i} + \mathbb{P}_0^{SC} : (\mathfrak{c}_0 - \mathfrak{c}^*))^{-1} + \phi_1 \mathfrak{c}_1 : (\mathfrak{i} + \mathbb{P}_1^{SC} : (\mathfrak{c}_1 - \mathfrak{c}^*))^{-1} \right] : \left[ \phi_0 (\mathfrak{i} + \mathbb{P}_0^{SC} : (\mathfrak{c}_0 - \mathfrak{c}^*))^{-1} + \phi_1 (\mathfrak{i} + \mathbb{P}_1^{SC} : (\mathfrak{c}_1 - \mathfrak{c}^*))^{-1} \right]^{-1}, \quad (3.2.17)$$

where the subscripts 0 and 1 refer to the matrix and inclusion phases, respectively. Moreover, the expression of the MT estimate of  $\mathfrak{c}^*$  for a two-phase material such as the US and the CB reads:

$$\mathfrak{c}^* = \left[ \phi_0 \mathfrak{c}_0 : \mathfrak{i} + \phi_1 \mathfrak{c}_1 : (\mathfrak{i} + \mathbb{P}_1^{MT} : (\mathfrak{c}_1 - \mathfrak{c}_0))^{-1} \right] : \left[ \left( \phi_0 \mathfrak{c}_0 : \mathfrak{i} + \phi_1 \mathfrak{c}_1 : (\mathfrak{i} + \mathbb{P}_1^{MT} : (\mathfrak{c}_1 - \mathfrak{c}_0))^{-1} \right) \right]^{-1}. \quad (3.2.18)$$

For the sake of synthesis, Eqs. (3.2.17)-(3.2.18) have been rewritten more compactly as:

$$g^{sch}(\mathfrak{c}^*; \{\phi_r\}, \{\mathfrak{c}_r\}) = 0, \quad r = 0, \dots, N_p - 1, \quad (3.2.19)$$

where  $g^{sch}$  refers to the application of the scheme *sch* (*i.e.* SC or MT) to the homogenized elastic tensor  $\mathfrak{c}^*$ , from  $\phi_r$  and  $\mathfrak{c}_r$ , the volume fraction and elastic tensor respectively, of the phase  $r$ . Note that the application  $g^{sch}$  also depends upon the Hill tensor which is computed numerically (Suvorov and Dvorak, 2002).

### Homogenization by Finite Element Method (FEM)

The finite element method (FEM) consists in the solution of a suitable *weak formulation* of the problem defined from Eq. (3.2.13) for a specific set of boundary conditions (prescribed displacement, traction, periodicity ...). More details on this standard technique can be found in Zohdi and Wriggers (2001).

In this work, the boundary condition used in the problem (see Eq. (3.2.13)) is given by:

$$\mathbf{u} = \mathbf{E}^* \mathbf{x} \quad \forall \mathbf{x} \in \partial\Omega, \quad (3.2.20)$$

where  $\mathbf{E}^*$  is a given strain tensor independent of  $\mathbf{x}$ .

A *weak formulation* is obtained from the equilibrium equations of elasticity and this boundary condition. From this formulation, the FEM is used to resolve this problem which leads to the solution in displacement field  $\mathbf{u}(\mathbf{x})$ . This field displacement allows to determine the strain field  $\mathbf{E}(\mathbf{x})$  from Eq. (3.2.10) and the stress field  $\mathbf{S}(\mathbf{x})$  from Eq. (3.2.9). The effective elastic properties of an heterogeneous RVE is obtained by a judicious choice of six sets of uniform displacements (KUBC, for kinematic uniform BC) boundary conditions following a well-documented procedure (see *e.g.* Zohdi and Wriggers (2001)) that amounts to simulating longitudinal traction tests in every direction. These computations yield a linear system of 36 equations, whose solutions form the components of the elasticity tensor  $\mathfrak{c}^*$  which defines the effective elastic properties of a heterogeneous RVE.

The boundary value problem in each RVE was solved with the commercial finite element code (Comsol Multiphysics (COMSOL Multiphysics, 2015)). The equations of linearized elasticity were discretized on an unstructured mesh of tetrahedral elements with characteristic size  $h$ . Comsol Multiphysics does not assign stiffness values to each element individually but uses a function which returns the local elastic coefficients at arbitrary coordinates  $(x_1, x_2, x_3)$ . The shape functions used in the discretized equations of linearized elasticity are Lagrange interpolation polynomials of second degree.

### Homogenization by Fast Fourier Transform (FFT) method

One of the main advantages of Fast Fourier Transform-based methods (Moulinec and Suquet, 1998) presented below is that they directly use numerical images of the microstructure, and all fields of interest (stress, strain, ...) are computed at every pixel of the image. Another important feature is that the required cpu time is roughly proportional to the size of the image (in pixels or voxels).

The FFT method is applied to solve the problem (3.2.13). To this aim, first of all a particular version of the equilibrium equation has to be defined. In general, the FFT method can be performed by means of the assignation of *periodic* boundary conditions to the strain field or to *antiperiodic* condition to the stress field. For simplicity, we describe the case of *periodic* conditions prescribed on the strain field.

As already mentioned, in order to compute the effective elastic tensor  $\mathfrak{c}^*$  of a heterogeneous RVE, 6 problems have to be solved corresponding to 6 linearly independent boundary conditions.

The problem consists in finding the displacement field  $\mathbf{u}(\mathbf{x})$  such that:

$$\begin{cases} \nabla \cdot \mathbf{S}(\mathbf{x}) = \mathbf{0}, & \forall \mathbf{x} \in \Omega \\ \mathbf{S}(\mathbf{x}) = \mathfrak{c}(\mathbf{x}) : \mathbf{E}(\mathbf{x}), & \forall \mathbf{x} \in \Omega \\ \mathbf{u}(\mathbf{x}) - \mathbf{E}^* \mathbf{x} & \text{periodic for all } \mathbf{x} \in \partial\Omega \end{cases} \quad (3.2.21)$$

By addition and subtraction of a homogeneous test elastic tensor  $\mathfrak{c}_0$ , the problem can be turned in:

$$\mathbf{S}(\mathbf{x}) = \mathfrak{c}_0 : \mathbf{E}(\mathbf{x}) + \mathbf{P}(\mathbf{x}) \quad \text{with} \quad \mathbf{P}(\mathbf{x}) := (\mathfrak{c}(\mathbf{x}) - \mathfrak{c}_0) : \mathbf{E}(\mathbf{x}) . \quad (3.2.22)$$

The tensor  $\mathbf{P}(\mathbf{x})$  is the so-called *polarization* tensor field. The equation (3.2.22) represents the stress field in a prestressed homogeneous medium. If  $\mathbf{P}(\mathbf{x})$  is supposed to be known, the solution of the new problem defined by:

$$\nabla \cdot (\mathfrak{c}_0 : \mathbf{E}(\mathbf{x})) = -\nabla \cdot (\mathbf{P}(\mathbf{x})), \quad (3.2.23)$$

is given by the strain field defined by:

$$\mathbf{E}(\mathbf{x}) = \mathbf{E}^* - (\mathbf{\Gamma}^0(\mathbf{x}) * \mathbf{P}(\mathbf{x})), \quad \text{or} \quad \mathbf{E}(\mathbf{x}) + \{\mathbf{\Gamma}^0(\mathbf{x}) * [\mathfrak{c}(\mathbf{x}) - \mathfrak{c}_0] : \mathbf{E}(\mathbf{x})\} = \mathbf{E}^* . \quad (3.2.24)$$

where  $\mathbf{\Gamma}^0$  is the Green operator for strains associated to the material characterized by the elastic tensor  $\mathfrak{c}_0$ . This equation is known as Lippman-Schwinger equation. Moreover, in this equation, the symbol “\*” designates the *convolution* operator which is defined by:

$$(g_1 * g_2)(\mathbf{x}) := \int_{\Omega} g_1(\mathbf{x} - \mathbf{y})g_2(\mathbf{y})d\mathbf{y} = \int_{\Omega} g_2(\mathbf{x} - \mathbf{y})g_1(\mathbf{y})d\mathbf{y} \quad (3.2.25)$$

where  $g_1$  and  $g_2$  are 2 functions. Equation (3.2.24) can be solved for  $\mathbf{E}(\mathbf{x})$  by transforming the problem in the Fourier space:

$$\begin{cases} \hat{\mathbf{E}}(\xi) = -\hat{\Gamma}^0(\xi) : \hat{\mathbf{P}}(\xi) & \forall \xi \neq 0, \\ \hat{\mathbf{E}}(\mathbf{0}) = \mathbf{E}^*, \end{cases} \quad (3.2.26)$$

where the Fourier transform is denoted by a hat superimposed on the quantity.

Equation (3.2.26) can be stated for any test material *-i.e.* irrespective of the symmetry class of  $\mathfrak{c}_0$ . However, assuming  $\mathfrak{c}_0$  to be isotropic,  $\hat{\Gamma}^0$  can be represented as:

$$\hat{\Gamma}_{khij}^0(\xi) = \frac{1}{4\mu^0|\xi|^2} (\delta_{ki}\xi_h\xi_j + \delta_{hi}\xi_k\xi_j + \delta_{kj}\xi_h\xi_i + \delta_{hj}\xi_k\xi_i) - \frac{\lambda^0 + \mu^0}{\mu^0(\lambda^0 + 2\mu^0)} \frac{\xi_i\xi_j\xi_k\xi_h}{|\xi|^4}, \quad (3.2.27)$$

where  $\lambda^0$  and  $\mu^0$  are the Lamé's coefficients characterizing the elastic tensor  $\mathfrak{c}_0$  of the homogeneous test material.

Equation (3.2.24) is an implicit expression of  $\mathbf{E}(\mathbf{x})$  to be solved iteratively. A iterative scheme allows to resolve the problem:

$$\begin{cases} [\mathbf{E}(\mathbf{x})]^{(0)} & = \mathbf{E}^*, \\ [\mathbf{E}(\mathbf{x})]^{(n+1)} & = \mathbf{E}^* - \left\{ \Gamma^0(\mathbf{x}) * [\mathbf{P}(\mathbf{x})]^{(n)} \right\}, \quad [\mathbf{P}(\mathbf{x})]^{(n)} = [\mathfrak{c}(\mathbf{x}) - \mathfrak{c}_0] : [\mathbf{E}(\mathbf{x})]^{(n)}. \end{cases} \quad (3.2.28)$$

At each iteration, four steps are performed:

1. the polarization tensor field  $[\mathbf{P}(\mathbf{x})]^{(n)}$  is evaluated in the Fourier space as  $[\hat{\mathbf{P}}(\xi)]^{(n)}$ ;
2. the Fourier problem, defined by:

$$\begin{cases} [\hat{\mathbf{E}}(\xi)]^{(n+1)} & = -\hat{\Gamma}^0(\xi) : [\hat{\mathbf{P}}(\xi)]^{(n)} \\ [\hat{\mathbf{E}}(\mathbf{0})]^{(n+1)} & = \mathbf{E}^* \end{cases} \quad (3.2.29)$$

is solved for  $[\hat{\mathbf{E}}(\xi)]^{(n+1)}$ ;

3. then,  $[\mathbf{E}(\mathbf{x})]^{(n+1)}$  is computed as the inverse Fourier transform of  $[\hat{\mathbf{E}}(\xi)]^{(n+1)}$ .
4. eventually,  $[\mathbf{S}(\mathbf{x})]^{(n+1)}$  is computed by means of the elastic law  $[\mathbf{S}(\mathbf{x})]^{(n+1)} = \mathfrak{c}(\mathbf{x}) : [\mathbf{E}(\mathbf{x})]^{(n+1)}$

The above procedure is iterated as long as the current estimate of the stress field does not satisfy the bulk balance and stops when the error, defined as:

$$\epsilon^{(n)} = \frac{\frac{1}{\sqrt{|\Omega|}} \|\nabla \cdot (\{\mathbf{S}(\mathbf{x})\}^{(n)})\|_{L^2}}{\|\langle \{\mathbf{S}(\mathbf{x})\}^{(n)} \rangle_{\Omega} \|_F}, \quad (3.2.30)$$

becomes smaller than a fixed threshold. It is worthy to observe that, by means of the Parseval identity applied to the stress tensor field  $\mathbf{S}(\mathbf{x})^{(n)}$ , the value of the error  $\epsilon^{(n)}$  can be estimated already at the previous step with respect of his Fourier transform  $\hat{\mathbf{S}}^{(n)}$ , as :

$$\epsilon^{(n)} \equiv \frac{\|\xi \times \hat{\mathbf{S}}(\xi)^{(n)}\|_{L^2}}{\|\hat{\mathbf{S}}(\mathbf{0})^{(n)}\|_F}. \quad (3.2.31)$$

### 3.2.7 Elastic properties of essential constituents

The models presented in this work are described as mixtures of three essential constituents which are mineral (hydroxyapatite), water and collagen. Elastic properties of these three constituents are supposed to be known and their values were adapted from Hellmich et al. (2004) and reported in Tab. 3.1. Specifically, the mineral and the water have been assumed as *isotropic* materials (with bulk modulus  $K$ , shear modulus  $G$ , Young's modulus  $Y$  and Poisson's ratio  $\nu$ ). Water has been assumed as a compressible fluid with zero shear modulus. (In the FEM models of cortical bone, in order to avoid numerical problems, the shear modulus of water filling the Haversian pores was assumed much smaller than its bulk modulus.) Collagen has been assumed as a *transversely isotropic* material with the axis of symmetry aligned with the pore direction (see the  $\mathbf{e}_3$ -direction in Fig. 3.3).

Table 3.1: Elastic properties of essential constituents of bone.

water	(MF)	$K = 2.3$ [GPa]	$G = 0$ [Pa]
	(HP / $\mu$ -mech.& FFT)	$K = 2.3$ [GPa]	$G = 0$ [Pa]
	(HP / FEM)	$K = 2.3$ [GPa]	$G = 1$ [MPa]
HA		$Y = 120$ [GPa]	$\nu = 0.27$ [-]
	Collagen	$c_{1111} = 11.7$ [GPa]	
		$c_{3333} = 17.9$ [GPa]	
		$c_{1122} = 5.1$ [GPa]	
		$c_{1133} = 7.1$ [GPa]	
		$c_{1313} = 3.3$ [GPa]	

### 3.2.8 Stochastic micromechanical ( $S\mu M$ ) model of cortical bone

The variability of the elastic properties of the cortical bone at the tissue scale can be described by introducing a suitable stochastic model of the input data ( $\overline{\text{TMD}}$ , HP) in the micromechanical model described in Sec. 3.2.6. Hereinafter, this will be referred to as a stochastic micromechanical ( $S\mu M$ ) model of cortical bone. A robust model of CB should reproduce at most the information officially declared on a typical input data.

#### Stochastic models of $\overline{\text{TMD}}$ and HP

Scattering of the experimental measures of  $\overline{\text{TMD}}$  and HP in the region of interest are represented in Fig. 3.5. Analysis of the *Calib* dataset (solid circles in Fig. 3.5) shows a low correlation between

$\overline{\text{TMD}}$  and HP with a correlation coefficient  $r(\overline{\text{TMD}}, \text{HP}) = 0.0915$ .

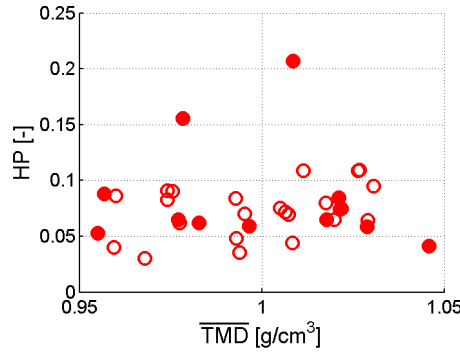


Figure 3.5: Scatter plot of the pairs of measures  $(\overline{\text{TMD}}, \text{HP})$  for each of  $\text{RVE}_i$  related to the *Calib* (solid circles) and *Ctrl* (empty circles) datasets.

Uncertainty on the actual values of  $\overline{\text{TMD}}$  and HP was accounted for by modeling them as random variables. Let  $\mathbf{X} := (X_1, X_2)$  be the random vector modeling the pair  $(\overline{\text{TMD}}, \text{HP})$ . In view of the very small correlation between  $\overline{\text{TMD}}$  and HP,  $X_1$  and  $X_2$  can be modeled as statistically independent random variables. Then, the probability density function (PDF) of  $\mathbf{X}$ , denoted by  $p_{\mathbf{X}}(\mathbf{x})$ , reads:

$$p_{\mathbf{X}}(\mathbf{x}) \equiv p_{X_1}(x_1) \times p_{X_2}(x_2), \quad (3.2.32)$$

where  $p_{X_1}(x_1)$  and  $p_{X_2}(x_2)$  are PDFs of  $X_1$  and  $X_2$  respectively.

The expression of each  $p_{X_i}(x_i)$  (with  $i = 1, 2$ ) was obtained by means of the Maximum-Entropy (denoted by MaxEnt) principle. The MaxEnt principle (Jaynes, 1957a,b) allows building the PDF  $p_X(x)$  of a random variable  $X$  by maximizing the *measure of uncertainty* given by the Shannon's entropy (Shannon, 1948) under a given set of constraints. These latter can be stated in terms of preservation of some statistics of  $X$  which are assumed to represent the only *available information*. The general form of the Shannon's entropy for the random variable  $X$  reads:

$$\mathcal{S}(p_X) = \int_{S_X} -\ln(p_X(x)) p_X(x) dx \quad (3.2.33)$$

where  $\ln$  designates the natural logarithm function and  $S_X$  is the support of the function  $p_X(x)$ . The constraints are expressed by prescribing the expected values of a set of functions  $f_i$  of the random variable  $X$ , *i.e.*:

$$\mathbb{E}(f_i(X)) = F_i, \quad i = 1, \dots, n, \quad (3.2.34)$$

where

$$\mathbb{E}(f(X)) = \int_{\mathbb{R}} f(x) \cdot p_X(x) dx, \quad (3.2.35)$$

where  $\mathbb{R}$  is the real axis and  $F_i$  is prescribed condition.

It is worth noting that Shannon's entropy of a random variable with value in a compact support, attains its maximum value for the uniform variable on that support. At the opposite side, for constant random variables, whose PDF is the *Dirac's* distribution, the Shannon's entropy

attains its minimum value (*i.e.*  $-\infty$ ). Since a deterministic variable can be seen as a constant random variable, this provides the interesting interpretation of the nominal model described in Sec. 3.2.9.

In the context of this work, the available information on  $X$  was assumed to be given in terms of its support  $S_X$ , mean value  $\mu_X$  and standard deviation  $\sigma_X$ —or, equivalently, dispersion  $\delta_X = \sigma_X/\mu_X$ . Thus, the constraints defined in Eq. (3.2.34), are specified by taking:

$$\begin{aligned} f_0(x) &= \mathbb{1}_{S_X}(x), & F_0 &= 1; \\ f_1(x) &= x, & F_1 &= \mu_X^{\text{exp}}; \\ f_2(x) &= x^2, & F_2 &= (\mu_X^{\text{exp}})^2 \times (1 + (\delta_X^{\text{exp}})^2). \end{aligned} \quad (3.2.36)$$

where  $\mathbb{1}_{S_X}(x)$  is the characteristic function of  $S_X$  and  $\mu_X^{\text{exp}}$  and  $\delta_X^{\text{exp}}$  are experimental statistics. The constraint  $f_0$  is the normalization condition on the PDF of  $X$ . Constraints  $f_1$  and  $f_2$  fix the values of the two first moments of  $X$  through the available *experimental information*. This is equivalent to enforce the mean value and dispersion of  $X$  to be equal to their corresponding experimental values, *i.e.*  $\mu_X = \mu_X^{\text{exp}}$  and  $\delta_X = \delta_X^{\text{exp}}$ . In particular, the support of  $X_1$  has been set to the image of the range of GLs associated to the US ( $\mathcal{GL}_{\text{US}}$ ) through Eq. (3.2.1), *i.e.*  $S_{X_1} = [0.7; 1.5]$ ; and the support of  $X_2$  has been set to  $S_{X_2} = [0, 1]$ .

Since the Shannon's entropy plays the role of a Lagrangian, the problem of maximizing the functional in Eq. (3.2.33) under the system of constraints in Eqs. (3.2.36) is equivalent to find the optimal vector of Lagrange multipliers (ML)  $\boldsymbol{\lambda}^* := [\lambda_0^*, \lambda_1^*, \lambda_2^*]$  that minimizes the corresponding Hamiltonian  $\mathcal{H}$ , that is:

$$\boldsymbol{\lambda}^* = \arg \min_{\boldsymbol{\lambda}} \mathcal{H}(\boldsymbol{\lambda}), \quad (3.2.37)$$

where the operator  $\arg \min$  designates argument of the minimum and, the Hamiltonian  $\mathcal{H}(\boldsymbol{\lambda})$  is defined by:

$$\mathcal{H}(\boldsymbol{\lambda}) := \lambda_0 + \lambda_1 \times \hat{\mu}(X) + \lambda_2 \times (1 + \hat{\delta}^2(X)) \hat{\mu}^2(X) + \int_{S_X} \exp\{-(\lambda_0 + \lambda_1 x + \lambda_2 x^2)\} dx. \quad (3.2.38)$$

The solution of the above constrained maximization problem leads to the PDF of  $X$ , reading:

$$p_X^{\boldsymbol{\lambda}^*}(x) := \mathbb{1}_{S_X}(x) \exp\{-(\lambda_0^* + \lambda_1^* x + \lambda_2^* x^2)\}. \quad (3.2.39)$$

Note that the PDF coming from this specific problem corresponds to the truncation of the PDF of the Gaussian random variable  $\mathcal{G}(\mu_g, \sigma_g)$  (with  $\sigma_g = 1/(2\lambda_2)$ ,  $\mu_g = -\lambda_1 \times \sigma_g$ ) on the support  $S_X$ .

### Numerical solution of the stochastic models of $\overline{\text{TMD}}$ and HP

The problem (3.2.37) has been solved in two steps.

#### Step 1/ Definition of the PDF of $\overline{\text{TMD}}$ and HP.

Firstly, the PDFs of  $\overline{\text{TMD}}$  and HP have been computed. This step implies the research of the optimal vector of *Lagrange's multipliers*  $\boldsymbol{\lambda}^* := [\lambda_0^*, \lambda_1^*, \lambda_2^*]$  minimizing the Hamiltonian functional  $\mathcal{H}$  given by Eq. (3.2.38). This operation has been accomplished using the built-in

optimization functions of MATLAB software (MATLAB, 2010). The minimum of unconstrained multivariable function is obtained by using a derivative-free method.

The convergence of any optimization problem depends on the choice of the first guess  $\lambda^{(0)} = [\lambda_0^{(0)} - 1, \lambda_1^{(0)}, \lambda_2^{(0)}]$ . Setting a “good” initial guess should be performed using some *heuristic*. It is possible to show that for a PDF like that defined by Eq. (3.2.39), the proximity of the *mode* to the *mean value* of  $X$  and the *integrability* conditions lead to the following choice for the first guess  $\lambda^{(0)}$ :

$$\begin{cases} \lambda_1^{(0)} := a \times \lambda_2^{(0)}, & \text{where } a = -2\mu_X, \\ \lambda_2^{(0)} > 0, & \lambda_1^{(0)} < 0, \\ \lambda_0^{(0)} = \ln \left( \int_{S_X} \exp -(\lambda_1^{(0)} x + \lambda_2^{(0)} x^2) dx \right). \end{cases} \quad (3.2.40)$$

Moreover, increasing the value of  $\lambda_2^{(0)}$  induces a reduction of the dispersion  $\delta_X$ .

### Step 2/ Collection of statistically independent realizations of $\overline{\text{TMD}}$ and HP

A set of statistically independent realizations of  $\overline{\text{TMD}}$  and HP were computed using the *pseudo-inverse* method (Devroye, 1986). Let  $X$  be any of  $X_1$  or  $X_2$  and  $F_X^{\lambda^*}(x)$  the repartition function of  $X$  *i.e.*:

$$F_X^{\lambda^*}(x) = \int_{\inf S_X}^x p_X^{\lambda^*}(y) dy. \quad (3.2.41)$$

Firstly, the *pseudo-inverse*  $(F_X^{\lambda^*})^{-1}$  of the repartition function was numerically computed. Then, a large number  $N$  of realizations of a *uniform* random variable  $U$  with values in  $[0, 1]$  were collected. Eventually, for each realization  $U(a_i)$  (with  $i = 1, \dots, N$ ), a realization of  $X$  was computed as:

$$X(a_i) = \left( F_X^{\lambda^*} \right)^{-1} (U(a_i)). \quad (3.2.42)$$

### Stochastic micromechanical model of cortical bone elasticity

Stochastic description of the uncertainty of cortical bone (CB) composition can be obtained by means of the realizations  $X_1(a_i)$  and  $X_2(a_j)$  (with  $i, j = 1, \dots, N$ ) of the random variables modeling the uncertain  $\overline{\text{TMD}}$  and HP, respectively. The use of two different indexes underlines the statistical independence between the realizations of  $X_1$  and  $X_2$ . Starting from these input data, the stochastic model of the elastic tensor of CB has been constructed in two steps.

In a first step, realizations of the random elastic tensors of the mineral foam (MF) and ultrastructure (US) were computed using the procedure proposed in Gagliardi et al. (2016 (submitted)). In short, the realizations  $X_1(a_i)$  (random  $\overline{\text{TMD}}$ ) were used to compute the corresponding values of random VFs at the US and MF scales through Eqs. (3.2.6)-(3.2.7) (hereinafter, capital letters will denote random VFs):

$$\begin{cases} \Phi_{\text{HA}}^{\text{US}}(a_i) = \hat{\phi}_{\text{HA}}^{\text{US}}(X_1(a_i)), & \Phi_{\text{Col}}^{\text{US}}(a_i) = \hat{\phi}_{\text{Col}}^{\text{US}}(X_1(a_i)), & \Phi_{\text{W}}^{\text{US}}(a_i) = \hat{\phi}_{\text{W}}^{\text{US}}(X_1(a_i)), \\ \Phi_{\text{HA}}^{\text{MF}}(a_i) = \hat{\phi}_{\text{HA}}^{\text{MF}}(X_1(a_i)), & \Phi_{\text{W}}^{\text{MF}}(a_i) = \hat{\phi}_{\text{W}}^{\text{MF}}(X_1(a_i)). \end{cases} \quad (3.2.43)$$

In turn, these values of random VFs were used to compute the realizations of the random elastic tensors of the MF and US through Eq. (3.2.17) and Eq. (3.2.18), respectively. Using the synthetic

form of Eq. (3.2.19), these equations read:

$$\begin{aligned} g_I^{\text{SC}}(\mathbb{C}_{\text{MF}}(a_i); \Phi_{\text{HA}}^{\text{MF}}(a_i), \{\mathbb{C}_{\text{HA}}, \mathbb{C}_{\text{W}}\}) = 0 & \quad \text{leads to } \mathbb{C}_{\text{MF}}(a_i), \\ g_{III}^{\text{MT}}(\mathbb{C}_{\text{US}}(a_i); \Phi_{\text{Col}}^{\text{US}}(a_i), \{\mathbb{C}_{\text{HA}}, \mathbb{C}_{\text{MF}}(a_i)\}) = 0 & \quad \text{leads to } \mathbb{C}_{\text{US}}(a_i). \end{aligned} \quad (3.2.44)$$

In a second step, realizations of the random elastic tensor of CB were computed by using the realizations  $X_2(a_j)$  (random HP) and  $\mathbb{C}_{\text{US}}(a_i)$  as input data of Eq. (3.2.18). Using the synthetic form of Eq. (3.2.19), these equations read:

$$g_{III}^{\text{MT}}(\mathbb{C}_{\text{CB}}(a_i, a_j); X_2(a_j), \{\mathbb{C}_{\text{W}}, \mathbb{C}_{\text{US}}(a_i)\}) = 0 \quad \text{leads to } \mathbb{C}_{\text{CB}}(a_i, a_j). \quad (3.2.45)$$

We observe here that all the realizations of the stochastic tensors stay in the same symmetry group of their deterministic counterparts;  $\mathbb{C}_{\text{MF}}(a_i)$  is isotropic whereas  $\mathbb{C}_{\text{US}}(a_i)$  and  $\mathbb{C}_{\text{CB}}(a_i, a_j)$  are transversely isotropic. Moreover, thanks to the *closure property* of the *elastic symmetry groups*, also the mean values of these stochastic tensors stay in the same symmetry classes (see the appendix in (Gagliardi et al., 2016 (submitted))).

### Statistical analysis of random elastic coefficients

An overall picture of the elasticity of bone at all scales (mineral foam, ultrastructure and cortical tissue) can be given in terms of statistics of individual *moduli* or whole tensors. On the one side, statistics (mean value, dispersion and confidence intervals) of elastic *moduli* were estimated by means of the stochastic estimators in Eq. (3.2.4). On the other side, mean value and scalar dispersion of a random tensor  $\mathbb{C}$  (named  $\mu_{[\mathbb{C}]}$  and  $\delta_{[\mathbb{C}]}$ , respectively, by making use of Kelvin representation for  $\mu_{[\mathbb{C}]}$ ) were estimated through the statistical estimators (Gagliardi et al., 2016 (submitted)):

$$\begin{aligned} \mu_{[\mathbb{C}]}^N &= \frac{1}{N} \sum_{k=1}^N [\mathbb{C}(a_k)], \\ \delta_{[\mathbb{C}]}^N &= \sqrt{\frac{\frac{1}{N} \sum_{k=1}^N \|\mathbb{C}(a_k) - \mu_{[\mathbb{C}]}^N\|_F^2}{\|\mu_{[\mathbb{C}]}^N\|_F^2}}, \end{aligned} \quad (3.2.46)$$

where  $\|\cdot\|_F$  is the Frobenius' norm of a square matrix. The scalar dispersion  $\delta_{[\mathbb{C}]}$  represents a global measure of the fluctuations of  $[\mathbb{C}]$  around its mean value  $\mu_{[\mathbb{C}]}$ .

### 3.2.9 Nominal micromechanical ( $N\mu\text{M}$ ) model of cortical bone

A nominal micromechanical ( $N\mu\text{M}$ ) model of cortical bone was developed corresponding to the mean model of the stochastic micromechanical  $S\mu\text{M}$  model. First, RVE-wise values of  $\overline{\text{TMD}}$  and HP were averaged on the *Calib* dataset ( $\mu(\overline{\text{TMD}}) = \mu_{\overline{\text{TMD}}}^{\text{exp}}$ ,  $\mu(\text{HP}) = \mu_{\text{HP}}^{\text{exp}}$ ) and used to obtain average values of the VFs of bone constituents by means of the relations introduced in Sec. 3.2.5:

$$\begin{aligned} \mu_{\text{HP}}^{\text{exp}} &\rightarrow \phi_{\text{HP}}^{\text{CB}} = \hat{\phi}_{\text{HP}}^{\text{CB}}(\mu_{\text{HP}}^{\text{exp}}), \\ \mu_{\overline{\text{TMD}}}^{\text{exp}} &\rightarrow \begin{cases} \phi_{\text{HA}}^{\text{US}} = \hat{\phi}_{\text{HA}}^{\text{US}}\left(\mu_{\overline{\text{TMD}}}^{\text{exp}}\right), & \phi_{\text{Col}}^{\text{US}} = \hat{\phi}_{\text{Col}}^{\text{US}}\left(\mu_{\overline{\text{TMD}}}^{\text{exp}}\right), & \phi_{\text{W}}^{\text{US}} = \hat{\phi}_{\text{W}}^{\text{US}}\left(\mu_{\overline{\text{TMD}}}^{\text{exp}}\right), \\ \phi_{\text{HA}}^{\text{MF}} = \hat{\phi}_{\text{HA}}^{\text{MF}}\left(\mu_{\overline{\text{TMD}}}^{\text{exp}}\right), & \phi_{\text{W}}^{\text{MF}} = \hat{\phi}_{\text{W}}^{\text{MF}}\left(\mu_{\overline{\text{TMD}}}^{\text{exp}}\right). \end{cases} \end{aligned} \quad (3.2.47)$$

Then, these average VFs were used to compute the nominal elastic tensors of MF, US and CB by means of Eq. (3.2.19), reading:

$$\begin{aligned} g_I^{\text{SC}}(\mathbb{c}_{\text{MF}}; \phi_{\text{HA}}^{\text{MF}}, \{\mathbb{c}_{\text{HA}}, \mathbb{c}_{\text{W}}\}) &= 0 \quad \text{leads to } \mathbb{c}_{\text{MF}}, \\ g_{II}^{\text{MT}}(\mathbb{c}_{\text{US}}; \phi_{\text{Col}}^{\text{US}}, \{\mathbb{c}_{\text{HA}}, \mathbb{c}_{\text{MF}}\}) &= 0 \quad \text{leads to } \mathbb{c}_{\text{US}}, \\ g_{III}^{\text{MT}}(\mathbb{c}_{\text{CB}}; \phi_{\text{HP}}^{\text{CB}}, \{\mathbb{c}_{\text{W}}, \mathbb{c}_{\text{US}}\}) &= 0 \quad \text{leads to } \mathbb{c}_{\text{CB}}. \end{aligned} \quad (3.2.48)$$

### 3.2.10 Micro-finite element ( $\mu$ FE) model of cortical bone

Finite element (FE, see Sec. 3.2.6) models of bone microstructure, referred to as  $\mu$ FE models, were used to compute the effective elastic properties of all the RVEs (*Calib* and *Ctrl* datasets) represented in Fig 3.3. These models accounted for the actual morphology of the RVEs and a simplified representation of their heterogeneous elastic properties.

The numerical procedure, shortly reported in (Sansalone et al., 2016), is outlined here below. Starting from a structured isotropic regular mesh ( $50^3$  cubic voxels points) of the RVE, a coarser tetrahedral mesh was generated using Simpleware software (Simpleware 5.0 ScanIP+, 2012) for reducing the computational cost. The region corresponding to the US (voxels with GL in  $\mathcal{GL}_{\text{US}}$ ) was divided in  $n_{ph}$  subregions by dividing the whole set of GL-range  $\mathcal{GL}_{\text{US}}$  in  $n_{ph}$  equal subsets  $\mathcal{GL}_{\text{US}}^{(n)}$ , with  $n = 1, \dots, n_{ph}$ . Grey levels in each subregion were further replaced by their mean value. The region corresponding to the HP and the subregions corresponding to the US were meshed by preserving mesh coherence between adjacent regions. The mesh and the GLs associated to each subregion were exported to COMSOL Multiphysics software (COMSOL Multiphysics, 2015). COMSOL Multiphysics was used with  $2^{nd}$  order Lagrangian finite elements based on the geometric mesh exported by Simpleware. Elastic properties of the FE were assigned based on their GLs. Material properties of finite elements belonging to the HP region were given by the elastic properties of water resumed in Tab. 3.1. Continuum micromechanics was used to compute the elastic properties of the FEs belonging to US regions. Specifically, the GL of each US region was converted in TMD (see Eq. (3.2.1)) and then in VFs of bone constituents at the MF and US scales (Eqs. (3.2.6)-(3.2.7)) which, in turn, were used to compute the elastic tensors of the MF and US (Eqs. (3.2.48), steps *I* and *II*).

The number  $n_{ph}$  of US subregions was defined by performing a preliminary parametric study and looking for stabilization of FE results with respect to  $n_{ph}$ . Results obtained for 8 and 16 subregions being quite similar, the value  $n_{ph} = 8$  was used hereinafter.

### 3.2.11 Micro-Fast Fourier Transform ( $\mu$ FFT) model of cortical bone

Models of bone microstructure based on the Fast Fourier Transform (FFT, see Sec. 3.2.6), referred to as  $\mu$ FFT models, were used to compute the effective elastic properties of all the RVEs (*Calib* and *Ctrl* datasets) represented in Fig 3.3. These models accounted for the actual morphology and heterogeneous distribution of elastic properties of the RVEs.

Calculations were performed by using the *CraFFT* software (Composite response and Fourier Transforms) (Moulinec and Suquet, 1998). Each RVE was represented as a vector collecting the GLs of all the  $N = N_1 \times N_2 \times N_3 = 50^3 = 125000$  voxels of the RVE. A threshold  $q = 131$  was used to separate the voxels belonging to the US from those belonging to the HP. Elastic

properties of water (see Tab. 3.1) were given to the voxels belonging to the HP. The material properties associated with the voxels belonging to the US were computed applying the first two steps of the continuum micromechanics model to those volume fractions corresponding to the specific grey level. Specifically, the GL of each voxel was converted in TMD (see Eq. (3.2.1)) and then in VFs of bone constituents at the MF and US scales (see Eqs. (3.2.6)-(3.2.7)) which, in turn, were used to compute the elastic tensors of the MF and US (see Eqs. (3.2.48), steps *I* and *II*).

The determination of the effective macroscopic elastic properties of any RVE is accomplished if the 36 components  $c_{ij}$  of any representation of the elastic tensor  $\mathbf{c}^*$  are defined. We have estimated  $\mathbf{c}^*$  column by column evaluating 6 stress vectors  $\mathbf{S}^*$  results corresponding to 6 linearly independent strain assignments  $\mathbf{E}^*$  according to the algorithm described in sect. 3.2.6. The calculation have been run until the error from equilibrium condition (see Eq. (3.2.30)) reduced to  $< 10^{-4}$ .

The six strain tests  $\mathbf{E}^*$  are expressed in the Kelvin representation:

$$[\mathbf{E}^*] = [\mathbf{E}^*]_1, [\mathbf{E}^*]_2, [\mathbf{E}^*]_3, [\mathbf{E}^*]_4, [\mathbf{E}^*]_5, [\mathbf{E}^*]_6 = \begin{bmatrix} 1 \\ 0 \\ 0 \\ 0 \\ 0 \\ 0 \end{bmatrix}, \begin{bmatrix} 0 \\ 1 \\ 0 \\ 0 \\ 0 \\ 0 \end{bmatrix}, \begin{bmatrix} 0 \\ 0 \\ 1 \\ 0 \\ 0 \\ 0 \end{bmatrix}, \begin{bmatrix} 0 \\ 0 \\ 0 \\ 1 \\ 0 \\ 0 \end{bmatrix}, \begin{bmatrix} 0 \\ 0 \\ 0 \\ 0 \\ 1 \\ 0 \end{bmatrix}, \begin{bmatrix} 0 \\ 0 \\ 0 \\ 0 \\ 0 \\ 1 \end{bmatrix}, \quad (3.2.49)$$

where  $[\mathbf{E}^*]_i$  for  $i = 1, \dots, 6$  designates the test given homogeneous strain.

### 3.3 Results and discussion

The presentation of the results is organized as follows: first, the numerical set up of the stochastic models of  $\overline{\text{TMD}}$  and HP is described; second, results of the stochastic micromechanical ( $S\mu M$ ) model of cortical bone are shown and compared with those of the nominal micromechanical ( $N\mu M$ ) model; then, the results of the microstructural  $\mu FE$  and  $\mu FFT$  models are presented; eventually, the  $S\mu M$  model is validated against the  $\mu FE$  and  $\mu FFT$  models and its accuracy assessed.

#### 3.3.1 Numerical set up of the stochastic models of $\overline{\text{TMD}}$ and HP.

Experimental statistics of  $\overline{\text{TMD}}$  and HP (estimated through Eqs. (3.2.4)-(3.2.5)) are reported in Tab. 3.2. Data refer to the *Calib* dataset. The average value of HP is 8.4%—a normal result in healthy subjects whose typical HP is in the range [5% – 10%]. Since the mineralization can vary significantly from one anatomical site to another (we have observed values of TMD of about  $1.2 g/cm^3$  in  $\mu CT$  images of human fibula, data not shown), the value of average mineralization of about  $1 g/cm^3$  is to be considered site- and patient-specific. It is worth noting that the dispersion of  $\overline{\text{TMD}}$  is very low ( $< 0.05$ ), while that of HP is quite high ( $> 0.5$ ).

Table 3.2: Experimental statistics of the *Calib* dataset.

HP [-]		$\overline{\text{TMD}}$ [ $g/cm^3$ ]	
$\mu^{\text{exp}}$	$\delta^{\text{exp}}$	$\mu^{\text{exp}}$	$\delta^{\text{exp}}$
0.084	0.547	0.999	0.028

Data in Tab. 3.2 have been considered as the available information about  $\overline{\text{TMD}}$  and HP and used to obtain the PDFs of the associated random variables. The optimal Lagrangian multipliers defined in the PDFs of Eq. (3.2.39) are obtained through the minimization problem given by Eq. (3.2.37):

$$\begin{aligned}\lambda_{\overline{\text{TMD}}}^* &= [580.86, -1167.89, 584.42], \\ \lambda_{\text{HP}}^* &= [-1.23, -22.45, 153.22].\end{aligned}\tag{3.3.1}$$

Convergence of the statistical estimators of the mean value and dispersion of the stochastic models of  $\overline{\text{TMD}}$  and HP towards the experimental values has been tested looking at the absolute and relative errors defined by:

$$\Delta^N(\cdot)_X = \left[ \widehat{(\cdot)}_X^N - (\cdot)_X^{\text{exp}} \right], \quad \Delta_{\text{rel}}^N(\cdot)_X = \frac{\Delta^N(\cdot)_X}{(\cdot)_X^{\text{exp}}},\tag{3.3.2}$$

where  $(\cdot)_X$  is a statistic of  $X$ . Convergence plots of the relative errors of the mean values and of the absolute errors of the dispersions are shown in Fig. 3.6. Convergence is assumed to be reached after  $N = 10^5$  realizations when all the errors are smaller than  $10^{-3}$ . This result was further validated looking at the convergence of the statistical estimators of the statistics of the elastic *moduli* of CB (see Fig. 3.7). In Fig. 3.7, the confidence interval (denoted by CI) is shown. Therefore, hereinafter, statistics of the stochastic models will refer to  $N = 10^5$  realizations.

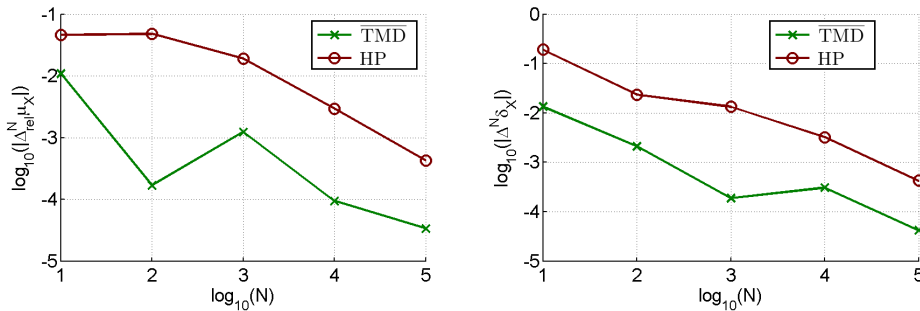


Figure 3.6: Convergence plots of the stochastic models of  $\overline{\text{TMD}}$  (green lines with ‘x’ markers) and HP (dark red lines with ‘o’ markers): Relative error of the mean values (on the left) and absolute error of the dispersions (on the right) as a function of the number of realizations.

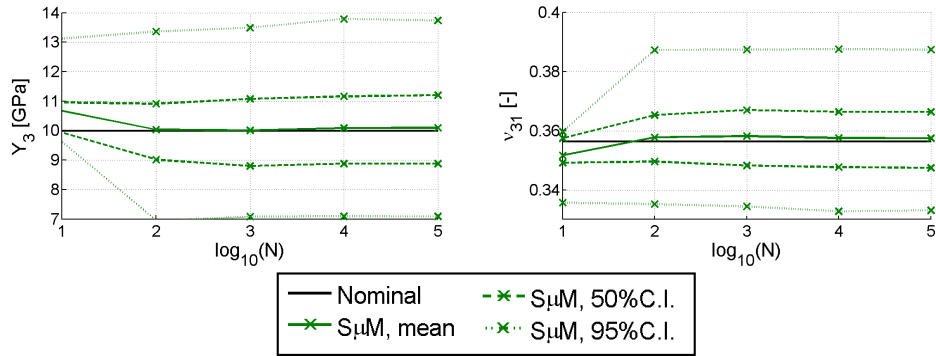


Figure 3.7: Convergence plots of the random elastic *moduli* of CB (green lines): Mean values and confidence intervals of the axial modulus  $Y_3$  (on the left) and of the lateral contraction ratio  $\nu_{31}$  (on the right) as a function of the number of realizations. Black lines depict the nominal values. Subscripts refer to the frames depicted in Fig. 3.3.

### 3.3.2 Stochastic and nominal micromechanical models of cortical bone elasticity

Statistics of the random elastic *moduli* ( $S\mu M$  model,  $N = 10^5$  realizations) and corresponding nominal values ( $N\mu M$  model) are reported in Tab. 3.3. The relative differences between the stochastic estimators of the mean values and the nominal values of all the elastic *moduli* are smaller than 1% (and even smaller than 0.1% for the ratio  $\nu_{31}$ ). This shows that the nominal model constitutes an accurate description of the mean elastic behavior of the cortical bone.

Table 3.3: Elastic *moduli* of cortical bone: *nominal* values and statistics (resulting from  $N = 10^5$  realizations) of the *stochastic* model.

Elastic <i>moduli</i>	$Y_1 (\equiv Y_2)$	$Y_3$	$G_{12}$	$G_{13} (\equiv G_{23})$	$\nu_{12} (\equiv \nu_{21})$	$\nu_{13}$	$\nu_{31}$
Units	[GPa]	[GPa]	[GPa]	[GPa]	[-]	[-]	[-]
<b>Nominal model</b>	7.84	10.00	2.94	3.12	0.333	0.280	0.356
<b>SM of (TMD,HP)</b>							
Mean value	7.91	10.10	2.97	3.15	0.336	0.279	0.358
$\Delta_{rel}^N$	-0.01	-0.01	-0.01	-0.01	-0.009	0.003	-0.003
Std Dev	1.55	1.71	0.63	0.64	0.027	0.016	0.014
Dispersion ([-])	0.20	0.17	0.21	0.20	0.080	0.056	0.039
25% quantile	5.50	7.49	1.99	2.15	0.296	0.252	0.336
75% quantile	8.93	11.20	3.39	3.57	0.353	0.290	0.366
5% quantile	6.81	8.88	2.52	2.70	0.317	0.268	0.348
95% quantile	10.57	13.07	4.06	4.24	0.383	0.304	0.382
2.5% quantile	5.11	7.09	1.83	1.98	0.292	0.247	0.333
97.5% quantile	11.15	13.73	4.30	4.47	0.394	0.307	0.388

An analysis of the Tab. 3.3 shows that the mean values of all the random *moduli* (except for  $\nu_{13}$ ) overestimate the corresponding nominal *moduli*. This can be explained by a qualitative analysis of Fig. 3.12 (a complete picture is shown in Fig. 3.14) and making use of the *Jensen's inequality* reported in App. C. In particular, these figures show that the surfaces representing the elastic *moduli* as a function of the model random variables ( $\overline{\text{TMD}}, \text{HP}$ ) are convex (except for  $\nu_{13}$ , which is concave) in the 99% *confidence region* of the space ( $\overline{\text{TMD}} \times \text{HP}$ ) (*i.e.* the region of the space ( $\overline{\text{TMD}} \times \text{HP}$ ) containing 99% of the realizations of the elastic *moduli*). Therefore, by making use of the Jensen's inequality, it is possible to conclude that the nominal value of each elastic modulus (except for  $\nu_{13}$ ) underestimates the mean value of the realizations of its stochastic counterpart. Moreover, this result will hold true also by changing the stochastic models of  $\overline{\text{TMD}}$  and HP as long as the 99% *confidence region* does not change noticeably.

Mean values and scalar dispersions (see Eq. (3.2.46)) of the elastic tensors of MF, US and CB are reported in Tab. 3.4 and Tab. 3.5, respectively. These two pieces of information ( $\hat{\mu}_{[\mathbb{C}_*]}^N$  and  $\hat{\delta}_{[\mathbb{C}_*]}^N$ ) constitutes the minimal necessary parameters for defining elastic tensors in the same symmetry class (see (Guilleminot and Soize, 2013)) and could be useful in further works.

The elastic tensors of MF, US and CB can be represented as linear combinations of the base tensors of their respective symmetry classes (see Appendix B). The mean values of the base coefficients (*i.e.* the coefficients of the linear combinations) predicted by the  $S\mu$ M model are reported in Tab. 3.4.

Table 3.4: Mean values of the base coefficients (see Appendix B) of the random elastic tensors of MF, US and CB.

Coeffs of $[\mathbb{C}_*] \in \text{Iso}$	$c_1$ ( $\equiv 3 \times K$ )	$c_2$ ( $\equiv 2 \times G$ )			
units	[GPA]	[GPA]			
$\hat{\mu}_{[\mathbb{C}_{MF}]}^N$	27.701	8.016			

Coeffs of $[\mathbb{C}_*] \in \text{TI}(\mathbf{e}_3)$	$c_1$	$c_2$	$c_3$	$c_4$	$c_5$
units	[GPA]	[GPA]	[GPA]	[GPA]	[GPA]
$\hat{\mu}_{[\mathbb{C}_{US}]}^N$	15.734	19.334	9.542	7.392	7.421
$\hat{\mu}_{[\mathbb{C}_{CB}]}^N$	14.382	16.890	8.499	5.944	6.292

The scalar dispersions of the elastic tensors of MF, US and CB are reported in Tab. 3.5. It can be noted that the scalar dispersion decreases when upscaling from the MF scale to the US scale—likely because of the weak dispersion of collagen (see Gagliardi et al. (2016 (submitted) for more details) then increases again when upscaling to the CB scale—likely because of the large dispersion of HP (see Tab. 3.2).

Table 3.5: Scalar dispersions of the random elastic tensors of MF, US and CB.

$\hat{\delta}_{[\mathbb{C}_{MF}]}^N$	$\hat{\delta}_{[\mathbb{C}_{US}]}^N$	$\hat{\delta}_{[\mathbb{C}_{CB}]}^N$
0.2033	0.1265	0.1435

### 3.3.3 Results of the $\mu$ FEM and $\mu$ FFT models

The FEM and FFT methods have been applied to all the RVEs (35 RVEs overall, 12 in the *Calib* dataset and 23 in the *Ctrl* dataset).

Both models produce anisotropic effective elastic tensors for the CB. Let  $\mathfrak{c}$  be an anisotropic elastic tensor. It was projected onto the classes of transversely isotropic and orthotropic tensors to investigate to what extent CB can be considered as a transversely isotropic material. In what follows, the transversely isotropic and orthotropic symmetry classes are denoted by TI for which the transverse axis is  $\mathbf{e}_3$ -direction and O respectively. Let  $[\mathfrak{c}]$  be the Kelvin's 2-order matrix representation of the elastic 4-th order tensor  $\mathfrak{c}$ , let  $\mathcal{P}_S([\mathfrak{c}])$  with  $S \in \{\text{TI}, \text{O}\}$  (see appendix B) be the projected matrix on the class of material symmetry  $S$  and,  $E_S([\mathfrak{c}])$  the distance of  $[\mathfrak{c}]$  from  $\mathcal{P}_S([\mathfrak{c}])$ :

$$\mathcal{P}_S([\mathfrak{c}]) := \sum_{i=1}^n \frac{[\mathfrak{c}] \cdot [\mathbf{b}_i]}{\|[\mathbf{b}_i]\|_F^2} [\mathbf{b}_i], \quad E_S([\mathfrak{c}]) := \frac{\|\mathcal{P}_S([\mathfrak{c}]) - [\mathfrak{c}]\|_F}{\|[\mathfrak{c}]\|_F}. \quad (3.3.3)$$

where  $n$  represents the dimension of the symmetry class  $S$ . Since the value of  $E_S([\mathfrak{c}])$  is in the interval  $[0, 1]$ , it represents a measure of the distance of the tensor  $\mathfrak{c}$  from the symmetry class  $S$ . Moreover, since the symmetry class O includes the one of TI, it turns out that  $E_O([\mathfrak{c}]) \leq E_{TI}([\mathfrak{c}])$ . Errors  $E_{TI}(\ast)$  and  $E_O(\ast)$  in the FEM and FFT simulations of the 35 RVEs are depicted in Fig. 3.9. For both methods, the mean values of  $E_{TI}(\ast)$  and of  $E_O(\ast)$  are about 2% and 1.5%, respectively. The FFT estimation generally returns slightly more anisotropic tensors. In both methods, highest errors are observed in the RVE #21 ( $E_{TI}(\ast) \sim 12\%$  and  $E_O \sim 4\%$ ), which is the most porous RVE (HP > 20%), and then in RVEs #35 (HP = 15.5%) and #6. These RVEs are shown in Fig. 3.8.

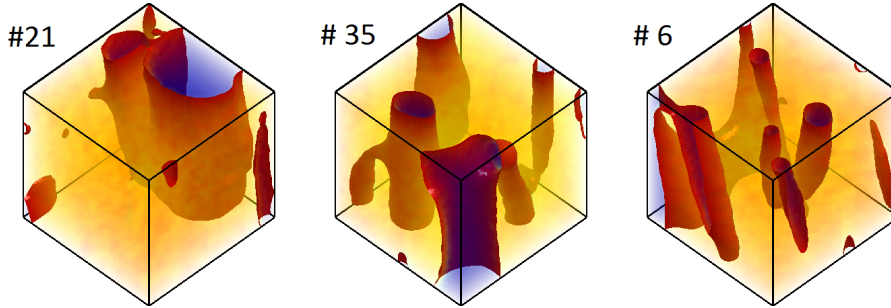


Figure 3.8: Reconstruction of the most anisotropic RVEs.

Base coefficients and relevant elastic *moduli* of the projection  $\mathcal{P}_{TI}([\mathfrak{c}])$  are reported in Tab. 3.8 and Tab. 3.9

Relative differences between the elastic *moduli* provided by the two methods are shown in Fig. 3.10. Lowest differences (most of time smaller than 5%) are observed for the axial *modulus*  $Y_3$  and contraction ratio  $\nu_{31}$ . Concerning this latter, the highest difference is found in RVE #6 (about 6%). Differences in the axial *moduli*  $Y_1$  and contraction ratios  $\nu_{13}$  and  $\nu_{12}$  are smaller than 10% excepting the RVE #35. Shear *moduli*  $G_{13}$  and  $G_{12}$  show differences smaller than 20%

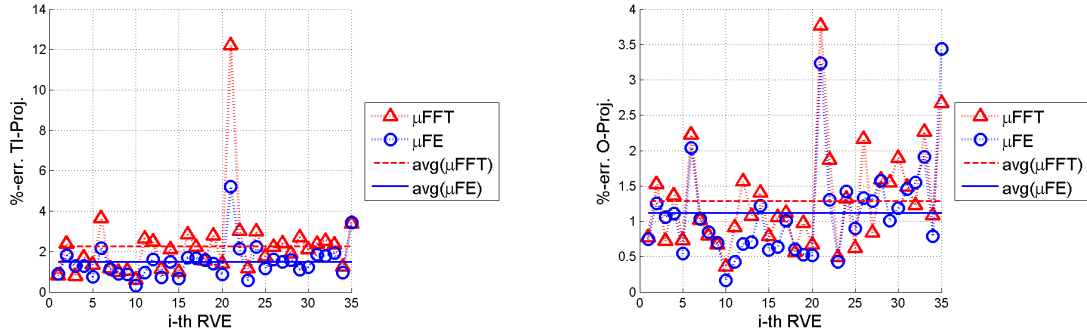


Figure 3.9: Distance of the anisotropic elastic tensors of the RVEs obtained by means of the  $\mu$ FFT and  $\mu$ FE models from transverse isotropy (on the left) and orthotropic (on the right) symmetry classes.

on all RVEs expect for RVEs #21 and #35. The high differences observed between  $\mu$ FE and  $\mu$ FFT results in the RVEs #21, #35 and #6 could be explained by the fact that they present big pores on their boundaries. This circumstance could introduce a big approximation in the periodic boundary displacement considered by the FFT method.

Average differences between the  $\mu$ FE and  $\mu$ FFT estimates of the elastic *moduli* are reported in Tab. 3.6. It can be noticed that, even including the RVEs #21, #35, and #6 (for which the highest differences can be observed), the average differences between the two models remain often quite limited. In particular, the average difference is (1) negligible ( $< 1\%$ ) for  $Y_3$  and  $\nu_{31}$ , (2) quite small (5%) for  $Y_1$ ,  $\nu_{13}$  and  $\nu_{12}$  and, (3) noticeable for  $G_{12}$  and  $G_{13}$  ( $> 10\%$ ). Focusing on the sign of these variations, we observe that most of times results of the  $\mu$ FE model overestimate those of the  $\mu$ FFT model (axial and shear *moduli* and  $\nu_{13}$ ). The opposite happens for  $\nu_{31}$  and  $\nu_{12}$  ratios. The origin of these differences, especially with respect to the contraction ratios and shear *moduli*, can have various interpretations. First, the two models are based on different representations of the heterogeneous microstructure of the RVEs. Whereas the  $\mu$ FFT model accounts for voxel-wise heterogeneity of the RVE and each voxel inherits its elastic properties based on its own GL (see Sec. 3.2.11), the  $\mu$ FE model considers a (small) number of homogeneous (sub)regions in the solid matrix and all the FEs inherit the elastic properties of the region that they belong to (see Sec. 3.2.10). Moreover, the two methods do not solve the same homogenization problem. Indeed, the  $\mu$ FE model solves BVPs with prescribed homogeneous strain on the boundary (*i.e.*  $\mathbf{u}(\mathbf{x}) = \mathbf{E}^*\mathbf{x}$  for all  $\mathbf{x} \in \partial\Omega$ ) whereas the  $\mu$ FFT model solves BVPs with prescribed periodic strain (*i.e.*  $\mathbf{u}(\mathbf{x}) - \mathbf{E}^*\mathbf{x}$  periodic for all  $\mathbf{x} \in \partial\Omega$ ). Eventually, it should be pointed out that the  $\mu$ FFT method could be affected by the mesh density (here  $50^3$  points).

### Computational time

From the point of view of computational time, the  $\mu$ FE model, despite its simplified representation of the RVEs, takes longer than the  $\mu$ FFT model. On a standard desktop computer,  $\mu$ FE simulations last about half an hour per RVE whereas  $\mu$ FFT simulations only a few minutes.

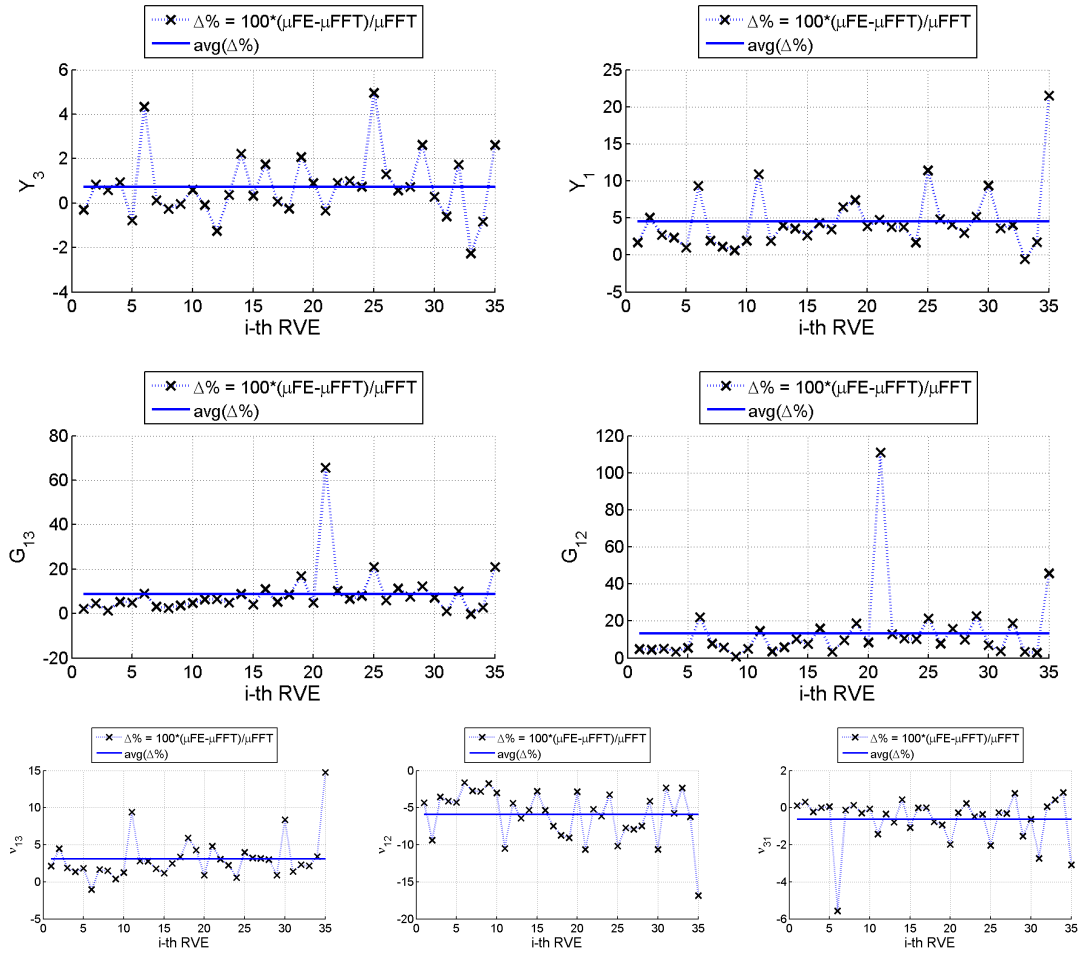


Figure 3.10: Elastic *moduli* of cortical bone. Differences between  $\mu$ FE and  $\mu$ FFT estimations on individual RVEs (crosses) and average differences (solid lines).

Table 3.6: Average differences between the  $\mu$ FE and  $\mu$ FFT estimations of the elastic *moduli* of cortical bone.

Elastic <i>moduli</i>	$Y_1$	$Y_2$	$Y_3$	$G_{12}$	$G_{13}$	$G_{23}$	$\nu_{12}$	$\nu_{13}$	$\nu_{31}$
$\% - \text{avg} \left( \frac{y^{\text{FEM}} - y^{\text{FFT}}}{y^{\text{FFT}}} \right)$	4.5	4.6	0.7	13.3	5.6	8.8	-5.92	3.08	-0.6271

### 3.3.4 Validation of the $S\mu$ M of cortical bone: by comparison with the $\mu$ FE and $\mu$ FFT estimates

In this section, the results of the stochastic micro-mechanical model will be compared with the approximations given by the FEM and FFT methods. Firstly, a RVE-wise analysis of the differences between the FFT and FEM approximations will be presented, then the FEM and

FFT results will be compared with the bounds defined by the confidence intervals and regions of the model.

**RVE-wise distance from FEM and FFT estimations** Each CB realization of the stochastic micro-mechanical model is the result of the application of the micro-mechanical model to a fictitious, idealized CB-RVE consisting in the 2-phase defined by a specific assignation of the couple  $(\overline{\text{TMD}}, \text{HP})$ . In Fig. 3.11, we report the relative differences between the finer estimations (FEM, FFT) of the database of 35 RVEs and the realizations of the  $S\mu\text{M}$  model corresponding to the real couple  $(\overline{\text{TMD}}, \text{HP})$  associated to each RVE. In Tab. 3.7 is reported the average values of the two set of errors.

Table 3.7: Stochastic model of *Cortical bone* approximation to  $\mu\text{FE}$  and  $\mu\text{FFT}$  estimations of elastic properties. Average value of the relative difference.

Elastic <i>moduli</i>	$Y_1$	$Y_2$	$Y_3$	$G_{12}$	$G_{13}$	$G_{23}$	$\nu_{12}$	$\nu_{13}$	$\nu_{31}$
$\% - \text{avg} \left( \frac{y^{\text{FEM}} - y^{\text{S}\mu\text{M}}}{y^{\text{S}\mu\text{M}}} \right)$	0.3	-1.3	0.6	-0.6	-1.0	-2.3	0.64	-0.27	0.0047
$\% - \text{avg} \left( \frac{y^{\text{FFT}} - y^{\text{S}\mu\text{M}}}{y^{\text{S}\mu\text{M}}} \right)$	-3.9	-5.5	-0.2	-11.0	-6.0	-9.7	7.06	-3.20	0.6544

From Tab. 3.7, we observe that generally the average error committed approximating the FEM reference model with the  $S\mu\text{M}$  model is lower than the FFT counterpart. The relative distance from the FEM-approximation is lower than 3% for each elastic *modulus*. Except for the shear moduli  $G_{12}$ ,  $G_{13}$  and  $G_{23}$ , the most of elastic *moduli* are not very distant from the FFT (about 5 – 10%) or, even returns no substantial difference ( $Y_3$  and  $\nu_{31}$ ) with the FEM-approximation. In general terms, the Tab. 3.7 however confirms that the  $S\mu\text{M}$  approximation overestimate the FFT approximation (except for the  $\nu_{12}$  ratio).

### 3.3.5 Accuracy of the stochastic model

In the preceding subsection, we underlined the average global distance of the set of RVE-wise predictions of the stochastic model. In this section we want to put this distance in the right perspective. For this reason, in Fig. 3.12, we plot the estimation of elastic *moduli* of the calibration subset of RVEs by FEM, FFT and  $S\mu\text{M}$  as function of the common information  $(\overline{\text{TMD}}, \text{HP})$ , against the background represented by the transformation of the confidence region at 50%, 95% and 99% of the  $S\mu\text{M}$  model driven by  $(\overline{\text{TMD}}, \text{HP})$ . The 95% confidence region of the stochastic model is able to envelope the most of the FEM and even the FFT estimates of the calibration dataset. Similarly, the 50% confidence region contains approximately the 50% results of the control set.

Figure 3.12 highlights also that the most of the worst approximations (*i.e.* #21 with HP 20% and #35 with HP 15%), being very close to the boundary of the 95% confidence region, could be considered outliers.

The same figure also shows how the elastic *moduli* are differently influenced by the  $\overline{\text{TMD}}$  and HP. More specifically, the elastic *moduli* are more influenced by the  $\overline{\text{TMD}}$  than the HP. Indeed, the intersections between the 99% confidence region and the two parametric study (two thin black lines) for the  $\mu(\text{HP})$ -fixed study  $\mu(\overline{\text{TMD}})$ -fixed line gives one insight of the difference.

For each parametric study, the minimum and maximum value of the elastic modulus can be estimated and the gap (max-min) of these values has been compared. The highest gap in the *moduli* of  $Y_1$ ,  $Y_3$ ,  $G_{31}$ ,  $G_{21}$  and  $\nu_{31}$  is attained for the  $\mu(\text{HP})$ -fixed study (variation of the  $\overline{\text{TMD}}$ ). Otherwise, the highest gap in the *moduli*  $\nu_{12}$  and  $\nu_{13}$  appears in the  $\mu(\overline{\text{TMD}})$ -fixed study.

This remark allows to observe that the variations  $Y_1$ ,  $Y_3$ ,  $G_{31}$ ,  $G_{21}$  and  $\nu_{31}$  *moduli*, in statistical terms, are mainly implied by that of  $\overline{\text{TMD}}$ . In other terms, the value of  $\overline{\text{TMD}}$  represents the main determinant of the elastic moduli listed above, because the estimates resulting from considering the same level of HP ( $\mu(\text{HP})$ ) for every RVEs would not differ significantly from that which considers each RVE to have a different value of HP. This constat is based on the confidence region obtained *via* the  $S\mu\text{M}$  model based on minimal information about the variables  $(\overline{\text{TMD}}, \text{HP})$  and could not be directly given by the very exiguous database of the calibration dataset.

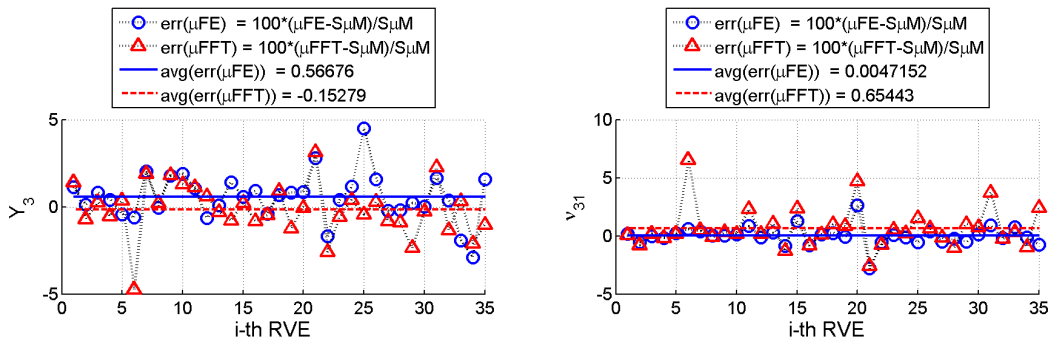


Figure 3.11: Relative differences of the FEM and FFT estimate from the  $S\mu\text{M}$  model. Axial *modulus* in the direction of bone axis ( $Y_3$ ) and lateral contraction ratio ( $\nu_{31}$ ).

Moreover, Fig. 3.13 shows the results of the FFT, FEM and  $S\mu\text{M}$  estimations for the whole dataset (calibration and control) and the confidence intervals of the stochastic model. As evidenced by this figure, the 95% confidence interval covers, not only, the 95% of the FEM and FFT estimations for the calibration dataset (*Calib* dataset), but also the control dataset (*Ctrl* dataset). This result shows that a stochastic model based on minimal information about two measures  $(\overline{\text{TMD}}, \text{HP})$  is able to reproduce the variability of a studied region of the cortical bone (at such a distance by the periosteum) and to capture finer estimation by FE and FFT methods for the most of elastic *moduli* (except for  $G_{12}$ ).

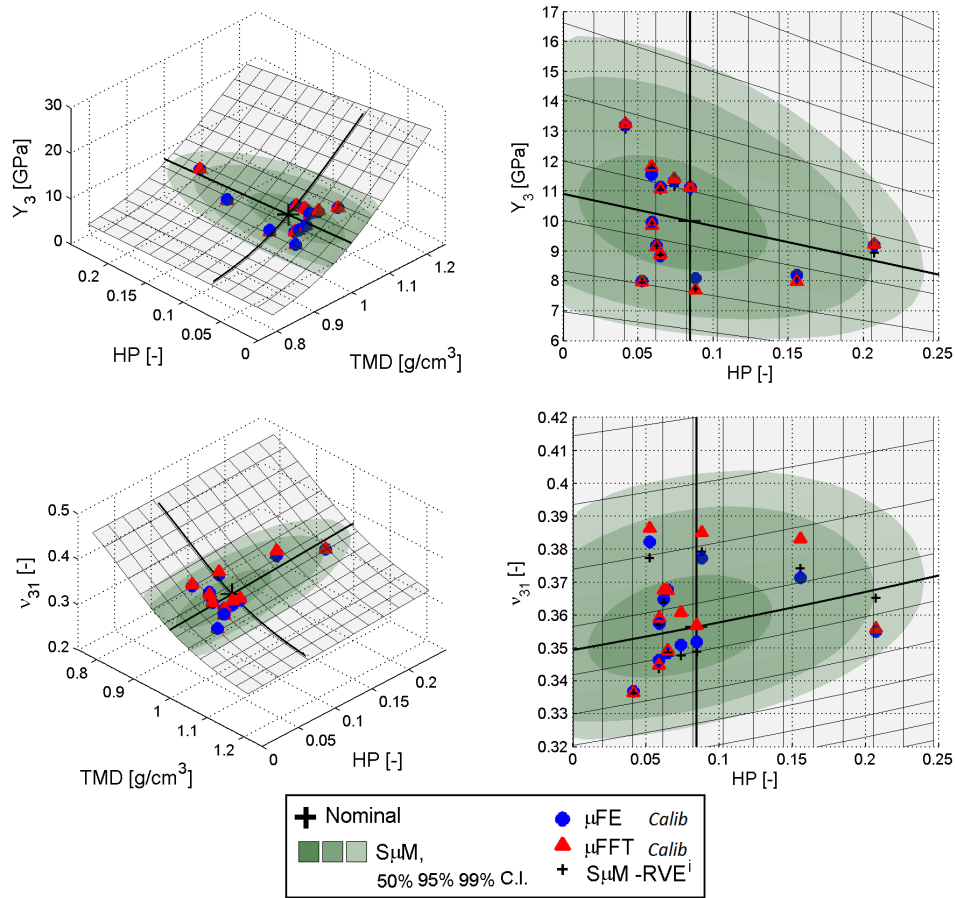


Figure 3.12: Comparison of the estimation of the elastic *moduli* as function of TMD and HP measure : (1) parametric study (gray surface); (2) region of the surface corresponding to the 50%, 95% and 99% confidence intervals of the stochastic model (green area with multiple transparencies); (3) estimations of the 12 RVEs by  $\mu$ FE (blue dots); (4) FFT (red triangles); (5) Nominal model (+).

### 3.4 Conclusion and perspective

In this chapter, a stochastic model of cortical bone based on the theory of micromechanical homogenization and the MaxEnt principle applied to a very exiguous information on TMD and HP measures estimated from  $\mu$ CT, has been presented. It has been shown that the information on the first two moments (mean and dispersion) for both TMD and HP measures at the resolution of scale (RVE) is sufficient for setting geometric-idealized model, able to compete with finer estimations. At millimeter scale, the choice of the Mori-Tanaka scheme for the homogenization with cylindrical inclusions allows to reproduce the same degree of anisotropy that the detailed models. Indeed, it has been shown that the *transverse isotropic* class of materials is the correct model, since it covers the 98% of the effective tensor estimated with both FE and FFT models.

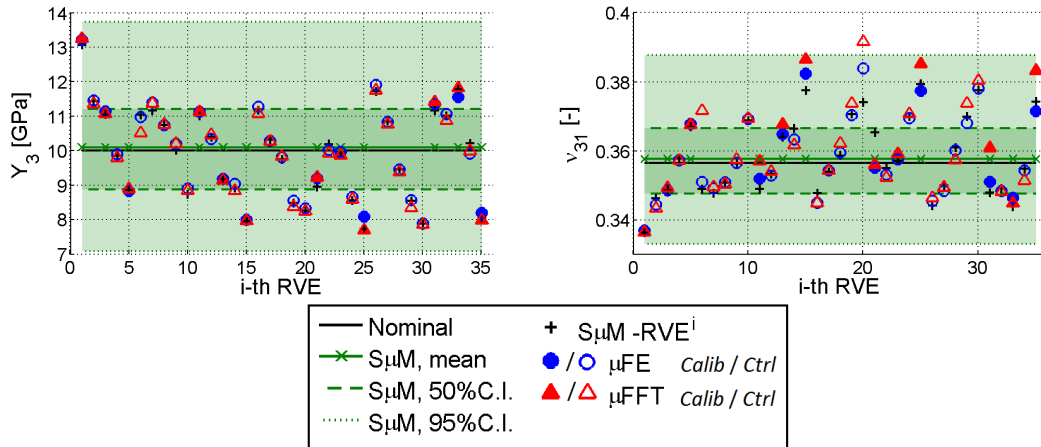


Figure 3.13: Axial *modulus* in the direction of bone axis  $Y_3$  and lateral contraction ratio  $\nu_{31}$

The class of orthotropic materials, benefiting of 4 more parameters, improve only of 1% the performances of the transverse isotropic class. Again, the stochastic model, contrarily to the FE and FFT methods applied to the same database, is able to determine confidence intervals and regions. These remarks allow to consider the  $S_{\mu M}$  as the first main benchmark to be applied before any deeper analysis on bone tissues. Furthermore, the confidence regions estimated with this method provides the probability landscape of the main six elastic *moduli* and represents a tool *a priori* for the interpretation of results given by other homogenization techniques. Finally, our simple  $S_{\mu M}$  based on the HP and mean value of the  $\overline{TMD}$  at the millimeter scale allows to verify that the most relevant factor in the estimation of elastic properties of cortical bone is given by the  $\overline{TMD}$ . Nevertheless, in terms of perspectives, the current model based on the  $(\overline{TMD}, HP)$  at millimeter RVE scale can be ameliorated including other interesting features as the correlation length of the main random variables  $(\overline{TMD}, HP)$  and other statistical constraints ( $f_2(x) = \log(x)$ ) allowing to improve the likelihood of the probability density function determined by the MaxEnt principle to the experimental one.

## 3.5 Appendix

### A Kelvin' representation of a 4th-order tensor

The elastic tensor  $\mathfrak{c}$  is defined as a 4th-order tensor in the tridimensional space describing the linear relation between the strain tensor  $\mathbf{E}$  and the stress tensor  $\mathbf{S}$ . This relation takes the form:

$$\mathbf{S} = \mathfrak{c} : \mathbf{E}, \quad S_{kl} = c_{klmn} E_{mn}, \quad (3.5.1)$$

where the symbol “:” between two tensors denotes a double contraction of adjacent indexes of tensors of rank two and higher.

The 3 symmetry conditions (*minor* and *major*) must be considered on the elastic tensor  $\mathfrak{c}$  (Podio-Guidugli, 2000):

$$c_{klmn} = c_{klnm}, \quad c_{klmn} = c_{lkmn}, \quad c_{klmn} = c_{mnlk}. \quad (3.5.2)$$

The second and fourth rank tensors in three dimensions are represented in a Euclidian six-dimensional space as vectors and tensors, respectively. To this end, the representation adopted in this work is called the *Kelvin's* representation in which the new indexes  $I$  et  $J$  vary in the set  $\{1, \dots, 6\}$  such as  $I = (k, \ell)$  and  $J = (m, n)$  where the indices  $k, \ell, m$  and  $n$  vary in the set  $\{1, \dots, 3\}$ . The relation between these indices is the following  $1 = (1, 1), 2 = (2, 2), 3 = (3, 3), 4 = (2, 3), 5 = (1, 3)$  and  $6 = (1, 2)$ . So, the symmetric matrix  $\tilde{\mathfrak{c}}$  associated with  $\mathfrak{c}$  is defined *via* these components by:

$$\tilde{c}_{IJ} = c_{klmn}. \quad (3.5.3)$$

The linear relation between the strain and stress vectors takes the form:

$$\begin{bmatrix} S_{11} \\ S_{22} \\ S_{33} \\ \sqrt{2}S_{13} \\ \sqrt{2}S_{23} \\ \sqrt{2}S_{12} \end{bmatrix} = \begin{bmatrix} \tilde{c}_{11} & \tilde{c}_{12} & \tilde{c}_{13} & \sqrt{2}\tilde{c}_{14} & \sqrt{2}\tilde{c}_{15} & \sqrt{2}\tilde{c}_{16} \\ \tilde{c}_{21} & \tilde{c}_{22} & \tilde{c}_{33} & \sqrt{2}\tilde{c}_{24} & \sqrt{2}\tilde{c}_{25} & \sqrt{2}\tilde{c}_{26} \\ \tilde{c}_{31} & \tilde{c}_{32} & \tilde{c}_{33} & \sqrt{2}\tilde{c}_{34} & \sqrt{2}\tilde{c}_{35} & \sqrt{2}\tilde{c}_{36} \\ \sqrt{2}\tilde{c}_{41} & \sqrt{2}\tilde{c}_{42} & \sqrt{2}\tilde{c}_{43} & 2\tilde{c}_{44} & 2\tilde{c}_{45} & 2\tilde{c}_{46} \\ \sqrt{2}\tilde{c}_{51} & \sqrt{2}\tilde{c}_{52} & \sqrt{2}\tilde{c}_{53} & 2\tilde{c}_{54} & 2\tilde{c}_{55} & 2\tilde{c}_{56} \\ \sqrt{2}\tilde{c}_{61} & \sqrt{2}\tilde{c}_{62} & \sqrt{2}\tilde{c}_{63} & 2\tilde{c}_{64} & 2\tilde{c}_{65} & 2\tilde{c}_{66} \end{bmatrix} \begin{bmatrix} E_{11} \\ E_{22} \\ E_{33} \\ \sqrt{2}E_{13} \\ \sqrt{2}E_{23} \\ \sqrt{2}E_{12} \end{bmatrix} \quad (3.5.4)$$

The transformation of the three-dimensional second rank tensor components to six-dimensional vector components is directly assured by these relations and *vice versa*. In particular, it has been shown in (Mehrabadi and Cowin, 1990) that the 2 and the  $\sqrt{2}$  factors introduced on certain *moduli* of  $\tilde{\mathfrak{c}}$  ensure that  $\tilde{\mathfrak{c}}$  is a tensor in Euclidian six-dimensional space. In addition, the  $\sqrt{2}$  factor on the vectors  $\tilde{\mathbf{S}}$  (whose the components are defined by  $[S_{11}, S_{22}, S_{33}, \sqrt{2}S_{13}, \sqrt{2}S_{23}, \sqrt{2}S_{12}]$ ) or  $\tilde{\mathbf{E}}$  guarantees that the scalar product of the six dimensional vectors is equal to the trace of the product of the corresponding second rank tensors  $\tilde{\mathbf{S}} \cdot \tilde{\mathbf{E}} = \text{Tra}(\mathbf{S}^T \mathbf{E})$  where Tra and "T" are is the trace and transposition operators, respectively

In the text body, the notation tilde has been dropped.

## B Representation of classes of material symmetry

In this section, we resume the representation of the symmetry class of isotropic materials used (1) for describing the result of micro-mechanical homogenization and (2) for approaching the problem of the classification of the results of the FE and FFT methods. For a wider overview on other symmetry classes we refer to the works of (Walpole, 1984) and (Guilleminot and Soize, 2013). In our presentation,  $N$  represent the number of necessary and sufficient coefficients  $c_i$  and elements of the orthogonal base (but generally non orthonormal)  $\{\mathfrak{b}_i\}$  for the complete definition of a isotropic symmetry class, denoted by  $S$ . For instance  $N = 5$  for a material in the *transverse isotropic* symmetry class,  $N = 9$  for the *orthotropic* one and  $N = 2$  for an *isotropic* one, and so on. This decomposition in the base is given by:

$$\mathfrak{c}_S := \sum_{i=1}^N c_i \mathfrak{b}_i . \quad (3.5.5)$$

### Isotropic material

An isotropic material is completely defined by two coefficients  $c_1$  and  $c_2$  and its base:

$$\begin{aligned} [\mathfrak{b}_1]_{ijkl} &= (1/3)\delta_{ij}\delta_{kl} \\ [\mathfrak{b}_2]_{ijkl} &= [\mathfrak{i}]_{ijkl} - [\mathfrak{b}_1]_{ijkl} \end{aligned} \quad (3.5.6)$$

where  $[\mathfrak{i}]$  denotes the fourth-order symmetric identity tensor (which is defined by the relation  $[\mathfrak{i}]_{ijkl} = 1/2(\delta_{ij}\delta_{kl} + \delta_{ik}\delta_{jl})$ ) and  $\delta_{ij}$  designates the Kronecker's symbol.

The two coefficients  $c_1$  and  $c_2$  can be related with other couples of coefficients as Lamés coefficients, or in the alternative way with Young's modulus and Poisson's ratio, according well known functions. For instance, it results that  $c_1 = 3 \times K$  and  $c_2 = 2 \times G$  where  $K$  and  $G$  are respectively the bulk and shear *moduli*.

### Transverse Isotropic material

A transverse isotropic material is completely defined by the direction of its axe of symmetry, hereafter noted  $\mathbf{e}_n$ . Once  $\mathbf{e}_n$  has been assigned, any transverse isotropic tensor is fully defined by:

$$\begin{aligned} \mathbf{p} &= \mathbf{e}_n \otimes \mathbf{e}_n, & \mathfrak{b}_1 &= \mathbf{p} \otimes \mathbf{p}; \\ \mathbf{q} &= \mathbf{i} - \mathbf{p}, & \mathfrak{b}_2 &= \mathbf{q} \otimes \mathbf{q}; \\ & & \mathfrak{b}_3 &= \frac{1}{\sqrt{2}} (\mathbf{p} \otimes \mathbf{q} + \mathbf{q} \otimes \mathbf{p}); \\ & & \mathfrak{b}_4 &= \mathbf{q} \boxtimes \mathbf{q} - \mathfrak{b}_2; \\ & & \mathfrak{b}_5 &= \mathbf{i} \boxtimes \mathbf{i} - \mathfrak{b}_1 - \mathfrak{b}_2 - \mathfrak{b}_4; \end{aligned} \quad (3.5.7)$$

where the  $\mathbf{i}$  represents the second order identity tensor and the products  $\otimes$  and  $\boxtimes$  operate as:

$$\begin{aligned} (g \otimes f)_{ij} &= g_i f_j; \\ [\mathbf{p} \otimes \mathbf{q}]_{ijkl} &= [\mathbf{p}]_{ij} [\mathbf{q}]_{kl}; \\ [\mathbf{p} \boxtimes \mathbf{q}]_{ijkl} &= \frac{1}{2} \left( [\mathbf{p}]_{ik} [\mathbf{q}]_{jl} + [\mathbf{p}]_{il} [\mathbf{q}]_{jk} \right). \end{aligned} \quad (3.5.8)$$

Throughout this work, the Haversian Porosity has been assumed to be aligned in the  $\mathbf{e}_3$  direction and the direction of the collagen molecules aligned to the direction of the HP. As consequence of the Mori-Tanaka scheme (MTs) of cylindrical inclusions in the  $\mathbf{e}_3$  direction and the micro-mechanical model of the Ultra-Structure transverse isotropic in the direction  $\mathbf{e}_n = \mathbf{e}_3$ . For the same reason, the application of the MTs to the cylindrical pores and the ultrastructure matrix produce a transverse isotropic (in the  $\mathbf{e}_n = \mathbf{e}_3$  direction) model of cortical bone.

We note  $\text{TI}(\mathbf{e}_n)$  the set of elastic tensors belonging to the symmetry transverse isotropic with axe  $\mathbf{e}_n$ .

### Orthotropic material

An orthotropic material is defined as a function of an orthonormal base described from the 3 vectors  $\mathbf{a}$ ,  $\mathbf{b}$  and  $\mathbf{c}$ . The nine base-tensors of 4-th order are given as function of its axis of symmetry. The general representation is given by:

$$\begin{aligned}
 \mathfrak{b}_1 &= \mathfrak{e}^{11}, & \mathfrak{e}^{11} &= (\mathbf{a} \otimes \mathbf{a}) \otimes (\mathbf{a} \otimes \mathbf{a}); \\
 \mathfrak{b}_2 &= \mathfrak{e}^{22}, & \mathfrak{e}^{22} &= (\mathbf{b} \otimes \mathbf{b}) \otimes (\mathbf{b} \otimes \mathbf{b}); \\
 \mathfrak{b}_3 &= \mathfrak{e}^{33}, & \mathfrak{e}^{33} &= (\mathbf{c} \otimes \mathbf{c}) \otimes (\mathbf{c} \otimes \mathbf{c}); \\
 \mathfrak{b}_4 &= (\mathfrak{e}^{12} + \mathfrak{e}^{21}) / 2, & \mathfrak{e}^{12} &= (\mathbf{a} \otimes \mathbf{a}) \otimes (\mathbf{b} \otimes \mathbf{b}); \\
 & & \mathfrak{e}^{21} &= (\mathbf{b} \otimes \mathbf{b}) \otimes (\mathbf{a} \otimes \mathbf{a}); \\
 \mathfrak{b}_5 &= (\mathfrak{e}^{23} + \mathfrak{e}^{32}) / 2, & \mathfrak{e}^{23} &= (\mathbf{b} \otimes \mathbf{b}) \otimes (\mathbf{c} \otimes \mathbf{c}); \\
 & & \mathfrak{e}^{32} &= (\mathbf{c} \otimes \mathbf{c}) \otimes (\mathbf{b} \otimes \mathbf{b}); \\
 \mathfrak{b}_6 &= (\mathfrak{e}^{13} + \mathfrak{e}^{31}) / 2, & \mathfrak{e}^{13} &= (\mathbf{a} \otimes \mathbf{a}) \otimes (\mathbf{c} \otimes \mathbf{c}); \\
 & & \mathfrak{e}^{31} &= (\mathbf{c} \otimes \mathbf{c}) \otimes (\mathbf{a} \otimes \mathbf{a}); \\
 [\mathfrak{b}_7]_{ijkl} &= (a_i b_j + a_j b_i) \cdot (a_k b_l + a_l b_k); \\
 [\mathfrak{b}_8]_{ijkl} &= (b_i c_j + b_j c_i) \cdot (b_k c_l + b_l c_k); \\
 [\mathfrak{b}_9]_{ijkl} &= (a_i c_j + a_j c_i) \cdot (a_k c_l + a_l c_k).
 \end{aligned} \tag{3.5.9}$$

where the used products are defined in Eq. (3.5.8). We denote by  $\mathcal{O}$  the set of elastic tensors belonging to the orthotropic symmetry class with respect to the axis  $(\mathbf{a}, \mathbf{b}, \mathbf{c})$ . This class is denoted by  $\mathcal{O}(\mathbf{a}, \mathbf{b}, \mathbf{c})$ .

### C Jensen' inequality

Let  $X$  be a  $d$ -dimensional random vector,  $h$  a *convex* function (respectively *concave*),  $Y$  a random variable defined by the image of  $X$  through  $h$  (*i.e.*  $Y = h(X)$ ), then:

$$h(\mathbb{E}(X)) \leq \mathbb{E}(Y) = \mathbb{E}(h(X)), \quad (h(\mathbb{E}(X)) \geq \mathbb{E}(Y) = \mathbb{E}(h(X))). \tag{3.5.10}$$

For detail on the proof see (Jacod and Protter, 2003).

Table 3.8: Estimation by FFT methods. Projection onto the transverse isotropic subspace  $\text{TIE}_n$ 

FFT														
RVE	$\theta$	z	%err.	$c_1$	$c_2$	$c_3$	$c_4$	$c_5$	$Y_1$	$Y_3$	$G_{12}$	$G_{13}$	$\nu_{12}$	$\nu_{13}$
#	[deg]	$\mu\text{m}$	[-]	[GPa]	[GPa]	[GPa]	[GPa]	[GPa]	[GPa]	[GPa]	[GPa]	[GPa]	[-]	[-]
1	-40	550	0.80	17.951	20.779	9.887	7.980	8.397	10.50	13.25	3.99	4.20	0.32	0.27
2	-40	450	2.38	15.684	17.861	8.790	6.235	6.822	8.41	11.36	3.12	3.41	0.35	0.26
3	-40	350	0.79	15.492	18.029	8.928	6.305	6.746	8.47	11.07	3.15	3.37	0.34	0.27
4	-40	250	1.71	14.178	17.075	8.650	5.811	5.987	7.79	9.80	2.91	2.99	0.34	0.28
5	-40	150	1.33	13.140	15.642	8.146	4.904	5.153	6.70	8.90	2.45	2.58	0.37	0.28
6	-30	550	3.64	14.744	16.990	8.458	5.754	6.193	7.81	10.53	2.88	3.10	0.36	0.26
7	-30	450	1.16	15.787	18.078	8.928	6.337	6.763	8.53	11.38	3.17	3.38	0.35	0.26
8	-30	350	0.99	15.253	18.147	9.028	6.490	6.743	8.61	10.76	3.25	3.37	0.33	0.28
9	-30	250	1.05	14.663	17.467	8.826	6.111	6.211	8.13	10.20	3.06	3.11	0.33	0.28
10	-30	150	0.61	13.229	15.980	8.365	5.069	5.178	6.88	8.85	2.53	2.59	0.36	0.29
11	-20	550	2.64	15.407	17.243	8.584	5.812	6.215	7.93	11.13	2.91	3.11	0.36	0.25
12	-20	450	2.48	14.789	17.152	8.614	5.919	6.138	7.96	10.46	2.96	3.07	0.34	0.27
13	-20	350	1.13	13.429	15.997	8.275	5.087	5.332	6.94	9.15	2.54	2.67	0.36	0.28
14	-20	250	2.13	13.119	15.678	8.186	4.889	5.157	6.69	8.85	2.44	2.58	0.37	0.28
15	-20	150	0.99	12.204	14.705	7.887	4.235	4.367	5.88	7.97	2.12	2.18	0.39	0.28
16	-10	550	2.84	15.437	17.784	8.805	6.150	6.551	8.30	11.08	3.07	3.28	0.35	0.26
17	-10	450	2.23	14.598	17.057	8.588	5.764	6.113	7.79	10.27	2.88	3.06	0.35	0.27
18	-10	350	1.56	14.103	16.407	8.370	5.338	5.638	7.28	9.83	2.67	2.82	0.36	0.27
19	-10	250	2.79	12.481	14.684	7.763	4.253	4.520	5.94	8.38	2.13	2.26	0.40	0.27
20	-10	150	1.40	12.569	15.230	8.105	4.523	4.622	6.23	8.26	2.26	2.31	0.38	0.28
21	0	550	12.22	12.914	13.412	7.027	3.479	4.259	5.11	9.23	1.74	2.13	0.47	0.20
22	0	450	3.04	14.077	16.203	8.200	5.279	5.638	7.22	9.93	2.64	2.82	0.37	0.26
23	0	350	1.16	14.226	16.794	8.558	5.494	5.856	7.47	9.87	2.75	2.93	0.36	0.27
24	0	250	2.99	12.753	14.940	7.881	4.351	4.710	6.08	8.60	2.18	2.36	0.40	0.26
25	0	150	1.76	11.788	13.895	7.531	3.701	3.936	5.26	7.71	1.85	1.97	0.42	0.26
26	10	550	2.22	16.214	18.645	9.122	6.706	7.131	8.96	11.75	3.35	3.57	0.34	0.26
27	10	450	2.40	15.080	17.400	8.664	5.903	6.384	8.00	10.77	2.95	3.19	0.36	0.26
28	10	350	1.90	13.584	15.996	8.196	5.177	5.505	7.05	9.39	2.59	2.75	0.36	0.27
29	10	250	2.70	12.482	14.789	7.820	4.333	4.720	6.03	8.35	2.17	2.36	0.39	0.27
30	10	150	2.11	11.949	14.169	7.605	3.981	4.199	5.58	7.87	1.99	2.10	0.40	0.27
31	20	550	2.38	15.945	17.775	8.974	6.290	6.687	8.42	11.41	3.14	3.34	0.34	0.26
32	20	450	2.53	15.085	16.962	8.454	5.624	6.250	7.70	10.87	2.81	3.12	0.37	0.25
33	20	350	2.34	16.318	18.915	9.227	6.893	7.289	9.17	11.82	3.45	3.64	0.33	0.27
34	20	250	1.24	14.275	16.933	8.509	5.741	5.989	7.74	10.00	2.87	2.99	0.35	0.27
35	20	150	3.38	11.809	13.160	7.083	3.281	3.701	4.80	8.00	1.64	1.85	0.46	0.23
$\mu$	-	-	2.26	14.193	16.513	8.401	5.406	5.746	7.35	9.91	2.70	2.87	0.37	0.27

## D Tables of the FFT and FEM results

## E Supplementary figures

## F Effects of the threshold $q$ on HP, $\overline{\text{TMD}}$ and nominal elastic *moduli*

Results of the stochastic and nominal micromechanical models may depend on the value of the threshold  $q$  discriminating the GLs attributed to the HP and US regions. In this section, this dependence is investigated with respect to the nominal model.

The variations of the elastic *moduli* of the CB for the nominal model, when changing the threshold  $q$  in the range  $[116, \dots, 146]$  are reported in Tab. 3.10. The results in this table show that the statistics of HP and  $\overline{\text{TMD}}$  are sensitive with respect to the value of  $q$ . More precisely, as the value of  $q$  increases, (1) the mean values of both HP and TMD increase; and (2) the dispersion of HP increases whereas that of  $\overline{\text{TMD}}$  decreases. Moreover, it can be noticed that the relative variation, denoted by %Var, of the statistics of HP is much higher than that of  $\overline{\text{TMD}}$ .

Interestingly, unlike HP and  $\overline{\text{TMD}}$ , the nominal elastic *moduli* appear to be quite insensitive

Table 3.9: Estimation by FEM methods. Projection onto the transverse isotropic subspace  $\text{TIE}_n$

FEM														
RVE	$\theta$	z	%err.	$c_1$	$c_2$	$c_3$	$c_4$	$c_5$	$Y_1$	$Y_3$	$G_{12}$	$G_{13}$	$\nu_{12}$	$\nu_{13}$
#	[deg]	$\mu\text{m}$	[-]	[GPa]	[GPa]	[GPa]	[GPa]	[GPa]	[GPa]	[GPa]	[GPa]	[GPa]	[-]	[-]
1	-40	550	0.91	17.918	20.773	9.892	8.286	8.500	10.75	13.21	4.14	4.25	0.30	0.27
2	-40	450	1.82	15.763	17.843	8.770	6.622	7.049	8.77	11.45	3.31	3.52	0.32	0.27
3	-40	350	1.28	15.543	17.975	8.901	6.561	6.878	8.69	11.13	3.28	3.44	0.32	0.27
4	-40	250	1.30	14.260	17.077	8.640	6.013	6.209	7.98	9.89	3.01	3.10	0.33	0.29
5	-40	150	0.74	13.042	15.498	8.081	5.094	5.308	6.86	8.83	2.55	2.65	0.35	0.29
6	-30	550	2.18	15.222	17.575	8.637	6.577	6.918	8.66	10.98	3.29	3.46	0.32	0.27
7	-30	450	1.14	15.808	18.135	8.949	6.660	7.013	8.82	11.39	3.33	3.51	0.32	0.27
8	-30	350	0.91	15.226	18.152	9.029	6.734	6.879	8.82	10.73	3.37	3.44	0.31	0.29
9	-30	250	0.86	14.648	17.413	8.801	6.166	6.351	8.18	10.20	3.08	3.18	0.33	0.29
10	-30	150	0.31	13.270	16.005	8.361	5.268	5.374	7.07	8.90	2.63	2.69	0.34	0.29
11	-20	550	0.95	15.449	17.659	8.739	6.597	6.880	8.69	11.12	3.30	3.44	0.32	0.27
12	-20	450	1.61	14.654	17.126	8.603	6.114	6.382	8.12	10.33	3.06	3.19	0.33	0.28
13	-20	350	0.73	13.423	15.933	8.221	5.379	5.564	7.20	9.18	2.69	2.78	0.34	0.29
14	-20	250	1.50	13.303	15.826	8.213	5.274	5.490	7.08	9.04	2.64	2.75	0.34	0.29
15	-20	150	0.67	12.200	14.635	7.840	4.457	4.598	6.09	8.00	2.23	2.30	0.37	0.29
16	-10	550	1.70	15.658	18.121	8.917	6.809	7.054	8.95	11.27	3.40	3.53	0.31	0.28
17	-10	450	1.68	14.591	17.037	8.567	6.027	6.316	8.03	10.28	3.01	3.16	0.33	0.28
18	-10	350	1.58	14.090	16.518	8.409	5.820	6.011	7.73	9.81	2.91	3.01	0.33	0.28
19	-10	250	1.41	12.659	14.979	7.844	4.867	5.049	6.57	8.55	2.43	2.52	0.35	0.28
20	-10	150	0.86	12.616	15.253	8.087	4.800	4.878	6.50	8.33	2.40	2.44	0.35	0.29
21	0	550	5.20	12.987	14.215	7.337	5.035	5.451	6.71	9.20	2.52	2.73	0.33	0.27
22	0	450	2.13	14.168	16.308	8.226	5.743	6.069	7.67	10.02	2.87	3.03	0.34	0.27
23	0	350	0.58	14.283	16.843	8.530	5.937	6.161	7.89	9.96	2.97	3.08	0.33	0.28
24	0	250	2.24	12.777	14.842	7.817	4.620	4.934	6.33	8.66	2.31	2.47	0.37	0.27
25	0	150	1.17	12.137	14.232	7.591	4.365	4.602	5.98	8.09	2.18	2.30	0.37	0.28
26	10	550	1.62	16.391	18.901	9.209	7.214	7.506	9.46	11.90	3.61	3.75	0.31	0.27
27	10	450	1.50	15.176	17.659	8.760	6.565	6.828	8.63	10.83	3.28	3.41	0.31	0.28
28	10	350	1.58	13.663	16.098	8.231	5.586	5.817	7.44	9.45	2.79	2.91	0.33	0.28
29	10	250	1.11	12.689	15.088	7.887	4.936	5.159	6.65	8.57	2.47	2.58	0.35	0.29
30	10	150	1.21	11.961	14.213	7.607	4.362	4.551	5.95	7.89	2.18	2.28	0.36	0.29
31	20	550	1.86	15.705	17.856	8.820	6.523	6.924	8.67	11.35	3.26	3.46	0.33	0.27
32	20	450	1.79	15.293	17.241	8.539	6.302	6.728	8.37	11.06	3.15	3.36	0.33	0.27
33	20	350	1.92	16.016	18.558	9.102	6.999	7.294	9.19	11.55	3.50	3.65	0.31	0.28
34	20	250	0.97	14.166	16.691	8.423	5.920	6.170	7.86	9.92	2.96	3.08	0.33	0.28
35	20	150	3.45	12.077	13.850	7.323	4.430	4.718	6.02	8.20	2.21	2.36	0.36	0.27
$\mu$	-	-	1.50	14.252	16.632	8.426	5.847	6.103	7.78	9.98	2.92	3.05	0.33	0.28

to the variations of  $q$ . Actually, a variation of  $q$  of more than 20% induces variations of the nominal elastic *moduli* smaller than 3%. This result can be interpreted as follows. By recalling that HP and  $\overline{\text{TMD}}$  are directly related to the volume fraction of the porosity and to the stiffness of the ultrastructure, respectively, increasing the value of  $q$  leads to two counteracting effects: on the one side, bone tissue becomes more porous (thus “softer”) and on the other side its solid matrix becomes “stiffer”. These two effects turn out to compensate each other leading to pretty insensitive effective elastic *moduli* of the homogenized medium.

Table 3.10: Effects of the variations of  $q$  on the first and second order statistics of HP,  $\overline{\text{TMD}}$  and *nominal elastic moduli* of cortical bone.

	$q$	TMD( $q$ )	$\mu_{\text{HP}}^{\text{exp}}$	$\delta_{\text{HP}}^{\text{exp}}$	$\mu_{\text{TMD}}^{\text{exp}}$	$\delta_{\text{TMD}}^{\text{exp}}$
	[-]	$g/cm^3$	[-]	[-]	$g/cm^3$	[-]
Ref.M.	131	0.6982	0.0844	0.5714	0.9992	0.0293
%-Var	22.90	27.92	25.00	16.30	0.65	4.23

Elastic moduli	$Y_1$	$Y_3$	$G_{12}$	$G_{13}$	$\nu_{12}$	$\nu_{13}$
	[GPa]	[GPa]	[GPa]	[GPa]	[-]	[-]
Ref.M.	7.842	9.997	2.941	3.120	0.333	0.280
%-Var	1.19	1.34	1.70	0.50	2.10	2.82

## Bibliography

- L. Apostol, V. Boudousq, O. Basset, C. Odet, S. Yot, J. Tabary, J.M. Dinten, E. Boiler, P.O. Kotzki, and F. Peyrin. Relevance of 2d radiographic texture analysis for the assessment of 3d bone micro-architecture. *Med Phys*, 33(9):3546–3556, 2006.
- A. Barkaoui and R. Hambli. Finite element 3d modeling of mechanical behavior of mineralized collagen microfibrils. *J Appl Biomater Biomech*, 9(3):199–205, 2011.
- A. Barkaoui and R. Hambli. Nanomechanical properties of mineralised collagen microfibrils based on finite elements method: biomechanical role of cross-links. *Computer Methods in Biomechanics and Biomedical Engineering*, 17(4):1590–1601, 2014.
- B. Brisard and L. Dormieux. FFT-based methods for the mechanics of composites: A general variational framework. *Computational Materials Science*, 49(3), 2010.
- J.J. Broz, S.J. Simske, and A.R. Greenberg. Material and compositional properties of selectively demineralised cortical bone. *Journal of Biomechanics*, 28(11):1357–1368, 1995.
- A.J. Burghardt, T.M. Link, and S. Majumdar. High-resolution computed tomography for clinical imaging of bone microarchitecture. *Clinical Orthopaedics and Related Research*, 469(8):2179–2193, 2011.
- COMSOL Multiphysics. *version 5.2*. COMSOL, Inc., Paris, France, 2015.
- S.C. Cowin. *Bone Mechanics Handbook*. Taylor and Francis, 2001.
- J.M. Crolet, B. Aoubiza, and A. Meunier. Compact bone: numerical simulation of mechanical characteristics. *Journal of biomechanics*, 26(6):677–687, 1993.
- L. Devroye. *Non Uniform Random Variate Generation*. Springer Verlag, New York, 1986.
- J.D. Eshelby. The determination of the elastic field of an ellipsoidal inclusion, and a related problems. *Proceeding Of The Royal Society of London*, 241(1226):376–396, 1957.

- D. Gagliardi, V. Sansalone, C. Desceliers, and S. Naili. Tissue mineral density measured at the sub-millimeter scale can provide reliable statistics of elastic properties of bone matrix. *Biomechanics and Modeling in Mechanobiology*, 2016 (submitted).
- M. Granke, Q. Grimal, W. J. Parnell, K. Raum, A. Gerisch, F. Peyrin, A. Saïed, and P. Laugier. To what extent can cortical bone millimeter-scale elasticity be predicted by a two-phase composite model with variable porosity? *Acta biomaterialia*, 12:207–215, 2015.
- J. Guilleminot and C. Soize. On the statistical dependence for the components of random elasticity tensors exhibiting material symmetry properties. *Journal of Elasticity*, 111(2):883–901, 2013.
- C. Hellmich, J. Barthelemy, and L. Dormieux. Mineral-collagen interactions in elasticity of bone ultrastructure - a continuum micromechanics approach. *European Journal of Mechanics - A/Solids*, 23:783–810, 2004.
- J. Jacod and P. E. Protter. *Probability Essentials*. Springer Science & Business Media, 2003.
- E.T. Jaynes. Information theory and statistical mechanics. *Physical Review*, 106(4):620–630, 1957a.
- E.T. Jaynes. Information theory and statistical mechanics. *Physical Review*, 108(2):171–190, 1957b.
- M. Langer, A. Pacureanu, H. Suhonen, Q. Grimal, P. Cloetens, and F. Peyrin. X-ray phase nanotomography resolves the 3d human bone ultrastructure. *PLoS One*, 7(8):e35691, 2012.
- N. Laws. The determination of stress and strain concentrations at an ellipsoidal inclusion in an anisotropic material. *Journal of Elasticity*, 7(1):91–97, 1977.
- N. Laws. A note on penny-shaped cracks in transversely isotropic materials. *Mechanics of Materials*, 4(2):209–212, 1985.
- MATLAB. *version 7.11 (R2010b)*. The MathWorks Inc., Natick, Massachusetts, 2010.
- M.M. Mehrabadi and S.C. Cowin. Eigentensors of linear anisotropic elastic materials. *Q. J. Mech. Appl. Math.*, 43(1):15–41, 1990.
- V. Monchiet. Combining FFT methods and standard variational principles to compute bounds and estimates for the properties of elastic composites. *Computer Methods in Applied Mechanics and Engineering*, 283:454–473, 2015.
- V. Monchiet and G. Bonnet. A polarization-based FFT iterative scheme for computing the effective properties of elastic composites with arbitrary contrast. *International Journal for Numerical Methods in Engineering*, 89(11):1419–1436, 2012.
- H. Moulinec and P. Suquet. A numerical method for computing the overall response of nonlinear composites with complex microstructure. *Computer Methods in Applied Mechanics and Engineering*, 157:69 – 94, 1998. ISSN 0045-7825.

- 
- S. Nemat-Nasser and M. Hori. *Micromechanics: overall properties of heterogeneous materials*. Applied Mathematics and Mechanics. North-Holland, 2nd edition, 1999.
- S. Nuzzo, F. Peyrin, P. Cloetens, J. Baruchel, and G. Boivin. Quantification of the degree of mineralization of bone in three dimensions using synchrotron radiation microtomography. *Med. Phys.*, 29(11):2672–2681, 2002.
- W.J. Parnell, M.B. Vu, Q. Grimal, and S. Naili. Analytical methods to determine the effective mesoscopic and macroscopic elastic properties of cortical bone. *Biomech Model Mechanobiol*, 39(21):5659–5678, 2011.
- P. Podio-Guidugli. *A Primer in Elasticity*, volume 58. Kluwer Academic Publishers, 2000.
- M. Racila and J.M. Crolet. Nano and macro structure of cortical bone: Numerical investigations. *Mechanics of Advanced Materials and Structures*, 14(8):655–663, 2007.
- E. Rohan, S. Naili, R. Cimirman, and T. Lemaire. Multiscale modeling of a fluid saturated medium with double porosity: Relevance to the compact bone. *Journal of the Mechanics and Physics of Solids*, 60(5):857–881, 2012.
- D. Ruffoni, P. Fratzl, P. Roschger, K. Klaushofer, and R. Weinkamer. Bone mineralization density distribution as a fingerprint of the mineralization process. *The Bone*, 40:1308–1319, 2007.
- V. Sansalone, S. Naili, V. Bousson, C. Bergot, F. Peyrin, J.D. Laredo, and G. Haiat. Determination of the heterogeneous anisotropic elastic properties of human femoral bone: from nanoscopic to organ scale. *J. Biomech.*, 43(10):1857–1863, 2010.
- V. Sansalone, S. Naili, and C. Desceliers. A stochastic homogenization approach to estimate bone elastic properties. *Comptes Rendus Mecanique*, 342(5):326–333, 2014.
- V. Sansalone, D. Gagliardi, C. Desceliers, V. Bousson, J.D. Laredo, F. Peyrin, G. Haiat, and S. Naili. Stochastic multiscale modelling of cortical bone elasticity based on high-resolution imaging. *Biomechanics and modeling in mechanobiology*, 15(1):111–131, 2016.
- C. Shannon. A mathematical theory of communication. *Tech. J.* 27, Bell Syst., 1948.
- Simpleware 5.0 ScanIP+. *version 5.0*. Simpleware Ltd, Exeter, UK, 2012.
- P. Suquet, editor. *Continuum micromechanics*. Number 377 in CISM Lecture Notes. Springer-Verlag, Wien, 1997.
- A. Suvorov and G. Dvorak. Rate form of the eshelby and hill tensors. *International Journal of Solids and Structures*, 2002.
- L.J. Walpole. Fourth-rank tensors of the thirty-two crystal classes: multiplication tables. *Proceeding of The Royal Society of London Serie A*, 391(1800):149–179, 1984.

A. Zaoui. Continuum micromechanics: Survey. *Journal of Engineering Mechanics (ASCE)*, 128(8):808–816, 2002.

T.I. Zohdi and P. Wriggers. Computational micro-macro material testing. *Archives of Computational Methods in Engineering*, 8(2):131–228, 2001.

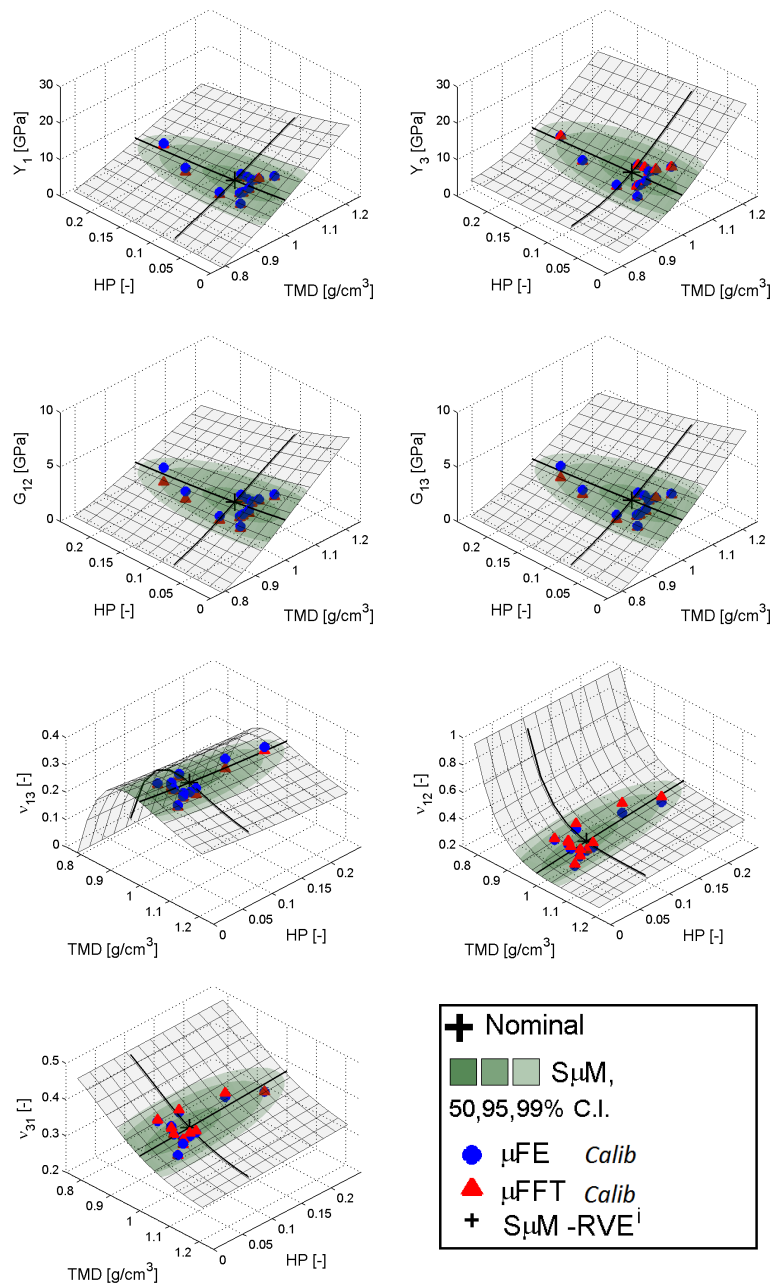


Figure 3.14: Comparison of the estimation of the elastic moduli as function of TMD and HP measure: (1) - parametric study (gray surface); (2) - region of the surface corresponding to the 50%; 95%; 99% confidence intervals of the of stochastic model ( green area with multiple transparencies); (3) - estimations of the 12 RVEs by  $\mu$ FE (blue dots); (4) - FFT (red triangles); (5) - Nominal model (+).

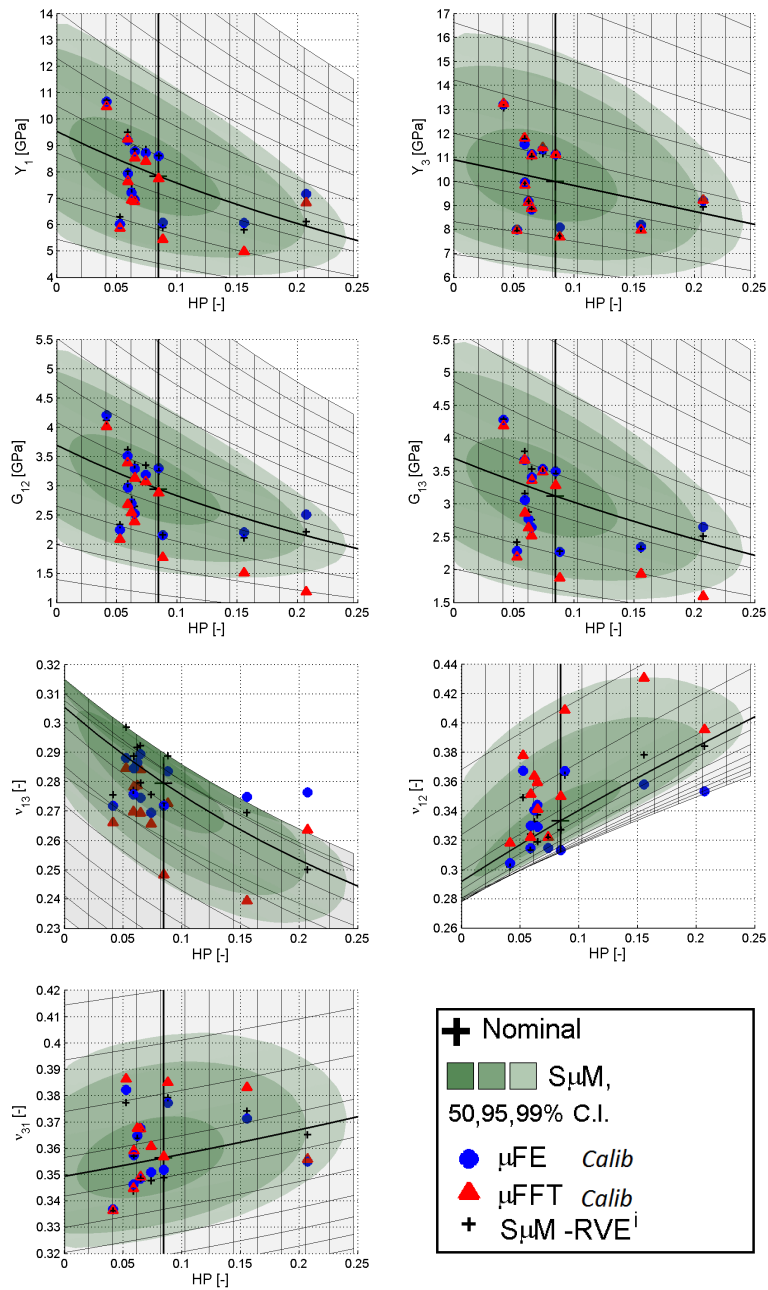


Figure 3.15: Comparison of the estimation of the elastic moduli as function of TMD and HP measure : (1) - parametric study (gray surface); (2) - region of the surface corresponding to the 50%; 95%; 99% confidence intervals of the of stochastic model ( green area with multiple transparencies); (3) - estimations of the 12 RVEs by  $\mu$ FE (blue dots); (4) - FFT (red triangles); (5) - Nominal model (+).

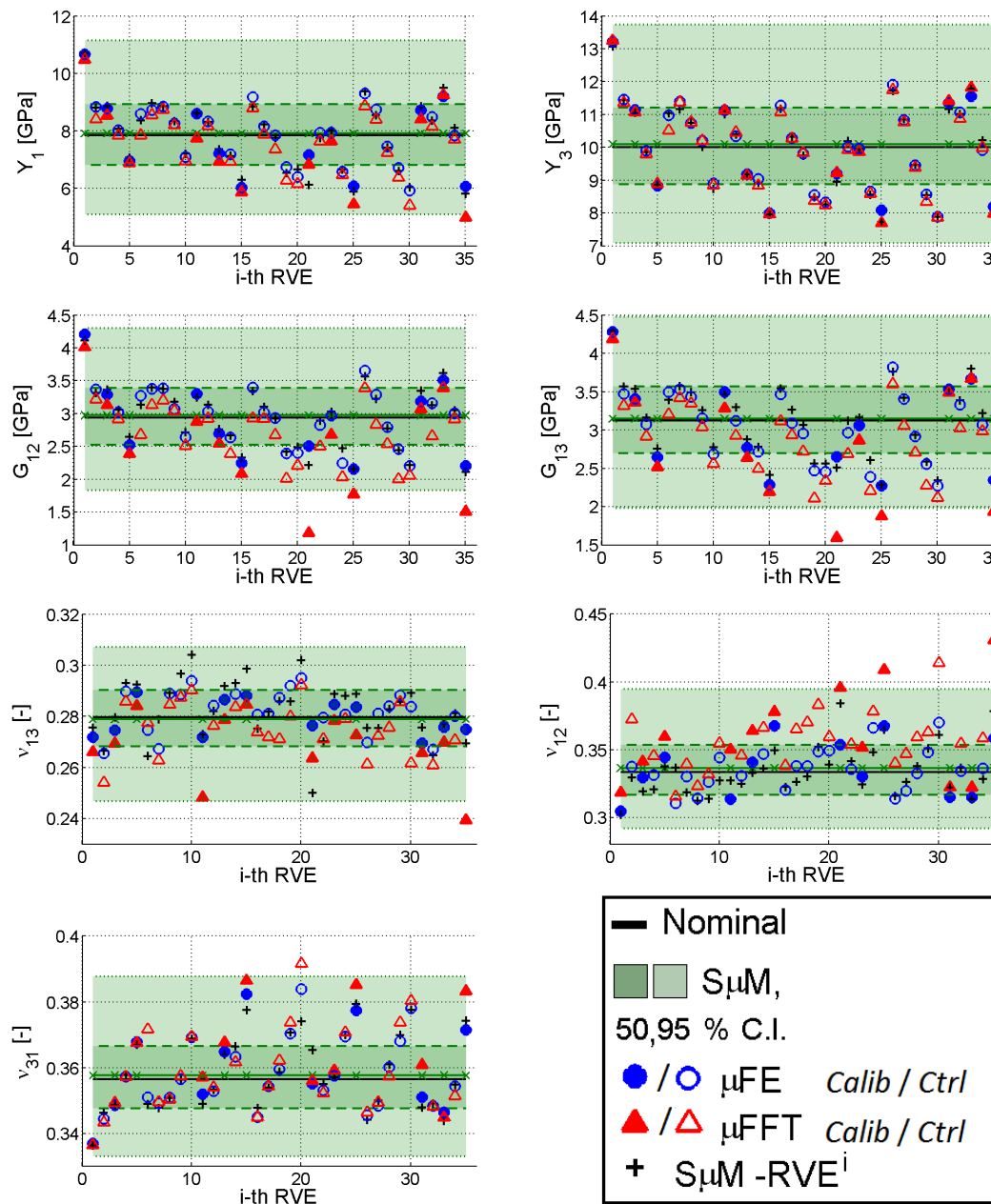


Figure 3.16: Comparison of estimation of elastic moduli as function of TMD and HP measure : 1 - Nominal model (black line) 2 - Average value of random realization of the Stoc. TMD-HP model, 3 - 50% and 95% Confidence interval of the Stoc. TMD-HP model 4 -  $\mu$ FE model realization

## Chapter 4

**The Matr-yoshka paradigm.  
Stochastic model for random  
matrices and fields with symmetry  
properties. Application to bone  
tissue.**

---

---

## Abstract

Bone tissue naturally presents heterogeneous mechanical properties which can vary not only from one person to another but also inside the same tissue. At a given anatomical site, mechanical properties can vary significantly but smoothly at the millimeter scale as well as at the deeper scales depending on the local bone microstructure. Representation of these local variations is a crucial issue for setting input data in reliable biomechanical models of bone.

Accurate assessment of spatial variations of bone microstructure can be hardly achieved using currently available imaging techniques. Therefore, there is a need for new modeling paradigms capable to account for uncertain experimental data.

Aiming at describing uncertain bone elastic properties, in this work we present a method for defining the random fields of elastic tensors for certain material symmetry classes of elasticity tensors currently found in bone tissue modeling. The solution of the problem allowing to obtain the random fields of elastic tensors has been given in the general framework of the theory of stochastic tensors—possibly represented as random matrices. The proposed construction allows to take into account the spatial heterogeneity *via* correlation length parameters. Simulations have been performed from the statistics of the first two moments (mean and variance or of derived quantities) obtained from *SR- $\mu$ CT* (synchrotron radiation micro-computed tomography) images. The proposed method allows to reproduce correctly the mean value and dispersion of the elastic tensor (without exiting from the material symmetry class). This point constitutes an extension of other works existing in literature.

## 4.1 Introduction

The aim of this work is to describe a robust and flexible method for constructing a random elastic tensor satisfying specific symmetry material properties. The focus will be set on the material symmetry classes currently found in modelling of bone tissue, *i.e.* isotropy, transverse isotropy, and orthotropy (see for instance (Gagliardi et al., 2016 (submitted))).

The general method has been developed by Soize and coworkers in a recent series of papers (see for instance (Guilleminot and Soize, 2013a,b, 2012; Soize, 2008)). In (Guilleminot and Soize, 2013a), the subject has been directly presented in terms of random fields of matrices expressing specific material symmetry properties (see Mehta (1991) for a general presentation of random matrix theory and (Soize, 2005) for its application in the context of linear elasticity theory). The overall methodology has been developed from the Maximum Entropy principle and information theory (Shannon, 1948; Jaynes, 1957a,b). In this chapter, we will proceed differently. We will present the subject placing greater emphasis on the general architecture and highlighting step by step the motivation of the different choices. The introduction of the spatial dependence in the method will be introduced afterwards.

Moreover, the original work of (Guilleminot and Soize, 2013a) introduced two sources of uncertainties in the representation of the random matrices (or random matrix fields). The first source produces a random matrix fluctuating in the prescribed symmetry group that the material is supposed to belong to; the second one is fully anisotropic. Such a parametrization offers some flexibility for both direct simulations and inverse identification thanks to the possibility to uncouple and separately control the levels of statistical fluctuations of the two sources of uncertainties. However, in the scope of this work, the material symmetry class is supposed to be already identified. Thus, we are only concerned with the part of the method describing the fluctuations inside a prescribed symmetry group, whereas the anisotropic contribution has been neglected. The reader interested in this latter topic can refer to Guilleminot and Soize (2013a) and find even more information in Soize (2006), where the subject is discussed more extensively. In any case, the anisotropic material symmetry class will be recalled separately in sec. 4.2.2 because it represents the base of the methodology and contains all the key-points to be discussed throughout the next sections.

The method for producing a random elasticity *matrix* with prescribed symmetry properties consists in a sequence of non-linear operations involving other random matrices, similarly to the assembling of a typical Russian doll called *Matryoshka*. Therefore, this method can be seen as the application of *random Matrix-Matryoshka* paradigm (or simply *Matr-yoshka* paradigm).

The work is presented following step by step a *Matryoshka*'s deconstruction procedure. The study is organized as follows. First, the weakest definition of a probability density function for an anisotropic tensor is specified and the basic problem is fixed. The general tool of the maximum entropy principle (denoted by MaxEnt) is delineated in its most general version. Then, the method allowing to assign a tensor to remain in a subspace of the material symmetry classes is presented. Specifically, it is shown how the formulation of the MaxEnt problem is applied to the underlying random matrices. Finally, the general procedure is applied to the three material symmetry classes (isotropic, transversely isotropic and orthotropic) of interest for modelling the bone tissue.

## 4.2 The general problem

In this study, we will respect almost integrally the notations adopted in (Guilleminot and Soize, 2013a). Therefore, some slight typographical adaptation has been necessary.

We denote by  $\mathbb{R}$  the set of real numbers and  $\mathbb{R}^+ := [0, +\infty)$  the set of positive real numbers. For any vectors  $x = (x_1, x_2, \dots, x_n)$  and  $y = (y_1, y_2, \dots, y_n)$  in  $\mathbb{R}^n$ , we designate by  $x \cdot y = \sum_i^n x_i y_i$  the Euclidean inner product in  $\mathbb{R}^n$  and by  $\|\bullet\|$  the norm  $\|x\|^2 = x \cdot x$ .

$\mathbb{M}_n(\mathbb{R})$  denotes the set of all  $(n \times n)$  square real matrices and  $\mathbb{M}_n^S(\mathbb{R})$  the subset of the symmetric ones.  $\mathbb{M}_n^+(\mathbb{R})$  denotes the subspace of symmetric-positive-definite matrices with the property  $\mathbb{M}_n^+(\mathbb{R}) \subset \mathbb{M}_n^S(\mathbb{R}) \subset \mathbb{M}_n(\mathbb{R})$ . The notations  $\det(\bullet)$ ,  $\text{tr}(\bullet)$  and  $(\bullet)^T$  designate respectively operators of determinant, trace and transposition of the matrices. Let  $[A]$  and  $[B]$  be 2 matrices in  $\mathbb{M}_n(\mathbb{R})$ , we denote by  $\langle [A], [B] \rangle := \text{tr}(A^T B)$  the inner product in  $\mathbb{M}_n(\mathbb{R})$ . We designate by  $\|[A]\|_F$  the Frobenius' (or Hilbert-Schmidt) norm of the matrix  $[A]$  obtained from the inner product ( $\|[A]\|_F^2 := \text{tr}(A^T A)$ ). Second order tensors are noted in bold letter (for instance,  $\mathbf{p}$ );  $[\mathbf{p}]$  designates the matrix representation of the tensor  $\mathbf{p}$ . Fourth order tensors are denoted by the blackboard font style as  $\mathbb{c}$ . Its matrix representation is denoted by  $[\mathbb{c}]$ . For any second order tensor  $\mathbf{p}$  and  $\mathbf{q}$ , the symbol  $\boxtimes$  denotes the symmetrized tensor product defined by the relation  $[\mathbf{p} \boxtimes \mathbf{q}]_{ijkl} = \frac{1}{2} ([\mathbf{p}]_{ik} [\mathbf{q}]_{jl} + [\mathbf{p}]_{il} [\mathbf{q}]_{jk})$ .

Random variables are denoted by *capital* letters, vectors by *capital* letters in a bold font style and matrices by *capital* letters in a *calligraphic* and *bold* font style. The generic random anisotropic elastic tensors is only slightly different. The operator of expected value of the random quantity  $\bullet$  in the brackets is denoted by  $\mathbb{E}(\bullet)$  whatever it represents (variable, vector or matrix).

### 4.2.1 Motivation and minimal available information

In this part, we want to set-up the material symmetry class of generalized non-parametric probabilistic problem for random matrices. Specifically, we consider a random matrix  $[\mathbb{C}]$  taking its values in the set of positive-definite matrices  $\mathbb{M}_n^+(\mathbb{R})$ . The matrix  $[\mathbb{C}]$  can represent (with  $n = 6$ ) the random elastic tensor  $\mathbb{C}$ . The minimal problem which we are interested is to produce a set of realization  $\{[\mathbb{c}_i] \in \mathbb{M}_n^+(\mathbb{R}), i = 1, \dots, N_r\}$ , where  $N_r$  is the realization number, representing the elastic tensor  $\mathbb{C}$  by matching with the assignation of its first and second order statistics defined by the *mean value*  $\mu_{[\mathbb{C}]}$  (sometimes here noted as  $[\underline{\mathbb{C}}]$ ) and the *dispersion*  $\delta_{[\mathbb{C}]}$  defined by:

$$\mu_{[\mathbb{C}]} = \mathbb{E}([\mathbb{C}]), \quad \delta_{[\mathbb{C}]}^2 = \frac{\mathbb{E}(\|[\mathbb{C}] - \mu_{[\mathbb{C}]}\|_F^2)}{\|\mu_{[\mathbb{C}]}\|_F^2}. \quad (4.2.1)$$

For sake of clarity, we recall that a random matrix (RM)  $[A]$  having a *finite* expected value is called *integrable* (*first order* RM, denoted as  $[A] \in L^1$ ), if it has a *finite* expectation value of  $\|[A]\|_F^2$  it is called *square-integrable* (*second order* RM, denoted by  $[A] \in L^2$ ). A RM  $[\mathbb{C}]$  fulfilling the requirements defined in Eq. (4.2.1) will necessarily belong to the set  $L^1 \cap L^2$ .

Let  $\{[\mathbb{c}_i], [\mathbb{c}_i] \in \mathbb{M}_n^+(\mathbb{R}), i = 1, \dots, N\}$  be a generic set of matrix representing the realizations of a random matrix  $[\mathbb{C}]$ , the first and second order statistics defined by Eq. (4.2.1) can be

approximated by the respective stochastic estimators defined by:

$$\hat{\mu}_{[\mathbb{C}]}^N = \frac{1}{N} \sum_{k=1}^N \mathbb{C}_k \quad \hat{\delta}_{[\mathbb{C}]}^N = \sqrt{\frac{\frac{1}{N-1} \sum_{k=1}^N \|\mathbb{C}_k - \hat{\mu}_{[\mathbb{C}]}^N\|_F^2}{\|\hat{\mu}_{[\mathbb{C}]}^N\|_F^2}}. \quad (4.2.2)$$

In general, for any set of matrix realizations  $\{[A_i], i = 1, \dots, N\}$  of any random matrix  $[A]$ , an index  $\mathcal{J}^\alpha$  measuring the proximity of the set of these realizations from those of the target random matrix  $[\mathbb{C}]$  can be defined as:

$$\mathcal{J}^\alpha([A]) = (1 - \alpha) \frac{\|\hat{\mu}_{[A]}^N - \mu_{[\mathbb{C}]}^N\|_F}{\|\mu_{[\mathbb{C}]}^N\|_F} + \alpha \frac{|\hat{\delta}_{[A]}^N - \delta_{[\mathbb{C}]}|}{\delta_{[\mathbb{C}]}} \quad (4.2.3)$$

where  $\alpha \in [0, 1]$ .

In the current practice, the requirement on the parameter of dispersion defined by Eq. (4.2.1) can be replaced by the following one:

$$\mathbb{E} \{ \ln [\det ([\mathbb{C}]))] \} = \nu_{[\mathbb{C}]} \quad (4.2.4)$$

where  $\nu_{[\mathbb{C}]}$  is an assigned constant such as  $\nu_{[\mathbb{C}]} < \infty$  and  $\ln$  is the natural logarithm. Indeed, it can be shown that the relation (4.2.4) implies the square-integrability of the random matrix  $[\mathbb{C}]$  (and its inverse (Soize, 2000)). This means that (at least implicitly) the assignation of the parameter  $\delta_{[\mathbb{C}]}$  can be fixed through a suitable choice of the parameter  $\nu_{[\mathbb{C}]}$  (with  $\delta_{[\mathbb{C}]} = \hat{\delta}_{[\mathbb{C}]}^N(\nu_{[\mathbb{C}]})$  where  $\hat{\delta}_{[\mathbb{C}]}^N$  designates the value of the function  $\hat{\delta}_{[\mathbb{C}]}^N$  for the value  $(\nu_{[\mathbb{C}]})$  and *vice-versa* (see Guilleminot and Soize (2012) for instance). Therefore, this implicit relation can be used for calibrating  $\delta_{[\mathbb{C}]}$  *via*  $\nu_{[\mathbb{C}]}$ . Consequently, the index defined by Eq. (4.2.3) can be replaced by the one expressed in terms of the proximity to the parameter  $\nu_{[\mathbb{C}]}$  (see Soize (2000) for more details).

Even if that is not really necessary for defining the solutions of the assigned isotropy problem in the following section, we will introduce to the reader to the general anisotropic problem because it represents the archetypal framework which we will refer to in the next sections.

## 4.2.2 Anisotropic problem from a minimal available information

The general problem of the construction of a random matrix expressing the properties of an elastic tensor (anisotropic case) can be set-up in the following terms.

We are interested in the construction of the *probability distribution*  $P_{[\mathbb{C}]}$  defined by *probability density function* (hereafter denoted by PDF)  $p_{[\mathbb{C}]}([\mathbb{C}])$  of a second order random matrix  $[\mathbb{C}]$ , the support  $\mathcal{S}$  of which, is represented by the open subset of  $\mathbb{M}_n^+(\mathbb{R})$  and the measure (volume element) is denoted by  $d[\mathbb{C}]$ :

$$[\mathbb{C}] \in \mathcal{S} \mapsto p_{[\mathbb{C}]}([\mathbb{C}]) \in \mathbb{R}^+ \quad P_{[\mathbb{C}]} := p_{[\mathbb{C}]}([\mathbb{C}]) d[\mathbb{C}], \quad \int_{\mathcal{S}=\mathbb{M}_n^+(\mathbb{R})} p_{[\mathbb{C}]}([\mathbb{C}]) d[\mathbb{C}] = 1. \quad (4.2.5)$$

Since  $\mathcal{S}$  is the set of symmetric-positive matrices, some algebra shows that  $d[\mathbb{C}]$  can be related to the product measure of its  $n \times (n+1)/2$  *diagonal* and *upper diagonal* elements as  $d[\mathbb{C}] = 2^{n(n-1)/4} \prod_{1 \leq i, j \leq n} d[\mathbb{C}]_{ij}$  (see Soize (2000)).

It is worthy to remark (already now) that this possibility to define the measure-element in  $\mathcal{S}$  as a function of the measure elements in a real space having as dimension the maximal number of degree of freedom of the symmetrical matrix ( $\mathbb{R}^{n \times (n+1)/2}$ ) is a key-ingredient that systematically will appear in the next sections.

The general problem of the research the PDF of a random matrix with *available information* on the first and second moment can be synthesized by the following system:

$$\begin{cases} \mathbb{E}\{\mathbf{1}_{\mathcal{S}}([\mathbb{C}])\} & = 1, \\ \mathbb{E}([\mathbb{C}]) & = \mu_{[\mathbb{C}]}, \quad \text{where } \mu_{[\mathbb{C}]} \in \mathbb{M}_n^+(\mathbb{R}) \\ \mathbb{E}\{\ln[\det([\mathbb{C}])]\} & = \nu_{[\mathbb{C}]}, \quad |\nu_{[\mathbb{C}]}| < \infty \end{cases} \quad (4.2.6)$$

where  $\mathbf{1}_{\mathcal{S}}(\bullet)$  denotes the characteristic function of the set  $\mathcal{S}$ .

Since the problem defined by the system (4.2.6) can generally admit an infinite solution, we need of a method to choose one of them. The Maximum Entropy (denoted by MaxEnt) principle which has been introduced firstly by Jaynes (Jaynes, 1957a,b) allows to select this PDF, among all possible candidates as the one that maximizes a measure of uncertainty represented by the Shannon's *entropy*. This cost function has been introduced by Shannon some year before in the the context of information theory (Shannon, 1948). The Shannon's entropy in the case of the random matrix theory can be defined as:

$$\mathcal{E}\{p_{[\mathbb{C}]}([\mathbb{c}])\} := - \int_{\mathcal{S}} \ln(p_{[\mathbb{C}]}([\mathbb{c}])) p_{[\mathbb{C}]}([\mathbb{c}]) d[\mathbb{C}]. \quad (4.2.7)$$

The PDF satisfying the MaxEnt principle is then defined by:

$$p_{[\mathbb{C}]}^*([\mathbb{c}]) = \arg \max_{p \in \mathcal{C}_{adm}} \mathcal{E}\{p_{[\mathbb{C}]}([\mathbb{c}])\} \quad (4.2.8)$$

where the operator  $\arg \max$  designates argument of the maximum,  $\mathcal{C}_{adm}$  represents the set of positive integrable PDF fulfilling the constraint of the available information given by (4.2.6). In the constrained optimization problem given by (4.2.8), the Shannon's entropy plays the role of the *Lagrangian* and the constrains can classically taken into account by using Lagrange's multipliers method. According to this method, an *augmented Lagrangian* denoted by  $\mathcal{L}_{aug}$  can be set-up by adding to the Lagrangian  $\mathcal{E}$  the suitable *internal-product* ( $\langle \bullet, \bullet \rangle$ ) between each constraint and quantities of the same specie (variables, vector, matrices), called Lagrange's multipliers (see Luenberger (1969) or (Kirk, 2004)).

The constraints given by (4.2.6) can be summarized by defining a function  $f : \mathcal{S} \mapsto \mathbb{R} \times \mathbb{M}_n^+(\mathbb{R}) \times \mathbb{R}$  and a target value  $f^{tar} \in \mathbb{R} \times \mathbb{M}_n^+(\mathbb{R}) \times \mathbb{R}$  as:

$$f([\mathbb{c}]) = \left\{ f^{(0)}, \left[ \mathbb{f}^{(1)} \right], f^{(2)} \right\}([\mathbb{c}]) := \{1, [\mathbb{c}], \ln[\det([\mathbb{c}])]\}, \quad f^{tar} = \{1, \mu_{[\mathbb{C}]}, \nu_{[\mathbb{C}]}\}. \quad (4.2.9)$$

Than, the available information turns to be defined by:

$$\int_{\mathcal{S}} f([\mathbb{c}]) p_{[\mathbb{C}]}([\mathbb{c}]) d[\mathbb{C}] = f^{tar}. \quad (4.2.10)$$

The augmented Lagrangian is defined by:

$$\begin{aligned} \mathcal{L}_{aug}(p_{[\mathbb{C}]}) &= \mathcal{E}(p_{[\mathbb{C}]}) - \{(\lambda^{(0)} - 1) [\int_{\mathcal{S}} p_{[\mathbb{C}]} - 1] + \\ &\quad + \langle [\Lambda^{(1)}], [\int_{\mathcal{S}} [\mathbb{f}] p_{[\mathbb{C}]} - \mu_{[\mathbb{C}]}] \rangle + (1 - \lambda^{(2)}) [\int_{\mathcal{S}} f^{(2)} p_{[\mathbb{C}]} - \nu_{[\mathbb{C}]}] \} . \end{aligned} \quad (4.2.11)$$

where the volume measure and the integration variable have been omitted for matter of compactness. The Lagrange's multipliers associated to the constrained given by (4.2.10) have been respectively denoted by  $(\lambda^{(0)} - 1)$ ,  $[\Lambda^{(1)}]$  and  $(1 - \lambda^{(2)})$ . The calculus of variation (*i.e.* Euler-Lagrange equation) applied to (4.2.11) implies that the solution of the MaxEnt optimization problem defined by (4.2.8) must have necessarily taken the following shape:

$$p_{[\mathbb{C}]}^{\{\lambda^{(0)}, [\Lambda^{(1)}], \lambda^{(2)}\}}([\mathbb{C}]) = c_0 \times \mathbf{1}_{\mathbb{M}_n^+(\mathbb{R})}([\mathbb{C}]) \times \det([\mathbb{C}])^{\lambda^{(2)}-1} \times \exp\left\{-\langle [\Lambda^{(1)}], [\mathbb{C}] \rangle\right\}, \quad (4.2.12)$$

where we have introduced the normalization constant  $c_0 = \exp\{-\lambda^{(0)}\}$ .

The expression  $p_{[\mathbb{C}]}^{\{\lambda^{(0)}, [\Lambda^{(1)}], \lambda^{(2)}\}}([\mathbb{C}])$ , represents a family of functions parametrized by  $\{\lambda^{(0)}, [\Lambda^{(1)}], \lambda^{(2)}\}$  and if it is integrable and normalized, it represents a probability density function. If  $p^{\{\lambda^{(0)}, [\Lambda^{(1)}], \lambda^{(2)}\}}$  is supposed to be integrable as the normalization constant  $c_0$ , and consequently, the parameter  $\lambda^{(0)}$  can be always implicitly fixed as a function of the other parameters  $[\Lambda^{(1)}], \lambda^{(2)}$ . Therefore, the integrability condition is uniquely based on the existence of a non-empty set  $\mathbb{D}_{\lambda} \subseteq \{\{[\Lambda^{(1)}], \lambda^{(2)}\}, \{[\Lambda^{(1)}], \lambda^{(2)}\} \in \mathbb{M}_n \times \mathbb{R}\}$  ( $\mathbb{M}_n$  being the set of the squared matrices of dimension  $n$ ) where the parameters  $\lambda^{(2)}$  and  $[\Lambda^{(1)}]$  can be picked. Fortunately,  $\mathbb{D}_{\lambda}$  is not empty because PDF defined by (4.2.12) is integrable for  $\lambda^{(2)} > 0$  and  $[\Lambda^{(1)}] \in \mathbb{M}_n^+(\mathbb{R})$  (see Siegle's integral and generalized Gamma function in (Soize, 2000)). Finally, the constraints on the first and second order are satisfied if there exists some suitable combination  $\{(\lambda^{(2)})^*, [\Lambda^{(1)}]^*\} \in \mathbb{D}_{\lambda}$ . Thanks to some algebra (Cholesky's decomposition of a definitive positive matrix and characteristic function of the random matrix  $[\mathbb{C}]$  (Soize, 2000)) it can be found that these optimal parameters should satisfy the explicit relation with the data  $\mu_{[\mathbb{C}]}$  and  $\delta_{[\mathbb{C}]}$ :

$$\delta_{[\mathbb{C}]} = \left\{ \frac{1}{n-1+2(\lambda^{(2)})^*} \left( 1 + \frac{\text{tr}(\mu_{[\mathbb{C}]})^2}{\text{tr}(\mu_{[\mathbb{C}]}^2)} \right) \right\}, \quad \mu_{[\mathbb{C}]} = \frac{n-1+2(\lambda^{(2)})^*}{2} \left\{ [\Lambda^{(1)}]^* \right\}^{-1}. \quad (4.2.13)$$

Similarly, but simpler, the dependencies between the target values and optimal Lagrange's multipliers will appear for a specific material symmetry class.

In the next section we will approach the solution of the problem of defining the PDF of a random matrix fluctuating in a prescribed space of symmetry.

More specifically, in the proposed procedure, the application of the MaxEnt principle is gradually displaced from the level of the final non-Gaussian result ( $[\mathcal{M}]$ ) to the level of the Gaussian component-vector ( $\Xi$ ) shown in Fig. 4.1. In other terms, the procedure is disassembled from outer layer of the Matryoshka scheme to the most intern one.

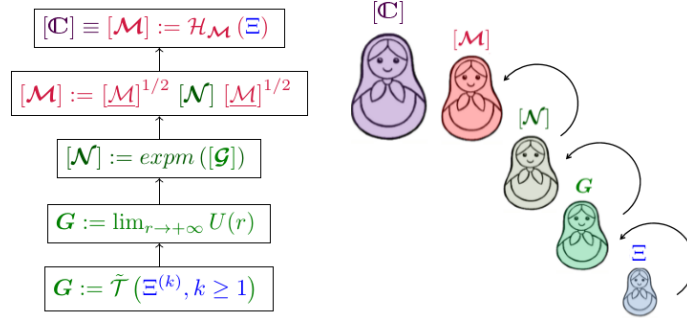


Figure 4.1: Scheme for the construction of the matrix representation of a random elastic tensor fluctuating inside a prescribed material symmetry class.

### 4.3 Constraint on the subspace of a material symmetry class

The concepts, we recall in the following, are borrowed from sect. 14, 15 and 16 of (Podio-Guidugli, 2000). The classification of a linear elasticity tensor  $\mathfrak{c}$  consists in the search of the set of antisymmetric tensor  $\mathbf{Q}$  representing rotation satisfying the relation:

$$\mathbf{Q}(\mathfrak{c}\mathbf{E})\mathbf{Q}^T = \mathfrak{c}(\mathbf{Q}\mathbf{E}\mathbf{Q}^T) \quad \forall \mathbf{E} \in \mathbb{M}_3^S \quad (4.3.1)$$

having  $\mathbf{E}$  the role of the symmetric part of the gradient of the deformation ( $\mathbf{E} \in \mathbb{M}_3^S$ ). For a given tensor  $\mathfrak{c}$ , the collection  $\mathcal{G}_{\mathfrak{c}}$  of admissible  $\mathbf{Q}$  satisfying (4.3.1) is called *symmetry group* of  $\mathfrak{c}$ . Hereafter the subset of  $\mathbb{M}_n^+(\mathbb{R})$  representing a tensor  $\mathfrak{c}$  that belongs to an assigned subset of symmetry will be denoted by  $\mathbb{M}_n^{sym}(\mathbb{R})$  ( $[\mathfrak{c}] \in \mathbb{M}_n^{sym}(\mathbb{R})$ ).

Let us suppose that the random matrix  $\mathbb{M}_n^+(\mathbb{R})$ -valued  $[\mathbf{C}]$  coincides with some  $\mathbb{M}_n^{sym}(\mathbb{R})$ -valued random matrix  $[\mathbf{M}]$  exhibiting a prescribed symmetry (with his mean value  $\underline{\mathcal{M}} \equiv \underline{\mathbf{C}}$ ). The available information to be submitted to the MaxEnt Principle can be updated to:

$$[\mathbf{M}] \text{-Max-Ent} : \begin{cases} \mathcal{S}_{[\mathbf{M}]} & = \mathbb{M}_n^{sym}(\mathbb{R}) \\ \mathbb{E}\{[\mathbf{M}]\} & = \underline{\mathcal{M}} \\ \mathbb{E}\{\ln(\det([\mathbf{M}]))\} & = \nu \end{cases} . \quad (4.3.2)$$

Let  $\{\mathbf{b}_i\}_{i=1}^N$  be the  $N$  elements of the orthogonal base representing the chosen symmetry class, for instance,  $N = 2$  for the *isotropic* symmetry class,  $N = 5$  for the *transverse isotropic* symmetry class,  $N = 9$  for the *orthotropic* symmetry class,  $\dots$ ,  $N = 21$  for the fully anisotropic case. Let  $\{[\mathbf{b}_i]\}_{i=1}^N$  their matrix representation in  $\mathbb{M}_n^{sym}(\mathbb{R})$  then the random matrix  $[\mathbf{M}]$  can be decomposed on these matrix-base as combination of an  $N$ -dimensional random vector defined by  $\mathbf{M} := (M_1, \dots, M_N)$  as follows:

$$[\mathbf{C}] \equiv [\mathbf{M}] = \sum_{i=1}^N M_i [\mathbf{b}_i]. \quad (4.3.3)$$

Since the base is fixed once and for all, the PDF of  $[\mathcal{M}]$  ( $p_{[\mathcal{M}]}$ ) is fully characterized by that of  $\mathbf{M}$  ( $p_{\mathbf{M}}$ ) provided with the preservation of the positivity constraint (the support of  $\mathbf{M}$  is given by  $\mathcal{S}_{\mathbf{M}} = \mathcal{C}^+$ ) of its linear combination with the base matrices (see Eq. (4.3.9))

$$\mathcal{C}^+ := \left\{ \mathbf{m} \in \mathbb{R}^N, \mathbf{m} \neq \mathbf{0} \mid \sum_{i=1}^N m_i [\mathbf{b}_i] \text{ is positive definite} \right\}. \quad (4.3.4)$$

Equivalently, the information on the mean value of the random matrix  $[\underline{\mathcal{M}}]$  can be transferred to the mean value of the random vector  $\underline{M}$ :

$$[\underline{\mathcal{M}}] = \mathbb{E}\{[\mathcal{M}]\} = \mathbb{E}\left\{\sum_{i=1}^N M_i [\mathbf{b}_i]\right\} = \sum_{i=1}^N \mathbb{E}\{M_i\} [\mathbf{b}_i] = \sum_{i=1}^N \underline{M}_i [\mathbf{b}_i], \quad \underline{M} = (\underline{M}_1, \dots, \underline{M}_N). \quad (4.3.5)$$

The constraint (4.3.4) is sufficient (see square-root matrix theorem (Gurtin, 1982)) for splitting any realization of the square matrix  $[\mathcal{M}]$  in the product of its square-root matrix  $[\mathcal{M}] = [\underline{\mathcal{M}}]^{1/2} [\mathcal{N}]^{1/2}$ .

The same decomposition applied to the main value  $[\underline{\mathcal{M}}]$  suggests another path:

$$[\underline{\mathcal{M}}] = [\underline{\mathcal{M}}]^{1/2} [\underline{\mathcal{M}}]^{1/2} = [\underline{\mathcal{M}}]^{1/2} [I_n] [\underline{\mathcal{M}}]^{1/2} \quad (4.3.6)$$

where  $I_n$  denotes the matrix identity of dimension  $n$ . Indeed, it is possible to define an auxiliary random matrix  $[\mathcal{N}]$  satisfying the condition:

$$[\mathcal{M}] = [\underline{\mathcal{M}}]^{1/2} [\mathcal{N}] [\underline{\mathcal{M}}]^{1/2} \quad (4.3.7)$$

and representable on the same base of  $[\mathcal{M}]$ . Once the mean value of  $\underline{M}$  is fixed, the MaxEnt problem can be transferred to the normalized random matrix  $[\mathcal{N}]$ .

### 4.3.1 Constraint on the subspace of a material symmetry class for the normalized random matrix

The MaxEnt problem given by (4.3.2) can be replaced by:

$$[\mathcal{N}] \text{-Max-Ent} : \begin{cases} \mathcal{S}_{[\mathcal{N}]} & = \mathbb{M}_n^{sym}(\mathbb{R}) \\ \mathbb{E}\{[\mathcal{N}]\} & = [I_n] \\ \mathbb{E}\{\ln(\det([\mathcal{N}]))\} & = \nu_{\mathcal{N}}, |\nu_{\mathcal{N}}| < +\infty \end{cases}. \quad (4.3.8)$$

where  $\nu_{\mathcal{N}}$  is a quantity derived of  $\nu$  from  $[\underline{\mathcal{M}}]$ . So, there exists a random vector  $\mathbf{N} := (N_1, \dots, N_n)$  such that:

$$[\mathcal{N}] = \sum_{i=1}^n N_i [\mathbf{b}_i]. \quad (4.3.9)$$

Note that in the one-dimension case if  $\mathcal{N} = X$  and  $\mathcal{M} = aX$ , with the relation  $a \in \mathbb{R}$  then  $\nu_{\mathcal{N}} = \nu_{\mathcal{M}} - \ln(a)$ .

The random matrix  $[\mathcal{N}]$  is defined on the same support as  $[\mathcal{M}]$ . Nevertheless, a non-linear transformation allows to relax this constraint (see further in this section).

The construction of  $[\mathcal{N}]$  can be indirectly provided by defining again another random matrix  $[\mathcal{G}]$  and setting  $[\mathcal{N}]$  as the matrix exponential of  $[\mathcal{G}]$ :

$$[\mathcal{N}] = \text{expm} [\mathcal{G}], \quad (4.3.10)$$

where  $\text{expm}(\bullet)$  denotes the matrix exponential.

The existence of this matrix is ensured by the Prop. 2.1 given in (Guilleminot and Soize, 2013a) that we reported below.

Let  $[N] \in \mathbb{M}_n^{\text{sym}}(\mathbb{R})$  and  $\{\mathbb{b}_i\}_{i=1}^N$  be the matrix basis of  $\mathbb{M}_n^{\text{sym}}(\mathbb{R})$ . Then there exists a unique symmetric  $[G] \in \text{span}(\{\mathbb{b}_i\}_{i=1}^N)$  such that:

$$[N] = \text{expm} [G]. \quad (4.3.11)$$

Note that the use of  $[\mathcal{G}]$  supplies many advantages:

1. the definite positivity of  $[\mathcal{N}]$  is automatically ensured by the matrix exponential such as  $\text{expm}(\bullet)$ ;
2.  $[\mathcal{G}]$  must not be necessarily positive definite;
3.  $[\mathcal{G}]$  can be expanded on the same base as  $[\mathcal{M}]$  such as  $[\mathcal{G}] = \sum_{i=1}^N G_i [\mathbb{b}_i]$
4. the coefficients  $G_i$ ,  $i = 1, \dots, N$  of  $[\mathcal{G}]$  are no longer constrained in proper subset of the real numbers.

Therefore, the MaxEnt problem for  $[\mathcal{N}]$  as a function of  $[\mathcal{G}]$  turns to be:

$$[\mathcal{N}]([\mathcal{G}])\text{-Max-Ent} : \begin{cases} \mathbb{E} \left\{ \text{expm} \left( \sum_{i=1}^N G_i [\mathbb{b}_i] \right) \right\} & = [I_n] \\ \mathbb{E} \left\{ \ln \left[ \det \left( \text{expm} \left( \sum_{i=1}^N G_i [\mathbb{b}_i] \right) \right) \right] \right\} & = \nu_{\mathcal{N}}, |\nu_{\mathcal{N}}| < +\infty \end{cases} \quad (4.3.12)$$

Setting  $t_i := \text{tr}([\mathbb{b}_i])$  and applying some algebraic manipulations, the expression (4.3.12) can be simplified in:

$$[\mathcal{N}]([\mathcal{G}])\text{-Max-Ent} : \begin{cases} \mathbb{E} \left\{ \text{expm} \left( \sum_{i=1}^N G_i [\mathbb{b}_i] \right) \right\} & = [I_n] \\ \mathbb{E} \left\{ \sum_{i=1}^N G_i t_i \right\} & = \nu_{\mathcal{N}}, |\nu_{\mathcal{N}}| < +\infty \end{cases} . \quad (4.3.13)$$

Note that in (4.3.13) the PDF of  $[\mathcal{N}]$  is obtained as a function of the PDF of the random vector  $\mathbf{G}$ .

The Max-Ent problem defined by (4.3.13) can be solved as usually (see sect. 4.2.2) by introducing two Lagrange's multipliers  $[\Lambda^{(1)}]$  and  $\lambda^{(2)}$  which allow to take into account all constraints

given by  $[\Lambda^{(1)}] \in \mathbb{M}_n^+(\mathbb{R})$ ,  $\lambda^{(2)} \in \mathbb{R}$ . Moreover, a dimensional argument shows that a good representation of  $[\Lambda^{(1)}]$  has to belong to the subset  $\mathbb{M}_n^{sym}(\mathbb{R}) \subset \mathbb{M}_n^+(\mathbb{R})$ . This remark implies that it can be expanded on the same base than  $[\mathcal{N}]$ :

$$[\Lambda^{(1)}] = \sum_{i=1}^N \lambda_i^{(1)} [\mathfrak{b}_i]. \quad (4.3.14)$$

Following the same path that the one of the fully anisotropic case (see sect. 4.2.2), the solution of the MaxEnt problem must have the following algebraic expression:

$$p_{\mathbf{G}}(\mathbf{g}) = c_0 \exp \left\{ - \left\langle [\Lambda^{(1)}], \expm \left( \sum_{i=1}^N g_i [\mathfrak{b}_i] \right) \right\rangle - \lambda^{(2)} \cdot \sum_{i=1}^N g_i t_i \right\} \quad (4.3.15)$$

As usually, the expression (4.3.15) represents a PDF if it is integrable and normalized. For this reason, an admissible set of the Lagrange's multipliers involved in (4.3.15) has to be defined. For a matter of clarity, we list the LM in a vector denoted by  $\boldsymbol{\lambda} := [\lambda_1^{(1)}, \lambda_1^{(1)}, \dots, \lambda_N^{(1)}, \lambda^{(2)}]$ . The admissible set of the LM is denoted by  $\mathbb{D}_{\boldsymbol{\lambda}} \subset \mathbb{R}^{N+1}$ . It could be shown that  $\mathbb{D}_{\boldsymbol{\lambda}}$  is defined by  $\boldsymbol{\lambda}$  such that  $[\Lambda^{(1)}] \in \mathbb{M}_n^{sym}(\mathbb{R})$  and  $\lambda^{(2)} < 1$  (see Guilleminot and Soize (2013a)).

Finally, before to define how to generate  $\mathbf{G}$ , note that this procedure (see next section) can be in principle used for  $\mathbf{N}$  but it would perform less efficiently because the samples can fall outside from the support of  $[\mathcal{N}]$  and should be rejected (see sect. 3.2.2 in (Guilleminot and Soize, 2012) for instance).

### 4.3.2 Generation of the random vector $\mathbf{G}$

The probability density function found for the random vector  $\mathbf{G}$  gives a simplest algebraic expression than the one of  $[\mathcal{N}]$  (see Eq. 2.34 in (Guilleminot and Soize, 2013a)). Indeed, it is possible to isolate a function of  $\mathbf{G}$  occurring as argument of the exponential function to interpret and to use as *potential*-function in a Fokker-Planck-like (see Soize (1988)) *convection-diffusion* equation whose stationary solution (steady-state) will fit with the PDF of  $\mathbf{G}$  (provided with some more technical hypothesis). In this case, the potential function is given by:

$$\Phi^{\boldsymbol{\lambda}}(\mathbf{u}) = \left\{ \left\langle \sum_{i=1}^N \lambda_i^{(1)} [\mathfrak{b}_i], \expm \left( \sum_{i=1}^N u_i [\mathfrak{b}_i] \right) \right\rangle + \lambda^{(2)} \times \sum_{i=1}^N u_i t_i \right\}. \quad (4.3.16)$$

Let  $\mathbf{Z}^{\boldsymbol{\lambda}}$  be the random vector defined by the PDF  $p^{\boldsymbol{\lambda}}(\mathbf{u}) : \mathbb{R}^N \mapsto \mathbb{R}^+$  given by:

$$p^{\boldsymbol{\lambda}}(\mathbf{u}) = c_{\boldsymbol{\lambda}} \exp -\Phi^{\boldsymbol{\lambda}}(\mathbf{u}) \quad (4.3.17)$$

(evidently  $\mathbf{Z}^{\boldsymbol{\lambda}} \equiv \mathbf{G}$ ). It could be shown that, under some additive hypothesis on the the potential  $\Phi^{\boldsymbol{\lambda}}$  (see below),  $\mathbf{Z}^{\boldsymbol{\lambda}}$  can be obtained as steady state (in Markovian sense) stochastic process driven by a specific Itô's stochastic differential equation.

Let  $(\Theta, \mathcal{T}, \mathcal{P})$  be an probability space. Let  $\mathbf{W} = (\mathbf{W}^1(r), \dots, \mathbf{W}^N(r))$  be a normalized- $\mathbb{R}^N$  Wiener process (see Lamberton and Lapeyre (2007); Krée (2012)) defined on  $(\Theta, \mathcal{T}, \mathcal{P})$ , *i.e.* a  $\mathbb{R}^N$  valued centred second order Gaussian process having the following properties:

1.  $\mathbf{W}(0) = 0$  almost surely;
2.  $\mathbf{W}$  is a continuous process;
3.  $\mathbf{W}$  has independent increments *i.e.*  $(\mathbf{W}(r) - \mathbf{W}(s)) \perp (\mathbf{W}(s) - \mathbf{W}(t)) \forall 0 \leq r \leq s \leq t$ ;
4. the increments follow the Gaussian distribution given by  $(\mathbf{W}(s) - \mathbf{W}(s)), \sim \mathcal{N}(0, t - s) \forall 0 \leq s \leq t$ .

Note that sometimes called directly Brownian motion (Baldi, 1984; Gardiner, 1985), referring to his archetypal physical application.

The properties just recalled are sufficient to rigorously characterize the expression of the stochastic differential  $d\mathbf{W}(r)$  and use the Itô's calculus.

Let  $(\mathbf{U}, \mathbf{V})$  a Markov stochastic process defined by  $(\Theta, \mathcal{T}, \mathcal{P})$  with values in  $\mathbb{R}^N \times \mathbb{R}^N$  and indexed by  $r \in \mathbb{R}^+$  satisfying the Itô's stochastic differential equation (ISDE):

$$\forall r \in \mathbb{R}^+, \begin{cases} d\mathbf{U}(r) &= \mathbf{V}(r) dr \\ d\mathbf{V}(r) &= -\nabla_{\mathbf{u}} \Phi^\lambda(\mathbf{U}(r)) dr - (f^0/2)\mathbf{V}(r) dr + \sqrt{f^0} d\mathbf{W}(r) \end{cases} \quad (4.3.18)$$

with the initial condition given by  $(\mathbf{U}(0), \mathbf{V}(0)) \equiv (\mathbf{U}_0, \mathbf{V}_0)$  almost surely where  $\mathbf{U}_0$  and  $\mathbf{V}_0$  are two given deterministic vectors of  $\mathbb{R}^N$ . The operator  $\nabla_{\mathbf{u}}$  designates the gradient involving differentiation with respect to the coordinate  $\mathbf{u}$ . The parameter  $f^0$  is a free parameter ( $f^0 > 0$ ) allowing to increase speed of convergence towards an eventual steady state, by *killing* the transient part of the evolution of the  $(\mathbf{U}, \mathbf{V})$  (see Soize (2008)).

Assumed the existence of the stationary distribution for the  $(\mathbf{U}(r), \mathbf{V}(r)) : p_S^\lambda(d\mathbf{u}, d\mathbf{v}) = \rho_S^\lambda(\mathbf{u}, \mathbf{v}) d\mathbf{u} d\mathbf{v}$  (where  $\rho_S^\lambda$  denotes its density). It can be shown that  $\rho_S^\lambda$  coincides with the steady state solution the Fokker-Planck-equation (FkPE) (see Soize (2008) for details) reported below:

$$\sum_{j=1}^N \frac{\partial}{\partial u_j} \{v_j \rho_{SFkP}^\lambda(\mathbf{u}, \mathbf{v})\} + \sum_{j=1}^N \frac{\partial}{\partial v_j} \left\{ \left( -\frac{\partial}{\partial u_j} \Phi^\lambda(\mathbf{u}) - (f^0/2)v_j \right) \rho_{SFkP}^\lambda(\mathbf{u}, \mathbf{v}) \right\} + \left( -\frac{f^0}{2} \sum_{j=1}^N \frac{\partial^2}{\partial v_j^2} \rho_{SFkP}^\lambda(\mathbf{u}, \mathbf{v}) \right) \quad \forall (\mathbf{u}, \mathbf{v}) \in \mathbb{R}^N \times \mathbb{R}^N \quad (4.3.19)$$

The necessary conditions for this identification are:

$$\left\{ \begin{array}{ll} \mathbf{u} \mapsto \Phi^\lambda(\mathbf{u}) & \text{continuous on } \mathbb{R}^N, \\ \mathbf{u} \mapsto \|\nabla_{\mathbf{u}} \Phi^\lambda(\mathbf{u})\|_{\mathbb{R}^N} & \text{is locally bounded function on } \mathbb{R}^N \\ \inf_{\|\mathbf{u}\|_{\mathbb{R}^N} > R} \Phi^\lambda(\mathbf{u}) \rightarrow +\infty & \text{as } R \rightarrow +\infty \\ \inf_{\mathbf{u} \in \mathbb{R}^N} \Phi^\lambda(\mathbf{u}) = \Phi^{\min}, & \Phi^{\min} \in \mathbb{R} \\ \int_{\mathbb{R}^N} \|\nabla_{\mathbf{u}} \Phi^\lambda(\mathbf{u})\|_{\mathbb{R}^N} \rho^\lambda(\mathbf{u}) d\mathbf{u} < \infty & \end{array} \right. \quad (4.3.20)$$

Under the conditions (4.3.20), the FkPE (4.3.19) has an unique stationary-solution given by:

$$\rho_{SFkP}^\lambda(\mathbf{u}, \mathbf{v}) = \tilde{c}_\lambda \exp - \left\{ \mathcal{H}^\lambda(\mathbf{u}, \mathbf{v}) \right\}, \quad \mathcal{H}^\lambda(\mathbf{u}, \mathbf{v}) = \frac{1}{2} \|\mathbf{v}\|_{\mathbb{R}^N}^2 + \Phi^\lambda(\mathbf{u}) \quad (4.3.21)$$

where  $\mathcal{H}^\lambda$  represents the Hamiltonian associated with the FKPE and  $\tilde{c}_\lambda$  is the normalization constant of the joint distribution. Finally, taking the marginal density in  $\mathbf{u}$  from the joint PDF (4.3.21), we obtain the wished result:

$$\forall \mathbf{u} \in \mathbb{R}^N, \quad p^\lambda(\mathbf{u}) := c_\lambda \exp -\Phi^\lambda(\mathbf{u}) \equiv \int_{\mathbb{R}^N} \rho_{SFKE}^\lambda(\mathbf{u}, \mathbf{v}) d\mathbf{v} \equiv \int_{\mathbb{R}^N} \rho_S^\lambda(\mathbf{u}, \mathbf{v}) d\mathbf{v} \quad (4.3.22)$$

or in other terms the stationary marginal PDF of  $\mathbf{U}$  coincides with that of the PDF of  $\mathbf{Z}^\lambda$  or again  $\mathbf{U}(r)$  converges in *probability* to  $\mathbf{Z}^\lambda$ :

$$\lim_{r \rightarrow +\infty} \mathbf{U}(r) \xrightarrow{p} \mathbf{Z}^\lambda. \quad (4.3.23)$$

We can conclude ultimately that the random vector  $\mathbf{G}$  can be deduced from the trajectories of stochastic process  $\mathbf{U}(r)$  driven by the Wiener process  $\{\mathbf{W}(r), r > 0\}$  according to the ISDE (4.3.18). This implicit relation between  $\mathbf{G}$  and  $\{\mathbf{W}(r), r > 0\}$  can be depicted by an implicit (measurable) operator  $\mathcal{T}$ :

$$\mathbf{G} = \mathcal{T}(\{\mathbf{W}(r), r > 0\}). \quad (4.3.24)$$

### Discretization scheme for the ISDE

Many schemes can be used to approximate (4.3.18). For instance, the most direct choice is the explicit Euler's scheme (see (Soize, 2008) or (Guilleminot and Soize, 2012)).

In this work, the *Störmel-Verlet* scheme (see (Verlet, 1967)) has been used as in Guilleminot and Soize (2013a). The *Störmer-Verlet* scheme was used in (Verlet, 1967) in the same form as *centred finite differences* for describing efficiently the motion of a big system of particles ( $\sim 1000$ ) interacting through the classical Lennard-Jones potential until achieving its steady states. It is not strange that the same scheme could be useful for other Hamiltonian systems as that described by (4.3.18) and even more for managing random correlated fields involving a large number of points (see the section on Random fields).

For the case of Eq. (4.3.20), the *Störmel-Verlet* approximation is given by:

$$\left\{ \begin{array}{l} r_k = (k-1)\Delta r, \forall k = 1, 2, \dots \\ \mathbf{U}^k = \mathbf{U}(r_k), \\ \mathbf{V}^k = \mathbf{V}(r_k), \\ \mathbf{W}^k = \mathbf{W}(r_k), \\ a = \frac{f^0 \Delta r}{4}, \end{array} \right. \left\{ \begin{array}{l} \mathbf{U}^{k+1/2} = \mathbf{U}^k + \frac{\Delta r}{2} \mathbf{V}^k \\ (\mathbf{L}^k)_j = - \left\{ \frac{\partial \phi^\lambda(\mathbf{u})}{\partial u_j} \right\}_{\mathbf{u}=\mathbf{U}^k}, j = 1, \dots, N \\ \mathbf{V}^{k+1} = \frac{a-1}{a+1} \mathbf{V}^k + \frac{\Delta r}{1+a} \mathbf{L}^{k+1/2} + \sqrt{f^0} \Delta \mathbf{W}^{k+1} \\ \mathbf{U}^{k+1} = \mathbf{U}^{k+1/2} + (\Delta r/2) \mathbf{V}^k \end{array} \right. \quad (4.3.25)$$

where  $\Delta r$  denotes the sampling step,  $r_k$  the discrete time variable,  $\Delta \mathbf{W}^{k+1}$  is the Gaussian independent increment of the Wiener process between  $r_{k+1}$  and  $r_k$  and is got as:

$$\Delta \mathbf{W}^{k+1} := \mathbf{W}(r_{k+1}) - \mathbf{W}(r_k) := \sqrt{\Delta r} \Xi^{k+1}, \quad \forall k \geq 1 \quad (4.3.26)$$

where  $\Xi^{k+1}$  represents the  $(k+1)$ -th copy of a  $\mathbb{R}^N$  valued second-order normalized Gaussian vector  $\Xi$ .

The solution  $\mathbf{Z}^\lambda$  should be thought as:

$$\mathbf{Z}^\lambda := \lim_{\Delta r \downarrow 0} \left( \lim_{r_k \rightarrow \infty} \mathbf{U}(r_k) \right) \quad (4.3.27)$$

and  $\mathbf{G}$  as the result of a measurable operator  $\tilde{\mathcal{T}}$  acting on the normalized Gaussian vector  $\Xi$ :

$$\mathbf{G} = \tilde{\mathcal{T}} \left( \left\{ \Xi^k, k \geq 1 \right\} \right). \quad (4.3.28)$$

Finally, there is another practical reason to prefer this scheme to the standard one. Only one iteration of this scheme is needed to transmit the random information from  $\Delta \mathbf{W}^k$  to  $\mathbf{U}^k$  (being a second order differential equation, the standard scheme would need two iterations).

**Remarks on convergence to the target** In section 4.3.2, we discussed the procedure for generating the the random vector  $\mathbf{G}$ . Here we want to remark some crucial aspect concerning these procedure.  $\mathbf{G}$  coincides with  $\mathbf{Z}^\lambda$  for  $\lambda$  fixed in the admissible set  $\mathbb{D}_\lambda$ , and this identification is allowed only provided by Eq. (4.3.20) (that are defined  $\lambda$ -wisely). Whereas we are interested to search the optimal  $\lambda^*$  making  $\mathbf{G}$  match the constraints Eq. (4.3.13), then the conditions Eq. (4.3.20) have to be checked for any  $\lambda$  in  $\mathbb{D}_\lambda$ .

### 4.3.3 Estimation of mathematical expectation

#### Convergence to the stationary regime

In order to compute the optimal Lagrange's multipliers  $\lambda^*$ , the left side of the constraint on the available information (see Eq. (4.3.13)) has to be estimated. This estimation can be performed considering  $n_s$  independent realizations  $\mathbf{Z}^\lambda(\theta_1), \mathbf{Z}^\lambda(\theta_2), \dots, \mathbf{Z}^\lambda(\theta_{n_s})$  of the random variable  $\mathbf{Z}^\lambda$  obtained by

$$\mathbf{Z}^\lambda(\theta_l) := \mathbf{U}(r, \theta_l) \quad l = 1, \dots, n_s, \quad (4.3.29)$$

for  $r$  sufficient large. In the real calculation, however, the previous relation is replaced by the discrete version of  $\mathbf{U}(r, \theta_l)$  :

$$\mathbf{Z}^\lambda(\theta_l) := \mathbf{U}(r_k, \theta_l) = \mathbf{U}^k(\theta_l) \quad l = 1, \dots, n_s, \quad (4.3.30)$$

with  $k$  sufficient large, where  $\mathbf{U}^k$  is defined in (4.3.25). In practice, two positive integers have to be fixed:  $M, M_0 < M$  ( $10^6$  and  $10^5$  for instance) and the discrete ISDE (4.3.25) is solved for  $r_k = (k-1)\Delta r$  on the interval  $[0, (M-1)\Delta r]$ ; the instant  $r_0 = (M_0-1)\Delta r$  is considered as the first instant for which the stationary regime is reached. The convergence to the stationary solution of the ISDE can be characterized by the map :  $k \mapsto convMes(k)$ ,  $k = 1, \dots, M$

$$convMes(k) := \frac{1}{k} \sum_{i=1}^k \|\mathbf{U}^i(\theta_l)\|^2. \quad (4.3.31)$$

Therefore the maps defined in Eq. (4.3.31) is used for fixing  $M_0$ .

### Sampling for mathematical expectation

Let  $f(\mathbf{g})$  be the function that resume the left side of Eq. (4.3.13).

$$f(\mathbf{g}) = \left\{ \left[ \mathbb{F}^{(1)} \right], f^{(2)} \right\}(\mathbf{g}) = \left\{ \sum_{i=1}^N g_i [\mathbb{b}_i], \sum_{i=1}^N g_i t_i \right\} \quad (4.3.32)$$

The constraint in Eq. (4.3.32) is then defined by :

$$\mathbb{E} \{ f(\mathbf{G}) \} = \{ I_n, \nu_N \}. \quad (4.3.33)$$

Two possible strategies are available for computing the mathematical expectations  $\mathbb{E} \{ f(\mathbf{g}) \}$ .

### Ergodic method

The first one can be obtained by invoking the *ergodic theorem* for the process defined by the Eq. (4.3.18). According to the property of *ergodicity*, a stochastic process will not change its statistical properties with time and its moments (such as the mathematical expectation) can be deduced sampling a single, sufficiently long trajectory of the process (Peebles et al., 2001). In other terms the *space-average* can be replaced by the *time-average*:

$$\mathbb{E} \left\{ f(\mathbf{Z}^\lambda) \right\} = \lim_{T \rightarrow +\infty} \frac{1}{T} \int_0^T f(\mathbf{U}(r, \theta_l)) dr \quad (4.3.34)$$

where  $\mathbf{U}(r, \theta_l)$  and  $f$  are defined respectively by Eq. (4.3.30) and Eq. (4.3.33). In practice the  $\mathbb{E} \{ f(\mathbf{Z}^\lambda) \}$  can be estimate by the tail (beyond the stationary regime) of a discrete trajectory of the ISDE:

$$\widehat{\mathbb{E}}^{ERG} \left\{ f(\mathbf{Z}^\lambda) \right\} = \frac{1}{M - M_0 + 1} \sum_{k=M_0}^M f(\mathbf{U}^k(\theta_l)). \quad (4.3.35)$$

### Monte Carlo method

The second method and more traditional and robust one is represented by the Monte Carlo method. According to this approach, the average value of any function of a random vector can be estimate by averaging the results of of the application of this function to independent realizations of the random vector. In our case, the random vector is the  $\mathbf{Z}^\lambda$  in the stationary regime. Let  $n_s$  independent realizations  $\mathbf{Z}^\lambda(\theta_1), \mathbf{Z}^\lambda(\theta_2), \dots, \mathbf{Z}^\lambda(\theta_{n_s})$  of the random variable  $\mathbf{Z}^\lambda$  defined in Eq. (4.3.29) then, the mathematical expectation  $\widehat{\mathbb{E}} \{ f(\mathbf{Z}^\lambda) \}$  is defined by

$$\mathbb{E} \left\{ f(\mathbf{Z}^\lambda) \right\} = \lim_{n_s \rightarrow +\infty} \frac{1}{n_s} \sum_{l=1}^{n_s} f(\mathbf{U}^k(\theta_l)). \quad (4.3.36)$$

In practice  $n_s$  (with  $n_s$  sufficiently high) trajectories of the ISDE have to be computed until  $r_0$ , then average is estimated on the collection of these last  $n_s$  values :

$$\widehat{\mathbb{E}}^{MC} \left\{ f(\mathbf{Z}^\lambda) \right\} = \frac{1}{n_s} \sum_{l=1}^{n_s} f(\mathbf{U}^{M_0}(\theta_l)). \quad (4.3.37)$$

*Remark*

The ergodic method demand to stock only one trajectory and consequently is less expensive in terms of allocation of memory than the Monte-Carlo method. The first one demands to select the tail of a trajectory after having estimated the stationary regime on the same trajectory. This necessarily need that the definition of stationary regime is given on the single trajectory. Moreover, the estimation by ergodic method appers to be *per se* not parallelizable. Otherwise the MC estimation is performed through independent trajectories that can be naturally be assigned to an independent computational process. The stationary limit can be checked in this case observing the stabilization of the estimate of Eq. (4.3.37) as function of  $M_0$ . For the research of the optimal  $\lambda^*$ , for the random matrix problem, both technique can be profitably used. For the random matrix problem (see next section) one estimation of  $\widehat{\mathbb{E}}\{f(\mathbf{Z}^\lambda)\}$  have to be computed for each single point; in this case the memory became the computation bottleneck and the ergodic method could be privileged.

## 4.4 From random matrix to random fields

In a typical scenario of modeling heterogeneous materials, a spatial domain  $\Omega \in \mathbb{R}^d$ , where  $d = 1, 2, 3$ , is given and the mechanical properties of a mesh  $\mathfrak{M} := \{x_i, x_i \in \Omega\}$  have to be assigned to all the nodes of a mesh. Let's suppose that the properties of each point  $x_i$  of this mesh belong to the same class of isotropy and imagine that they were produced randomly, then the list of all properties of the mesh would represent one realization of a random fields with assigned symmetry. Let  $\{[\mathcal{M}](x), x \in \Omega\}$  note the random field with assigned symmetry class. The good news is that such a basic realization of the random field can be simply built assigning to each point a realization of a the random matrix  $[\mathcal{M}]$  previously defined. The bad news is that, since the realizations are independent (as a function of independent Gaussian vectors  $\Xi$ ), their assembly in form of field-realization will be spatially independent (and than spatially uncorrelated). Another step of the *Matr-yoska paradigm* is required. The properties of the random field  $\{[\mathcal{M}](x), x \in \Omega\}$  with *spatial correlation* can be built as a result of the injection of *spatially correlated* Gaussian field  $\{\Xi(x), x \in \Omega\}$ . Different strategies are available to produce this random field and can depend on the number of points of the field (Soize, 2006).

### 4.4.1 Small or moderate number of points

For small or moderate number of points standard techniques can be applied. Let  $n_p$  be the number of points, the standard approach involves the definition of the covariance matrix  $[C]^l \in \mathbb{M}_{n_p}$  relying each component of the field  $\Xi^l(x_i)$ ,  $l = 1, \dots, N$  in terms of their relative distance:

$$[C]_{ij}^l = R^l(x_i - x_j) \quad (4.4.1)$$

modulated by an *autocorrelation function*  $R^l$  such that:

$$y \in \mathbb{R}^d, R^l(y) := \mathbb{E}\left(\Xi^l(x+y)\Xi^l(x)\right), (R^l(0) = 1), \lim_{|y| \rightarrow +\infty} R^l(y) = 0. \quad (4.4.2)$$

Each component of the correlated random field  $\Xi^l(x)$  is got as a function of an uncorrelated random field  $\tilde{\Xi}^l(x)$  (as that earlier presented) in this way:

$$\Xi^l(x) = [L]\tilde{\Xi}^l(x) \quad (4.4.3)$$

where  $[L]$  is factor-matrix resulting by the Cholesky's factorization of the covariance matrix ( $[C]^l = [L]^{lT}[L]^l$ ).

#### 4.4.2 Large number of points

For fields with a large number of points an approach derived from the signal theory can be followed. In this case the autocorrelation function  $R^l(y)$  can be assigned by applying the Inverse Fourier Transform of the power spectral density (PSD) function  $S^l(k)$  of the Gaussian field  $\Xi^l(x)$ :

$$R^l(y) = \int_{\mathbb{R}^d} \exp\{i\langle y, k \rangle\} S^l(k) dk. \quad (4.4.4)$$

The previous operation gives explicit solution of  $R^l(y)$  in some noteworthy case. For instance, an useful choice for  $R^l$  can be given by:

$$R^l(y) = \prod_{i=1}^d r_j^l(y_j), \quad y = (y_1, y_2, \dots, y_d) \in \mathbb{R}^d \quad (4.4.5)$$

with the relations:

$$r_j^l(y_j) := \begin{cases} \left(\frac{2L_j^l}{\pi y_j}\right)^2 \sin\left(\frac{\pi y_j}{2L_j^l}\right)^2 & \forall y_j \neq 0; \\ 1 & \text{if } y_j = 0. \end{cases} \quad (4.4.6)$$

where  $L_j^l$ ,  $j = 1, \dots, d$  are constant parameters allowing to scale spatially  $R^l(y)$  and consequently can be interpreted as *autocorrelation lengths*.

The PDF corresponding to the autocorrelation function  $R^l(y)$  is given by:

$$S^l(k) = \prod_{j=1}^d s_j^l(k_j) \quad (4.4.7)$$

$$s_j^l(k_j) := \begin{cases} \frac{L_j^l}{\pi} \left(1 - \left|\frac{k_j L_j^l}{\pi}\right|\right) & \text{if } \left|\frac{k_j L_j^l}{\pi}\right| < 1 \\ 0 & \text{otherwise} \end{cases}$$

$$j = 1, \dots, d$$

Each function  $s_j^l(k_j)$  is a rescaled version of the function:

$$q(\tau) := \begin{cases} (1 - |\tau|) & |\tau| < 1 \\ 0 & \text{otherwise} \end{cases} \quad (4.4.8)$$

that can be discretized, by symmetrically discretizing the interval  $(-1, 1)$ .

Then, fixing a even integer  $\nu$  the discrete version the interval  $(-1, 1)$  is given by the sampling point  $\tau_1, \dots, \tau_\nu$  with constant step  $\Delta = 2/\nu$ :

$$\tau_\beta = -1 + \left(\beta - \frac{1}{2}\right) \frac{2}{\nu}, \quad \beta = 1, \dots, \nu. \quad (4.4.9)$$

The discretized version of the variable  $k_j$  is then given by  $k_{j\beta} = \pi \frac{\tau_\beta}{L_j^l}$ , and the corresponding values  $s_j^l(k_{j\beta})$  are given by:

$$s_j^l(k_{j\beta}) = \frac{L_j^l}{\pi \Delta} S_\beta, \quad S_\beta = \frac{2}{\nu} q(\tau_\beta), \quad \beta = 1, \dots, \nu. \quad (4.4.10)$$

Given the mesh-points  $\mathfrak{M} := \{x^1, \dots, x^{n_p} : x^j \in \Omega \subset \mathbb{R}^d\}$ , let  $x_i = (x_i^1, \dots, x_i^{n_p})$ ,  $i = 1, \dots, d$  denote the list formed by the component  $i$  of all mesh-points; then the  $\nu$ -order approximation  $\widehat{\Xi}^\nu$  of the field  $\Xi$  on the mesh  $\mathfrak{M}$  is got by the expression:

$$\Xi \sim \widehat{\Xi}^\nu(\Psi_{\beta_1 \dots \beta_d}, \Phi_{\beta_1 \dots \beta_d}) = \sum_{\beta_1=1}^\nu \dots \sum_{\beta_d=1}^\nu \sqrt{2S_{\beta_1} \times \dots \times S_{\beta_d}} \cdot \ln \sqrt{-\Psi_{\beta_1 \dots \beta_d}} \cdot \cos \left\{ \Phi_{\beta_1 \dots \beta_d} + \frac{\pi}{L_1} \tau_{\beta_1} x_1 + \dots + \frac{\pi}{L_d} \tau_{\beta_d} x_d \right\} \quad (4.4.11)$$

as a function of a set of uniform independent random variables  $\{\Psi_{\beta_1 \dots \beta_d}, \Phi_{\beta_1 \dots \beta_d}\}_{\beta_1 \dots \beta_d}$  such that  $\Psi_{\beta_1 \dots \beta_d} \sim \mathcal{U}_{[0,1]}$ ,  $\Phi_{\beta_1 \dots \beta_d} \sim \mathcal{U}_{[0,2\pi]}$ .

Some example of one component of the the random fields  $\widehat{\Xi}^\nu$  is depicted in Fig. (4.2).

The three examples have been produced according with the following settings:

- (a)  $\Omega = [0, 4]^3$ ,  $L_1 \equiv L_2 \equiv L_3 = 1$ ,  $n_p = 4913$ ,  $\nu = 30$  ;
- (b)  $\Omega = [0, 2] \times [0, 4] \times [0, 6]$ ,  $L_1 = 1, L_2 = 2, L_3 = 3$ ,  $n_p = 3825$ ,  $\nu = 10$  ;
- (c)  $\Omega = [0, 10]^3$ ,  $L_1 \equiv L_2 = 1, L_3 = 10$ ,  $n_p = 68921$ ,  $\nu = 10$  .

To highlight the smoothness of the spatial gradient of the Gaussian field, the iso-surfaces are traced.

**Remark** The construction of random fields of matrix with assigned symmetry is follows quite straightforwardly that of homologous random matrices. We recall briefly the step chain to be accomplished.

#### Algorithm for the random matrices

1. collect Gaussian independent random variable  $\{\Xi^k, k \geq 1\}$  ;
2. fix the ML  $\lambda$  and run a number of trajectory (according to the choice of the the Ergodic or Monte-Carlo estimation) of the discrete ISDE  $Z^\lambda = \tilde{\mathcal{T}}(\{\Xi^k, k \geq 1\})$  ;

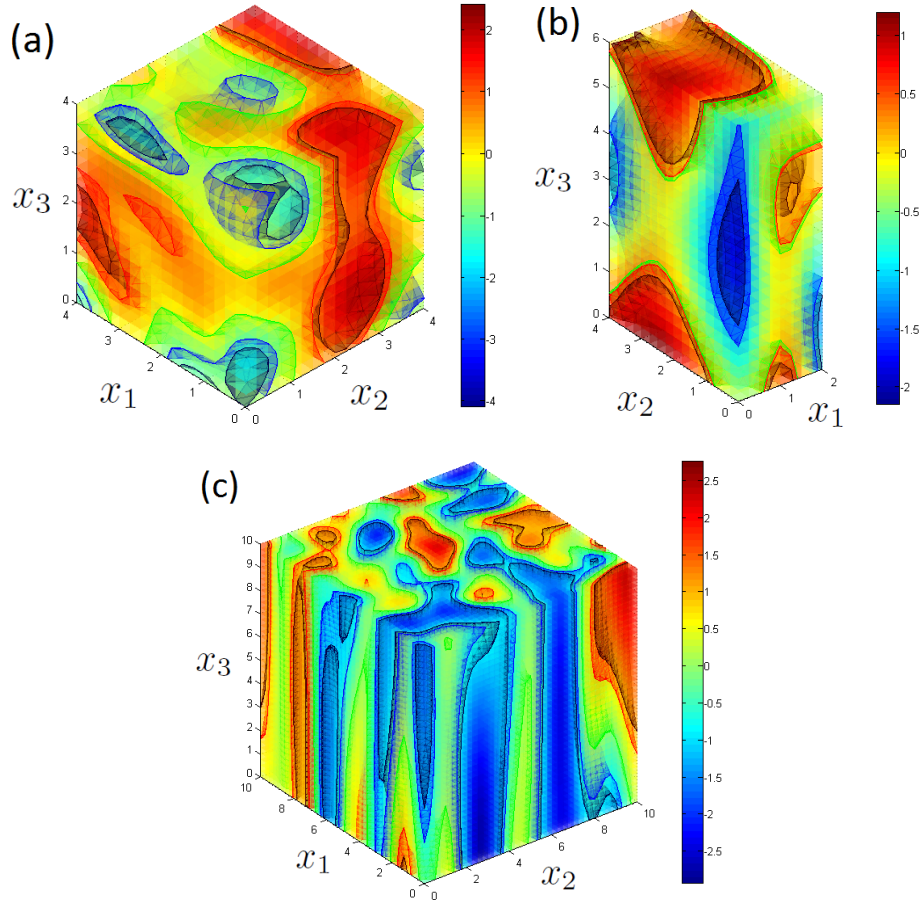


Figure 4.2: Drawing of some example of realization of random field with spatial correlation. Three iso-surfaces of these fields are plotted.

3. fit the ML  $\lambda^*$  to make the cost-index match the prescribed constraints  $G = Z^{\lambda^*} = \tilde{\mathcal{T}}(\{\Xi^k, k \geq 1\})$  ;
4. evaluate  $\mathcal{N}(G)$  ;
5. reconstruct  $\mathcal{M}$  from  $\mathcal{N}$ .

**Algorithm for the random matrix fields**

1. collect a set of Gaussian independent Random Fields  $\{\{\Xi^k(x), x\}, k \geq 1\}$  ;
2. fix the ML  $\lambda_x$  and run a number of trajectory (according to the choice of the the Ergodic or Monte-Carlo estimation) of the discrete ISDE for each point  $x$  of the field:  $Z^{\lambda_x} = \tilde{\mathcal{T}}(\{\Xi^k(x), k \geq 1\})$  ;

3. fit the ML  $\lambda_x^*$  to make the cost-index match the prescribed constraints  $\mathbf{G}(x) = \mathbf{Z}^{\lambda_x^*} = \tilde{\mathcal{T}}(\{\Xi^k(x), k \geq 1\})$ .
4. evaluate  $\mathcal{N}(x)$  form  $\mathbf{G}(x)$  ;
5. reconstruct  $\mathcal{M}(x)$  from  $\mathcal{N}(x)$ .

## 4.5 Applications to random matrices

In this next sections, we will apply the procedure recalled in the previous section to some specific classes. Hereafter, the notation  $[\bullet]$  denotes the Kelvin's representation of the tensors (see Appendix A). The reason for doing so is that the multiplication tables in symmetry-groups provided by Walpole can be used directly.

### 4.5.1 Isotropic class

Any isotropic elastic tensor can be expanded on a base of two orthogonal tensors  $\{\mathbb{b}_i\}_{i=1}^2$  (see Appendix B):

$$[\mathcal{M}] = M_1 [\mathbb{b}_1] + M_2 [\mathbb{b}_2], \quad \text{with } M_1, M_2 > 0. \quad (4.5.1)$$

From Walpole (1984), we know that  $\mathbb{b}_1$  and  $\mathbb{b}_2$  are commutative projectors such as:

$$\mathbb{I} = \mathbb{b}_1 + \mathbb{b}_2, \quad (4.5.2)$$

where  $\mathbb{I}$  denotes the 4th-order identity tensor whose the definition is given in Appendix B. These operators satisfy the multiplication rules:

$$(\mathbb{b}_i)^2 = \mathbb{b}_i, \quad i = 1, 2 \quad \text{and} \quad \mathbb{b}_1 \mathbb{b}_2 = \mathbb{b}_2 \mathbb{b}_1 = \mathbb{O} \quad (4.5.3)$$

We want to show that there exists  $[\mathbf{G}]$  satisfying expression (4.3.10) in the isotropic case. Let's suppose that exists  $[\mathbf{G}] = G_1 [\mathbb{b}_1] + G_2 [\mathbb{b}_2]$  than by definition we have:

$$\begin{aligned} \expm[\mathbf{G}] &= \sum_{k=0}^{\infty} \frac{[\mathbf{G}]^k}{k!} = [\mathbb{I}] + [\mathbf{G}]^1 + \frac{[\mathbf{G}]^2}{2!} + \dots = \\ &= [\mathbb{I}] + (G_1 [\mathbb{b}_1] + G_2 [\mathbb{b}_2]) + \frac{(G_1 [\mathbb{b}_1] + G_2 [\mathbb{b}_2])^2}{2!} + \dots = \\ &= [\mathbb{b}_1] + [\mathbb{b}_2] + \left( G_1 [\mathbb{b}_1] + \frac{(G_1 [\mathbb{b}_1])^2}{2!} + \dots \right) + \left( G_2 [\mathbb{b}_2] + \frac{(G_2 [\mathbb{b}_2])^2}{2!} + \dots \right) = \\ &= \left( 1 + G_1 + \frac{(G_1)^2}{2!} + \dots \right) [\mathbb{b}_1] + \left( 1 + G_2 + \frac{(G_2)^2}{2!} + \dots \right) [\mathbb{b}_2] \\ &= \exp G_1 [\mathbb{b}_1] + \exp G_2 [\mathbb{b}_2]. \end{aligned} \quad (4.5.4)$$

Then, given  $[\mathcal{N}] = N_1 [\mathbb{b}_1] + N_2 [\mathbb{b}_2]$ , it exists  $[\mathbf{G}]$  such that  $[\mathcal{N}] = \expm[\mathbf{G}]$  and can be expanded on the same base. The coefficients of  $[\mathcal{N}] = N_1 [\mathbb{b}_1] + N_2 [\mathbb{b}_2]$  can be rewritten as:

$$N_1 = \exp G_1, \quad N_2 = \exp G_2. \quad (4.5.5)$$

The PDF of  $[\mathcal{N}] (\mathbf{G})$  is obtained particularizing the expression of the potential Eq. (4.3.16) to the current case:

$$\begin{aligned}
 \Phi^\lambda(\mathbf{g}) &= \left\{ \left\langle \sum_{i=1}^N \lambda_i^{(1)} [\mathbb{b}_i], \exp\left(\sum_{j=1}^N g_j [\mathbb{b}_j]\right) \right\rangle + \lambda^{(2)} \times \sum_{i=1}^N g_i t_i \right\} \\
 &= \left\{ \left\langle \sum_{i=1}^N \lambda_i^{(1)} [\mathbb{b}_i], \sum_{j=1}^N \exp g_j [\mathbb{b}_j] \right\rangle + \lambda^{(2)} \times \sum_{i=1}^N g_i t_i \right\} \\
 &= \left\{ \sum_{i=1}^N \lambda_i^{(1)} \exp g_i (t^2)_i + \lambda^{(2)} \times \sum_{i=1}^N g_i t_i \right\}
 \end{aligned} \tag{4.5.6}$$

where we have  $(t^2)_i = \text{tr}[\mathbb{b}_i]^2$ .

In the isotropic case, thanks to Eq. (4.5.3), it results that:

$$\text{tr}[\mathbb{b}_i]^2 \equiv \text{tr}[\mathbb{b}_i], \quad \text{tr}[\mathbb{b}_1] = 1, \quad \text{tr}[\mathbb{b}_2] = 5. \tag{4.5.7}$$

The potential and its gradient become:

$$\Phi^\lambda(\mathbf{u}) = \left\{ \left( \lambda_1^{(1)} \exp u_1 + \lambda^{(2)} u_1 \right) + 5 \left( \lambda_2^{(1)} \exp u_2 + \lambda^{(2)} u_2 \right) \right\}, \tag{4.5.8}$$

$$\nabla_{\mathbf{u}} \Phi^\lambda(\mathbf{u}) = \begin{bmatrix} \lambda_1^{(1)} \exp u_1 \\ 5 \times \lambda_2^{(1)} \exp u_2 \end{bmatrix} + \lambda^{(2)} \begin{bmatrix} 1 \\ 5 \end{bmatrix}. \tag{4.5.9}$$

The final form of the PDF is therefore:

$$p_{\mathbf{G}}^\lambda(\mathbf{g}) := c_\lambda \exp - \left\{ \left( \lambda_1^{(1)} \exp g_1 + \lambda^{(2)} g_1 \right) + 5 \left( \lambda_2^{(1)} \exp g_2 + \lambda^{(2)} g_2 \right) \right\}. \tag{4.5.10}$$

For a fixed  $\lambda = [\lambda_1^{(1)}, \lambda_2^{(1)}, \lambda^{(2)}]$ , the PDF  $p_{\mathbf{G}}^\lambda(\mathbf{g})$  is obtained as stationary measure of (4.3.18) according to the potential given by Eq. (4.5.9). The proof of existence of the stationary solution associated with this potential (*i.e.* verification of Eq. (4.3.25)) is given in the Appendix of Guilleminot and Soize (2013a).

Nevertheless, a generic  $\lambda$  does not solve yet the MaxEnt problem for  $[\mathcal{M}](\mathbf{G})$ . The condition (4.3.13) written for the isotropic case has the following form:

$$\left\{ \begin{array}{l} \left\{ \begin{array}{l} \mathbb{E}\{[\mathcal{M}](\mathbf{G})\} = \mathbb{E}\{N_1(\mathbf{G})\} [\mathbb{b}_1] + \mathbb{E}\{N_2(\mathbf{G})\} [\mathbb{b}_2] \\ [I_6] = [\mathbb{b}_1] + [\mathbb{b}_2] = 1 [\mathbb{b}_1] + 1 [\mathbb{b}_2] \end{array} \right. \\ \mathbb{E}\{1 \times G_1 + 5 \times G_2\} = \nu_{[\mathcal{M}]} \end{array} \right. \tag{4.5.11}$$

and then we get the final system:

$$\begin{aligned}
 \mathbb{E}\{\exp G_1\} &= 1, \\
 \mathbb{E}\{\exp G_2\} &= 1, \\
 \mathbb{E}\{G_1\} + 5 \times \mathbb{E}\{G_2\} &= \nu_{[\mathcal{M}]}.
 \end{aligned} \tag{4.5.12}$$

The final value for the PDF  $p_{\mathbf{G}}^{\lambda^*}$  of  $\mathbf{G}$  is found by minimizing a strictly convex penalty function ( $\mathcal{I}_\alpha(\lambda)$ ,  $\alpha \in (0, 1)$ ) of the distance of the generic  $p_{\mathbf{G}}^\lambda$  from the target defined by Eq. (4.5.12) over the admissibility set of Lagrange's multipliers:

$$\lambda^* = \arg \min_{\lambda \in \mathbb{D}_\lambda} \mathcal{I}_\alpha(\lambda), \quad \mathcal{I}_\alpha(\lambda) := (1 - \alpha) \frac{\|\widehat{e}(\lambda) - e\|^2}{\|e\|^2} + \alpha \frac{(\widehat{\nu}_{[\mathcal{M}]}(\lambda) - \nu_{[\mathcal{M}]})^2}{\nu_{[\mathcal{M}]}^2} \tag{4.5.13}$$

where  $\mathbf{e}$  and  $\nu_{\mathcal{M}}$  are the *right side* of the constraints defined by (4.5.12);  $\widehat{\mathbf{e}}(\boldsymbol{\lambda})$  and  $\widehat{\nu_{\mathcal{M}}}$  represent the Monte Carlo estimation of the *left side* of (4.5.12) according to the choice of a sampling method for the ISDE (using the *ergodicity* of this ISDE or simply the *independence* of its trajectories (see sect. 4.3.3).

The admissible set of the LM in this case is defined by:

$$\mathbb{D}_{\boldsymbol{\lambda}} = \left\{ \boldsymbol{\lambda} = \left[ \lambda_1^{(1)}, \lambda_1^{(1)}, \lambda^{(2)} \right] \in \mathbb{R}^3, \lambda_1^{(1)}, \lambda_2^{(1)} > 0, \lambda^{(2)} < 0 \right\}. \quad (4.5.14)$$

The admissible set given by (4.5.14) for the ML is found by analysing the form of the PDF (4.5.10) by imposing its integrability. First, the PDF can be separated in the product of two functions depending on only one variable of  $g_1$  or  $g_2$ , highlighting the stochastic independence of the two components of the random vector  $\mathbf{G}$ :

$$\begin{aligned} p_{\mathbf{G}}^{\boldsymbol{\lambda}}(\mathbf{g}) &: &= p_{G_1}^{\{\lambda_1^{(1)}, \lambda^{(2)}\}}(g_1) \times p_{G_2}^{\{\lambda_2^{(1)}, \lambda^{(2)}\}}(g_2) \\ p_{G_1}^{\{\lambda_1^{(1)}, \lambda^{(2)}\}}(g_1) &= c_{G_2} \times \exp\left\{-\left(\lambda_1^{(1)} \exp g_1 + \lambda^{(2)} g_1\right)\right\} \\ p_{G_2}^{\{\lambda_2^{(1)}, \lambda^{(2)}\}}(g_2) &= c_{G_2} \times \exp\left\{-5 \times \left(\lambda_2^{(1)} \exp g_2 + \lambda^{(2)} g_2\right)\right\} \end{aligned} \quad (4.5.15)$$

where  $c_{G_1}$  and  $c_{G_2}$  are normalization constants such that  $c_{G_1} \times c_{G_2} = c_{\boldsymbol{\lambda}}$ . Second, by applying the transformation  $[G_1, G_2] \rightarrow [N_1, N_2]$  (4.5.5), we can obtain the PDF of  $N_1$  and  $N_2$  as:

$$\begin{aligned} p_{N_1}^{\{\lambda_1^{(1)}, \lambda^{(2)}\}}(y) &= c_{G_1} \times \mathbb{1}_{\mathbb{R}^+}(y) \times \exp(-\lambda_1^{(1)} y) \times y^{-\lambda^{(2)}-1} \\ p_{N_2}^{\{\lambda_2^{(1)}, \lambda^{(2)}\}}(y) &= c_{G_2} \times \mathbb{1}_{\mathbb{R}^+}(y) \times \exp(-5\lambda_2^{(1)} y) \times y^{-5\lambda^{(2)}-1} \end{aligned} \quad (4.5.16)$$

and, by comparison with the PDF of a Gamma random variable  $Y \sim \Gamma_{\alpha, \beta}$  (which is integrable for  $\alpha, \beta > 0$ )

$$p_Y(y) := \frac{1}{\Gamma(\alpha)} \mathbb{1}_{\mathbb{R}^+}(y) \frac{y^{\alpha-1} \exp(-y/\beta)}{\beta^\alpha}, \quad (4.5.17)$$

where  $\Gamma(\alpha)$  is the Gamma function which is obtained from:

$$\begin{aligned} N_1 &\sim \Gamma_{\alpha_1, \beta_1}, \quad \text{with} \quad (\alpha_1, \beta_1) = \left(-\lambda^{(2)}, \frac{1}{\lambda_1^{(1)}}\right) \\ N_2 &\sim \Gamma_{\alpha_2, \beta_2}, \quad \text{with} \quad (\alpha_2, \beta_2) = \left(-5 \times \lambda^{(2)}, \frac{1}{5 \times \lambda_2^{(1)}}\right) \end{aligned} \quad (4.5.18)$$

and the integrability condition  $\lambda_1^{(1)}, \lambda_2^{(1)} > 0, \lambda^{(2)} < 0$ .

**Remark** Since the expected value of a Gamma random variable  $Y \sim \Gamma_{\alpha, \beta}$  is given by  $\mathbb{E}\{Y\} = \alpha\beta$ , the constraints on the expected value of  $N_1$  and  $N_2$  turns to a parametric constraint among the ML parameters:

$$\lambda_1^{(1)} = -\lambda^{(2)}/\underline{N}_1 = -\lambda^{(2)}, \quad \lambda_2^{(1)} = -\lambda^{(2)}/\underline{N}_2 = -\lambda^{(2)}. \quad (4.5.19)$$

These conditions have be satisfied by the optimal ML. It is would verified only in the idealized case consisting in estimation on a huge set if samples of the ISDE in a perfectly stationary solution. Nevertheless, since the condition allows to drive a 3d-space of parameter from only the parameter  $\lambda^{(2)}$ , it is useful for selecting appropriately good initial solution for the optimization procedure. Moreover, it is worthy to note that the condition (4.5.19) somehow represents an homologue condition of that found for the anisotropic case in (4.2.13).

**Remark** We recall that we want to collect realizations of the  $[\mathcal{M}]$  random matrix. Each of them can be reconstructed in this way:

$$[\mathcal{M}](a_k) = \underline{M}_1 N_1(a_k) [\mathbf{b}_1] + \underline{M}_2 N_2(a_k) [\mathbf{b}_2]. \quad (4.5.20)$$

The cost index in (4.5.13) is defined with respect to the parameter to the  $\nu_{[\mathcal{M}]}$  that indirectly fixes the constraint  $\delta_{[\mathcal{M}]}$ . Nevertheless, we are really interested to fix this last parameter then a modified version of the index function is needed to complete the problem. We propose to use the following one:

$$\mathcal{J}_\alpha(\boldsymbol{\lambda}) := (1 - \alpha) \frac{\|\widehat{\mathbf{e}}(\boldsymbol{\lambda}) - \mathbf{e}\|^2}{\|\mathbf{e}\|^2} + \alpha \frac{\left(\widehat{\delta}_{[\mathcal{M}]}(\boldsymbol{\lambda}) - \delta_{[\mathcal{M}]}\right)^2}{\delta_{[\mathcal{M}]}} \quad (4.5.21)$$

where  $\delta_{[\mathcal{M}]}$  can be can be directly expressed as a function of  $N_1, N_2, \underline{M}_1$  and  $\underline{M}_2$ . Firstly, we can note that the square of Frobenius' norm of the matrix representation  $[M]$  of an isotropic tensor can be written as:

$$[n_F^{iso}]^2(\mathbf{m}) := \|[M]\|_F^2 \equiv (t^2)_1 \times (m_1)^2 + (t^2)_2 \times (m_2)^2 = 1 \times (m_1)^2 + 5 \times (m_2)^2 \quad (4.5.22)$$

where  $\mathbf{m} = [m_1, m_2]$  is the vector of the coefficients of its expansion on the basis. Then, we obtain the wished expression:

$$\begin{aligned} \widehat{\delta}_{[\mathcal{M}]}^2(\boldsymbol{\lambda}) &= \frac{\widehat{\mathbb{E}}(\|[ \mathcal{M} ] - [ \mathcal{M} ]\|_F^2)}{\|[ \mathcal{M} ]\|_F^2} = \frac{\widehat{\mathbb{E}}\{[n_F^{iso}]^2([\underline{M}_1(N_1-1), \underline{M}_2(N_2-1)])\}}{[n_F^{iso}]^2([\underline{M}_1, \underline{M}_2])} = \\ &= \frac{\widehat{\mathbb{E}}\{(\underline{M}_1)^2(N_1-1)^2 + 5(\underline{M}_2)^2(N_2-1)^2\}}{(\underline{M}_1)^2 + 5(\underline{M}_2)^2}. \end{aligned} \quad (4.5.23)$$

Using this specific expression for the dispersion of a matrix instead of the standard one is evidently more advantageous in terms of computational time because it doesn't requires any computation of the whole matrix and neither matrix multiplications. The current definition of dispersion has been applied in the section on numerical results. Equivalent versions of (4.5.22) can be found for the other isotropy classes.

## 4.5.2 Transversely isotropic class

Firstly, we will pay attention to specializing (4.3.13) to the current case. We will proceed fixing the symmetry axis  $\mathbf{e}_n$  in the third direction  $\mathbf{e}_3$  the specific transverse isotropic group hereafter has been noted as TI( $\mathbf{e}_3$ ) (the 4-th order representation is given in Appendix B. Note

that is not restrictive because any other representation can be reduced to this choice by the composition with two independent rotations of the Euclidean space. The matrix representation associated with the current subset is noted as  $\mathbb{M}_6^{\text{TI}(\mathbf{e}_3)}$ . Specifically, we will refer to the Kelvin's representation in the next calculation. Since the transversely isotropic material class, as any group of symmetry, includes the identity, the first step for setting the available information is to give the representation (by projecting) of the identity in that subspace (or at least in the chosen representation). This means find the  $\underline{N}_i$  coefficients in the following expression:

$$I_6 = [\underline{\mathcal{M}}] = \mathbb{E}\{[\underline{\mathcal{N}}]\} = \sum_{i=1}^5 \underline{N}_i [\mathbb{b}_i] \quad \underline{N}_i := \mathbb{E}\{N_i\}. \quad (4.5.24)$$

Since the representation  $\{[\mathbb{b}_i]\}_{i=1}^5$  is orthogonal but not orthonormal, we obtain:

$$\underline{N}_i = \frac{\langle I_6, [\mathbb{b}_i] \rangle}{\|[\mathbb{b}_i]\|_F^2} = \frac{t_i}{(t^2)_i} \quad (4.5.25)$$

Therefore, for the subspace  $\mathbb{M}_6^{\text{TI}(\mathbf{e}_3)}$ , we obtain:

$$\{t_i\}_{i=1}^5 = \{1, 1, 0, 2, 2\}, \quad \{(t^2)_i\}_{i=1}^5 = \{1, 1, 2, 2, 2\} \quad (4.5.26)$$

and the coefficients of the identity are given by:

$$\{\underline{N}_i\}_{i=1}^5 = \{1, 1, 0, 1, 1\}. \quad (4.5.27)$$

From the multiplication rules on  $\mathbb{M}_6^{\text{TI}(\mathbf{e}_3)}$  in Kelvin's notation (see (Walpole, 1984)), we know that for any matrix  $[A] \in \mathbb{M}_6^{\text{TI}(\mathbf{e}_3)}$  is possible to give the following symbolic expression on this coefficients, reflecting the underlying algebra:

$$[A] := \{[A_{123}], A_4, A_5\}, \quad [A_{123}] := \begin{bmatrix} A_1 & A_3 \\ A_3 & A_2 \end{bmatrix} \quad (4.5.28)$$

provided by this commutative multiplication rule with any other matrix  $B \in \mathbb{M}_6^{\text{TI}(\mathbf{e}_3)}$ :

$$AB = \{[A_{123}][B_{123}], A_4 B_4, A_5 B_5\} \quad (4.5.29)$$

The previous expression is sufficient for ensuring that:

$$\expm\{A\} = \{\expm\{[A_{123}]\}, \exp A_4, \exp A_5.\} \quad (4.5.30)$$

Then let  $\{N_i\}_{i=1}^5$  be the coefficients of  $[\underline{\mathcal{N}}]$  ( $N_4, N_5 > 0, [\underline{\mathcal{N}}_{123}] > 0$ ) exists another set of coefficients  $\{G_i\}_{i=1}^5$  defining  $[\underline{\mathcal{G}}]$  on the same base of  $[\underline{\mathcal{N}}]$  such that  $[\underline{\mathcal{N}}] = \expm[\underline{\mathcal{G}}]$  and their coefficients can be arranged according to Eq. (4.5.30). The same evidently results for the target  $\{\underline{N}_i\}_{i=1}^5$ . The information constraint on the first moment can be resumed as:

$$\mathbb{E} \left\{ \begin{bmatrix} N_1 & N_3 \\ N_3 & N_2 \\ N_4 \\ N_5 \end{bmatrix} \right\} = \mathbb{E} \left\{ \expm \begin{bmatrix} G_1 & G_3 \\ G_3 & G_2 \end{bmatrix} \right\} = \begin{bmatrix} \begin{bmatrix} 1 & 0 \\ 0 & 1 \end{bmatrix} \\ 1 \\ 1 \end{bmatrix}. \quad (4.5.31)$$

The constraint on the second moment, by means of Eq. (4.5.26), turns to:

$$\mathbb{E}\{G_1 + G_2 + 2(G_4 + G_5)\} = \nu_{[\mathcal{M}]}. \quad (4.5.32)$$

Equations (4.5.31) and (4.5.32) represent the homologue conditions of Eq. (4.5.12) for the transverse isotropic case.

Let's focus now on the specification of the potential function Eq. (4.3.16). We consider the original form:

$$\Phi^\lambda(\mathbf{u}) = \left\{ \left\langle \left[ \Lambda^{(1)} \right], \expm \left( \sum_{i=1}^N u_i [\mathbb{b}_i] \right) \right\rangle + \lambda^{(2)} \cdot \sum_{i=1}^N u_i t_i \right\}. \quad (4.5.33)$$

The LM  $[\Lambda^{(1)}]$ , as already remarked, belongs to the same subspace of its counterparts  $\mathbb{M}_6^{\text{TI}(\mathbf{e}_3)}$  than it can be rewritten in the form defined by (4.5.29) as:

$$[\Lambda^{(1)}] := \left\{ \left[ \Lambda_{123}^{(1)} \right], \Lambda_4^{(1)}, \Lambda_5^{(1)} \right\}, \quad \left[ \Lambda_{123}^{(1)} \right] := \begin{bmatrix} \lambda_1^{(1)} & \lambda_3^{(1)} \\ \lambda_3^{(1)} & \lambda_2^{(1)} \end{bmatrix}, \quad (4.5.34)$$

with  $\det \left[ \Lambda_{123}^{(1)} \right] > 0, \Lambda_4^{(1)} > 0, \Lambda_5^{(1)} > 0$ .

Applying (4.5.26) and (4.5.29) to the dual product of  $[\Lambda^{(1)}]$  and  $[\mathcal{N}]$ , we obtain the first part of the expression at (4.5.33):

$$\left\langle \left[ \Lambda^{(1)} \right], [\mathcal{N}] \right\rangle = \left\langle \left[ \Lambda_{123}^{(1)} \right], [\mathcal{N}_{123}] \right\rangle + 2\lambda_4 N_4 + 2\lambda_5 N_5 \quad (4.5.35)$$

and the potential turns to be:

$$\begin{aligned} \Phi^\lambda(\mathbf{u}) &= \left\langle \begin{bmatrix} \lambda_1^{(1)} & \lambda_3^{(1)} \\ \lambda_3^{(1)} & \lambda_2^{(1)} \end{bmatrix}, \expm \begin{bmatrix} u_1 & u_3 \\ u_3 & u_2 \end{bmatrix} \right\rangle + \\ &+ 2\lambda_4^{(1)} \exp u_4 + 2\lambda_5^{(1)} \exp u_5 + \lambda^{(2)} [u_1 + u_2 + 2(u_4 + u_5)] \end{aligned} \quad (4.5.36)$$

This gradient becomes :

$$\nabla_{\mathbf{u}} \Phi^\lambda(\mathbf{u}) = \left\{ \left[ \begin{array}{c} \lambda_1^{(1)} n_1(\mathbf{g}) + \lambda_3^{(1)} n_3(\mathbf{g}) \\ \lambda_2^{(1)} n_2(\mathbf{g}) + \lambda_3^{(1)} n_3(\mathbf{g}) \\ (\lambda_1^{(1)} + \lambda_2^{(1)}) n_3(\mathbf{g}) + \lambda_3^{(1)} (n_2(\mathbf{g}) + n_3(\mathbf{g})) \\ 2\lambda_4^{(1)} n_4(\mathbf{g}) \\ 2\lambda_5^{(1)} n_5(\mathbf{g}) \end{array} \right]_{|_{\mathbf{g}=\mathbf{u}}} + \lambda^{(2)} \begin{bmatrix} 1 \\ 1 \\ 0 \\ 2 \\ 2 \end{bmatrix} \right\}^T \quad (4.5.37)$$

where  $(n_1, n_2, n_3, n_4, n_5)$  depend on  $(g_1, g_2, g_3, g_4, g_5)$  through:

$$\begin{bmatrix} n_1 & n_3 \\ n_3 & n_2 \end{bmatrix} = \expm \left\{ \begin{bmatrix} g_1 & g_3 \\ g_3 & g_2 \end{bmatrix} \right\}, \quad n_4 = \exp g_4, n_5 = \exp g_5. \quad (4.5.38)$$

The final result can be expressed more compactly as:

$$\nabla_{\mathbf{u}} \Phi^{\lambda}(\mathbf{u}) = \boldsymbol{\lambda}^T \begin{bmatrix} n_1 & & & n_3 & & \\ & n_2 & & n_3 & & \\ n_3 & n_3 & n_1 + n_2 & & & \\ & & & & n_4 & \\ & & & & & n_5 \\ 1 & 1 & 0 & 2 & 2 & \end{bmatrix} (\mathbf{u}) \quad (4.5.39)$$

The admissibility set for the LM is defined by:

$$\mathbb{D}_{\boldsymbol{\lambda}} = \left\{ \begin{aligned} \boldsymbol{\lambda} &= [\lambda_1^{(1)}, \lambda_2^{(1)}, \lambda_3^{(1)}, \lambda_4^{(1)}, \lambda_5^{(1)}, \lambda^{(2)}] \in \mathbb{R}^6 : \\ \lambda_1^{(1)} \lambda_2^{(1)} - \left(\lambda_3^{(1)}\right)^2 &> 0, \\ \lambda_4^{(1)}, \lambda_5^{(1)}, -\lambda^{(2)} &> 0, \\ \lambda_4^{(1)} = \lambda_5^{(1)} = -\lambda^{(2)} &\} \end{aligned} \right. \quad (4.5.40)$$

where the conditions  $\lambda_4^{(1)}, \lambda_5^{(1)}, -\lambda^{(2)} > 0$ ,  $\lambda_4^{(1)} = \lambda_5^{(1)} = -\lambda^{(2)}$ , as in the *isotropic* case, come from the observation that:

$$N_i \sim \Gamma_{\alpha_i, \beta_i} \quad \text{for } i = 4, 5 \quad \text{where } (\alpha_i, \beta_i) = \left( -2\lambda^{(2)}, \frac{1}{2\lambda^{(1)}_i} \right). \quad (4.5.41)$$

The proof of the existence of the stationary solution associated to this potential should be verified (see Eq. (4.3.20)). Actually, it can be shown that numerical solutions for  $\boldsymbol{\lambda}$  in  $\mathbb{D}_{\boldsymbol{\lambda}}$  attains stationary regime for standard indicators of convergence. As in the isotropic case, the Frobenious's norm can be used to define a version of the dispersion depending by the coefficient of the matrix  $[\mathcal{N}]$  and the constants of  $[\mathcal{M}]$ :

$$[n_F^{\text{TI}}]^2(\mathbf{m}) := \|[M]\|_F^2 \equiv 1 \times ((m_1)^2 + (m_1)^2) + 2 \times ((m_3)^2 + (m_4)^2 + (m_5)^2) \quad (4.5.42)$$

where we have used the expression of the trace defined by (4.5.26).

### 4.5.3 Orthotropic class

The construction of the information constraints and the potential function in the *orthotropic* case is exactly the same as that found for the *transverse isotropic* case. In the following we report only the final results and the main variations. An orthotropic material, as all others symmetry classes, is completely defined by its base. This, in turns is completely defined by three orthonormal axis  $(\mathbf{a}, \mathbf{b}, \mathbf{c})$ . Hereafter, we will refer to  $\text{O}(\mathbf{a}, \mathbf{b}, \mathbf{c})$  to indicate the set of elastic tensors belonging to the Orthotropic symmetry with respect to the axis  $(\mathbf{a}, \mathbf{b}, \mathbf{c})$ . In the next calculation have been performed on  $\text{O}(\mathbf{e}_1, \mathbf{e}_2, \mathbf{e}_3)$ . The matrix representation associated to the current subset is noted as  $\mathbb{M}_6^{\text{O}(\mathbf{e}_1, \mathbf{e}_2, \mathbf{e}_3)}$ . As before, we used the Kelvin's representation in the next calculation. As usual, the first step is the representation of the identity matrix on the 9

elements of the orthotropic base (see Appendix **B**). The coefficients of  $I_6$  (and then of  $[\underline{\mathcal{N}}]$ ) are found as a function of the trace of  $[\mathbf{b}_i]$  and  $[\mathbf{b}_i]^2$  for  $i = 1, \dots, 9$ :

$$\{t_i\}_{i=1}^9 = \{1, 1, 1, 0, 0, 0, 1, 1, 1\}, \quad \{t_i^2\}_{i=1}^9 = \{1, 1, 1, 2, 2, 2, 1, 1, 1\} \quad (4.5.43)$$

$$\underline{N}_i = \frac{t_i}{(t^2)_i}, \quad \{\underline{N}_i\}_{i=1}^9 = \{1, 1, 1, 0, 0, 0, 1, 1, 1\}. \quad (4.5.44)$$

For any  $[A] \in \mathbb{M}_6^{\mathcal{O}(\mathbf{e}_1, \mathbf{e}_2, \mathbf{e}_3)}$ , from (Guilleminot and Soize, 2013b), we know that is possible to give an symbolic expression of its coefficients (equivalent to Eq. (4.5.28) in the transversely isotropic case), reflecting the underlying algebra (4.5.45) and repeat the same steps seen for (4.5.30):

$$\{[A_{1,\dots,6}], A_7, A_8, A_9\}, \quad [A]_{1,\dots,6} = \begin{bmatrix} A_1 & A_4 & A_6 \\ & A_2 & A_5 \\ \text{Sym} & & A_3 \end{bmatrix}. \quad (4.5.45)$$

Let  $[\mathcal{N}]$  be the random matrix valued in  $\mathbb{M}_6^{\mathcal{O}(\mathbf{e}_1, \mathbf{e}_2, \mathbf{e}_3)}$ , whose the mean value is given by  $[\underline{\mathcal{N}}]$ . Let  $\{N_i\}_{i=1}^9$  be its coefficients then by (4.5.45), it admits the representation given by:

$$\{[\mathcal{N}_{1,\dots,6}], N_7, N_8, N_9\}, \quad [\mathcal{N}]_{1,\dots,6} = \begin{bmatrix} N_1 & N_4 & N_6 \\ & N_2 & N_5 \\ \text{Sym} & & N_3 \end{bmatrix} \quad (4.5.46)$$

and, since the matrix is definite positivity, their coefficients must satisfy  $N_7, N_8, N_9 > 0, [\mathcal{N}_{1,\dots,6}] > 0$ . In the same way exists  $[\mathcal{G}]$  such that  $[\mathcal{N}] = \text{expm}[\mathcal{G}]$  and can be decomposed on the same base of  $[\mathcal{N}]$ . The set of its coefficients  $\{G_i\}_{i=1}^9$  can be equivalently arranged as:

$$\{[\mathcal{G}_{1,\dots,6}], G_7, G_8, G_9\}, \quad [\mathcal{G}]_{1,\dots,6} = \begin{bmatrix} G_1 & G_4 & G_6 \\ & G_2 & G_5 \\ \text{Sym} & & G_3 \end{bmatrix}. \quad (4.5.47)$$

The constraint on the first moment can be resumed as:

$$\mathbb{E} \left\{ \begin{bmatrix} N_1 & N_4 & N_6 \\ & N_2 & N_5 \\ \text{Sym} & & N_3 \\ N_7 \\ N_8 \\ N_9 \end{bmatrix} \right\} = \mathbb{E} \left\{ \text{expm} \begin{bmatrix} G_1 & G_4 & G_6 \\ & G_2 & G_5 \\ \text{Sym} & & G_3 \\ \exp G_7 \\ \exp G_8 \\ \exp G_9 \end{bmatrix} \right\} = \begin{bmatrix} \begin{bmatrix} 1 & 0 & 0 \\ 0 & 1 & 0 \\ 0 & 0 & 1 \end{bmatrix} \\ 1 \\ 1 \\ 1 \end{bmatrix}. \quad (4.5.48)$$

The constraint on the second moment, by means of (4.5.43), turns to:

$$\mathbb{E}\{G_1 + G_2 + G_3 + G_7 + G_8 + G_9\} = \nu_{[\mathcal{N}]}. \quad (4.5.49)$$

Let's focus now on the specification of the potential function (4.3.16). As before, the Lagrange's multipliers associated with  $[\mathcal{N}]$  belong to  $\mathbb{M}_6^{\text{Ortho}(e_1, e_2, e_3)}$  and benefit from the algebraic decomposition:

$$\left\{ \left[ \Lambda_{1, \dots, 6}^{(1)} \right], \lambda_7^{(1)}, \lambda_8^{(1)}, \lambda_9^{(1)} \right\}, \quad \left[ \Lambda_{1, \dots, 6}^{(1)} \right] = \begin{bmatrix} \lambda_1^{(1)} & \lambda_4^{(1)} & \lambda_6^{(1)} \\ & \lambda_2^{(1)} & \lambda_5^{(1)} \\ \text{Sym} & & \lambda_3^{(1)} \end{bmatrix}. \quad (4.5.50)$$

As consequence of (4.5.46), (4.5.47) and (4.5.50), the potential function assumes the algebraic form:

$$\begin{aligned} \Phi^\lambda(\mathbf{u}) &= \left\langle \begin{bmatrix} \lambda_1^{(1)} & \lambda_4^{(1)} & \lambda_6^{(1)} \\ & \lambda_2^{(1)} & \lambda_5^{(1)} \\ \text{Sym} & & \lambda_3^{(1)} \end{bmatrix}, \text{expm} \begin{bmatrix} u_1 & u_4 & u_6 \\ & u_2 & u_5 \\ \text{Sym} & & u_3 \end{bmatrix} \right\rangle + \\ &+ \lambda_7^{(1)} \exp u_7 + \lambda_8^{(1)} \exp u_8 + \lambda_9^{(1)} \exp u_9 + \\ &+ \lambda^{(2)} [u_1 + u_2 + u_3 + u_7 + u_8 + u_9] \end{aligned} \quad (4.5.51)$$

Its gradient assumes the form given by:

$$\nabla_{\mathbf{u}} \Phi^\lambda(\mathbf{u}) = \boldsymbol{\lambda}^T \begin{bmatrix} n_1 & & & n_4 & & n_6 & & & \\ & n_2 & & n_4 & n_5 & & & & \\ & & n_3 & & n_5 & n_6 & & & \\ n_4 & n_4 & & n_1 + n_2 & n_6 & n_5 & & & \\ & n_5 & n_5 & n_6 & n_2 + n_3 & n_4 & & & \\ n_6 & & n_6 & n_5 & n_4 & n_1 + n_3 & & & \\ & & & & & & n_7 & & \\ & & & & & & & n_8 & \\ & & & & & & & & n_9 \\ 1 & 1 & 1 & & & & & 1 & 1 & 1 \end{bmatrix} (\mathbf{u}) \quad (4.5.52)$$

where  $(n_1, n_2, n_3, n_4, n_5, n_6, n_7, n_8, n_9)$  depend on  $(g_1, g_2, g_3, g_4, g_5, g_6, g_7, g_8, g_9)$  through:

$$\begin{bmatrix} n_1 & n_4 & n_6 \\ & n_2 & n_5 \\ \text{Sym} & & n_3 \end{bmatrix} = \text{expm} \left\{ \begin{bmatrix} g_1 & g_4 & g_6 \\ & g_2 & g_5 \\ \text{Sym} & & g_3 \end{bmatrix} \right\}, \quad \begin{aligned} n_7 &= \exp g_7, \\ n_8 &= \exp g_8, \\ n_9 &= \exp g_9 \end{aligned} \quad (4.5.53)$$

The admissibility set for the LM is defined by:

$$\begin{aligned} \mathbb{D}_\lambda = \{ & \boldsymbol{\lambda} = [\lambda_1^{(1)}, \lambda_2^{(1)}, \lambda_3^{(1)}, \lambda_4^{(1)}, \lambda_5^{(1)}, \lambda_6^{(1)}, \lambda_7^{(1)}, \lambda_8^{(1)}, \lambda_9^{(1)}, \lambda^{(2)}] \in \mathbb{R}^{10} : \\ & \det \left[ \Lambda_{1, \dots, 6}^{(1)} \right] > 0, \\ & \lambda_7^{(1)}, \lambda_8^{(1)}, \lambda_9^{(1)}, -\lambda^{(2)} > 0, \\ & \lambda_7^{(1)} = \lambda_8^{(1)} = \lambda_9^{(1)} = -\lambda^{(2)} \} \end{aligned} \quad (4.5.54)$$

where the conditions  $\lambda_7^{(1)} = \lambda_8^{(1)} = \lambda_9^{(1)}$ ,  $-\lambda^{(2)} > 0$  and  $\lambda_7^{(1)} = \lambda_8^{(1)} = \lambda_9^{(1)} = -\lambda^{(2)}$ , as in the *isotropic* case, come from the remark that:

$$N_i \sim \Gamma_{\alpha_i, \beta_i} \quad \text{for } i = 7, 8, 9 \quad \text{where } (\alpha_i, \beta_i) = \left( -\lambda^{(2)}, \frac{1}{\lambda^{(1)}_i} \right). \quad (4.5.55)$$

As in the *transversely isotropic* case, the Frobenius's norm can be used to define a version of the dispersion depending on the coefficient of the matrix  $[\mathcal{M}]$  and the constants of  $[\underline{\mathcal{M}}]$ :

$$\begin{aligned} [n_F^{ortho}]^2(\mathbf{m}) : &= \|[M]\|_F^2 \\ &\equiv 1 \times ((m_1)^2 + (m_2)^2 + (m_3)^2 + (m_7)^2 + (m_8)^2 + (m_9)^2) + \\ &\quad + 2 \times ((m_4)^2 + (m_5)^2 + (m_6)^2) \end{aligned} \quad (4.5.56)$$

where we have used the expression of the trace defined in (4.5.43).

## 4.6 Numerical results

The procedure detailed in the preceding section has been applied to some case of study.

### 4.6.1 Examples of random matrices for the isotropic material class

The following elaborations refer to the statistics collected in the previous chapter starting from stochastic homogenization method. In this chapter, a four-scale description of cortical bone was proposed in (Sansalone et al., 2010). Below the organ scale, at the scale of several hundreds micrometers (tissue scale), cortical bone (CB) was considered as constituted of Haversian pores (HP) embedded in a solid matrix called ultrastructure (US). At the scale of a few tens micrometers (US scale), US was considered as made up of collagen (Col) fibers embedded in a mineral foam (MF). We re-proposed them in Tab. 4.1.

Table 4.1: Average tensors of three homogenized materials: mineral foam (MF), ultra-structure (US) and cortical bone (CB). Coefficients of the representations on the respective basis.

Coeff.s of $[\mathbf{C}_*] \in \text{Iso}$	$c_1$ ( $\equiv 3 \times K$ )	$c_2$ ( $\equiv 2 \times G$ )			
units	[GPa]	[GPa]			
$\hat{\mu}_{[\mathbf{C}_{MF}]}^N$	27.701	8.016			

Coeffs of $[\mathbf{C}_*] \in \text{TrIso}(e_3)$	$c_1$	$c_2$	$c_3$	$c_4$	$c_5$
units	[GPa]	[GPa]	[GPa]	[GPa]	[GPa]
$\hat{\mu}_{[\mathbf{C}_{US}]}^N$	15.734	19.334	9.542	7.392	7.421
$\hat{\mu}_{[\mathbf{C}_{CB}]}^N$	14.382	16.890	8.499	5.944	6.292

We applied the Matr-yoshka paradigm to the case of isotropic mineral foam detailed in Tab. 4.1. The available information is defined by  $(\underline{M}_1, \underline{M}_1) = (27.701, 8.016)$  [GPa] and  $\delta_{[\mathcal{M}]} = 0.2033$ . The trajectories of the discrete ISDE have been computed with the parameters given

Table 4.2: Overall measure of variation of stochastic tensor of for mineral-foam (MF), ultra-structure (US) and cortical bone (CB), resulting from the stochastic model.

$\hat{\delta}_{[\text{C}_{\text{MF}}]}^N$	$\hat{\delta}_{[\text{C}_{\text{US}}]}^N$	$\hat{\delta}_{[\text{C}_{\text{CB}}]}^N$
0.2033	0.1265	0.1435

by  $\Delta r = 10^{-3}$ ,  $f_0 = 1$  with the initial condition  $\mathbf{U}_0 = (0, 0)$  and  $\mathbf{V}_0 = (0, 0)$ . The Lagrange's Multipliers have been initially fixed to the values:

$$\boldsymbol{\lambda}^{init} = [\lambda_1^{(1)}, \lambda_2^{(1)}, \lambda^{(2)}], \quad \lambda_1^{(1)} = \lambda_2^{(1)} = -\lambda^{(2)} = 5.0700., \quad (4.6.1)$$

The convergence to the stationary solution of the ISDE has been confirmed evaluating the map  $k \mapsto \text{convMES}(k)$  defined by (4.3.31) on the interval  $k \in \{1, \dots, 10 \times 10^6\}$ . Figure 4.3 depicts the evolution of the map  $k \mapsto \text{convMES}(k)$  and that of its maximum and minimum values. It is seen that the convergence of the stochastic process is obtained for  $M_0 \geq 10^6$ . The optimization of the Lagrange's multipliers has been then performed with respect this choice of parameters  $M_0 = 1 \times 10^6$ ,  $M = 2 \times 10^6$  and the ergodic estimation (4.3.35) has been used for approximating the constraints. Figure 4.4 shows the probability density functions for the vector  $[G_1, G_2]$  on the interval  $[M_0, M]$  corresponding to the initial LM. The first instants of evolution of  $[\mathbf{U}_1^k, \mathbf{V}^k]$  after  $k = M_0$  have been depicted too. The index cost used for fitting the LM is given by (4.5.21) with the definition of dispersion given by (4.5.23), where the parameter  $\alpha$  has been fixed to a value of 0.6. The unconstrained-optimization Matlab-function  $fminsearch(\bullet)$  has been used for minimizing the cost-index with respect to  $\boldsymbol{\lambda}$ . The solution Lagrange multipliers are found to be  $\boldsymbol{\lambda}^* = [4.4828, 4.4631, -4.4631]$  corresponding to a value of the index function of  $\mathcal{J}_{0.6}(\boldsymbol{\lambda}^*) = 2.55 \times 10^{-6}$ . More details on the estimations of the constraints are synthesized in Tab. 4.3.

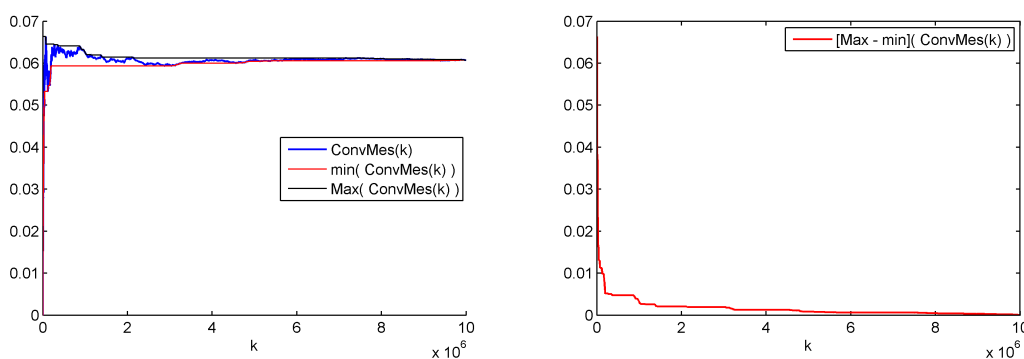


Figure 4.3: Evolution of the map  $k \mapsto \text{convMes}(k)$  defined by (4.3.31) for  $k = 1, \dots, 10^7$ .

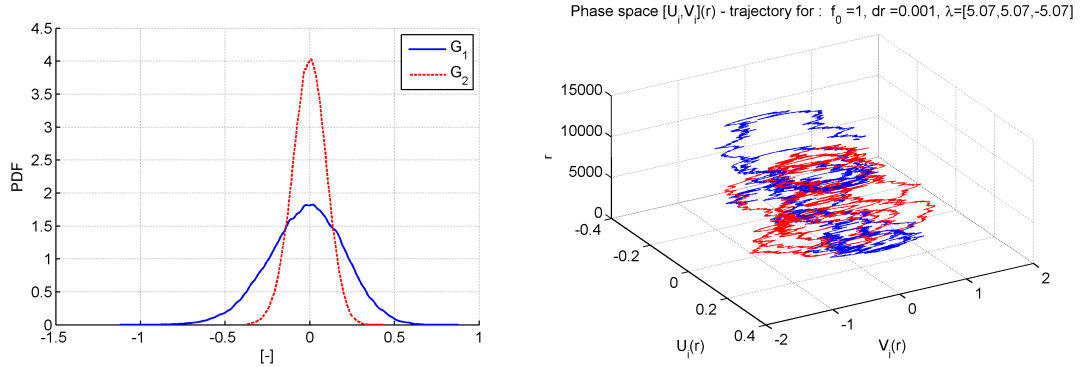
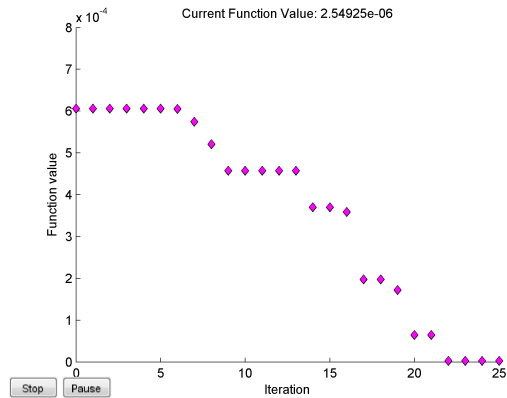


Figure 4.4: PDF of the couple  $[G_1, G_2]$  corresponding to the initial Lagrange’s multiplier(left) on the interval  $k \in [M_0, M]$ . Evolution of the couple  $[U_1^k, V^k]$  for the first instants after  $k = M_0$ (right).

Table 4.3: Results of the optimization of the index function through MATLAB Optimization toolbox. Evolution of the cost index defined by (4.5.21).

		$\lambda^{init}$	$\lambda^*$
		5.0700	4.4828
		5.0700	4.4631
		-5.0700	-4.4631
Target	value	estim.	estim.
$\mathbb{E}\{\exp G_1\}$	1	1.0019	0.9977
$\mathbb{E}\{\exp G_2\}$	1	1.0015	1.0017
$\delta_{[\mathcal{M}]}$	0.2033	0.1921	0.2038
		Index	Index
		6.0632e-04	2.5493e-06
$[\mathcal{M}]$ - Target	value	estim.	estim.
$\underline{M}_1$	27.701	27.7529	27.6383
$\underline{M}_2$	8.016	8.0283	8.0298
$\delta_{[\mathcal{M}]}$	0.2033	0.1921	0.2038



### 4.6.2 Example of the random field for isotropic material class

In this section, we want to give an example of a realization of random field for the isotropic case. As in the homologous section on the isotropic matrix, we model the *mineral foam* corresponding to the Tab. 4.1. Specifically we want to depict one realization of the resulting field corresponding to the bulk and shear moduli ( $K(x)$  and  $\mu(x)$  respectively) as function of their mean values ( $\underline{k}$  and  $\underline{\mu}$ ) and the realization of the ISDE to the Gaussian fields with correlation lengths. In the

current study, the domain  $\Omega = [0, 4]^3$  has been regular discretized in  $n_p = 17^3 = 4913$  points and the approximations  $\widehat{K(x)}^\nu$  and  $\widehat{\mu(x)}^\nu$  have been computed. We summarized below the key steps performed to complete this task. We recall that the matrix field  $[\mathcal{M}](x)$ :

$$[\mathcal{M}](x) = M_1(x) [\mathbb{b}_1] + M_2(x) [\mathbb{b}_2], \quad [\mathcal{M}](x) = [\underline{\mathcal{M}}]^{1/2} [\mathcal{N}](x) [\underline{\mathcal{M}}]^{1/2} \quad (4.6.2)$$

Thanks to the specific structure of the representation of the isotropic basis,  $M_1(x)$  and  $M_2(x)$  are the auto-values of multiplicity 1 and 5 relative to orthogonal spaces (the *spheric* and *deviatoric* one) than, the operation of square root returns simply

$$[\underline{\mathcal{M}}]^{1/2} = \sqrt{\underline{M}_1} [\mathbb{b}_1] + \sqrt{\underline{M}_2} [\mathbb{b}_2]$$

thanks to the product rule, we obtain:

$$\begin{aligned} [\mathcal{M}](x) &= \underline{M}_1 N_1(x) [\mathbb{b}_1] + \underline{M}_2 N_2(x) [\mathbb{b}_2] = \\ &= 3 \underbrace{\underline{k} N_1(x)}_{K(x)} [\mathbb{b}_1] + 2 \underbrace{\underline{\mu} N_2(x)}_{\mu(x)} [\mathbb{b}_2] = \end{aligned} \quad (4.6.3)$$

The bulk and shear fields formally result from the expression given by:

$$K(x) = \underline{k} N_1(x) = \underline{k} \exp G_1(x) \quad \mu(x) = \underline{\mu} N_2(x) = \underline{\mu} \exp G_1(x). \quad (4.6.4)$$

The realization of the field  $\mathbf{G}(x) = [G_1, G_2](x)$  in the previous expression is found as usually by applying (4.3.28) given by  $\mathbf{G} = \tilde{\mathcal{T}}(\{\Xi^k, k \geq 1\})$ .

Specifically, an approximation  $\widehat{\Xi}^\nu$  of the 2-dimensional Gaussian field  $\Xi$  on the cubic regular mesh has been computed. Both his components  $\widehat{\Xi}^1(x)$ ,  $\widehat{\Xi}^2(x)$  have been simulated with the same autocorrelation length  $L_1 = L_2 = L_3 = 1$  and parameter  $\nu = 30$  (see sect. 4.4).

The realization of the approximation  $\widehat{\mathbf{G}}(x)^\nu$  has been computed by applying one iteration of the discretized isotropic-ISDE with the optimal LM found for random isotropic matrices (see previous section) to the  $\widehat{\Xi}^\nu$ .

$$\{\widehat{\Xi}^\nu, x\} \rightarrow \text{1-step-iso.-ISDE} \rightarrow \left\{ \left[ \widehat{\mathbf{U}}(x)^\nu, \widehat{\mathbf{V}}(x)^\nu \right]^{(1)}, x \right\} \rightarrow \left\{ \widehat{\mathbf{G}}(x)^\nu, x \right\}^{(1)}. \quad (4.6.5)$$

Finally, the realization  $\left\{ \widehat{K}(x)^\nu, x \right\}^{(1)}$  and  $\left\{ \widehat{\mu}(x)^\nu, x \right\}^{(1)}$  have been found by:

$$\begin{aligned} \left\{ \widehat{K}(x)^\nu, x \right\}^{(1)} &= \left\{ \underline{k} \exp \left\{ \widehat{G}_1(x)^\nu, \right\}, x \right\}^{(1)} \\ \left\{ \widehat{\mu}(x)^\nu, x \right\}^{(1)} &= \left\{ \underline{\mu} \exp \left\{ \widehat{G}_2(x)^\nu, \right\}, x \right\}^{(1)}, \end{aligned} \quad (4.6.6)$$

The results concerning the bulk and shear fields are depicted in Fig. 4.5.

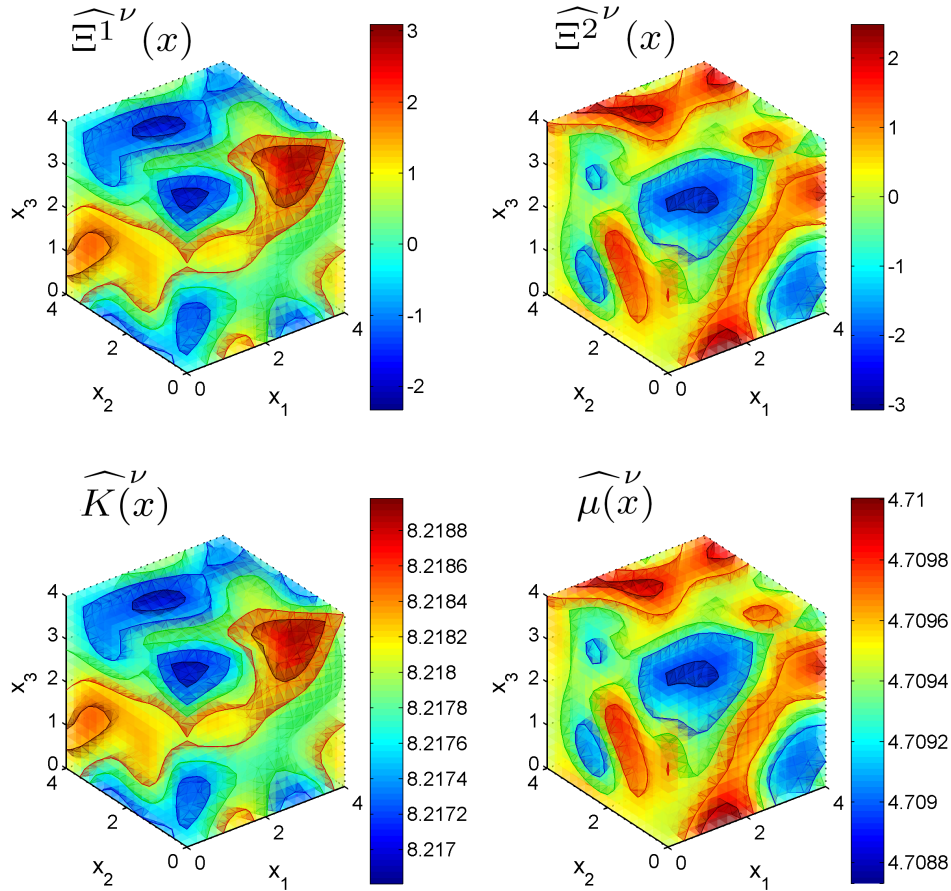


Figure 4.5: Random fields with spatial correlation. Regular discretization of the set  $\Omega = [0, 4]^3$  in  $n_p = 4913$  points. On the top the components of the auxiliary Gaussian random fields  $\widehat{\Xi}^1(x)$  and  $\widehat{\Xi}^2(x)$  simulated with the same autocorrelation length  $L_1 = L_2 = L_3 = 1$  and parameter  $\nu = 30$ . On the bottom the realizations of the bulk *modulus* random field  $K(x)$  and the shear *modulus* random field  $\mu(x)$  corresponding to the auxiliary random fields. The isosurfaces corresponding to the estimated quantiles  $q = 5\%, 25\%, 50\%, 75\%$  and  $95\%$  are added.

## 4.7 Conclusion and perspective

In this chapter, a general framework (*re-baptised* Matr-yoska paradigm) of the modeling random matrices and fields exhibiting assigned material symmetry has been exposed. The method introduced by other authors (Guilleminot and Soize, 2013a) has been applied to isotropic composite of the nanometric *mineral foam* ensuring the matching with statistical constraints becoming from other studies (micro-mechanical homogenization). The optimization of Lagrange's multipliers has been applied to an original cost function specifically simplified for the isotropic case. The

method, even though, was originally defined for all symmetry classes, (Guilleminot and Soize, 2013a) has been applied to the isotropic class. Here, we provided the necessary calculation (gradient of the potential function, admissibility domain for the Legrange's multipliers) for being applied in future in modeling other typical classes concerned in bone anisotropy (*transversely isotropic* and *orthotropic* material symmetry classes).

## 4.8 Appendix

### A Kelvin' representation of a 4th-order tensor

The elastic tensor  $\mathfrak{c}$  is defined as a 4th-order tensor in the tridimensional space describing the linear relation between the strain tensor  $\mathbf{E}$  and the stress tensor  $\mathbf{S}$ . This relation takes the form:

$$\mathbf{S} = \mathfrak{c} : \mathbf{E}, \quad S_{kl} = c_{klmn} E_{mn}, \quad (4.8.1)$$

where the symbol “:” between two tensors denotes a double contraction of adjacent indexes of tensors of rank two and higher.

The 3 symmetry conditions (*minor* and *mayor*) must be considered on the elastic tensor  $\mathfrak{c}$  (Podio-Guidugli, 2000):

$$c_{klmn} = c_{klnm}, \quad c_{klmn} = c_{lkmn}, \quad c_{klmn} = c_{mnlk}. \quad (4.8.2)$$

The second and fourth rank tensors in three dimensions are represented in a Euclidian six-dimensional space as vectors and tensors, respectively. To this end, the representation adopted in this work is called the *Kelvin's* representation in which the new indexes  $I$  et  $J$  vary in the set  $\{1, \dots, 6\}$  such as  $I = (k, \ell)$  and  $J = (m, n)$  where the indices  $k, \ell, m$  and  $n$  vary in the set  $\{1, \dots, 3\}$ . The relation between these indices is the following  $1 = (1, 1), 2 = (2, 2), 3 = (3, 3), 4 = (2, 3), 5 = (1, 3)$  and  $6 = (1, 2)$ . So, the symmetric matrix  $\tilde{\mathfrak{c}}$  associated with  $\mathfrak{c}$  is defined *via* these components by:

$$\tilde{c}_{IJ} = c_{klmn}. \quad (4.8.3)$$

The linear relation between the strain and stress vectors takes the form:

$$\begin{bmatrix} S_{11} \\ S_{22} \\ S_{33} \\ \sqrt{2}S_{13} \\ \sqrt{2}S_{23} \\ \sqrt{2}S_{12} \end{bmatrix} = \begin{bmatrix} \tilde{c}_{11} & \tilde{c}_{12} & \tilde{c}_{13} & \sqrt{2}\tilde{c}_{14} & \sqrt{2}\tilde{c}_{15} & \sqrt{2}\tilde{c}_{16} \\ \tilde{c}_{21} & \tilde{c}_{22} & \tilde{c}_{23} & \sqrt{2}\tilde{c}_{24} & \sqrt{2}\tilde{c}_{25} & \sqrt{2}\tilde{c}_{26} \\ \tilde{c}_{31} & \tilde{c}_{32} & \tilde{c}_{33} & \sqrt{2}\tilde{c}_{34} & \sqrt{2}\tilde{c}_{35} & \sqrt{2}\tilde{c}_{36} \\ \sqrt{2}\tilde{c}_{41} & \sqrt{2}\tilde{c}_{42} & \sqrt{2}\tilde{c}_{43} & 2\tilde{c}_{44} & 2\tilde{c}_{45} & 2\tilde{c}_{46} \\ \sqrt{2}\tilde{c}_{51} & \sqrt{2}\tilde{c}_{52} & \sqrt{2}\tilde{c}_{53} & 2\tilde{c}_{54} & 2\tilde{c}_{55} & 2\tilde{c}_{56} \\ \sqrt{2}\tilde{c}_{61} & \sqrt{2}\tilde{c}_{62} & \sqrt{2}\tilde{c}_{63} & 2\tilde{c}_{64} & 2\tilde{c}_{65} & 2\tilde{c}_{66} \end{bmatrix} \begin{bmatrix} \mathbf{e}_{11} \\ E_{22} \\ E_{33} \\ \sqrt{2}E_{13} \\ \sqrt{2}E_{23} \\ \sqrt{2}E_{12} \end{bmatrix} \quad (4.8.4)$$

The transformation of the three-dimensional second rank tensor components to six-dimensional vector components is directly assured by these relations and *vice versa*. In particular, (Mehrabadi

and Cowin, 1990) have shown that the  $1/2$  factor introduced on the three shear *moduli* of  $\tilde{\mathbf{c}}$  ensures that  $\tilde{\mathbf{c}}$  is a tensor in Euclidian six-dimensional space. In addition, the  $\sqrt{2}$  factor on the vectors  $\tilde{\mathbf{S}}$  whose the components are defined by  $[S_{11}, S_{22}, S_{33}, \sqrt{2}S_{13}, \sqrt{2}S_{23}, \sqrt{2}S_{12}]$  or  $\tilde{\mathbf{E}}$  guarantees that the scalar product of the six dimensional vectors is equal to the trace of the product of the corresponding second rank tensors  $\tilde{\mathbf{S}} \cdot \tilde{\mathbf{E}} = \text{Tra}(\mathbf{S} \mathbf{E})$  where  $\text{Tra}$  is the trace operator.

In the text body, the notation tilde has been dropped.

## B Representation of classes of material symmetry

In this section, we resume the representation of the symmetry class of isotropic materials used (1) for describing the result of micro-mechanical homogenization and (2) for approaching the problem of the classification of the results of the FE and FFT methods. For a wider overview on other isotropic classes we refer to the works of (Walpole, 1984) and (Guilleminot and Soize, 2013b). In our presentation,  $N$  represent the number of necessary and sufficient coefficients  $c_i$  and elements of the orthogonal base (but generally non orthonormal)  $\{\mathbb{b}_i\}$  for the complete definition of a isotropic symmetry class, denoted by  $S$ . For instance  $N = 5$  for a material in the *transverse isotropic* symmetry class,  $N = 9$  for the *orthotropic* one and  $N = 2$  for an *isotropic* one, and so on. This decomposition in the base is given by:

$$\mathbb{c}_S := \sum_{i=1}^N c_i \mathbb{b}_i . \quad (4.8.5)$$

### Isotropic material

An isotropic material is completely defined by two coefficients  $c_1$  and  $c_2$  in its base:

$$\begin{aligned} [\mathbb{b}_1]_{ijkl} &= (1/3)\delta_{ij}\delta_{kl} \\ [\mathbb{b}_2]_{ijkl} &= [\mathbb{I}]_{ijkl} - [\mathbb{b}_1]_{ijkl} \end{aligned} \quad (4.8.6)$$

where  $[\mathbb{I}]$  denotes the fourth order symmetric identity tensor :  $[\mathbb{I}]_{ijkl} = 1/2(\delta_{ij}\delta_{kl} + \delta_{ik}\delta_{jl})$  and  $\delta_{ij}$  designates the Kronecker's symbol.

The projectors  $\mathbb{b}_q$ ,  $q = 1, 2$  satisfy the relation:

$$(\mathbb{b}_q)^2 = \mathbb{b}_q, \quad q = 1, 2. \quad (4.8.7)$$

Indeed, for  $q = 1$ , we have:

$$\begin{aligned} [\mathbb{b}_1^2]_{ijmn} &= \sum_{kl}^3 \left(\frac{1}{3}\delta_{ij}\delta_{kl}\right) \left(\frac{1}{3}\delta_{kl}\delta_{mn}\right) = \frac{1}{9}\delta_{ij}\delta_{mn} \sum_{kl}^3 \delta_{kl} = \\ &= \frac{1}{9}\delta_{ij}\delta_{mn} \times 3 = \frac{1}{3}\delta_{ij}\delta_{mn} = [\mathbb{b}_1]_{ijmn} \end{aligned} \quad (4.8.8)$$

The two coefficients  $c_1$  and  $c_2$  can be related with other couples of coefficients as Lamés coefficients, or in the alternative way with Young's coefficient and Poisson's ratio, according well known functions. For instance, it results that  $c_1 = 3 \times K$  and  $c_2 = 2 \times G$  where  $K$  and  $G$  are respectively the bulk and shear *moduli*.

### Transversely isotropic material

A transversely isotropic material is completely defined by the direction of its axe of symmetry, hereafter noted  $\mathbf{e}_n$ . Once  $\mathbf{e}_n$  has been assigned, any transverse isotropic tensor is fully defined by:

$$\begin{aligned}
 \mathbf{p} &= \mathbf{e}_n \otimes \mathbf{e}_n, & \mathfrak{b}_1 &= \mathbf{p} \otimes \mathbf{p}; \\
 \mathbf{q} &= \mathbf{i} - \mathbf{p}, & \mathfrak{b}_2 &= \mathbf{q} \otimes \mathbf{q}; \\
 & & \mathfrak{b}_3 &= \frac{1}{\sqrt{2}} (\mathbf{p} \otimes \mathbf{q} + \mathbf{q} \otimes \mathbf{p}); \\
 & & \mathfrak{b}_4 &= \mathbf{q} \boxtimes \mathbf{q} - \mathfrak{b}_2; \\
 & & \mathfrak{b}_5 &= \mathbf{i} \boxtimes \mathbf{i} - \mathfrak{b}_1 - \mathfrak{b}_2 - \mathfrak{b}_4;
 \end{aligned} \tag{4.8.9}$$

where the  $\mathbf{i}$  represents the second order identity tensor and the products  $\otimes$  and  $\boxtimes$  operate as:

$$\begin{aligned}
 (g \otimes f)_{ij} &= g_i f_j; \\
 [\mathbf{p} \otimes \mathbf{q}]_{ijkl} &= [\mathbf{p}]_{ij} [\mathbf{q}]_{kl}; \\
 [\mathbf{p} \boxtimes \mathbf{q}]_{ijkl} &= \frac{1}{2} \left( [\mathbf{p}]_{ik} [\mathbf{q}]_{jl} + [\mathbf{p}]_{il} [\mathbf{q}]_{jk} \right).
 \end{aligned} \tag{4.8.10}$$

Throughout this work, the Haversian Porosity has been assumed to be aligned in the  $\mathbf{e}_3$  direction and the direction of the collagen molecules aligned to the direction of the HP. As consequence of the Mori-Tanaka scheme (MTs) of cylindrical inclusions in the  $\mathbf{e}_3$  direction and the micro-mechanical model of the Ultra-Structure transverse isotropic in the direction  $\mathbf{e}_n = \mathbf{e}_3$ . For the same reason, the application of the MTs to the cylindrical pores and the ultrastructure matrix produce a transverse isotropic (in the  $\mathbf{e}_n = \mathbf{e}_3$  direction) model of cortical bone.

We note  $\text{TI}(\mathbf{e}_n)$  the set of elastic tensors belonging to the symmetry transverse isotropic with axe  $\mathbf{e}_n$ .

### Orthotropic material

An orthotropic material is defined as a function of an orthonormal base described from the 3 vectors  $\mathbf{a}$ ,  $\mathbf{b}$  and  $\mathbf{c}$ . The nine base-tensors of 4-th order are given as function of its axis of symmetry. The general representation is given by:

$$\begin{aligned}
 \mathfrak{b}_1 &= \mathfrak{e}^{11}, & \mathfrak{e}^{11} &= (\mathbf{a} \otimes \mathbf{a}) \otimes (\mathbf{a} \otimes \mathbf{a}); \\
 \mathfrak{b}_2 &= \mathfrak{e}^{22}, & \mathfrak{e}^{22} &= (\mathbf{b} \otimes \mathbf{b}) \otimes (\mathbf{b} \otimes \mathbf{b}); \\
 \mathfrak{b}_3 &= \mathfrak{e}^{33}, & \mathfrak{e}^{33} &= (\mathbf{c} \otimes \mathbf{c}) \otimes (\mathbf{c} \otimes \mathbf{c}); \\
 \mathfrak{b}_4 &= (\mathfrak{e}^{12} + \mathfrak{e}^{21}) / 2, & \mathfrak{e}^{12} &= (\mathbf{a} \otimes \mathbf{a}) \otimes (\mathbf{b} \otimes \mathbf{b}) \\
 & & \mathfrak{e}^{21} &= (\mathbf{b} \otimes \mathbf{b}) \otimes (\mathbf{a} \otimes \mathbf{a}); \\
 \mathfrak{b}_5 &= (\mathfrak{e}^{23} + \mathfrak{e}^{32}) / 2, & \mathfrak{e}^{23} &= (\mathbf{b} \otimes \mathbf{b}) \otimes (\mathbf{c} \otimes \mathbf{c}) \\
 & & \mathfrak{e}^{32} &= (\mathbf{c} \otimes \mathbf{c}) \otimes (\mathbf{b} \otimes \mathbf{b}); \\
 \mathfrak{b}_6 &= (\mathfrak{e}^{13} + \mathfrak{e}^{31}) / 2, & \mathfrak{e}^{13} &= (\mathbf{a} \otimes \mathbf{a}) \otimes (\mathbf{c} \otimes \mathbf{c}) \\
 & & \mathfrak{e}^{31} &= (\mathbf{c} \otimes \mathbf{c}) \otimes (\mathbf{a} \otimes \mathbf{a});
 \end{aligned} \tag{4.8.11}$$

$$\begin{aligned}
 [\mathfrak{b}_7]_{ijkl} &= (a_i b_j + a_j b_i) \cdot (a_k b_l + a_l b_k); \\
 [\mathfrak{b}_8]_{ijkl} &= (b_i c_j + b_j c_i) \cdot (b_k c_l + b_l c_k); \\
 [\mathfrak{b}_9]_{ijkl} &= (a_i c_j + a_j c_i) \cdot (a_k c_l + a_l c_k).
 \end{aligned}$$

where the used products are defined in Eq. (4.8.10). We denote by  $O$  the set of elastic tensors belonging to the orthotropic symmetry class with respect to the axis  $(\mathbf{a}, \mathbf{b}, \mathbf{c})$ . This class is denoted by  $O(\mathbf{a}, \mathbf{b}, \mathbf{c})$ .

## Bibliography

- P. Baldi. *Equazioni differenziali stocastiche e applicazioni*, volume 28. Pitagora, 1984.
- D. Gagliardi, V. Sansalone, C. Desceliers, and S. Naili. Tissue mineral density measured at the sub-millimeter scale can provide reliable statistics of elastic properties of bone matrix. *Biomechanics and modeling in mechanobiology*, 2016 (submitted).
- C. W. Gardiner. *Handbook of stochastic methods*, volume 3. Springer Berlin, 1985.
- J. Guilleminot and C. Soize. Generalized stochastic approach for constitutive equation in linear elasticity: a random matrix model. *International Journal for Numerical Methods in Engineering*, 90(5):613–635, 2012.
- J. Guilleminot and C. Soize. Stochastic model and generator for random fields with symmetry properties: Application to the mesoscopic modeling of elastic random media. *SIAM Multiscale Modeling & Simulation*, 11(3):840–870, 2013a.
- J. Guilleminot and C. Soize. On the statistical dependence for the components of random elasticity tensors exhibiting material symmetry properties. *Journal of Elasticity*, 111(2):883–901, 2013b.
- M. Gurtin. *An introduction to continuum mechanics*. Academic Press, 1982.
- E.T. Jaynes. Information theory and statistical mechanics. I. *Physical Review*, 106(4):620–630, 1957a.
- E.T. Jaynes. Information theory and statistical mechanics. II. *Physical Review*, 108(2):171–190, 1957b.
- D. E. Kirk. *Optimal control theory: an introduction*. Mineola, NY: Dover Publications, Inc, 2004.
- C. Krée, P. and Soize. *Mathematics of random phenomena: random vibrations of mechanical structures*, volume 32. Springer Science & Business Media, 2012.
- D. Lamberton and B. Lapeyre. *Introduction to stochastic calculus applied to finance*. CRC press, 2007.
- D. G. Luenberger. *Optimization by vector space methods*. John Wiley & Sons, 1969.
- M.M. Mehrabadi and S.C. Cowin. Eigentensors of linear anisotropic elastic materials. *Q. J. Mech. Appl. Math.*, 43(1):15–41, 1990.
- M.L. Mehta. *Random matrices*. Academic Press, San Diego, USA, second edition, 1991.
- P. Z. Peebles, J. Read, and P. Read. *Probability, random variables, and random signal principles*, volume 3. McGraw-Hill Boston, Mass, USA, 2001.

- P. Podio-Guidugli. *A Primer in Elasticity*, volume 58. Kluwer Academic Publishers, 2000.
- V. Sansalone, S. Naili, V. Bousson, C. Bergot, F. Peyrin, J.D. Laredo, and G. Haiat. Determination of the heterogeneous anisotropic elastic properties of human femoral bone: from nanoscopic to organ scale. *J. Biomech.*, 43(10):1857–1863, 2010.
- C. Shannon. A mathematical theory of communication. *Tech. J.* 27, Bell Syst., 1948.
- C. Soize. Steady-state solution of fokker-planck equation in higher dimension. *Probabilistic Engineering Mechanics*, 3(4):196–206, 1988.
- C. Soize. A nonparametric model of random uncertainties for reduced matrix models in structural dynamics. *Probabilistic engineering mechanics*, 15(3):277–294, 2000.
- C. Soize. Random matrix theory formodeling uncertainties in computational mechanics. *Computer Methods in Applied Mechanics and Engineering*, 194(12-16):1333–1366, 2005.
- C. Soize. Non-gaussian positive-definite matrix-valued random fields for elliptic stochastic partial differential operators. *Computer Methods in Applied Mechanics and Engineering*, 195:26–64, 2006.
- C. Soize. Construction of probability distributions in high dimension using the maximum entropy principle: Applications to stochastic processes, random fields and random matrices. *International Journal for Numerical Methods in Engineering*, 76(10):1583–1611, 2008.
- L. Verlet. Computer “experiments” on classical fluids. I. thermodynamical properties of Lennard-Jones molecules. *Physical review*, 159(1):98, 1967.
- L.J. Walpole. Fourth-rank tensors of the thirty-two crystal classes: multiplication tables. *Proceedings of the Royal Society of London A: Mathematical, Physical and Engineering Sciences*, 391(1800):149–179, 1984.

# Appendix A

## Scientific Production

### Articles

- D. Gagliardi, V. Sansalone, C. Desceliers and S. Naili. *Estimation of bone-elasticity. A priori influence of the couple TMD-HP by a MaxEnt-stochastic model based on  $\mu$ CT Imaging. A multi-techniques validation.*, European Journal of Mechanics - A/Solids, (submitted) Mar. 2017.
- D. Gagliardi, S. Naili, C. Desceliers and V. Sansalone. *Tissue mineral density measured at the sub-millimeter scale provides reliable statistical estimates of elastic properties of bone matrix.*, Biomechanics and Modeling in Mechanobiology, (submitted) Nov. 2016.
- V. Sansalone, D. Gagliardi, C. Desceliers, V. Bousson, J. D.Laredo, F. Peyrin, G. Haiat and S. Naili, *Stochastic multiscale modelling of cortical bone elasticity based on high-resolution imaging*, Biomechanics and Modeling in Mechanobiology, Feb. 2016, 15(1) 111-131.
- D. Gagliardi, V. Sansalone, C. Desceliers, G. Haiat and S. Naili, *Prise en compte des incertitudes dans la modélisation multiéchelle de l'élasticité de l'os à partir de l'imagerie*, 22<sup>e</sup> Congrès Français de Mécanique 2015 24-28 August Lyon FRA.
- V. Sansalone, D. Gagliardi, C. Desceliers, G. Haiat, *On the uncertainty propagation in multiscale modeling of cortical bone elasticity.*, Computer methods in biomechanics and biomedical engineering, Feb. 2015, 18(1) 2054-2055.
- D. Gagliardi, Ohtsuka T. and del Re L. , *Direct C/GMRES control of the air path of a diesel engine.*, IFAC Proceedings Volumes, 2014, 47(3) 3000–3005.

### Proceedings

- D. Gagliardi, Y. Bala, R. Vayron, H. Follet, S. Naili and V. Sansalone, *On uncertain quantification in image-based micro-mechanical modelling of bone elasticity*, 22<sup>nd</sup> European Society of Biomechanics Congress 10-13 July 2016 Lyon FRA.

- V. Sansalone, D. Gagliardi, S. Naili, C. Desceliers, F. Pled, L. Teresi and S. Gabriele, *Image-based multi-scale modelling of bone elasticity: how to make the most out of uncertainty?*, 12<sup>th</sup> World congress on Computational Mechanics 24-26 July 2016 Seoul KR.
- D. Gagliardi, S. Naili, C. Desceliers, and V. Sansalone, *Coupling Max-Ent principle and  $\mu$ CT imaging to model uncertain bone microstructure*, 36<sup>th</sup> International Workshop on Bayesian Inference and Maximum Entropy Methods in Science and Engineering Conference 10-15 July 2016 Ghent BEL.
- D. Gagliardi, V. Sansalone, R. Vayron, S. Naili Y. Bala and H. Follet *A stochastic model for characterizing cortical bone composition based on  $\mu$ CT imaging*, 12<sup>th</sup> World congress on Computational Mechanics 24-26 July 2016 Seoul KR.
- V. Sansalone, D. Gagliardi, C. Desceliers, G. Haiat and S. Naili, *On the uncertainty propagation in multiscale modeling of cortical bone elasticity*, 40<sup>e</sup> Congrès de la Société de Biomécanique 2015 28-30 October 2015 Paris FRA.
- D. Gagliardi, V. Sansalone, C. Desceliers, G. Haiat and S. Naili, *Prise en compte des incertitudes dans la modélisation multiéchelle de l'élasticité de l'os à partir de l'imagerie*, 22<sup>e</sup> Congrès Français de Mécanique 2015 24-28 August Lyon FRA.
- V. Sansalone, D. Gagliardi, C. Desceliers, V. Bousson, J. D.Laredo, F. Peyrin, G. Haiat and S. Naili, *Bone elasticity: 3D Synchrotron imaging, multi-scale modelling, and uncertainties*, 4<sup>th</sup> International Conference on Computational and Mathematical Biomedical Engineering, 29 June-1 July 2015, Cachan FRA.
- V. Sansalone, D. Gagliardi, S. Naili, Y. Bala and C. Desceliers, *A stochastic homogenization approach to estimate bone elastic properties*, 7<sup>th</sup> World Congress of Biomechanics 2014, July 6-11 July Boston (MA) USA.
- D. Gagliardi, T. Ohtsuka and L. del Re, *Direct C/GMRES Control of the Air Path of a Diesel Engine*, 19<sup>th</sup> IFAC World Congress, August 24-29, 2014, Cape Town, South Africa.

## Oral presentations

- D. Gagliardi, S. Naili C. Desceliers, and V. Sansalone, *Coupling Max-Ent principle and  $\mu$ CT imaging to model uncertain bone microstructure*, 36<sup>th</sup> International Workshop on Bayesian Inference and Maximum Entropy Methods in Science and Engineering Conference 10-15 July 2016 Ghent BEL (Poster).
- D. Gagliardi, V. Sansalone, R. Vayron, S. Naili Y. Bala and H. Follet *A stochastic model for characterizing cortical bone composition based on  $\mu$ CT imaging*, 12<sup>th</sup> World congress on Computational Mechanics 24-26 July 2016 Seoul KR.
- D. Gagliardi, V. Sansalone, and S. Naili, *Vers une prédiction robuste de l'élasticité du tissu osseux en utilisant des données issues de la micro-tomographie*, Journée du laboratoire MSME Créteil. FRA

- 
- D. Gagliardi, V. Sansalone, C. Desceliers, G. Haïat and S. Naili, *Prise en compte des incertitudes dans la modélisation multiéchelle de l'élasticité de l'os à partir de l'imagerie*, 22<sup>e</sup> Congrès Français de Mécanique 2015 24-28 August Lyon FRA.
  - D. Gagliardi, V. Sansalone, C. Desceliers, G. Haïat, and S. Naili, *Prise en compte des incertitudes dans la modélisation multiéchelle de l'élasticité de l'os à partir de l'imagerie*, Rencontres franciliennes de mécanique Fédération de recherche F2M-msp, 11-12 May 2015. Fontainebleau FRA.



## Abstract

The hierarchical structure of bone tissues, as well as the heterogeneity and anisotropy of its physical properties and the uncertainty on *in vivo* experimental measures make it impossible to establish a deterministic reliable model of bone mechanical properties. Aiming at providing a valuable aide to diagnostics in orthopaedic, the purpose of this thesis is to develop a robust mechanical model able to account for the experimental uncertainty.

Therefore we developed a multi-scale stochastic model, based on continuum *micromechanics* and *maximum entropy principle* which has proved effective predicting the heterogeneous and anisotropic elastic properties of bone tissue at the organ scale accounting for experimental uncertainty affecting image-based input data.

Aiming to clarify the mechanism of propagation of these uncertainties through the chosen principal multi-scale model, others versions have been analyzed. First, the principal model, which uses the volume fractions of the essential constituents (mineral, water, collagen), as primary variables, has been analyzed scale-by-scale (mineral foam, ultra-structure, cortical bone). The effect of the chosen homogenization methods and volume fractions on the resulting composites (as layers of a random Matryoshka) have been discussed. Thanks to this analysis, this model has been simplified and relied directly to the measures straightly accessible from medical imaging of the bone: the tissue mineral density (TMD) and the haversian porosity (HP) and their calibration at sub-millimeter scale. This version of the stochastic model, proved to be as accurate as the proceeding one and, more effective in the description of the bone.

Finally, the stochastic model of bone has been completed with the direct modeling of the elastic tensors of the involved materials. For this purpose, the random matrix theory has been applied. This theory can be seen as another declination of the *matryoshka* paradigm. In this case, the uncertainty on the random tensor propagate from the inside (random germ) to outside (each layer of random matrix) through a suitable sequence of nonlinear operations. Thanks to the proposed decomposition, at once, the isotropic material class of the resulting material and his spatial variability has been included in the model.

**Keywords:** Stochastic modeling, Multi-Scale models, Homogenization methods, Continuum micromechanics, Elasticity, Uncertainty quantification, Maximum entropy (Max-Ent) principle, Bone, Tissue mineral density, Haversian porosity, Microtomography.



## Résumé

Non seulement la structure hiérarchisée du tissu osseux mais aussi son hétérogénéité, son anisotropie et les incertitudes expérimentales de mesures liées aux matériaux vivants rendent en pratique impossible la définition d'un modèle déterministe fiable de ses propriétés matérielles. Dans une démarche d'aide au diagnostic clinique, l'objectif de cette thèse est de développer une modélisation robuste desdites propriétés à l'échelle de l'organe en intégrant l'incertitude expérimentale de mesures.

Pour ce-faire, nous avons développé un modèle multi-échelle stochastique basé sur le principe du *maximum d'entropie* et des méthodes d'homogénéisation en *champs moyens* (micromécanique) qui s'est montré capable de prédire les propriétés matérielles du tissu osseux à l'échelle de l'organe en prenant en compte les incertitudes expérimentales de données issues de l'imagerie. Dans la perspective d'identifier le mécanisme de propagation de l'incertitude à travers le modèle multi-échelle, plusieurs versions de ce modèle ont été analysées.

Le modèle principal utilise comme variables primaires la fraction volumique des constituants essentiels (le minéral, l'eau et le collagène) pour lesquelles une discussion est proposée échelle par échelle en examinant leur effet sur les propriétés effectives à chaque échelle. Cette description est à l'image d'une *matryoshka*, plus communément appelée poupée russe, via l'aspect multi-échelle. Chaque matryoshka est une série de poupées de tailles décroissantes placées les unes à l'intérieur des autres. Grâce à cette analyse, cette version du modèle a pu être liée de façon directe aux mesures expérimentales issues de l'imagerie médicale que sont la densité minérale du tissu (TMD) et la porosité haversienne (HP) de l'os cortical lors d'une calibration à l'échelle millimétrique. Cette version a été validée en utilisant plusieurs méthodes numériques telles que la méthode aux éléments finis et la méthode de la transformée de Fourier rapide. On a ainsi pu non seulement évaluer la précision de la méthode proposée mais aussi analyser le processus de transfert d'incertitudes entre les échelles.

Enfin, la modélisation stochastique de l'os cortical a été complétée en introduisant des champs de tenseurs d'élasticité des matériaux impliqués dans le processus d'homogénéisation pour l'obtention des propriétés effectives. L'incertitude est introduite via un tenseur aléatoire et se propage spatialement en respectant des longueurs de corrélation et en une suite de réalisations. Ici encore, cette approche peut être vue comme une déclinaison des *matryoshka* via les champs de tenseurs d'élasticité qui se déclinent dans la procédure stochastique.

**Mots clefs :** Modélisation Stochastique, Modélisation Multi-Échelle, Élasticité, Méthodes d'Homogénéisation, Micromécanique, Quantification de l'Incertainitude, Principe du maximum d'entropie (Max-Ent), Os, Densité minérale du tissu, porosité Haversienne, Microtomographie.